X-Ray Scattering Studies of Surfaces and Interfaces

Thesis submitted by
Christopher Andrew Lucas

for the Degree of
Doctor of Philosophy
University of Edinburgh

October 1989

Declaration

Except where otherwise stated, the research undertaken in this thesis is the unaided work of the author. Collaboration with others is indicated in the table of published work.

Acknowledgements

I would like to thank my supervisor Professor R.A. Cowley for introducing me to x-ray scattering and who, despite moving to Oxford, made considerable effort to provide advice and encouragement during the final year. I would also like to thank my second supervisor Dr P.D. Hatton for his help in the laboratory and for showing boundless enthusiasm when nothing seemed to work.

I am grateful to all the members of the experimental solid state physics group at Edinburgh University, in particular, Tom Ryan for his early encouragement, Simon Bates for his flights of fancy, Caolán Patterson for driving under adverse companion conditions and Des McMorrow for his ever cheerful disposition.

I acknowledge the award of a Science and Engineering Research Council grant and the financial assistance provided by G.E.C. I would also like to thank my parents for their unsolicited contributions which helped to keep me marginally above the poverty line.

Finally, I would like to dedicate this thesis to Fiona Murdoch, for providing constant support and exhilarating companionship during the most exciting years of my life.

Contributions

Parts of this thesis are based on the following articles, and the contribution of the other authors is gratefully acknowledged.

Chapter II

C.A. Lucas, E. Gartstein and R.A. Cowley, Acta Crystallographa A45, 416 (1989)

Chapter III

R.A. Cowley and C.A. Lucas, J. de Physique, in press (1989)

Chapter IV

C.A. Lucas, P.D. Hatton, S. Bates, T.W. Ryan, S. Miles and B.K. Tanner, J. Appl. Phys. 36, 1936 (1988).

C.A. Lucas, D.F. McMorrow and S. Bates, in 'Heteroepitaxial Approaches in Semiconductors: Lattice Mismatch and its Consequences'. Electrochem. Soc. (1989).

T.W. Ryan, C.A. Lucas, P.D. Hatton and S. Bates, J. de Physique Colloq., C5, 109 (1987).

S. Bates, P.D. Hatton, C.A. Lucas, T.W. Ryan, S.J. Miles and B.K. Tanner, Advances in X-ray Analysis, 31, 155 (1987).

Abstract

This thesis describes the development of x-ray scattering techniques for the study of microscopic structural properties of surfaces and interfaces down to the Ångstrom level. Experiments were performed using a triple-crystal x-ray diffractometer based on a rotating-anode source. The resolution function of the instrument is discussed in detail, in particular with reference to surface scattering and x-ray reflectivity measurements. Measurements are compared with a Gaussian description of the resolution function and it is found that this is accurate to better than 25%. Results from a variety of Si/SiO_2 structures show how a combination of x-ray reflectivity and crystal truncation rod measurements provide detailed information about amorphous surface films and also, probe the crystallinity at the Si/SiO_2 interface. New features in the crystal truncation rod scattering are caused by distortions in the top three monolayers of the silicon crystal. The reflectivity measurements are extremely sensitive to contaminant layers at the oxide surface and correct interpretation of the results is critically dependent upon their presence in the scattering model. The x-ray reflectivity and crystal truncation rod techniques provide complementary information when applied to the study of thin-layer single quantum well semiconductor devices, thus enabling full structural characterisation on an Ångstrom scale. The lattice parameter strain can be obtained by modelling of the intensity distribution of the crystal truncation rod. The versatility of the x-ray reflectivity technique is demonstrated in characterising the photo-dissolution reaction in thin-film silver/chalcogenide samples. New information on the reaction process indicates the importance of sample preparation techniques in the manufacture of high-resolution devices by micro-lithography.

Contents

CHAPTER ONE

Introduction

The physics of surfaces and interfaces is a fascinating subject, both from a fundamental and from a technological point of view. The properties of a surface, or of a thin film, are intimately connected with the atomic structure and can thus be greatly influenced by microscopic irregularities. In recent years, the development of crystal growth techniques, such as molecular-beam-epitaxy, has yielded a whole new range of thin-film materials in which the electronic properties are controlled by the details of the structure. This has renewed interest in surface-sensitive structural characterisation techniques, such as low energy electron diffraction (Jona, Strozier and Yang, 1982), ion scattering (van der Veen, 1986) and scanning-tunneling microscopy (Binnig, Rohrer, Gerber and Weibel, 1983). However, the surface sensitivity of these experimental probes is a consequence of their strong interaction with matter, and this can lead to difficulties in interpreting data because of multiple scattering effects.

X-ray scattering has been used for many years to study the bulk structural properties of crystalline and amorphous materials (Compton and Allison, 1935: James, 1949). Recently, developments in x-ray optics and the availability of intense x-ray sources, such as synchrotron radiation, have enabled new areas in phase transitions and surface science to be explored. The ability to probe the reciprocal space of a sample crystal with a momentum resolution as small as 10^{-4}Å^{-1} (Eisenberger, Alexandropolous and Platzmann, 1972) means that the contributions due to diffuse scattering and Bragg scattering may be separated in the region of a reciprocal lattice point. Huang scattering (Dederichs, 1971) has been used to study defects in nearly perfect crystals with cluster diameters of the order of one micron (Iida and Kohra, 1979; Lomov, Zaumseil and Winter, 1985) and diffuse scattering due to critical fluctuations has also been observed (Andrews and Cowley, 1986). The use of synchrotron radiation as a high-brilliance, tunable x-ray source has been exploited in a wide area of physics, for example to measure the phonon dispersion curve in beryllium (Dorner, Burkel, Illini and Peisl, 1987) and in measuring the

scattering that arises due to the magnetic order in holmium crystals (Gibbs, Moncton, D'Amico, Bohr and Grier, 1985).

X-rays travelling through matter are weakly scattered in the forward direction, and the interference between the forward scattered wave and the incident wave builds up a wave that travels through the material with a phase velocity that is slightly larger than the speed of light. This means that the index of refraction is slightly less than one and, at an incident angle below a certain critical angle, x-rays undergo total external reflection in matter (Darwin, 1914; Compton, 1923). In the angular region of total external reflection the penetration depth of the x-rays in the medium is greatly reduced. Typically the depth resolution under these conditions is between 10Å and 100Å, comparable with the resolution attained in many other surface analytical techniques. This phenomenon has given rise to several x-ray scattering techniques which may be roughly divided into the following categories:

(1) X-ray reflectivity.

A measurement of the x-ray reflectivity as a function of the angle of incidence provides information about the refractive index, and hence electron density, of a material as a function of depth. Reflectivity in this context means the specularly reflected beam, ie. with the angle of incidence equal to the angle of exit with respect to the sample surface. This is, strictly speaking, an interference rather than diffraction-based technique and was first exploited by Kiessig (1931) to measure film thicknesses. The technique is non-destructive and may be applied to crystalline and amorphous materials with equal facility.

The x-ray reflectivity technique underwent a period of intensive study in the 1960s (Wainfan, Scott and Parratt, 1959; Wainfan and Parratt, 1960; Sauro, Fankuchen and Wainfan, 1963; Guentert, 1965a; Sauro, Bindell and Wainfan, 1966), following a paper by Parratt (1954) solving the electromagnetic equations governing the scattering of an x-ray beam from a series of stratified homogeneous media. The details of these calculations are reproduced in Appendix II and are used in this thesis for analysing x-ray reflectivity data. Renewed interest in the x-ray reflectivity technique has been generated in recent years, coinciding with improved

sample growth facilities. In particular, the development of layered synthetic x-ray mirrors (Pardo, Megademini and André, 1988) has led to refinements in the experimental technique and theoretical treatment of x-ray reflectivity (Névot and Croce, 1980; Spiller, 1988; Underwood and Barbee, 1981; Névot, Pardo and Corno, 1988; Piecuch, 1988; Rosen, Brown, Gilfrich and Burkhalter, 1988). This development of the technique has led to its application in a wide variety of studies, for example, diffusion in metal thin film couples (Wagendristel, Schurz, Ehrmann-Falkenau and Bangert, 1980), phase transitions in liquid crystals (Gramsbergen, de Jeu and Als-Nielsen, 1986: Pershan, Braslau, Weiss and Als-Nielsen, 1987), phase transitions in metal surfaces (Ocko and Mochrie,1988; Gibbs, Ocko, Zehner and Mochrie, 1988), liquid surfaces (Lu and Rice, 1978; Braslau, Deutsch, Pershan, Weiss, Als-Nielsen and Bohr, 1985; Braslau, Pershan, Swislow, Ocko and Als-Nielsen, 1988) and even the long-term equilibrium behaviour of polymer droplets (Daillant, Benattar, Bosio and Leger, 1988). Recently, neutron spectrometers for reflectivity measurements have been designed (Hayter, Highfield, Pullman, Thomas and Penfold, 1981), enabling reflectivity studies to be used as a probe of surface magnetism (Felcher, 1981). The simplicity of the reflectivity technique and the ease with which the data may be interpreted has led to an increasing awareness of its possibilities in several areas of physics.

(2) Grazing-incidence x-ray diffraction.

The study of the x-ray specular reflection gives information only about the change in the electron density near to the surface. In order to obtain direct information about the crystalline structure of near-surface regions it is necessary to perform diffraction measurements. Until recently, x-ray diffraction was considered as a bulk characterisation technique, due to the deep penetration depth of the x-rays into a crystal. However, if the total external reflection regime may be incorporated into the x-ray diffraction geometry, then the method becomes extremely sensitive to the surface layers.

One way of achieving surface sensitivity is to adopt a highly asymmetrical diffraction geometry, either by cutting the crystal so that its surface makes approximately the Bragg angle with the chosen reflecting plane, or by choosing a reflection which inherently satisfies this condition

(Fukahara and Takano, 1977; Wolcryz and Lukaszewich, 1982). This method has the obvious disadvantage of requiring a special orientation of the sample surface, which is not always experimentally possible.

A second scheme was demonstrated in the pioneering work of Marra, Eisenberger and Cho (1979), in which the direction of the diffracted beam is rotated with respect to that of the incident beam by approximately twice the Bragg angle. Diffraction, therefore, occurs from planes perpendicular to the sample surface and both the incident and diffracted beams make small angles with the surface, thus experiencing specular reflection. This method was called "total-external reflection Bragg diffraction" or "parallel Bragg diffraction" (Eisenberger and Marra, 1981), and was used to study the surfaces of semiconductor crystals grown by molecular-beam-epitaxy.

The development of synchrotron radiation sources, providing x-ray beams with intensities 100 times higher than that of x-ray tubes, allowed the method to be used for the investigation of monolayers on ultraclean surfaces of single crystals. This has stimulated studies of surface reconstruction (Robinson, 1983; Robinson, Kuk and Feldman, 1984; Bohr, Feidenhans'l, Nielsen, Toney, Johnson and Robinson, 1985; Feidenhans'l, 1986), surface phase transitions (Marra, Fuoss and Eisenberger, 1982) and measurements of the two-dimensional compressibility of electrochemically absorbed lead on silver (Melroy, Toney, Borges, Samant, Kortright, Ross and Blum, 1988; Kortright, 1989). This progress in experimental work has been matched by theoretical development in scattering theory to explain new results (Vineyard, 1982; Dietrich and Wagner, 1983; Andreeva, Borisova and Stepanov, 1986).

(3) Crystal truncation rods.

In the classical derivation of the diffraction pattern of a crystal lattice, the lattice is assumed to be infinite in extent, resulting in delta function diffraction peaks or Bragg spots. However, if the sample crystal is terminated in one direction, for example at a surface or interface, the diffraction peaks are broadened in reciprocal space, in a direction perpendicular to the surface plane. This results in a rod, or streak of scattering, through the Bragg peaks, the intensity dependence of which

contains detailed information about the termination of the crystal lattice (Appendix I; Robinson, 1986; Andrews and Cowley, 1985). Although analysis of the truncation rod can be performed under grazing-incidence conditions (Vlieg, Denier van der Gon, van der Veen, Macdonald and Norris, 1987), it is not a pre-requisite to obtaining surface information. Many theoretical and experimental papers using standard diffractometer configurations have been published (Afanas'ev, Aleksandrov, Imanov, Lomov and Zavyalova, 1984; Afanas'ev, Aleksandrov, Fanchenko, Chaplanov and Yakimov, 1986; Kashihara, Kimura and Harada, 1989; Shen, Blakely, Bedzyk and Finkelstein, 1989).

(4) Extended X-ray Absorption Fine Structure (EXAFS).

The oscillating character of the extended fine structure of x-ray spectra above the absorption edge is determined by the interference of the outgoing wave with the backscattered waves from the surrounding atoms. The Fourier transform of the oscillating part of the spectrum represents a radial distribution of the electron density of the atom species being probed (Lee, Citrin, Eisenberger and Kincaid, 1981). Under total external reflection conditions, the radiation is concentrated near to the surface (Martens and Rabe, 1981) and therefore provides information about the surface atoms (Barrett, Greaves, Pizzini and Roberts, 1989).

(5) X-ray Fluorescence.

The detection of secondary radiation under the total external reflection condition provides another technique for obtaining information about surface atoms. The fluorescence yield resulting from a given atomic species is determined by the depth profile of the atoms and the energy flow in the material. By varying the incident angle of the x-ray beam, the atomic profile of a given species in a material may be probed (Bloch, Sansone, Rondelez, Peiffer, Pincus, Kim and Eisenberger, 1985; Kröl, Sher and Kao, 1988).

(6) X-ray standing waves.

When an x-ray beam is Bragg diffracted by a perfect crystal, a standing-wave field is generated inside the crystal, due to the interaction

of the coherently related incident and diffracted plane waves (Dev, Materlik, Johnson, Kranz and Funke, 1986). The antinodal planes of the standing wave field are parallel to the diffraction planes, with the same period, and their position is determined by the angle of incidence of the x-ray beam. It is therefore possible to modulate the electric-field intensity to which an atom in the crystal is exposed. The angular response of a secondary process, such as fluorescence, is proportional to the x-ray intensity at the centre of the atom and therefore, depends on its position (Batterman, 1964; Vlieg, Fischer, van der Veen, Dev and Materlik, 1986).

(7) Scattering due to surface roughness.

The Fresnel formulae describing the specular reflection of an x-ray beam are applicable only to scattering from an ideally flat and smooth surface. In a real situation, surface roughness induces a change in the reflection conditions, often leading to an angular broadening of the scattered beam (Croce and Névot, 1974; Névot and Croce, 1975). For angles of incidence slightly exceeding the critical angle, other features in the scattered intensity may be observed. In particular, a peak at a scattering angle equal to the critical angle was observed by Yoneda (1963), and subsequently subjected to a number of theoretical and experimental studies (Kapp and Wainfan, 1965; Warren and Clarke, 1965; Nigam, 1965; Guentert, 1965b; Torrance and Sparrow, 1967; Bindell and Wainfan, 1970; Rovinskii, Sinaiskii and Sidenko, 1972; Petrashen', Kovyev, Chukhovskii and Degtyarev, 1983). This 'anomalous' or 'off-specular' reflection is not reproduced within a kinematical scattering theory. Recent calculations have shown that the effect can be explained within a distorted-wave Born approximation to scattering theory (Andreev, 1985; Wong and Bray, 1988; Sinha, Sirota, Garoff and Stanley, 1988).

The work described in this thesis fits mainly into sections one, three and seven of the above review. The majority of the experiments were performed at Edinburgh University, using the triple-crystal x-ray spectrometers which are based on a rotating-anode source. The instrument was first commissioned in 1981 and a full review of its development and original uses is given by Ryan (1986).

The remainder of this thesis describes the experimental work of the author and is organised as follows:

Chapter 2 describes, in detail, the properties of a triple-crystal x-ray spectrometer, based on a rotating-anode source, and at a synchrotron radiation source. Measurements of the instrumental resolution are presented, and compared with the results of a simple calculation (Cowley, 1987), and with the full, dynamical theory (Gartstein, 1989). The simple calculation is shown to have obvious advantages in allowing an analytical de-convolution of the resolution effects. The importance of understanding the resolution function in a variety of surface scattering experiments is discussed.

Chapter 3 describes the application of x-ray reflectivity and crystal truncation rod measurements to the study of the Si/SiO_2 structure. This is an extension of the work by Cowley and Ryan (1987), and uncovers new features in the observed scattering which lead to a greater understanding of the properties of both the Si/SiO_2 interface, and the surface of the oxide layer. A detailed description of the experimental techniques required for reflectivity and crystal truncation rod measurements is given. This chapter also contains some neutron reflectivity measurements, taken during the commissioning stage of the CRISP reflectometer at the Rutherford Appleton Laboratory, and explains the advantages in using neutrons for reflectivity experiments.

Chapter 4 discusses the application of the scattering techniques to investigate the structural properties of single quantum well semiconductor devices. These crystalline, thin film devices are at the forefront of semiconductor growth technology and traditional structural characterisation methods, such as x-ray rocking curve analysis, are incapable of probing the detailed microscopic properties which can greatly influence device performance. By combining the available x-ray scattering techniques, and utilising the high resolution achievable with a triple-crystal diffractometer, samples grown by molecular-beam-epitaxy and metal organic chemical vapour deposition are studied on the Ångstrom scale.

Chapter 5 departs from the relatively 'perfect' world of crystalline, semiconductor materials and describes some measurements of the

silver/chalcogenide system as it proceeds through a photo-dissolution reaction (Kostychin, Mikhailovskya and Romanenko, 1966). An understanding of the structural evolution of this process is important because of its applications in sub-micron photolithography. Although the system consists of polycrystalline and amorphous materials, x-ray reflectivity results can still provide detailed information about the photo-reaction, despite the difficulties encountered in interpreting the data due to the complexity of the system. Preliminary studies of an artificially modulated system are also described, with a review of the possible future applications of this x-ray technique.

Finally, some brief conclusions are drawn from the experimental work and the thesis finishes with two appendices describing the basic formulations of x-ray scattering theory, relevant to the study of surfaces and interfaces.

CHAPTER TWO

The Resolution Function of an X-ray Triple Crystal Diffractometer

1. Introduction

With the availability of intense x-ray sources, such as high-brilliance rotating-anode generators and synchrotron radiation sources, the triple-crystal diffractometer has found increasing use in high-resolution diffraction experiments. However, even when using perfect crystals as monochromator and analyser, a thorough understanding of the instrumental resolution is required in order to quantitatively measure the nature of the scattered intensity in an experiment. In addition, a detailed knowledge of the resolution function in wave-vector space can enable the measurement of relatively weak, diffuse scattering from critical fluctuations or surfaces, without interference from the strong scattering arising from a Bragg reflection (Andrews and Cowley, 1986).

Although the resolution function of a neutron three-axis spectrometer has been dealt with, both theoretically and experimentally, by several authors, (Cooper and Nathans, 1967; Stedman, 1968; Bjerrum-Møller and Nielsen, 1969; Chesser and Axe, 1973) the corresponding calculation for an x-ray diffractometer has received comparatively little attention. The use of nearly perfect crystals for monochromator and analyser in the x-ray case, means that their scattering must be described by dynamical diffraction theory (Zachariasen, 1945; Batterman and Cole, 1964). Reflection from a perfect crystal is governed by the characteristic long-tailed asymmetric form of the Darwin profile, (Figure 2.1) and not by the Gaussian form, assumed for the case of mosaic crystals, and used in the neutron scattering calculations. Unlike the Gaussian approximation, which may be solved largely analytically, convolution of these non-Gaussian profiles requires a complex numerical integration. Pynn, Fujii and Shirane (1983) have applied the formalism of Bjerrum-Møller and Nielsen to the case of the perfect crystal x-ray diffractometer, and calculated the central part of the resolution function. They compared their calculations with experimental measurements of the peak shapes of the Bragg reflections from perfect germanium and silicon crystals and

found good agreement. Recently Cowley (1987), following a suggestion by Pynn et al (1983), approximated the results of the dynamical theory by a Gaussian, enabling the central part of the resolution function to be obtained analytically in terms of relatively simple expressions. It was hoped that, after convolution with other resolution elements, the calculations would be sufficiently accurate to allow a straightforward analysis of experimental results.

The aim of this chapter is to describe some further studies of the resolution function of a triple crystal x-ray diffractometer with a rotating anode source, and with a synchrotron source. Experiments with the rotating anode source have been performed with three different sets of monochromator and analyser crystals; perfect germanium, distorted germanium and pyrolytic graphite. Measurements at a variety of different wave-vector transfers are described in section 2, and these are compared with the widths calculated using the Gaussian approximation in section 3. However, as previously mentioned, the tails of the resolution are far from Gaussian in form when perfect crystals are used for monochromator and analyser. This is because their scattering is described by the Darwin curve which has $1/\theta^2$ wings, rather than the more rapidly decreasing Gaussian wings assumed in the Gaussian theory. An understanding of these tails is essential if measurements are to be performed close to the Bragg reflections. In section 2 a qualitative description of the origin of these tails (Ryan, 1986; Pick, Bickman, Pofahl, Zwoll and Wenzl, 1977) is presented. A quantitative description necessarily requires a numerical convolution over the different resolution elements (Zaumseil and Winter, 1982; Gartstein, 1989). The results of such calculations are compared with the measurements, down to 10^{-3} of the Bragg peak intensity, in section 3. Section 4 describes similar measurements performed using a synchrotron source; the SRS at Daresbury Laboratory, Warrington, U.K. Finally, section 5, briefly discusses the importance and application of the resolution work to the experiments described in chapters three, four and five.

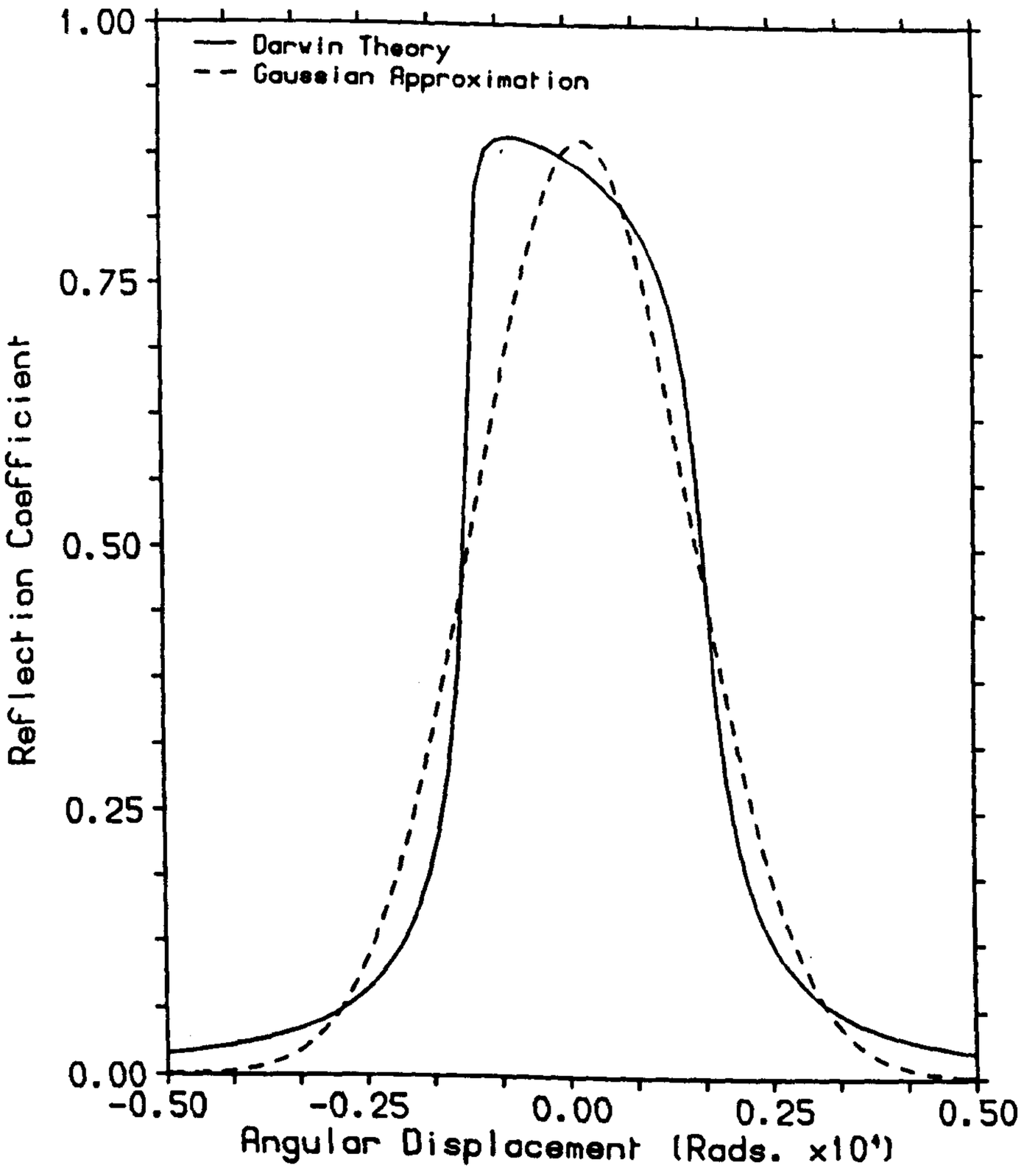

Figure 2.1. The theoretical 'Darwin' profile for diffraction from a perfect crystal, and the Gaussian approximation, for the GaAs (4 0 0) Bragg reflection.

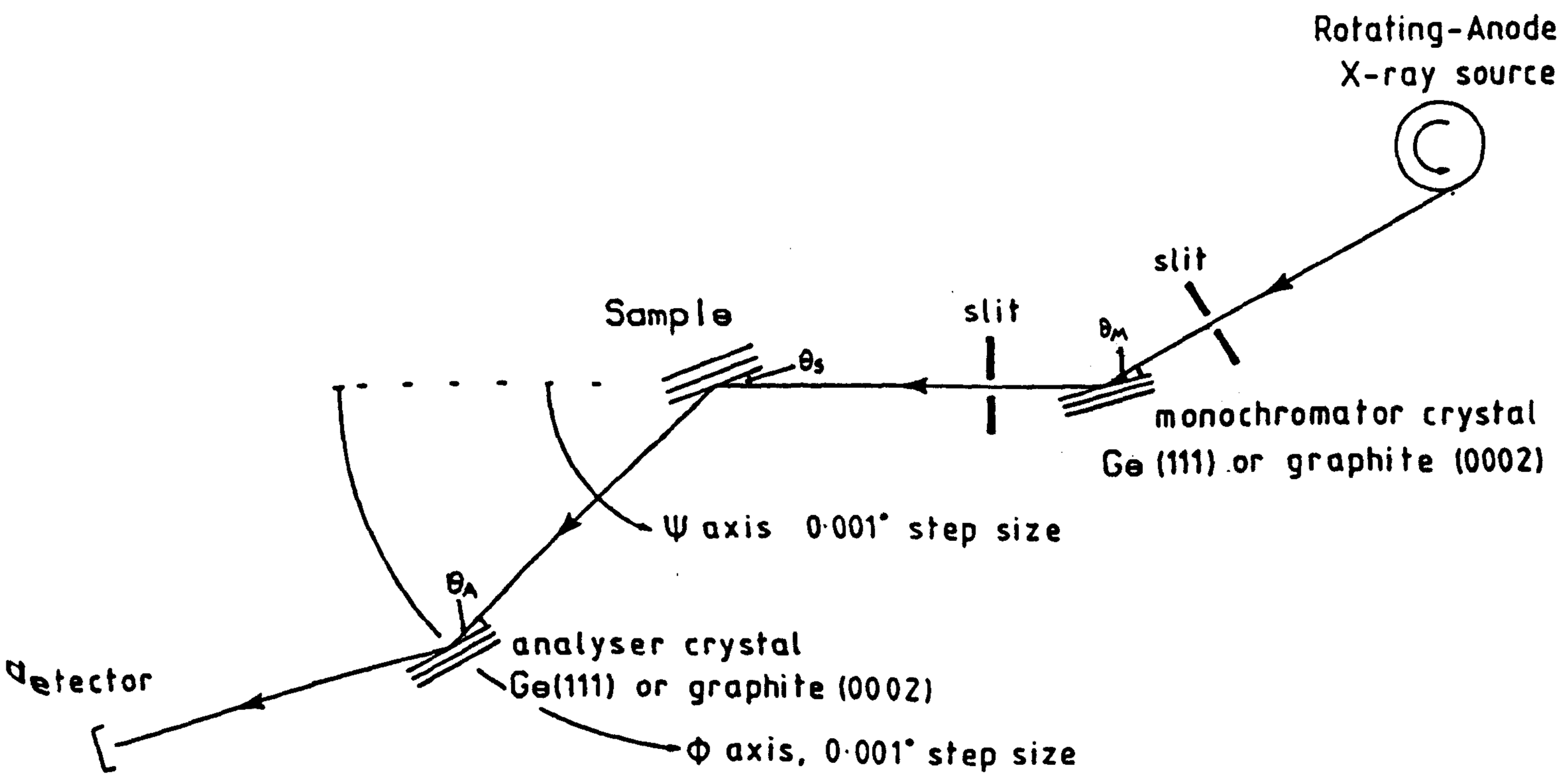

Figure 2.2. Schematic diagram of a triple crystal x-ray diffractometer.

2. Experiments and Results

(2.1) The Experiments

The experiments were performed at Edinburgh University using a triple-axis x-ray diffractometer based on a Huber 430/440 goniometer, and utilizing a GEC Avionics GX21 rotating anode x-ray generator operating at 2.7 kW with a copper target. CuKα_1 x-rays (λ = 1.54051Å, $\Delta\lambda$ = 0.00058Å) were used, and the focal spot of the rotating anode tube was a vertical line of height 3mm and width 0.3mm, viewed at a take-off angle of 6°. Figure 2.2 shows a schematic picture of the diffractometer in the (+, -, +) configuration. The arrangement (+1, -S, +1), in which $\theta_M = \theta_A \neq \theta_S$, was used throughout the experiments. A variable width slit, immediately in front of the monochromator crystal, was used to limit the angular range of the x-ray beam incident on the monochromator and hence, for the perfect germanium crystals, to eliminate the Kα_2 line. The monochromator was at a distance of 200 mm from the source. An additional slit, placed between the monochromator and sample crystals, limited the vertical divergence of the x-rays and ensured that the incident beam was fully intercepted by the sample. No other collimators were present between the monochromator crystal and the detector. The detector was a proportional counter with about 1.5KeV FWHM energy resolution at 8KeV.

Three different sets of crystals were used for the monochromator and analyser:

(1) High resolution: The (1 1 1) reflections of perfect germanium crystals were used for both monochromator and analyser. These reflections have a Darwin width of 4.3×10^{-3} degrees.

(2) Intermediate resolution: The (1 1 1) reflections of poor quality germanium crystals were used as monochromator and analyser. These crystals had a measured mosaic spread (FWHM) of about 0.021° .

(3) Low resolution: The (0 0 0 2) planes of pyrolytic graphite (Union Carbide UCAR grade ZYA) were used as monochromator and

analyser. These crystals have a mosaic structure with an approximately Gaussian distribution of orientations and a mosaic spread of 0.4° ±0.1° (FWHM).

These three arrangements then provide for changes in the resolution of the diffractometer by two orders of magnitude.

Unfortunately the resolution function of the diffractometer cannot be measured directly, especially in its high resolution mode, because the scattering from the sample is not a delta-function in reciprocal space. Clearly the sample must be a material which has a perfect crystal structure, with a fairly large number of accessible reciprocal lattice points to enable the theory to be tested over a range of wave-vector transfers. For these reasons single crystals of InP or GaAs, grown in wafer form for use as substrates for the MBE growth of semiconductor heterostructures, were selected as sample crystals. Each wafer had the [1 0 0] axis perpendicular to the surface plane and was etched to remove any surface damage. The sample was oriented in an extended face geometry on the diffractometer, with either a [0 0 1] or [0 1 $\bar{1}$] axis vertical and perpendicular to the scattering plane. Clearly the Darwin width of the InP or GaAs crystal has an effect on the observed scattering, especially in the high resolution configuration. In this case, in comparing experiment and theory, it is necessary to incorporate the effect of the Darwin widths and this is described in section 3.

For each experimental arrangement, the resolution function, at a wave-vector transfer Q, was measured in the transverse ($\delta Q_{\perp}$) and longitudinal ($\delta Q_{||}$) directions by rocking the sample (a ψ scan in the notation of figure 2.2) or by scanning the sample and analyser arm in a ratio of 1:2 ($\delta\phi = 2\delta\psi$ scan). The ψ and ϕ axes have an angular precision of better than 0.001°. These measurements were performed for the InP (2 0 0), (4 0 0) and (6 0 0) symmetric reflections and for the (3 1 1), (4 2 2), (5 1 1) and (6 2 2) asymmetric reflections. The crystal was then rotated by 45° in the surface plane, enabling additional measurement at the (4 2 0), (4 4 0) and (6 2 0) Bragg reflections. For all the asymmetric reflections both shallow and deep entry angles of incidence were used, to study, for example, both the (3 1 1) and (3 $\bar{1}$ $\bar{1}$) reflections. The results of these experiments are shown in figures 2.5, 2.6 and 2.7.

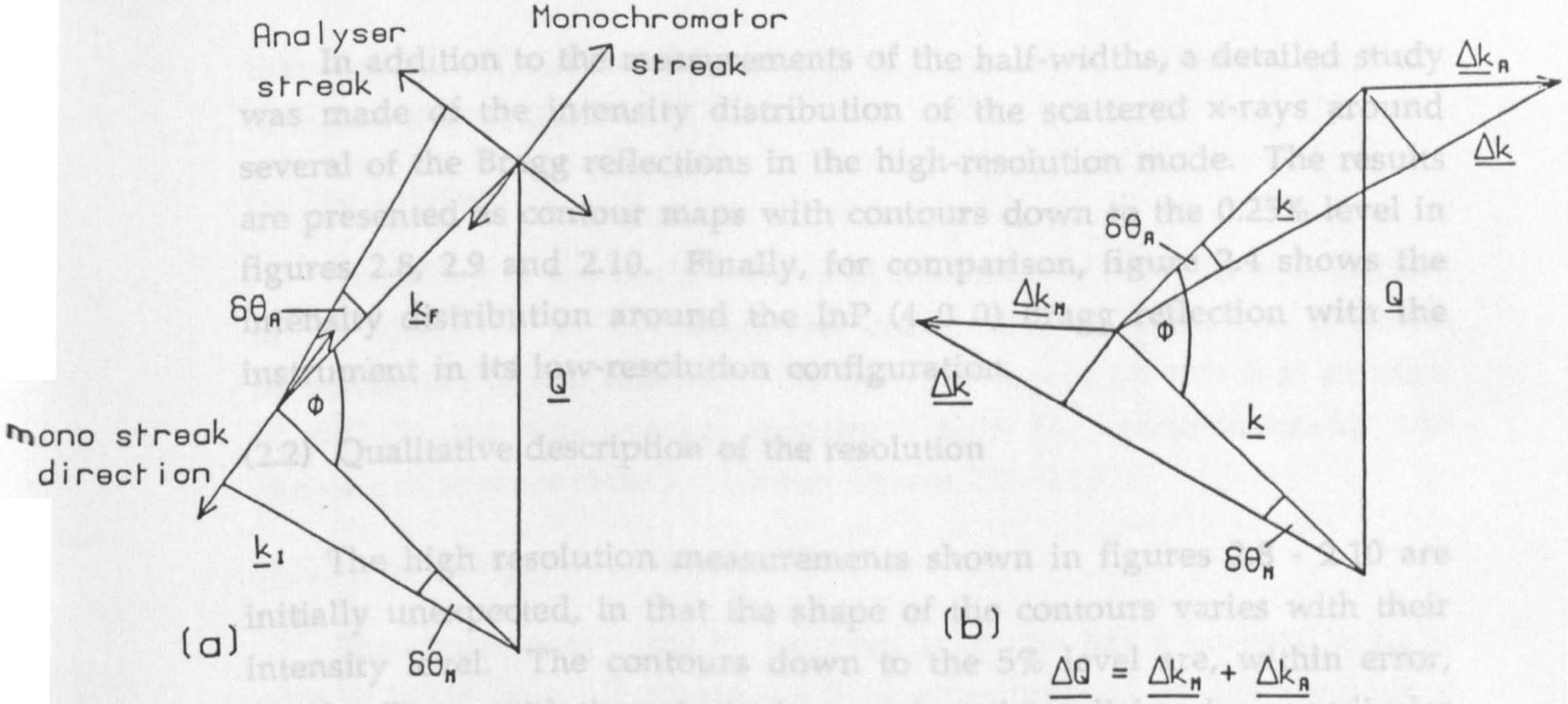

Figure 2.3. The origin of the streaks in the wings of the resolution function. Part (a) shows the direction of the monochromator and analyser streaks, while (b) shows the effect of a wavelength spread.

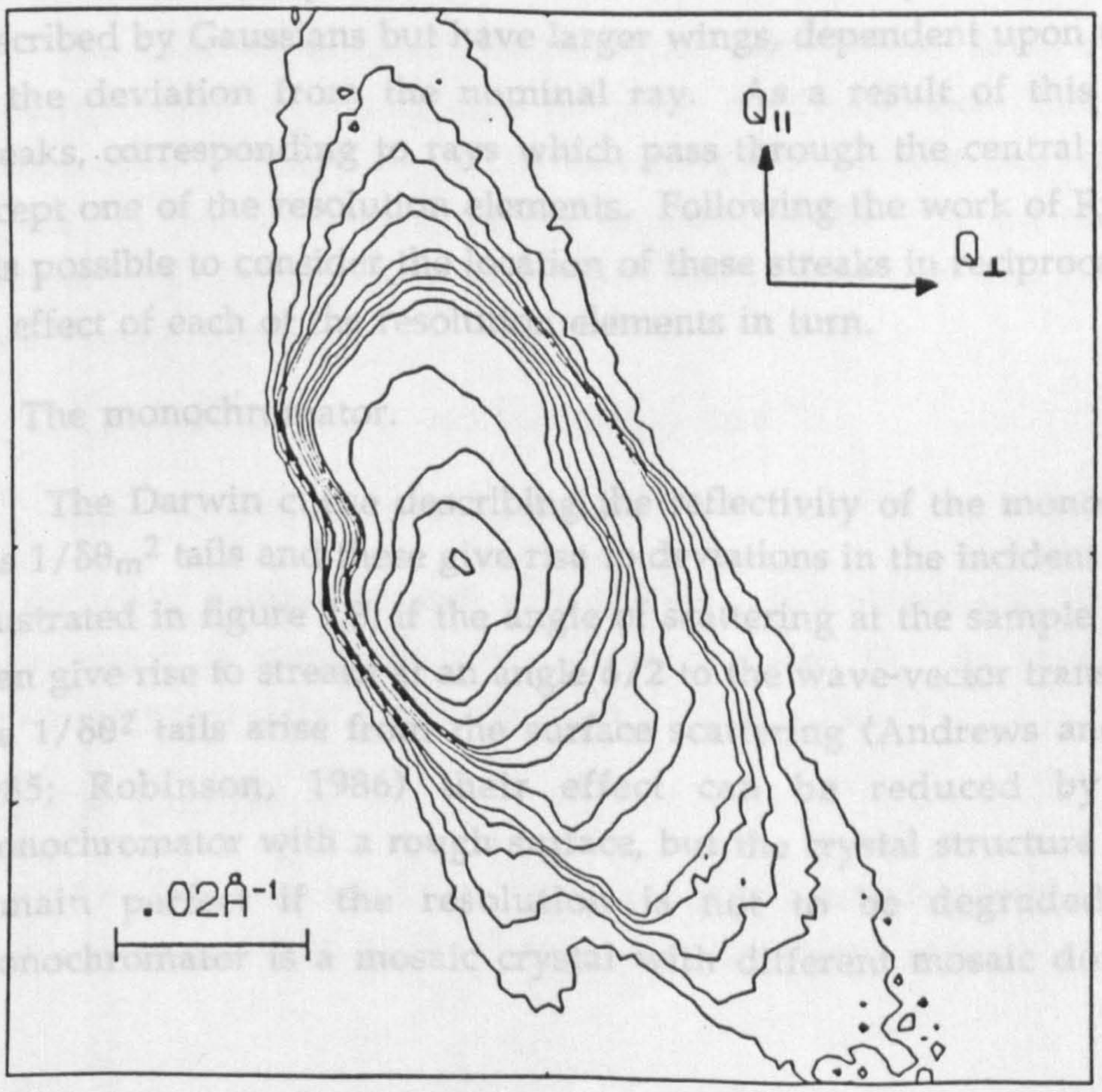

Figure 2.4. A contour map of the scattered intensity around the InP (6 0 0) Bragg reflection in the low resolution configuration ie. graphite monochromator and analyser. The lowest contour level is .0025 of the peak intensity.

In addition to the measurements of the half-widths, a detailed study was made of the intensity distribution of the scattered x-rays around several of the Bragg reflections in the high-resolution mode. The results are presented as contour maps with contours down to the 0.25% level in figures 2.8, 2.9 and 2.10. Finally, for comparison, figure 2.4 shows the intensity distribution around the InP (4 0 0) Bragg reflection with the instrument in its low-resolution configuration.

(2.2) Qualitative description of the resolution

The high resolution measurements shown in figures 2.8 - 2.10 are initially unexpected, in that the shape of the contours varies with their intensity level. The contours down to the 5% level are, within error, simple ellipses with the principal axes oriented parallel and perpendicular to the wave-vector transfer. This is as expected on the basis of the Gaussian theory of the resolution function (Cowley, 1987). However, the lower contours have a much more complex shape and this cannot be explained by the Gaussian theory. These effects arise because the resolution determining elements, the line width of the source and the reflectivities of the perfect monochromator and analyser crystals, are not described by Gaussians but have larger wings, dependent upon the square of the deviation from the nominal ray. As a result of this there are streaks, corresponding to rays which pass through the central part of all except one of the resolution elements. Following the work of Ryan (1986) it is possible to consider the location of these streaks in reciprocal space as an effect of each of the resolution elements in turn.

a) The monochromator.

The Darwin curve describing the reflectivity of the monochromator has $1/\delta\theta_m^2$ tails and these give rise to deviations in the incident beam. As illustrated in figure 2.3, if the angle of scattering at the sample is ϕ, these then give rise to streaks at an angle $\phi/2$ to the wave-vector transfer. Since the $1/\delta\theta^2$ tails arise from the surface scattering (Andrews and Cowley, 1985; Robinson, 1986) their effect can be reduced by using a monochromator with a rough surface, but the crystal structure must then remain perfect if the resolution is not to be degraded. If the monochromator is a mosaic crystal with different mosaic domains this

may produce a similar streak with a form which reflects the mosaic structure (Figure 2.4).

b) The analyser.

The effect of the Darwin curve of the analyser is to allow deviations in the direction of the scattered beam, and so produces a streak perpendicular to that direction. As shown in figure 2.3, this is at an angle of $-\phi/2$ to the wave-vector transfer. Both the monochromator and analyser streaks are clearly visible in figures 2.8 - 2.10.

c) The wavelength spread.

The characteristic line in the x-ray spectrum has a Lorentzian form, with $(1/\Delta\lambda)^2$ tails. Furthermore it is superimposed on the continuous spectrum which has $\sim 10^{-3}$ of the intensity of the characteristic line. For measurements at low levels of intensity it is then essential to understand the effects of the spread in incident wavelength. Experimentally the spread in wavelength is reduced by a slit in front of the monochromator and the detailed shape of the effect of the wavelength spread depends critically on the positioning of this slit.

The effect of different wavelengths, from a very small spot on the rotating anode, is to give, after reflection on the monochromator, a beam whose direction depends on the wavelength or wave-vector, as shown in figure 2.3. For a triple-crystal spectrometer in the focusing configuration of figure 2.2, the changé in the wave-vector, δK, results in a change in the wave-vector transfer

$$\delta Q_{||} = \delta K \, (2 \tan \phi/2 - \tan \theta_M - \tan\theta_A) \cos \phi/2$$

$$\delta Q_{\perp} = \delta K \, (\tan \theta_M - \tan \theta_A) \sin \phi/2$$

In the usual symmetric case with $\theta_M = \theta_A$, this shows that the spread in wavelength is along the wave-vector transfer, Q. As is well known, focusing occurs if the scattering angle $\phi = 2\theta_M = 2\theta_A$.

(d) The specimen.

An ideal, extended face sample also has its reflectivity given by the Darwin curve, with $(1/\delta q)^2$ tails resulting from the surface scattering

(Andrews and Cowley, 1985; Robinson, 1986). Consequently the sample Bragg reflection is broadened in reciprocal space perpendicular to the extended face of the crystal in real space. For symmetric reflections, for which the wave-vector transfer is perpendicular to the sample surface, it is then impossible to distinguish between the $\Delta\lambda$ and specimen streaks, unless the reflection is one with no wavelength dispersion. However, for asymmetric reflections the specimen and $\Delta\lambda$ streaks are in different directions. For a mosaic sample crystal, the Bragg condition may be satisfied for a range of setting angles, $\delta\psi$, whilst the angle ϕ is constant and well defined. This leads to a spread in intensity perpendicular to the wave-vector transfer.

In figures 2.8 - 2.10 the directions of the different streaks are clearly seen, and support the predictions of the simple theory given above. If the contour maps are extended to lower levels then these streaks become even more prominent. In the low-resolution configuration the resolution is dominated by the analyser and monochromator streaks, due to the mosaic spreads of the graphite crystals. This leads to the intensity distribution shown in figure 2.4.

3. Comparison with theory

(3.1) Gaussian theory

The Gaussian theory of the resolution function is derived by assuming that all the resolution elements can be described by Gaussian response functions (Cowley, 1987). For example the reflectivity of the monochromator is given by

$$P(\gamma_0,\gamma_1,\Delta k) = P_M \exp\left\{-\tfrac{1}{2}[(\gamma_0 + \gamma_1)/2\eta_M]^2\right\}$$

$$\times \exp\left\{-\tfrac{1}{2}[(\gamma_1 - \gamma_0 + 2\Delta k(\tan\theta_M)/k)/2D_M]^2\right\}$$

where γ_0,γ_1 are the angular deviations of the incident and scattered wave-vectors from the nominal ray, and Δk is the difference between the incident wave-vector k_M and the nominal wave-vector k. This approximation is illustrated in figure 2.1. In the case of perfect crystals the mosaic width $\eta_M \rightarrow 0$ and the scattering is determined by the Darwin width $2D_M$ (Zachariasen, 1945). With each resolution element represented in a similar form, the theory then predicts that the resolution function is an ellipse in reciprocal space, with its principal axes parallel and perpendicular to the wave-vector transfer. Furthermore the theory gives explicit and relatively simple expressions for the widths of the resolution function.

Figure 2.5 shows the longitudinal and transverse widths of the resolution function as a function of wave-vector transfer. These were calculated using the theoretical Darwin width for the monochromator and analyser of 4.3×10^{-3} degrees. The experimental results were measured as described in section 2, and corrected for the Darwin width of the InP sample crystal. The correction was calculated by using the Gaussian formalism and convoluting the calculated resolution function with a Gaussian representing the sample Darwin width. Except for the two reflections at the smallest wave-vector transfers, (2 0 0) and (3 1 1), the resulting corrections were smaller than the error bars. For these two points both the uncorrected widths and corrected widths are shown in figure 2.5. The experimental results are clearly in reasonable agreement with the theory, especially in view of the fact that there are no adjustable

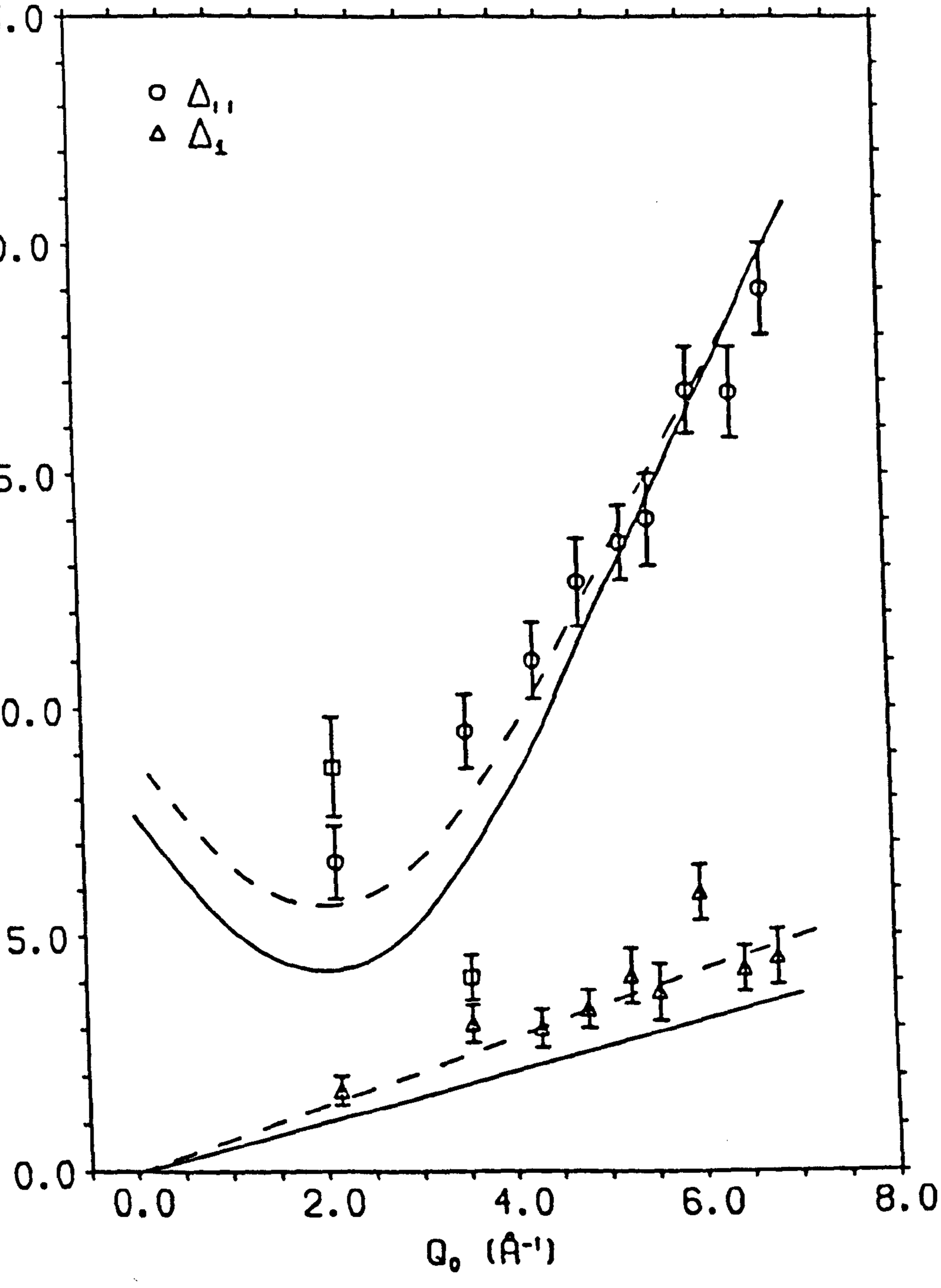

Figure 2.5. The widths of the resolution function for the high resolution mode with perfect germanium monochromator and analyser. The experimental results have been corrected for the Darwin width of the InP sample (circles). The correction is smaller than the error bars except for two low Q points where the uncorrected data is shown by squares. The solid line is the calculated width using the theoretical Darwin width of Ge (1 1 1) planes and the dotted line is calculated with the Darwin width increased by 33%.

parameters in the theoretical calculations. Nevertheless the calculated transverse widths are approximately 75% of the measured ones and the minimum in the longitudinal widths at $2Å^{-1}$ is also too small. Both of these features are largely dependent on the germanium Darwin widths of the monochromator and analyser, whereas the longitudinal widths for wave-vectors Q = 5-7 $Å^{-1}$, which are largely dependent on the wavelength spread, give excellent agreement between theory and experiment. Consequently in figure 2.5 calculations with the Darwin width increased to 5.7×10^{-3} degrees are also shown. There is then very satisfactory agreement between the calculations and experiment.

There are two possible reasons why the agreement is better with a larger than theoretical Darwin width. It may be that the germanium is not perfect, but has a small mosaic width in addition to the Darwin width. Alternatively it may be that the Gaussian approximation underestimates the width because the Darwin curve is not of a Gaussian form. The convolution of two equal width Gaussians, gives a Gaussian of width $\sqrt{2}$ larger than a single Gaussian, whereas the convolution of two Lorentzians gives a curve of twice the width. The larger width then may result from the inadequacy of the Gaussian approximation to the Darwin curve.

The results of the experiments performed with poor quality germanium monochromator and analyser, and a GaAs sample, are shown in figure 2.6. In this case corrections for the Darwin width of the sample are negligible. The widths were calculated by adjusting the mosaic widths of the monochromator and analyser, and a good description of the transverse widths was obtained when these both had a width of 0.023°, as shown in figure 2.6. The measured mosaic spread of the monochromator was 0.021°. The longitudinal widths are then in good agreement with the experiment for wave-vectors greater than $4Å^{-1}$, but at smaller wave-vectors the observed widths are significantly smaller than those calculated. The origin of this discrepancy is not understood.

In figure 2.7 are shown the results obtained in the low-resolution configuration, with pyrolytic graphite monochromator and analyser, and with the InP sample. The mosaic spread of the graphite crystals was found by adjusting the calculated transverse widths and gave agreement

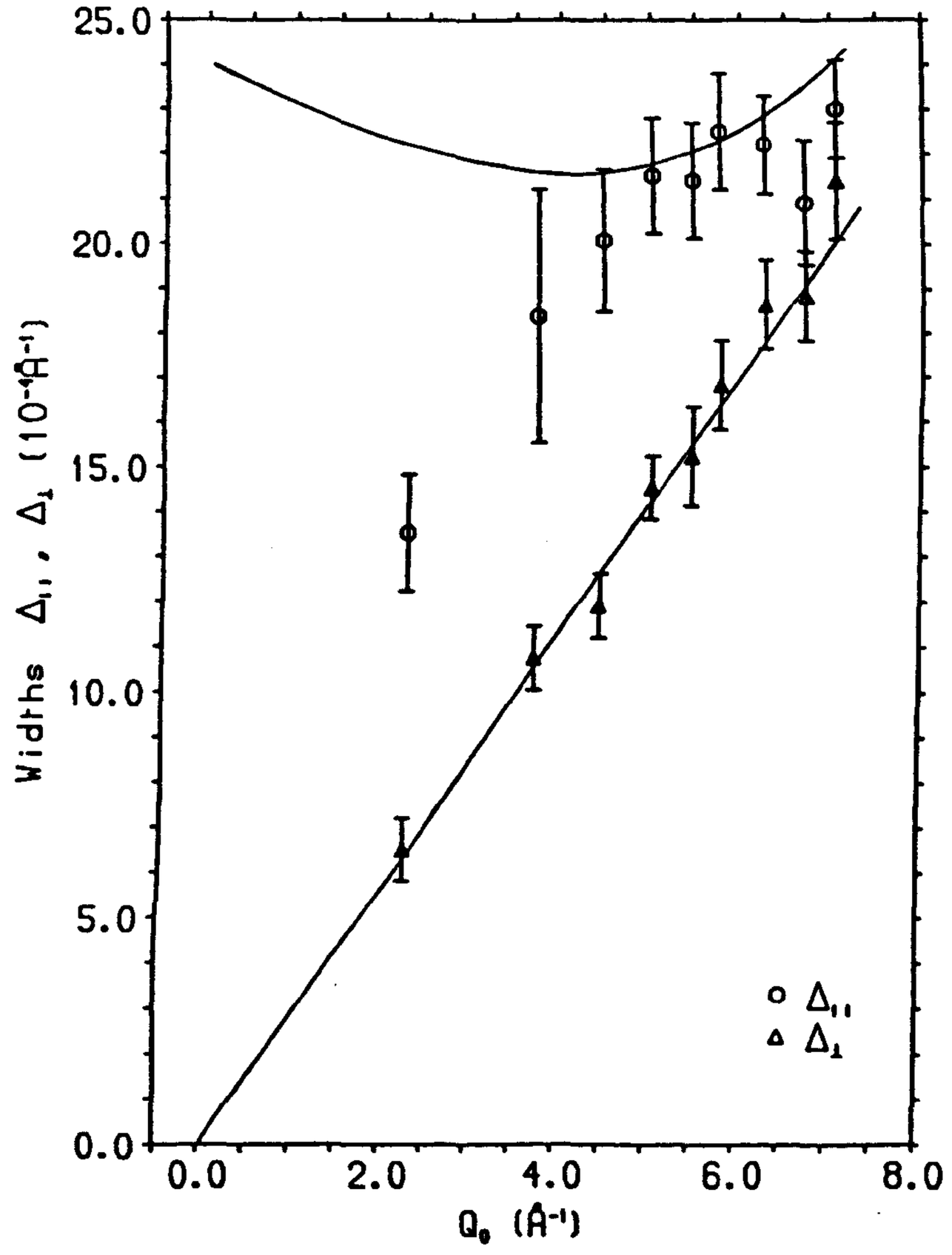

Figure 2.6. The widths of the resolution function with the distorted Ge monochromator and analyser. The solid lines are the Gaussian theory with each Ge crystal having a mosaic width of 0.023°.

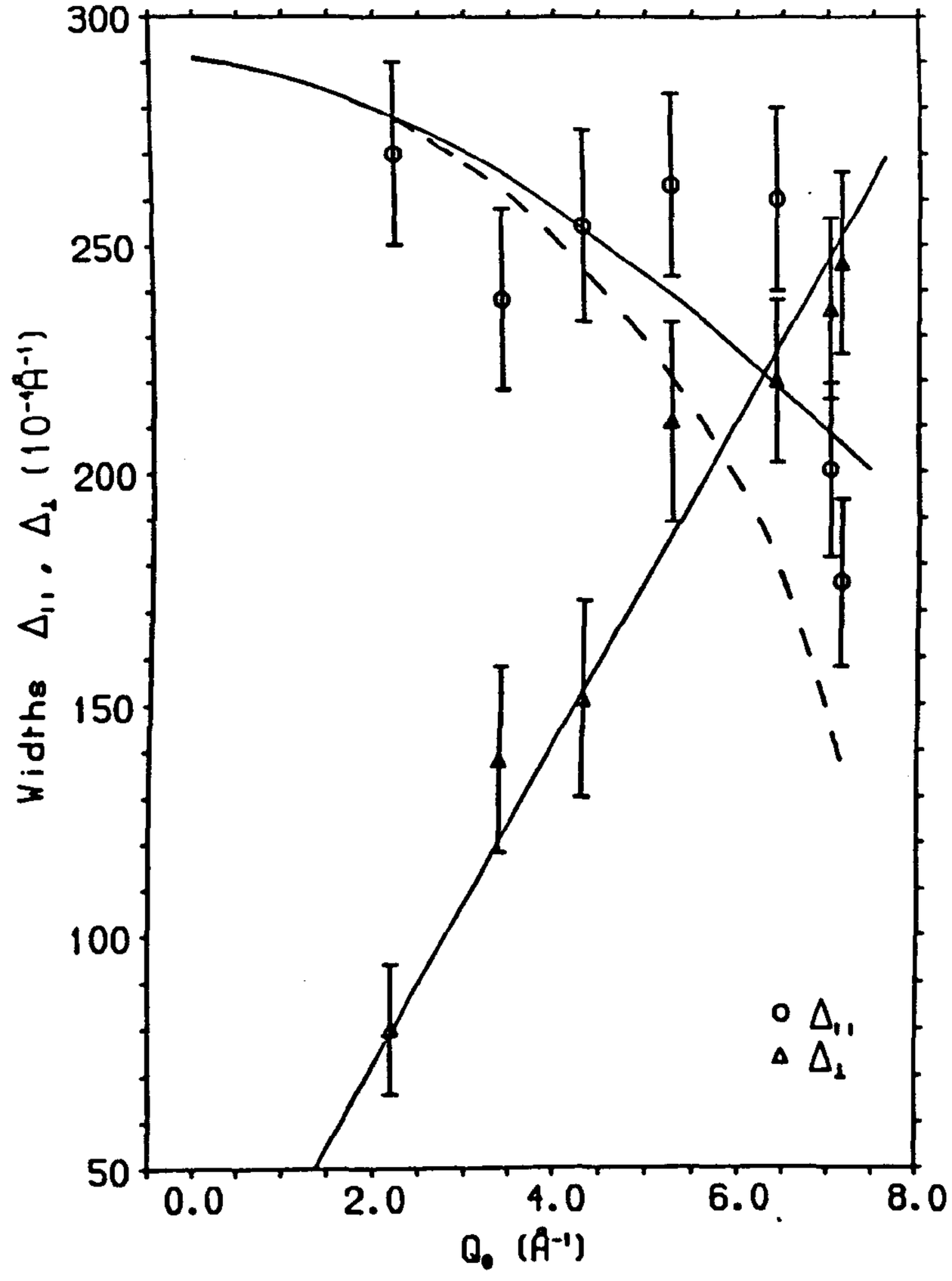

Figure 2.7. The widths of the resolution function with the pyrolytic graphite monochromator and analyser. The dotted curve is the Gaussian theory with $\Delta\lambda/\lambda=3.5\times10^{-4}$ and mosaic 0.29°, while the solid curve has $\Delta\lambda/\lambda=2.5\times10^{-3}$.

with experiment with $\eta_M = 0.29°$. Calculations of the longitudinal width were then made with a wavelength spread equal to the width of the $K\alpha_1$ line, shown by the dotted line, and with $\Delta\lambda/\lambda = 2.5 \times 10^{-3}$, the separation between the $K\alpha_1$ and $K\alpha_2$ lines. As would be expected for mosaic crystals, the calculations clearly give a good description of the experimental results.

(3.2) The convolution theory

The reflectivity of perfect crystals is described by the Darwin curve rather than a Gaussian curve and, therefore, a detailed description of the triple-crystal resolution function of a triple-crystal diffractometer requires a convolution of Darwin profiles. In the dynamical theory of Bragg diffraction (Zachariasen, 1945; Batterman and Cole, 1964) the intensity diffracted by a perfect crystal

$$I = I_0 |b| \{L - | L^2 - (1 + 4K^2) 2| 1/2\}$$

where $K = \Psi_H'' / \Psi_H'$

and

$$L = | \{(-1 + y^2 - g^2)^2 + 4(gy - K)^2\}^{1/2} | + y^2 + g^2$$

The two parameters, y and g, are defined according to

$$g = \frac{-(1 - b)\,\mu_0 \lambda}{4\pi K |\Psi_H'| |b|^{1/2}}$$

$$y = \frac{(1 - b)(n - 1) + b\chi/2}{K |\Psi_H'| |b|^{1/2}}$$

where μ_0 is the absorption coefficient of the crystal and n is its refractive index. K is the polarisation factor and

$$\chi = 4 \sin\theta_B \{\sin\theta_B - \sin\theta_1\}$$

where θ_1 is the angle that the incident beam makes with the diffracting plane. Ψ_H' and Ψ_H'' are the real and imaginary parts of Ψ_H which is related to the structure factor F_H. The parameter b represents the offcut of the sample surface with respect to the diffracting planes. The results of this theory are encapsulated in figure 2.1.

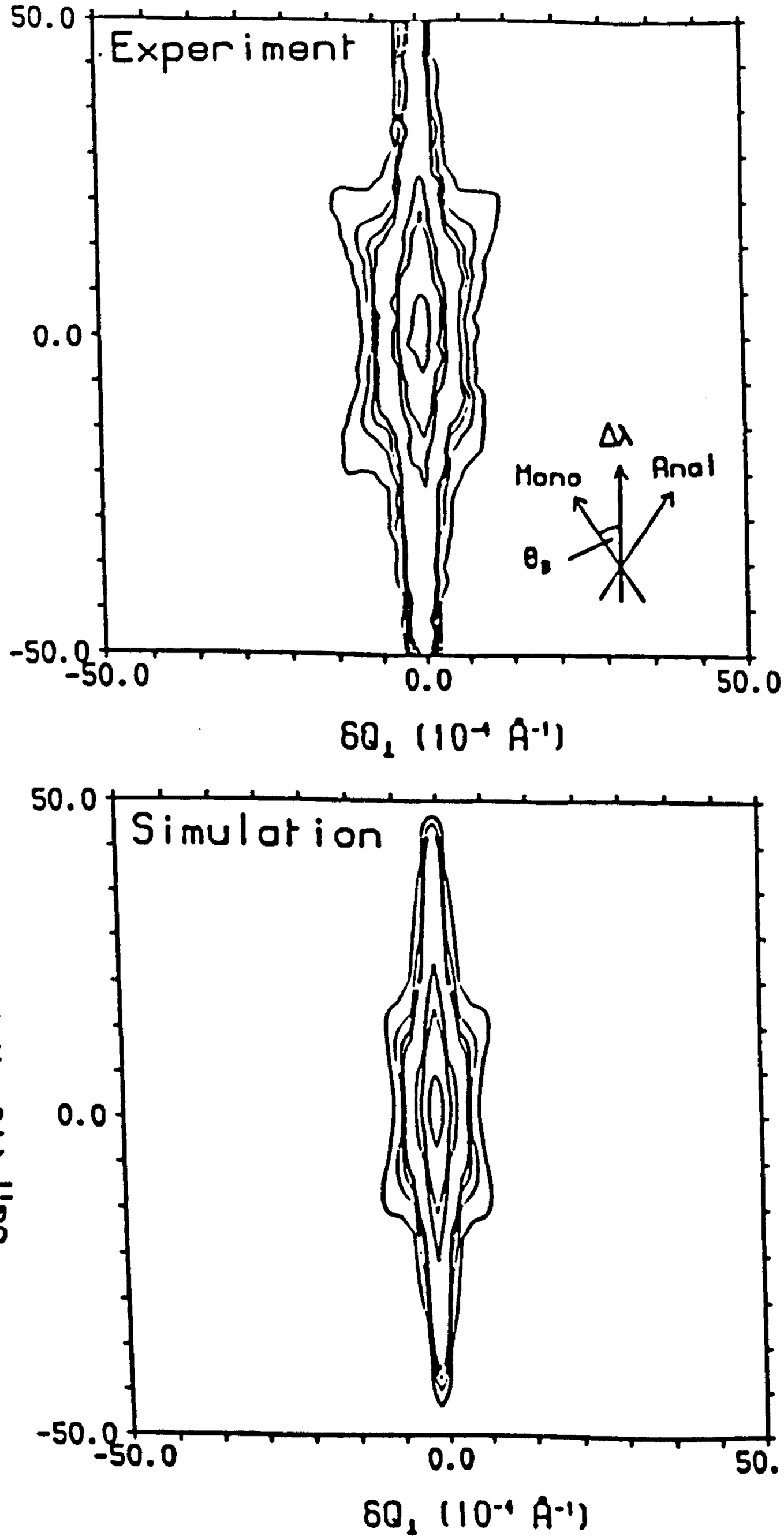

Figure 2.8. A contour map of the scattered intensity in the high resolution configuration around the InP (4 0 0) reflection, as measured, and as calculated by the convolution theory. The figure shows the direction of monochromator, analyser, and $\Delta\lambda$ streaks. The contour levels are 0.5, 0.1, 0.05, 0.01, 0.0075, 0.005 and 0.0025 of the peak intensity. The Bragg angle for this reflection, θ_B, is ~31.6°.

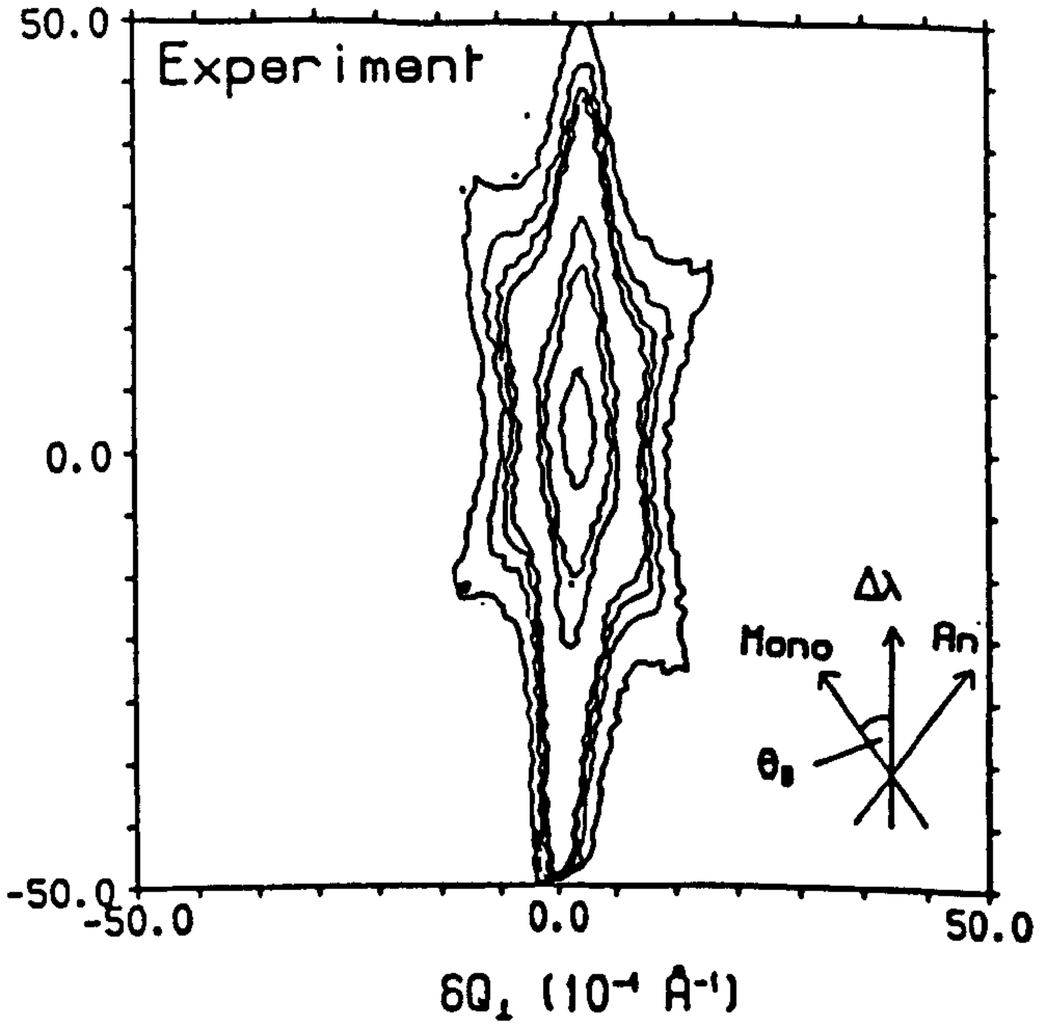

Figure 2.9. The InP (4 2 0) reflection in the same representation as figure 2.8.

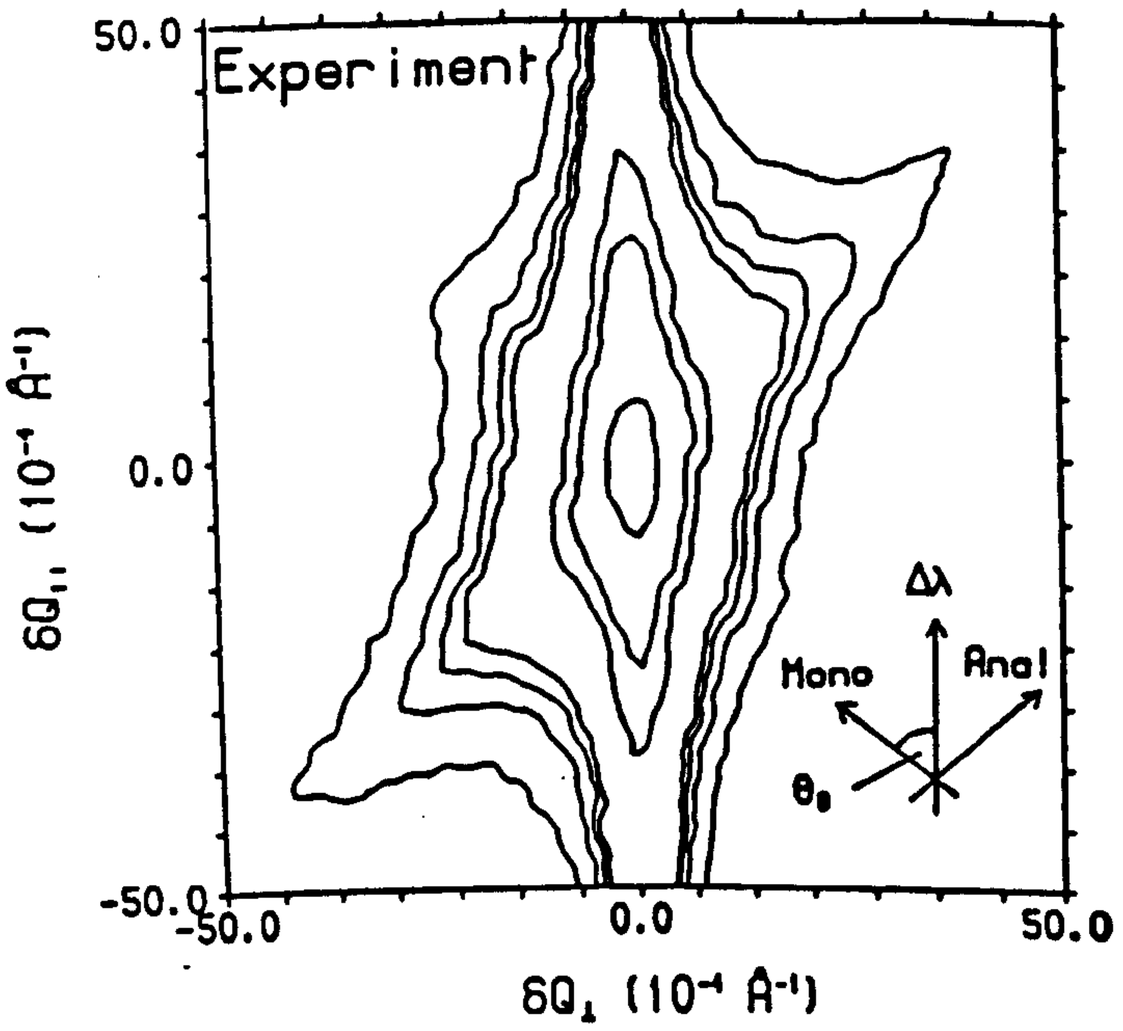

Figure 2.10. The InP (4 $\bar{4}$ 0) reflection in the same representation as figure 2.8.

Taking a Lorentzian distribution around the wavelength of the characteristic spectral line, successive convolutions may be performed to obtain a detailed form of the intensity distribution around Bragg reflections (Gartstein, 1989). The details of the calculations are not repeated here but, it should be noted that accurate numerical calculations require a careful treatment of the different rays in the diffractometer, leading to quite lengthy numerical convolutions.

Calculations were performed to compare with the observed scattering for three reflections, (4 0 0), (4 2 0) and (4 $\bar{4}$ 0), taking into account the Darwin widths of the InP sample. The results are shown as contour maps in figures 2.8 - 2.10, with the same contour levels as those plotted for the experiment. Clearly there is reasonable agreement between experiment and theory, although the experimental results are slightly broader in the direction perpendicular to the wave-vector transfer. An alternative comparison is of the longitudinal and transverse scans through the centres of the Bragg reflections, and these are shown in figure 2.11 - 2.13. The theoretical transverse widths are systematically smaller than the measured widths by about 20%, in reasonable agreement with the discrepancy between the Gaussian theory and the measured transverse widths shown in figure 2.5. The longitudinal widths for the (4 0 0) and (4 2 0) reflections are in good agreement with experiment but the calculation for the (4 $\bar{4}$ 0) reflection is slightly broader than expected. This may be due to a reduction in the wavelength spread caused by the positioning of the pre-monochromator slit in the experiment.

The convolution theory described in this section, not only successfully describes the central part of the resolution function, but also the qualitative features of the scattered intensity away from the Bragg peak. The streaks, which appear at low intensity levels, are caused by the asymmetric form of the monochromator and analyser response functions. A simple account of the origin and direction of these streaks was given in section 2. Unfortunately a detailed description requires a full knowledge of the monochromator and analyser response functions. These depend critically on the surface roughness of the crystals which is not usually controlled in an experiment.

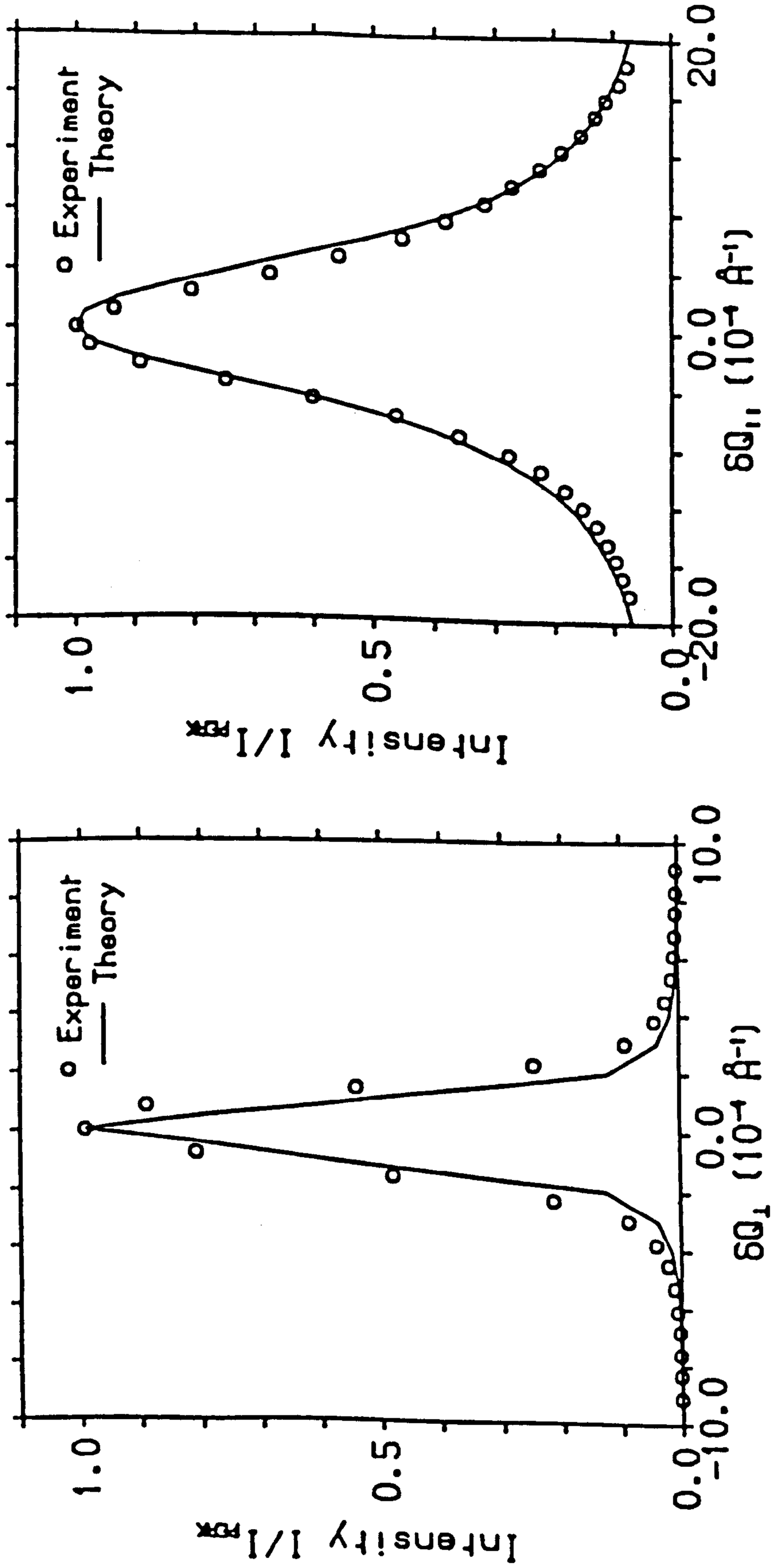

Figure 2.11. The longitudinal and transverse profiles through the InP (4 0 0) reflection, as measured, and as calculated with the convolution theory using the nominal Darwin width values for the high resolution configuration.

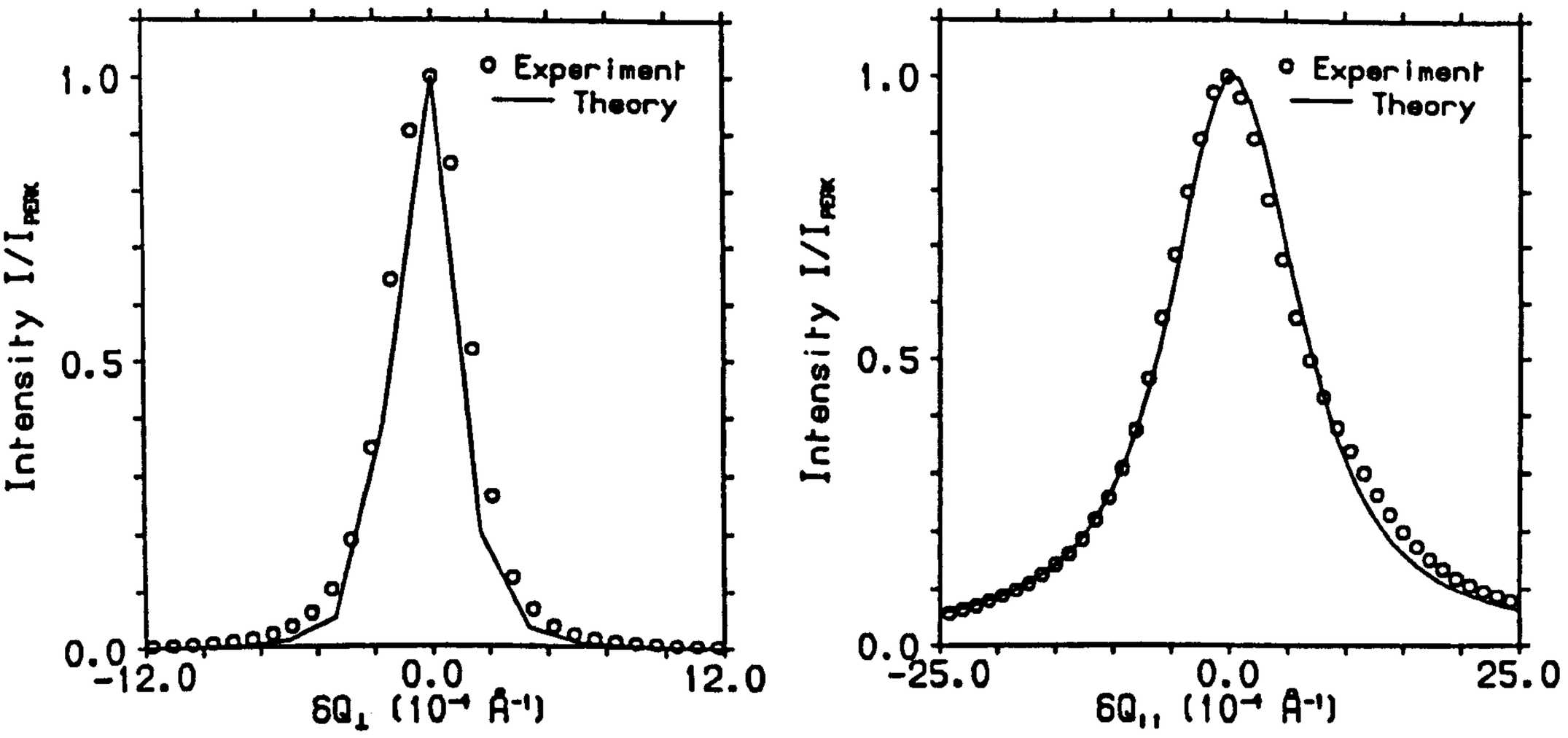

Figure 2.12. The InP (4 2 0) reflection as for figure 2.11.

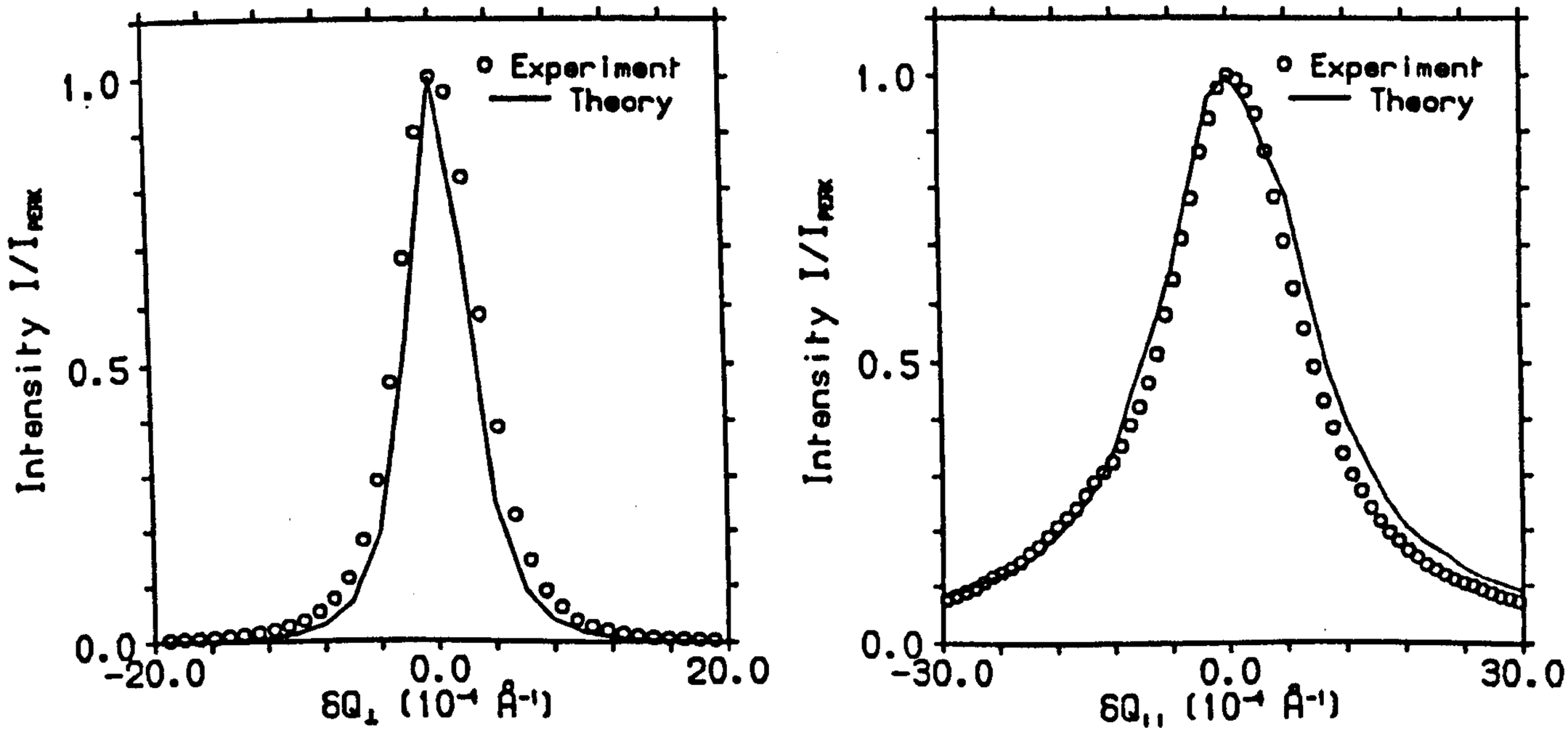

Figure 2.13. The InP (4 $\bar{4}$ 0) reflection as for figure 2.11.

4. The Resolution Function at a Synchrotron Source

(4.1) Experimental details

A similar experiment to those previously described has also been performed on a triple-crystal diffractometer based on a synchrotron source; the SRS at Daresbury Laboratory, Warrington, U.K. The instrument used was the 5-circle surface diffractometer based on the Wiggler beamline 9.4. A monolithic, channel-cut Si (1 1 1) monochromator (Beaumont and Hart, 1974; Parish, Hart, Erickson, Masciocci and Huang, 1986), situated ~35m from the source, was used to select the incident wavelength. The collimation of the x-ray beam was determined by a pre-monochromator slit, 0.5mm high by 2mm wide, and by the finite source height. During the experiment the diffractometer, which has been described elsewhere (Norris, Taylor, Moore and Harris, 1987), was operated in a two-circle mode so as to give a vertical scattering plane. The nominal stepping accuracy of the diffractometer circles is 0.000125°. A silicon wafer, with a [1 0 0] crystallographic surface normal, was used as the sample crystal and was aligned with the [0 $\bar{1}$ 1] direction perpendicular to the scattering plane. The detector system comprised of a single-bounce Si(1 1 1) analyser crystal and a scintillation counter.

As in the rotating-anode experiments, measurements of the resolution function parallel and perpendicular to the wave-vector transfer were performed over a range of wave-vector transfers. With the incident wavelength selected at 1.3804Å the accessible Bragg reflections were (4 0 0), (5 1 1), (4 2 2) and (5 3 3), as well as the symmetry related reflections (h $\bar{k}$ $\bar{l}$). The results are shown in figure 2.14. In addition, the distribution of scattered x-rays around the (4 0 0) reflection was measured and is depicted in figure 2.15. The discontinuity in the centre of the figure is not physically significant, but is a consequence of the stepping accuracy of the instrument.

There are two major differences between this experiment and the rotating-anode experiments described in the previous sections. On a conventional source, an important resolution element is the line width of the characteristic radiation. However, on a synchrotron source the wavelength resolution is completely controlled by the effective

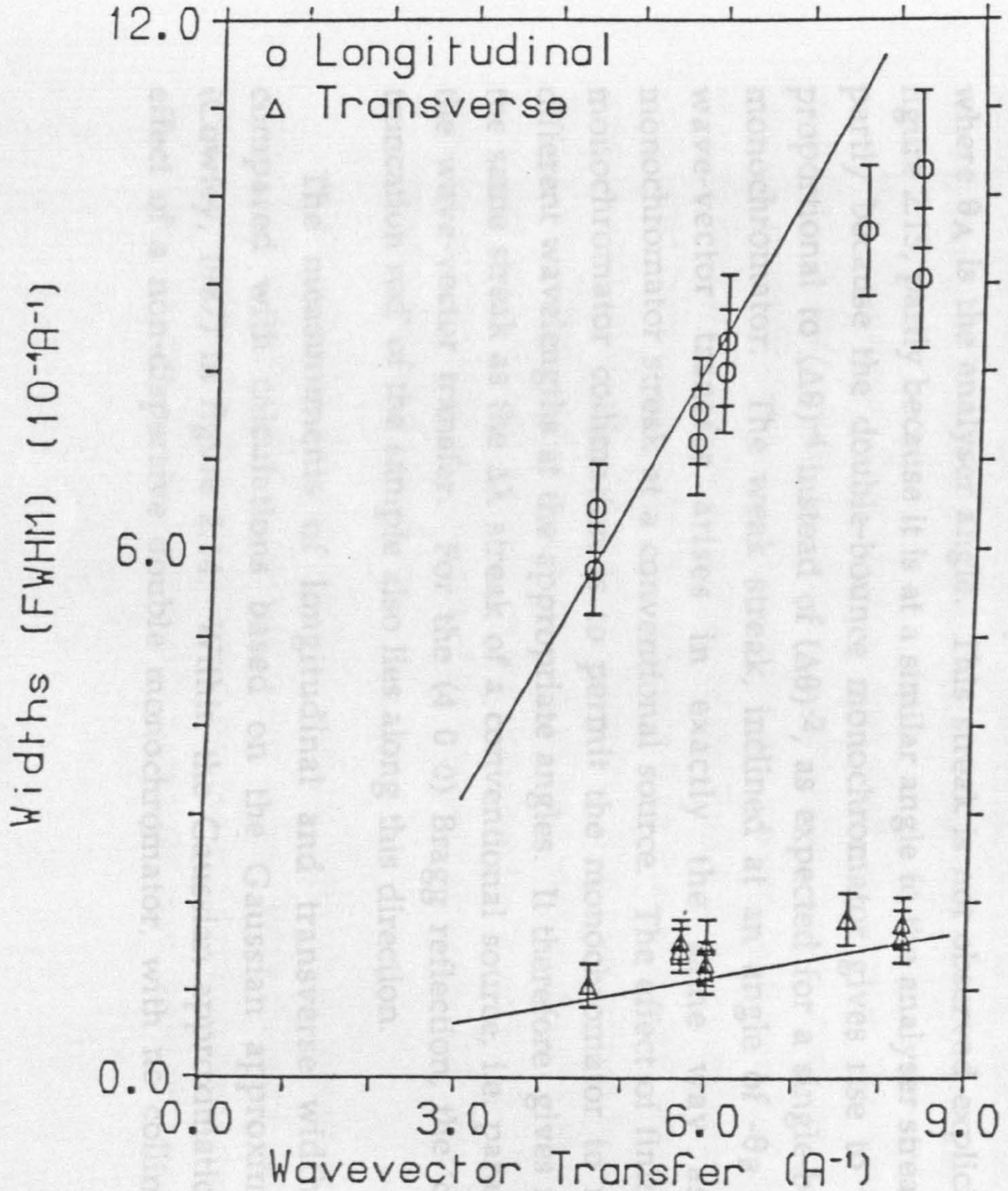

Figure 2.14. Variations of the widths (FWHM) of the Bragg reflections from Si, at λ=1.3804Å. The line is the calculation according to the Gaussian theory, as described in the text.

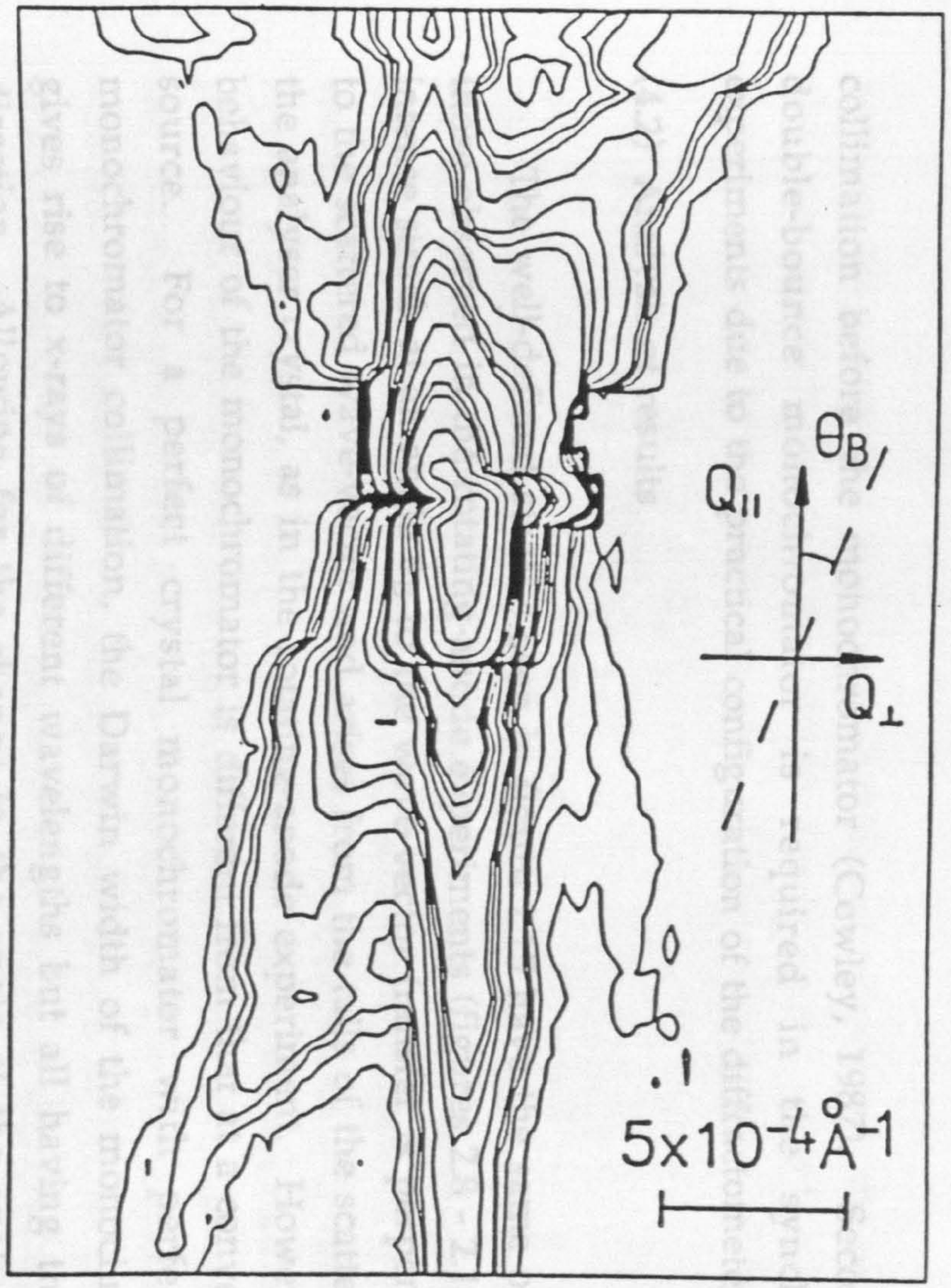

Figure 2.15. A contour plot of the scattered intensity around the Si(4 0 0) Bragg reflection. The contour levels are on a quasi-logarithmic scale over four orders of magnitude.

collimation before the monochromator (Cowley, 1987). Secondly, a double-bounce monochromator is required in the synchrotron experiments due to the practical configuration of the diffractometer.

(4.2) Analysis of results

The well-defined streaks seen in figure 2.15 have the same origin as those observed in the rotating-anode experiments (figures 2.8 - 2.10). The intense streak at an angle θ_B to the wave-vector transfer is perpendicular to the scattered wave-vector and arises from the tails of the scattering by the analyser crystal, as in the rotating-anode experiment. However, the behaviour of the monochromator is different from that at a conventional source. For a perfect crystal monochromator with perfect pre-monochromator collimation, the Darwin width of the monochromator gives rise to x-rays of different wavelengths but all having the same direction. Allowing for the change in the angle at the analyser, the monochromator will then give rise to a streak with an angle to the wave-vector transfer given by

$$\tan^{-1}\left[\frac{\tan\theta_A \tan\theta}{2\tan\theta - \tan\theta_A}\right]$$

where θ_A is the analyser angle. This streak is not observed explicitly in figure 2.15, partly because it is at a similar angle to the analyser streak and partly because the double-bounce monochromator gives rise to wings proportional to $(\Delta\theta)^{-4}$ instead of $(\Delta\theta)^{-2}$, as expected for a single-bounce monochromator. The weak streak, inclined at an angle of $-\theta_B$ to the wave-vector transfer arises in exactly the same way as the monochromator streak at a conventional source. The effect of finite pre-monochromator collimation is to permit the monochromator to reflect different wavelengths at the appropriate angles. It therefore gives rise to the same streak as the $\Delta\lambda$ streak of a conventional source, i.e. parallel to the wave-vector transfer. For the (4 0 0) Bragg reflection, the 'crystal truncation rod' of the sample also lies along this direction.

The measurements of longitudinal and transverse widths are compared with calculations based on the Gaussian approximation (Cowley, 1987) in figure 2.14. Within the Gaussian approximation the effect of a non-dispersive double monochromator, with no collimation

between the crystals, is that the probability of reflection is the product of the two monochromator response functions (Cowley, 1987). The outgoing beam then has an effective Darwin width.

$$D_M^2 = \left[\left(\frac{1}{D_{M1}}\right)^2 + \left(\frac{1}{D_{M2}}\right)^2 \right]^{-1}$$

For the double-bounce monochromator used in the experiment the Darwin width would be $\sqrt{2}$ smaller than that of a single bounce crystal. It is clear that the Gaussian approximation fails in this respect, as it has been shown that the Darwin width is relatively unchanged in a double-bounce system (Beaumont and Hart, 1974). For this reason, the calculations were performed assuming that the monochromator produced a Gaussian with the Darwin width of the Si(1 1 1) reflection, i.e. 3×10^{-5} radians at λ = 1.3804Å. The results of the calculation are shown in figure 2.14, for a beam divergence of 0.3×10^{-4} radians. This value is slightly larger than the nominal beam divergence, as it was adjusted to fit the data for the longitudinal widths in figure 2.14. There was some uncertainty in the setting of the pre-monochromator slit, which may account for the increase. However, the transverse widths are largely independent of the collimation and the calculated widths in figure 2.14 are consistently too small. It seems that the Gaussian approximation fails in this case, when the resolution is determined by reflection from four perfect crystals.

The numerical convolution described in section 3.2 was also modified to take account of the synchrotron source and the double-bounce monochromator. The results are shown in figure 2.16 for the longitudinal and transverse widths of the Si (4 0 0) Bragg reflection. The calculated transverse width is narrower than that observed, whereas the longitudinal width is, if anything, broader. The calculations by Cowley (1987) predicted that the resolution ellipse may not have one of its principal axes exactly parallel to the wave-vector transfer, Q. With the instrument operating at the limit of its stepping accuracy, this may lead to the discrepancies in figure 2.16.

In comparing the synchrotron results with those obtained on a conventional source one important factor arises. With the very tight pre-monochromator collimation, adopted for the synchrotron measurements, the resolution widths are appreciably narrower than those obtained with

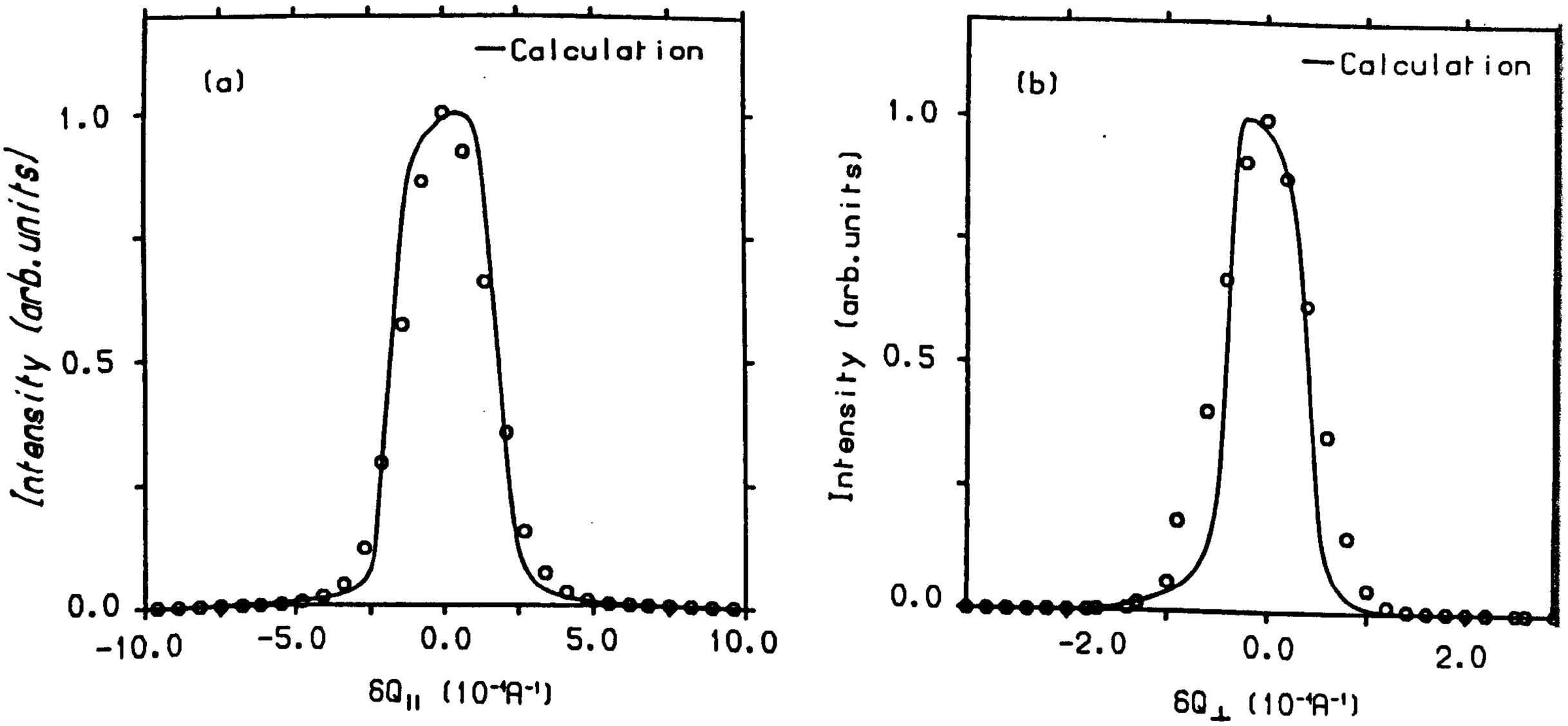

Figure 2.16. Longitudinal (a) and transverse (b) scans through the Si (4 0 0) reflection,as measured, and as calculated with the convolution theory.

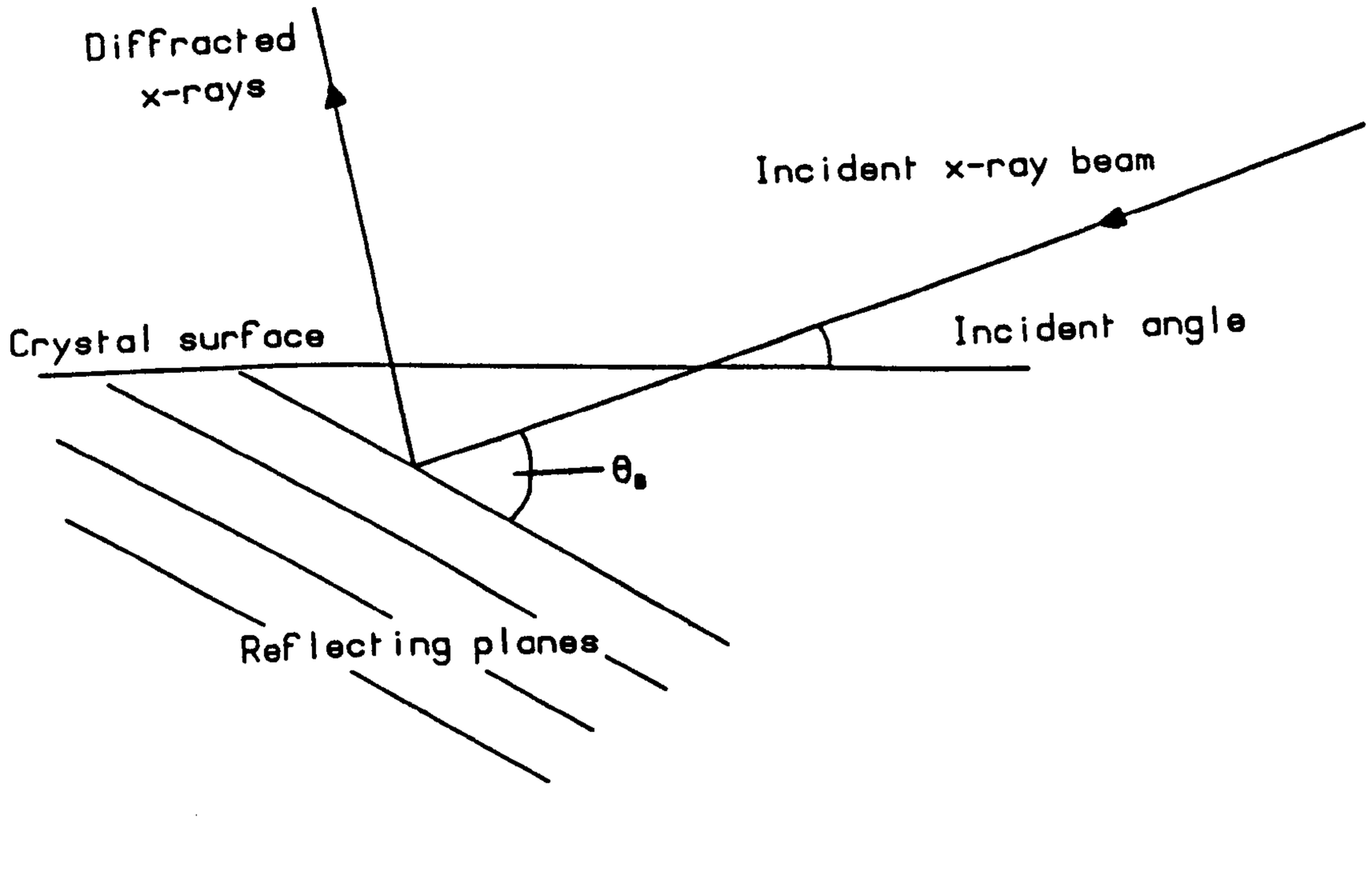

Figure 2.17. Schematic illustration of an asymmetric scattering geometry.

the rotating-anode source. This is particularly true in the direction parallel to the wave-vector transfer, where the line width of the CuKα radiation has an important effect in the rotating-anode's case. The results, therefore, play a vital role in the planning of experiments at the synchrotron source, as will be discussed in the following section.

5. Application of Resolution Measurements to X-ray Scattering from Surfaces and Interfaces

The termination of the bulk crystal lattice of a sample gives rise to scattered intensity around Bragg reflections in reciprocal space. This scattering is confined to a rod along the surface normal direction (Appendix I). The variation of intensity along the rod gives detailed information about the crystallography of the surface (Chapter 3), or about the structure of additional layers grown on the bulk crystal (Chapter 4). In order to uniquely observe this scattering, particularly close in the Bragg reflections, it is advantageous to adjust the scattering geometry so that the resolution streaks (Figures 2.8 - 2.10) do not interfere with the scattering from the surface. This can be achieved by adopting an asymmetric scattering geometry as illustrated in figure 2.17. The experiment is performed by varying the wave-vector transversely through the rod of scattering to obtain an integrated intensity at each point along the rod. By performing the experiment in this way, any dependence of the result upon the scattering geometry is removed (Cowley, 1987). Using the results of the Gaussian theory (Section 3.1), it is possible simply to convolute a Gaussian function of the appropriate width with the calculated scattering profile to enable direct comparison with the measured intensity distribution.

For x-ray reflectivity measurements, when the angle of incidence, ψ, is small, the reflected intensity is proportional to the area of the surface illuminated by the x-ray beam (the 'footprint'). This introduces a surface factor

$$R_s = (\sin \psi)^{-1}$$

into the formula for the scattered intensity. Also, when using the high-resolution triple-crystal arrangement for reflectivity experiments, the sample is scanned in angle through the rod of scattering, rather than transverse wave-vector as described above. This gives another ψ^{-1} factor for the integrated intensity observed by scanning through the rod in constant angular steps. Together with the ψ^{-2} factor, arising from the kinematical theory of x-ray diffraction (Appendix I), this gives a

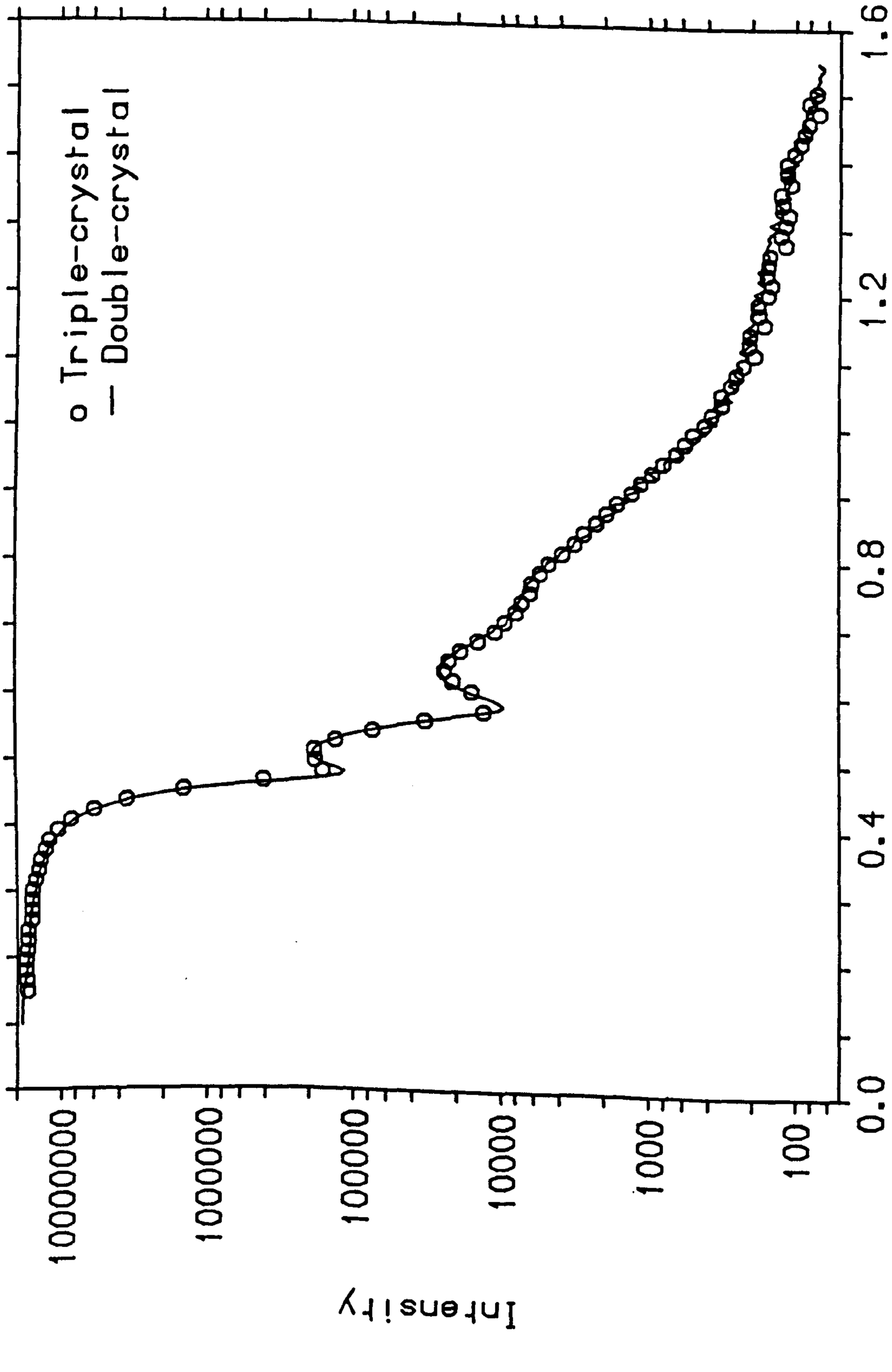

Figure 2.18. X-ray reflectivity measurements from a thin silver film, deposited on a glass substrate, with the instrument operating in its triple-crystal and its double-crystal configurations. The data had been adjusted only by a scale factor.

reflectivity proportioned to ψ^{-4}, in agreement with the Fresnel formula and the dynamical theory (Appendix II).

Reflectivity measurements may also be performed with the diffractometer in a double-crystal configuration, when the analyser is replaced by a narrow slit. This has the advantage of being quick, as the reflectivity curve is obtained simply by performing a θ - 2θ scan along the rod of scattering. In this case, the resolution is dominated by the angular acceptance of the slit, i.e. perpendicular to the scattered wave-vector (see Figure 2.3). The resolution element is, therefore, inclined at the scattering angle to the 'reflectivity rod' and so, in this symmetric case, contributes a ψ^{-1} factor to the scattered intensity. As the sample is not scanned at each point along the rod, the measured reflectivity has the same ψ^{-4} dependence as in the triple-crystal case. Figure 2.18 shows a comparison of triple-crystal and double-crystal reflectivity data measured in the ways described above. The data have been adjusted only by a scale factor and clearly show the same angular dependence. Although the double-crystal technique has the advantage of being quick, it should be noted that there are often cases when only the triple-crystal technique will give the correct results. In particular this is true if the sample is macroscopically bent (Chapter 3), or if it is necessary to separate diffuse scattering from the bulk scattered intensity (Als-Nielsen, 1989; Chapter 5 of this thesis).

Finally, in all x-ray scattering studies, it is important to select the correct diffractometer configuration for a particular experiment. In section 4 of this chapter the resolution at a synchrotron source was found to be extremely high if the diffractometer was operated using an analyser crystal (Figure 2.14). Although this has many advantages, in particular for background reduction, it may be unsuited to the measurement of weak scattering features, away from Bragg reflections. In this case it is better to use a slit in front of the detector which, despite increasing the background level, may allow measurement of scattering right across the Brillouin zone (Robinson, Waskiewicz, Tung and Bohr, 1986; Robinson, 1989).

CHAPTER THREE

Scattering Measurements of Silicon Oxides on Silicon

1. Introduction

The Si/SiO_2 structure plays a dominant role in silicon technology due to its unique electronic and structural properties. As the desire for smaller devices becomes apparent, new problems arise, concerning degradation of the reliability of device performance, due to structural imperfections. For this reason many attempts have been made to understand the structural properties of the Si/SiO_2 interface, and of SiO_2 itself (The Physics of SiO_2 and its Interfaces, 1978; Hollinger and Himpsel, 1984; Grunthaner and Grunthaner, 1986) Several experimental techniques have been used to examine the structure, e.g. transmission electron microscopy (TEM) (Ourmazd, Taylor, Rentschler and Bevk, 1987), low energy electron diffraction (LEED) (Wollschläger and Henzler, 1989) x-ray photoelectron spectroscopy (XPS) (Grunthaner, Grunthaner, Vasquez, Lewis, Maserjian and Madhukar, 1979) and ellipsometry (Aspnes and Theeten, 1980). The results obtained vary according to the different probing techniques, but generally agree in identifying a near-interface region, of a few atomic layers, containing Si atoms in intermediate oxidation states.

X-ray scattering has the advantage of being a non-destructive technique, in which the device characteristics are unaltered by measurement, and allows detailed information about the silicon lattice and oxide overlayers to be obtained (Fuoss, Norton, Brennan and Fischer-Colbrie, 1988). In this chapter two different types of x-ray measurements are described, which have been used to study the structural properties of a variety of Si/SiO_2 systems.

The first of these is a study of the scattering that arises around Bragg reflections, due to the termination of the silicon crystal lattice (Appendix I). This scattering is now commonly known as the 'crystal truncation rod' (Robinson, 1986). In extending the work by Cowley and Ryan (1987), a new feature of the scattering is discovered, previously unaccounted for in

theoretical treatments (Andrews and Cowley, 1985). These measurements are presented in section 2, together with a development of the scattering theory (Kashihara, Kawamura, Kashiwagura and Harada, 1987), which reveals new information about the Si/SiO_2 interface.

The second technique is a measurement of the x-ray reflectivity as a function of incident angle (Appendix II). Reflectivity measurements of a variety of samples are described in section 3 and demonstrate the sensitivity of the technique to the study of thin amorphous layers, as well as crystalline material. The problems of interpreting reflectivity data in the presence of contamination are discussed, as well as the advantages of using a triple-crystal diffractometer for these experiments.

The final section contains some neutron reflectivity measurements performed on the C.R.I.S.P. facility at the Rutherford Appleton Laboratory, and outlines some possible advantages of using neutrons for reflectivity experiments.

2. Crystal Surface Scattering

(2.1) Experiments and Results.

As described in Appendix I, the termination of the sample crystal at the surface leads to scattering around Bragg reflections, at wave-vector transfers $\underline{Q} = \underline{G} + \underline{q}$, where $\underline{G}$ is a reciprocal lattice vector and $\underline{q}$ is a wave-vector perpendicular to the surface plane. The $\underline{q}$ dependence of this 'crystal truncation rod' gives detailed information about the surface crystallography of the sample crystal (Feidenhans' l, 1989; Vlieg, 1988). If there are surface layers absorbed on the bulk crystal the technique probes the buried interface between the surface layer and the crystal.

Crystal truncation rod experiments have been carried out at Edinburgh University, using the x-ray triple-crystal diffractometer in its high-resolution configuration. This configuration is described in detail in the previous chapter. With the sample oriented in an extended face geometry, it is possible to measure the x-ray scattering in a plane of sample reciprocal space (Ryan, 1986). The rod of scattering thus becomes a line, extending in a direction perpendicular to the physical crystal surface, and resolution-limited in the direction parallel to the surface. Figure 3.1 illustrates schematically the scattering geometry used for the measurements described here. The intensity dependence is obtained by scanning through the 'crystal truncation rod' in transverse wave- vector, $q_{||}$, to give an integrated intensity at each point, $q_{\perp}$, along the rod. This allows subtraction of the background scattering, including the thermal diffuse scattering (TDS), which forms a broad background under the resolution-limited surface streak. Typical $q_{||}$ scans through the truncation rod are shown in figure 3.2, at three values of wave-vector transfer given by $(3 + q_{\perp}, 1 + q_{||}, 1 + q_{||})$ where $q_{\perp} = 0.01$, 0.05 and 0.10 reciprocal lattice units. In each case the peak is resolution-limited and shows no broadening along $q_{||}$ (Andrews and Cowley, 1985; Kashiwagura, Kashihara, Sakata, Harada, Wilkins and Stevenson, 1987). In the experiments, the physical surface was always found to be offcut from the crystallographic surface by up to 0.2 degrees. This implies an averagely stepped surface, albeit with large terrace lengths, and the effects of this have been observed with electron diffraction (Lent and Cohen, 1984;

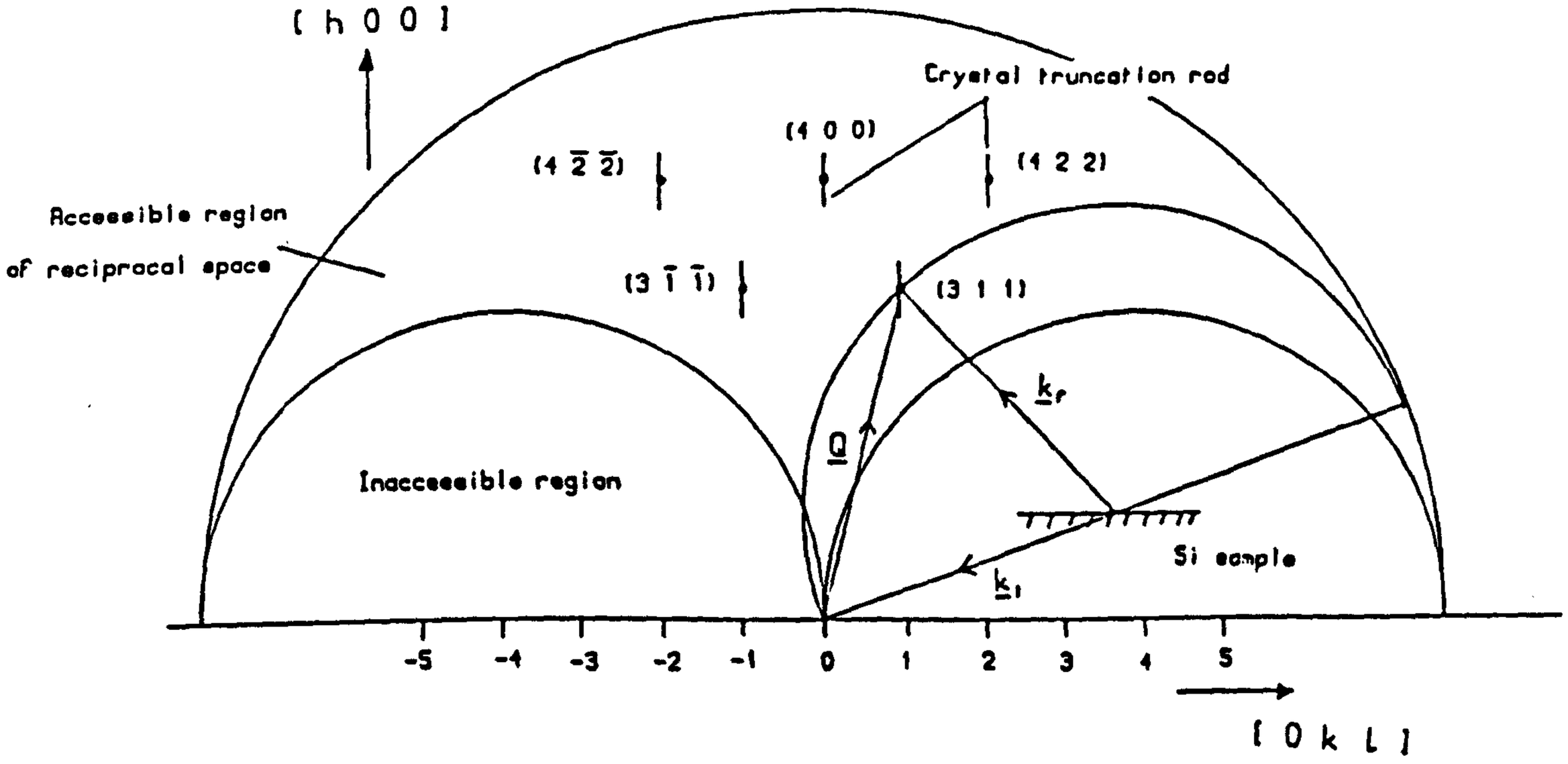

Figure 3.1. The scattering geometry used for the crystal truncation rod measurements. The direction of the scattering around each Bragg reflection is shown.

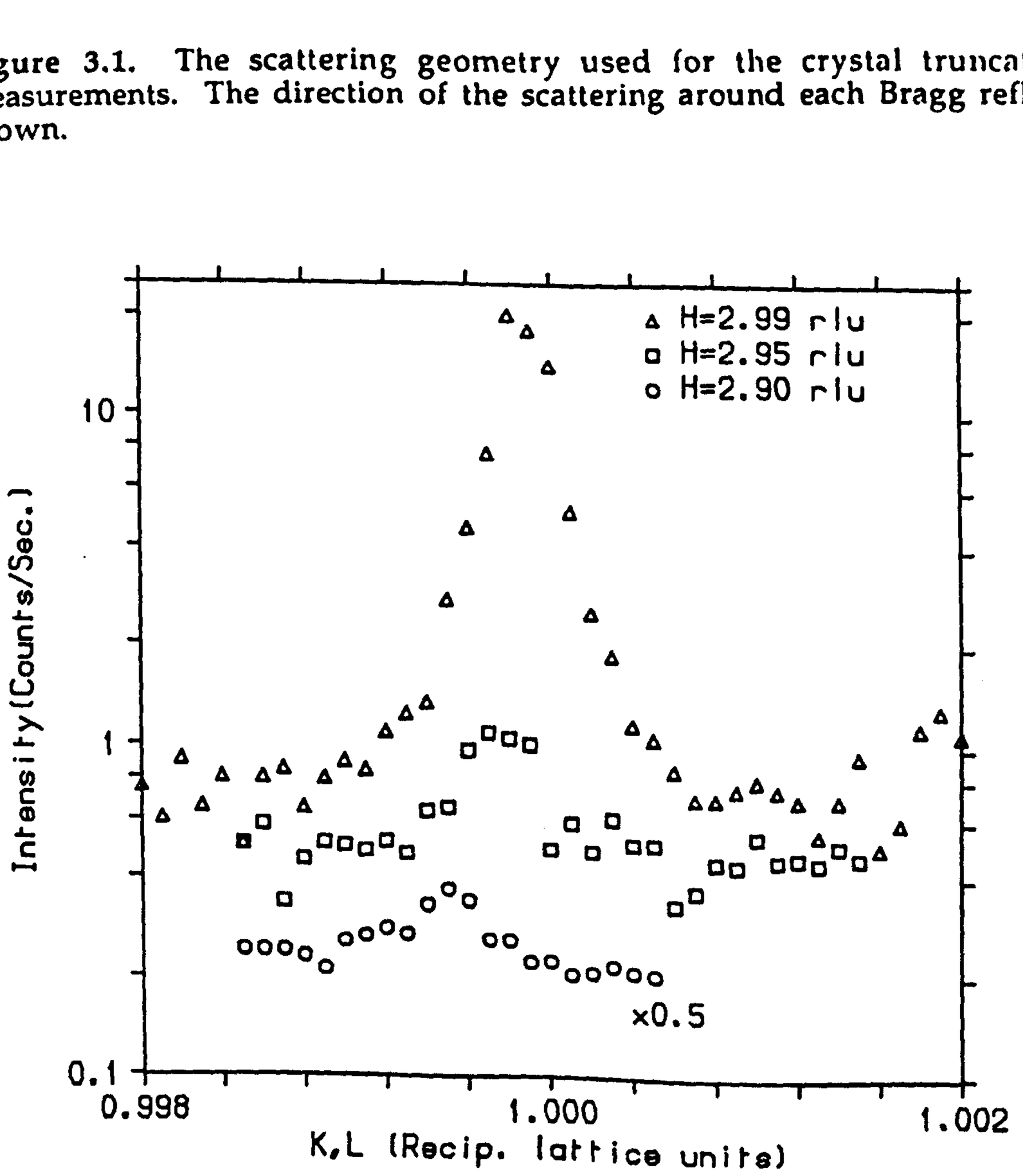

Figure 3.2. The $q_{\parallel}$-scan profiles of the crystal truncation rod scattering at $q_{\perp}$=0.01, 0.05, 0.10 reciprocal lattice units, around the Si (3 1 1) Bragg reflection.

Pukite, Lent and Cohen, 1985) and by x-ray diffraction (Norris, 1989). However, this property of the surface has a negligible effect on the measurements described in this section, due to the large lengthscales involved.

Two silicon samples, one with a native oxide and the other with a thermally grown oxide, were specifically studied using the crystal truncation rod technique. The wafers were grown and prepared at the Microfabrications Facility, Edinburgh University, and at RSRE, Malvern. Both wafers had [1 0 0] surface normals and were oriented with the [0 1 1] direction in the scattering plane (see Figure 3.1). Measurements of the truncation rod were then made around the (3 1 1) Bragg reflection, thus avoiding the characteristic resolution degrading streaks. Figure 3.4 shows the measurements from the native oxide sample, i.e. the background subtracted integrated intensity as a function of $q_\perp$ over four decades of intensity. Similar results for the thermally oxidised sample, with an oxide nominally 270 Å thick, are shown in figure 3.6. In both cases the measurements extend out to $q_\perp = \pm 0.15$ reciprocal lattice units. At larger values of $q_\perp$, the signal was lost in the background noise, even with a count time of 1500 seconds/point.

(2.2) Description of Results.

The kinematical theory of the x-ray scattering arising from the flat, sharp surface of a crystal is described in Appendix I, and was developed independently by Andrews and Cowley (1985) and Robinson (1986). The prediction that the intensity is proportional to $q_\perp^{-2}$ along the truncation rod also arises in the dynamical theory of x-ray diffraction (Darwin, 1914; Zachariasen, 1945). Deviations from this ideal behaviour have been described in a variety of ways, e.g. partial occupation of surface layers (Robinson, 1986) and a fractal description of the surface (Andrews and Cowley, 1985).

Cowley and Ryan (1987) have studied the Si/SiO_2 interface in (1 1 1) silicon slices and their results are reproduced in figure 3.3. A $1/q_\perp^n$ power law was fitted to the data and in each case the value of n was found to be slightly less than two. The origin of this discrepancy was not understood, but it was concluded that the termination of the silicon lattice was

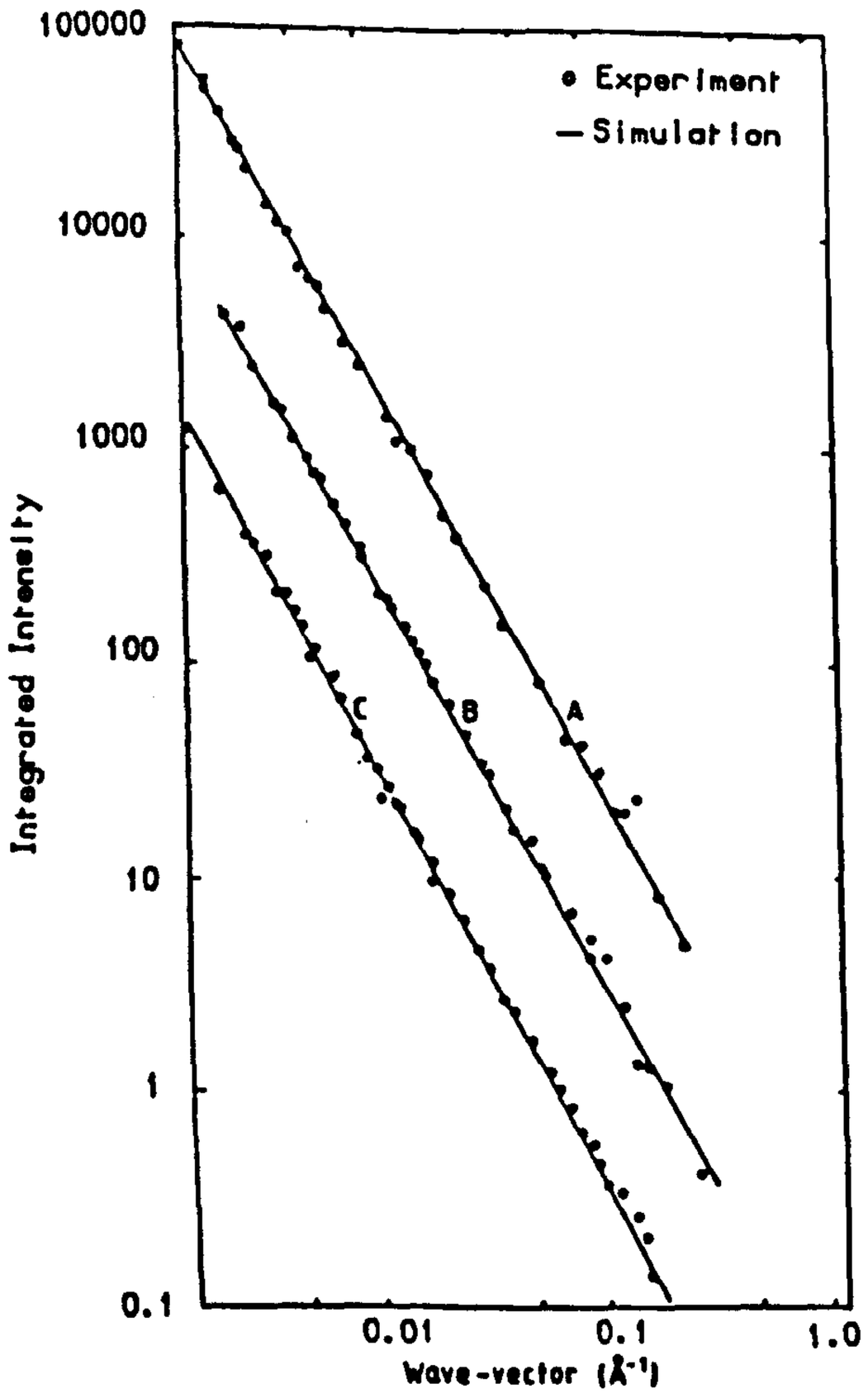

Figure 3.3. The intensity of the surface scattering near the (1 1 1) Bragg reflection for three Silicon wafers of different oxide thicknesses. The solid lines are a $1/q_{\perp}^{n}$ power law, where n is slightly less than 2. Nominal oxide thicknesses, A:30Å, B:50Å, C:10Å.

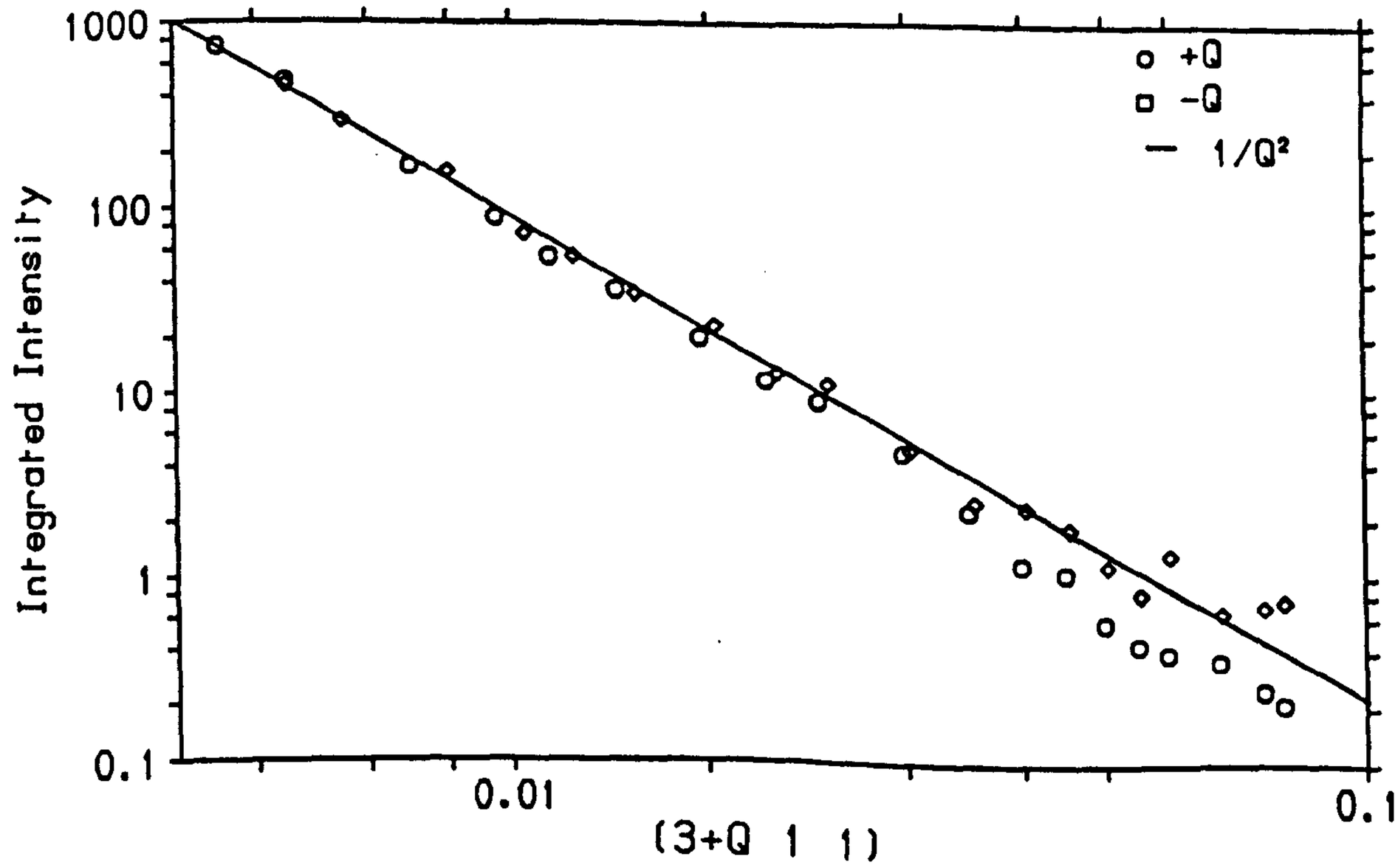

Figure 3.4. The intensity dependence of the crystal truncation rod for the native oxide [1 0 0] silicon slice around the (3 1 1) Bragg reflection ie. for wavevector transfers Q=(3+q, 1,1).

atomically abrubt. After these measurements were made two further experiments were reported (Kashihara, Kawamura, Kashiwagura and Harada, 1987; Robinson, Waskiewicz, Tung and Bohr, 1986) in which asymmetry in the intensities on the $+q_\perp$ and $-q_\perp$ sides of the Bragg reflection were detected. As can be seen from figure 3.4 this is clearly the case for the native oxide data, in which the $+q_\perp$ intensity dependence departs from the ideal $1/q_\perp^2$ behaviour.

The asymmetry of the crystal truncation rod can be described by a phenomenological model, in terms of a deviation in lattice parameter and atomic population of the surface layers (Kashihara, Kawamura, Kashiwagura and Harada, 1978; Harada and Kashiwagura, 1989] The details of the calculation for a [1 0 0] silicon surface are outlined below.

For a one-dimensional array of scatterers (Figure 3.5) the scattering amplitude at wave-vector transfer K, perpendicular to the surface, is given by

$$F(K) = A \sum_{j=0}^{\infty} P_j \exp\left[iK\left(Z_j + U_j\right)\right] \exp\left(-jB\right) \qquad (1)$$

where A is an amplitude constant, P_j is the population and U_j is the deviation of the lattice spacing from the ideal bulk spacing of the j-th atomic plane, and B is an absorption correction given by (figure 3.5)

$$B = \mu c \left(\frac{1}{\sin\theta_i} + \frac{1}{\sin\theta_e}\right) \qquad (2)$$

μ is the linear absorption coefficient for silicon. The modulations are written as

$$P_j = 1 - \eta \exp\left(Z_j/\xi\right) \qquad (3)$$

$$U_j = U^\circ \exp\left(Zj/\xi\,'\right) \qquad (4)$$

ξ and $\xi\,'$ represent the characteristic depths of each modulation. $(1 - \eta)$ and U° are the population and lattice parameter deviation at the crystal surface. Z_j is defined in figure 3.5 and B is simply a function of the scattering geometry. Expanding the series, and approximating $\exp(iKU_j) \approx 1 + iKU_j$, the expression becomes

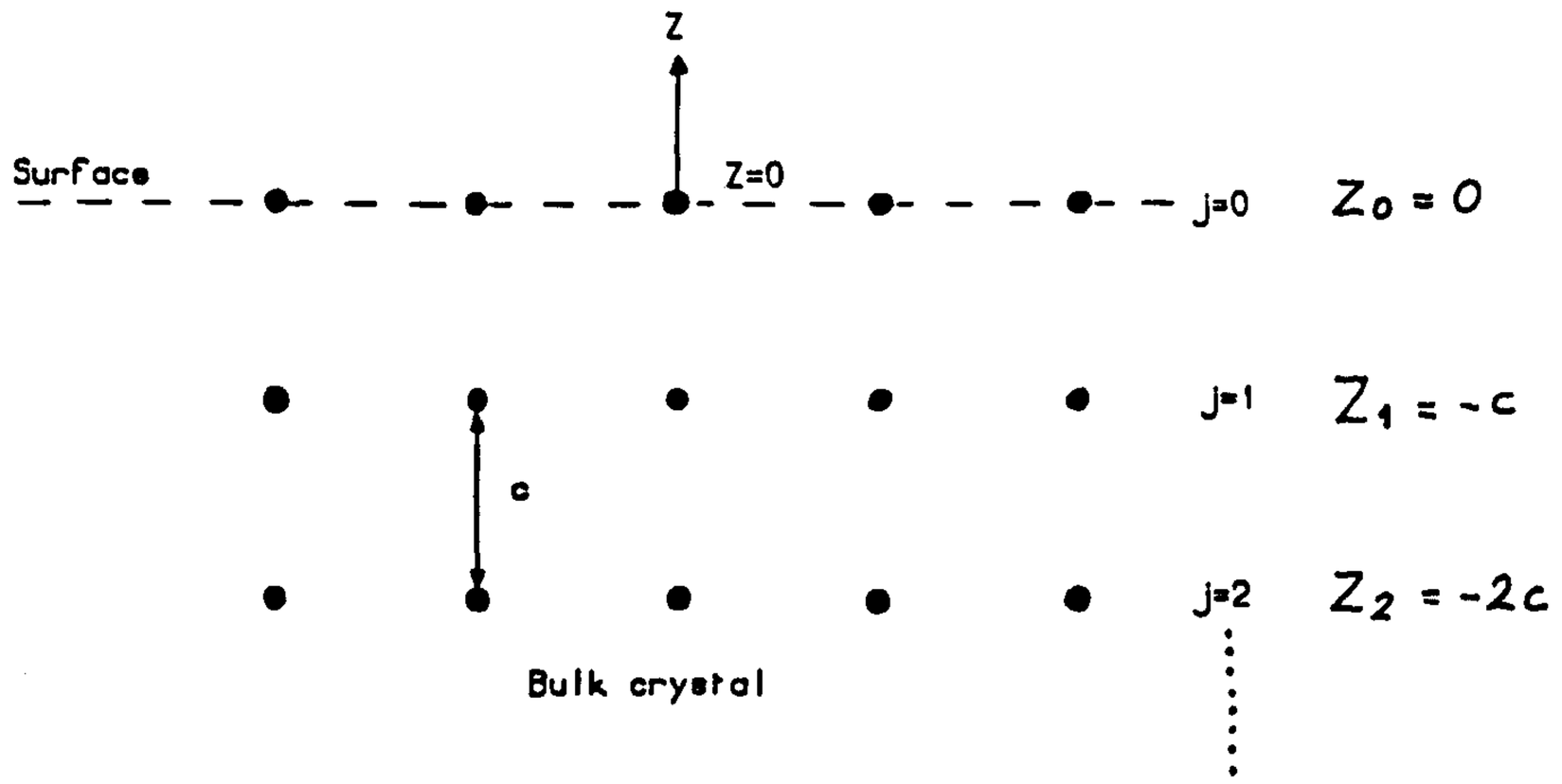

Figure 3.5. One dimensional scattering model illustrating two distortions at the sample surface.

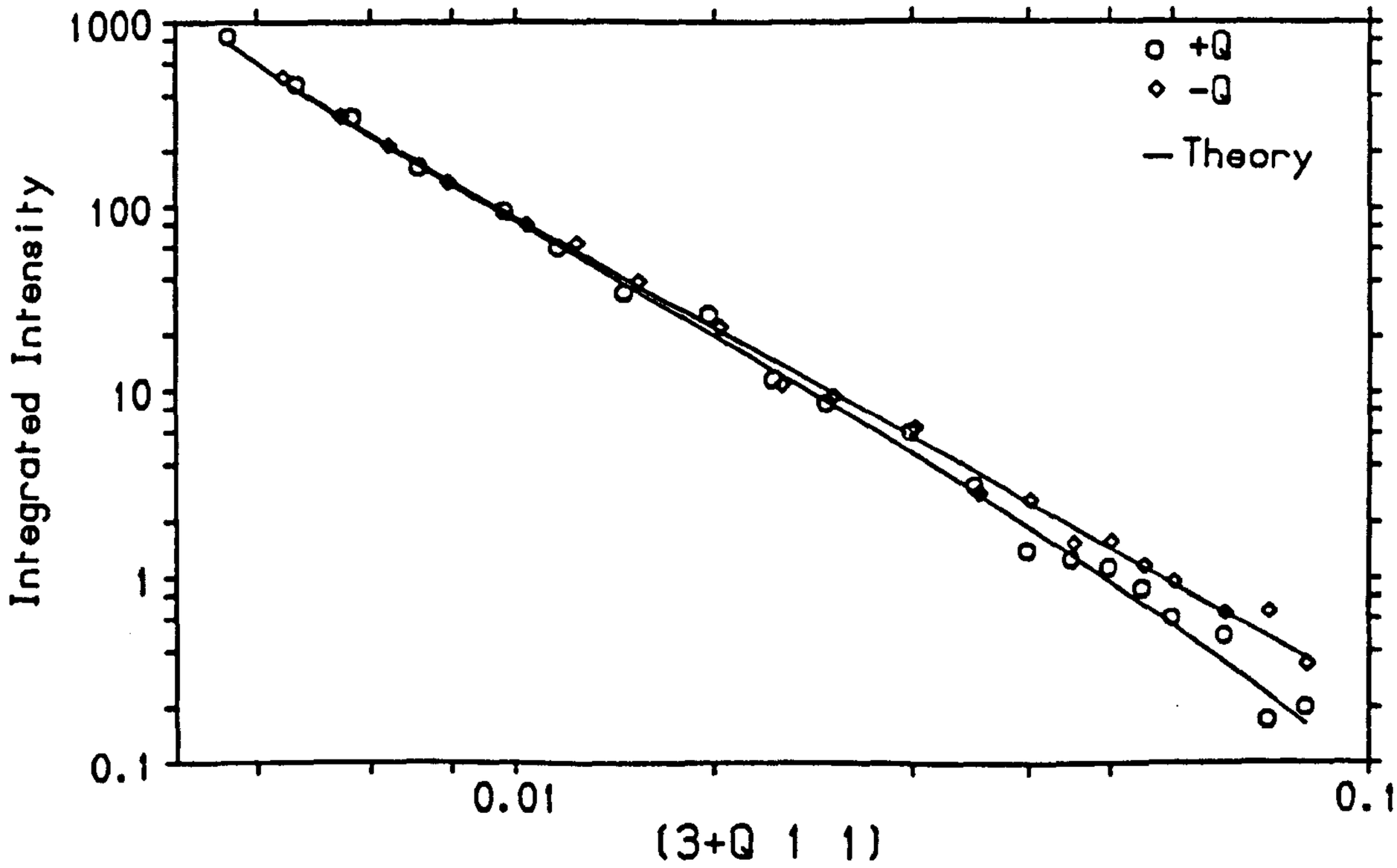

Figure 3.6. The intensity dependence of the crystal truncation rod for the thermally oxidised [1 0 0] silicon slice, around the (3 1 1) Bragg reflection. The calculated line is according to the model described in the text and the parameters in Table 3.1.

$$F(K) = \frac{A}{[1 - \exp(-iKc)\exp(-B)]} + \frac{AiKU^0}{[1 - \exp(-iKc)\exp(-c/\xi')\exp(-B)]}$$

$$- \frac{A\eta}{[1 - \exp(-iKc)\exp(-c/\xi)\exp(-B)]} \qquad (5)$$

$$- \frac{A\eta iKU^0}{[1 - \exp(-iKc)\exp(-c/\xi)\exp(-c/\xi')\exp(-B)]}$$

where c is the lattice parameter of the unit cubic cell. In this equation the second and third terms are the individual contributions to the scattering by the two distortions and the fourth is a cross-over term. Intensity profiles have been calculated using equation (5) and, by refining the parameters A, η, U^0, ξ and ξ' in a least squares fitting program, it is possible to obtain fits to the data. These are shown in figures 3.6 and 3.7, according to the parameters in Table 3.1, and demonstrate that the theory is quite capable of reproducing the observed features of the scattering.

The parameters in Table 3.1 indicate a slight difference between the thermally oxidised sample and the native oxide sample in the sharpness of the Si/SiO_2 interface. Although difficult to draw any wide-ranging conclusions, the results indicate a rougher interface with the native oxide, consistent with oxide formation at a low temperature. In both cases the lattice distortion is largely confined to a region approximately one unit cell thick at the interface. This result is consistent with recent core-level spectroscopy measurements (Himpsel, McFeely, Taleb-Ibrahami, Yarmoff and Hollinger, 1988) which indicated a graded $Si(100)/SiO_2$ interface, 1-2 monolayers in width.

It would be of considerable interest to use the phenomenological theory as the basis for a full structural characterisation of the $Si(100)/SiO_2$ interface. Such a calculation has been performed for $Si(1\ 1\ 1)/SiO_2$ by Robinson, Waskiewicz, Tung and Bohr (1986). The structural refinement could then be compared to existing interface models (Ohdomari, Akatsu, Yamakoshi and Kishimoto, 1987; Herman and Kasowski, 1981) and even be extended to take account of ordered SiO_2 in the interface region (Fuoss, Norton, Brennan and Fischer-Colbrie, 1988). However such a calculation would require further development of the technique, to allow measurement of the surface scattering at larger values of $q_\perp$, well away from the Bragg reflection. Such measurements may be possible using

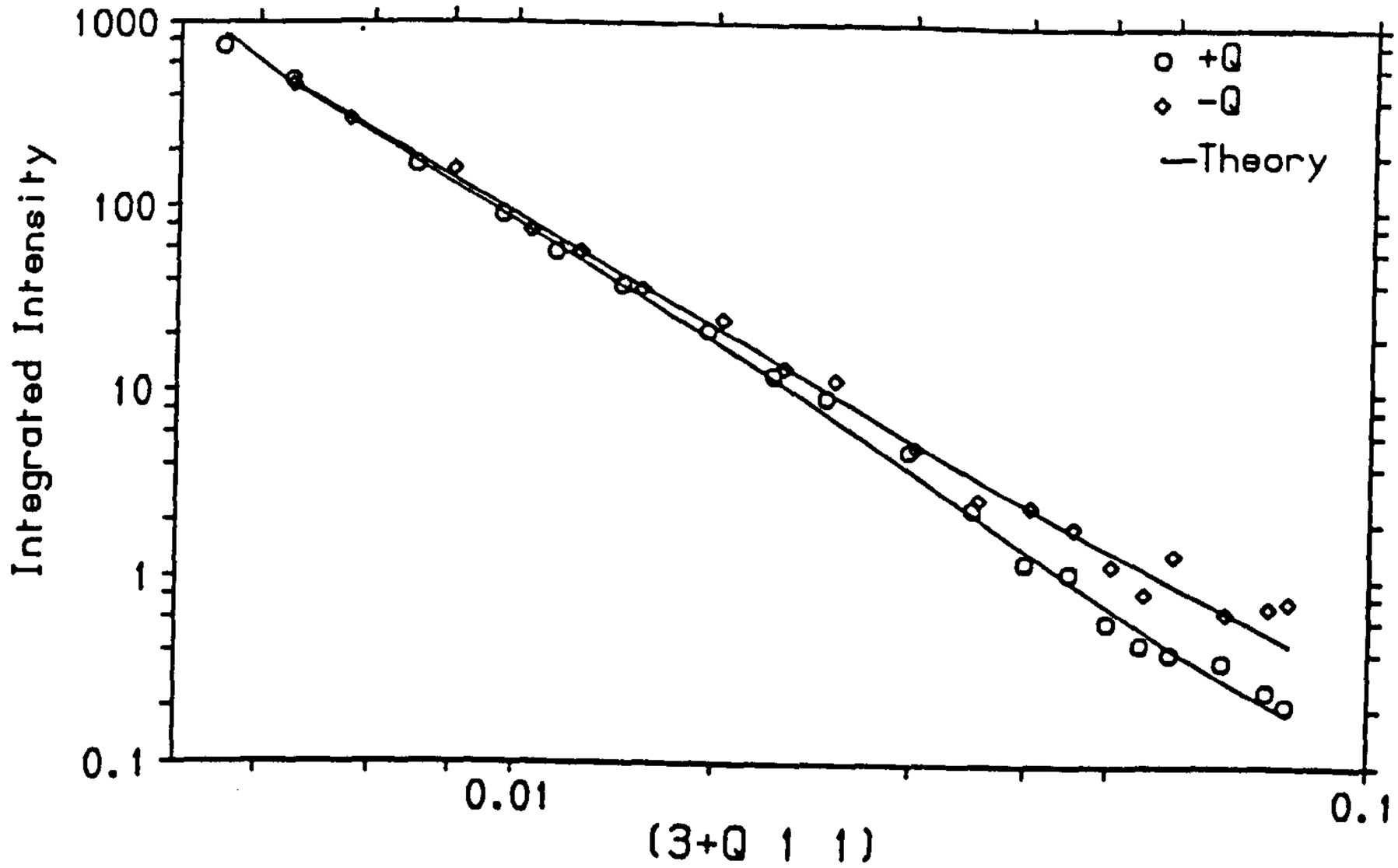

Figure 3.7. As for figure 3.6, but for the native oxide silicon slice.

	η	ξ (Å)	U^0	ξ^1 (Å)
Thermal Oxide	0.205±.03	4.5±2.3	0.068±.02	1.9±1.6
Native Oxide	0.137±.03	25±10	0.082±.02	4.4±1.6

Table 3.1. The parameters representing lattice distortion in the silicon slices.

synchrotron sources or by the modification of existing laboratory techniques.

3. X-ray Reflectivity

(3.1) Experimental technique.

The index of refraction for x-rays in matter is less than unity and therefore, at incident angles lower than a certain critical angle, x- rays are totally externally reflected in matter. The critical angle is determined by the electron density of the medium. Kiessig (1931) showed that a thin surface film gives rise to oscillations in the reflected intensity as a function of incident angle. The form of this scattering, and its dependence on the incident angle, thus provide information on the quality and thickness of any surface layers, via the electron density profile as a function of depth (Appendix II; Parratt, 1954). The technique is therefore sensitive to amorphous as well as crystalline material.

X-ray reflectivity measurements have been performed on three samples using the triple-crystal diffractometer at Edinburgh University in its high-resolution configuration. In addition to the two samples described in the previous section a Si (1 0 0)/SiO_2 wafer, oxidised nominally to 50Å, was also examined. The use of a high-resolution triple-crystal diffractometer for these experiments was essential for two main reasons.

Firstly, it is important in a reflectivity experiment to measure only the specular component of the scattered intensity, subtracting any background due to diffuse scattering (Pershan, Braslau, Weiss, and Als-Nielsen, 1987). In particular, a second peak often occurs in the scattering when the detector is positioned at the critical angle to the sample surface (Yoneda, 1963; Andreev, 1985), as illustrated in figure 3.8. This second peak is characteristic of the scattering from all rough surfaces and can be explained qualitatively, using the Distorted-Wave Born Approximation to scattering theory (Vineyard, 1982; Sinha, Sirota, Garoff and Stanley, 1988). The high-resolution of the triple-crystal diffractometer enables this second peak to be distinguished (figure 3.9) and therefore discriminated against. This scattering becomes a more severe problem for rougher surfaces.

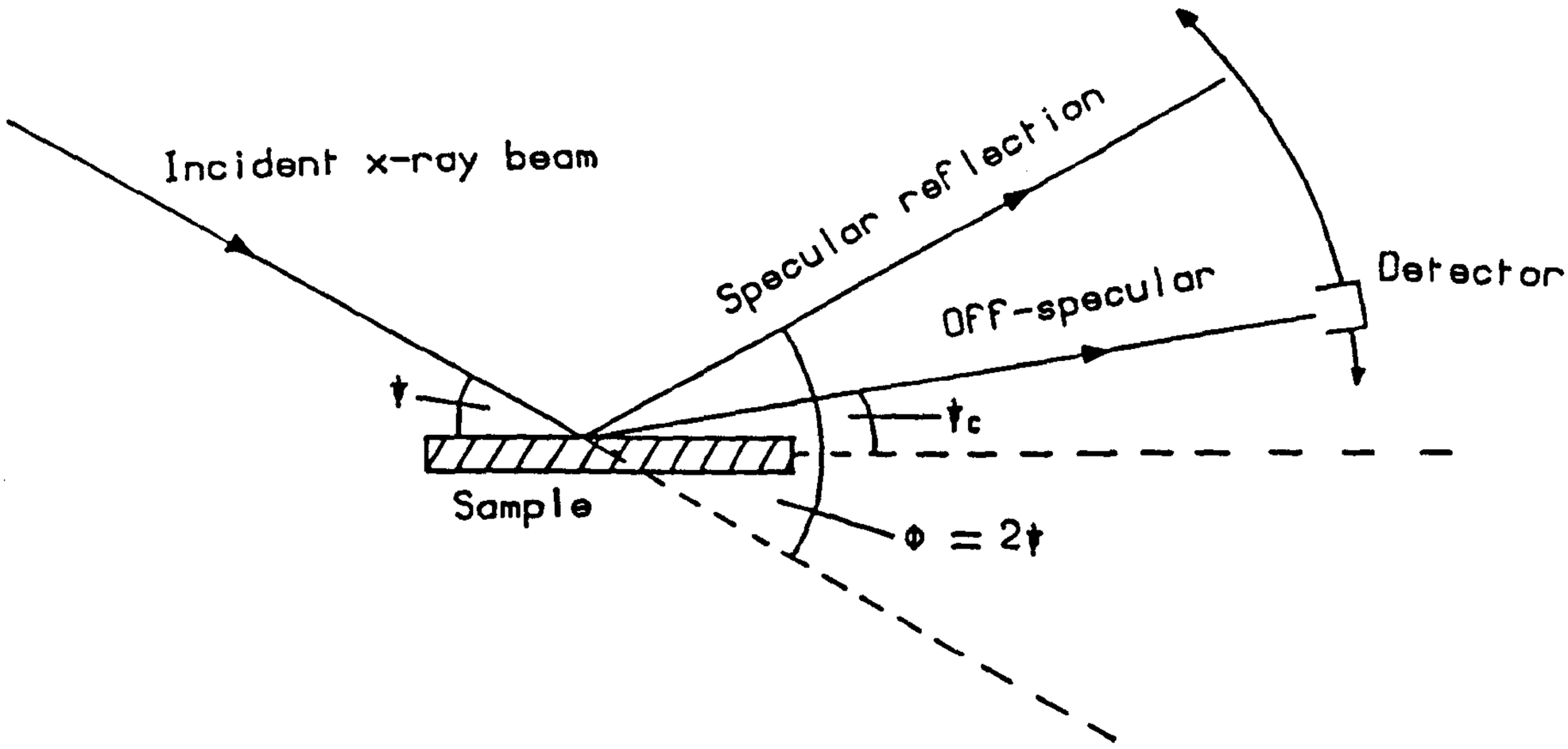

Figure 3.8. The angular dependence of the 'off-specular' scattering. The angles involved are greatly exaggerated in the diagram.

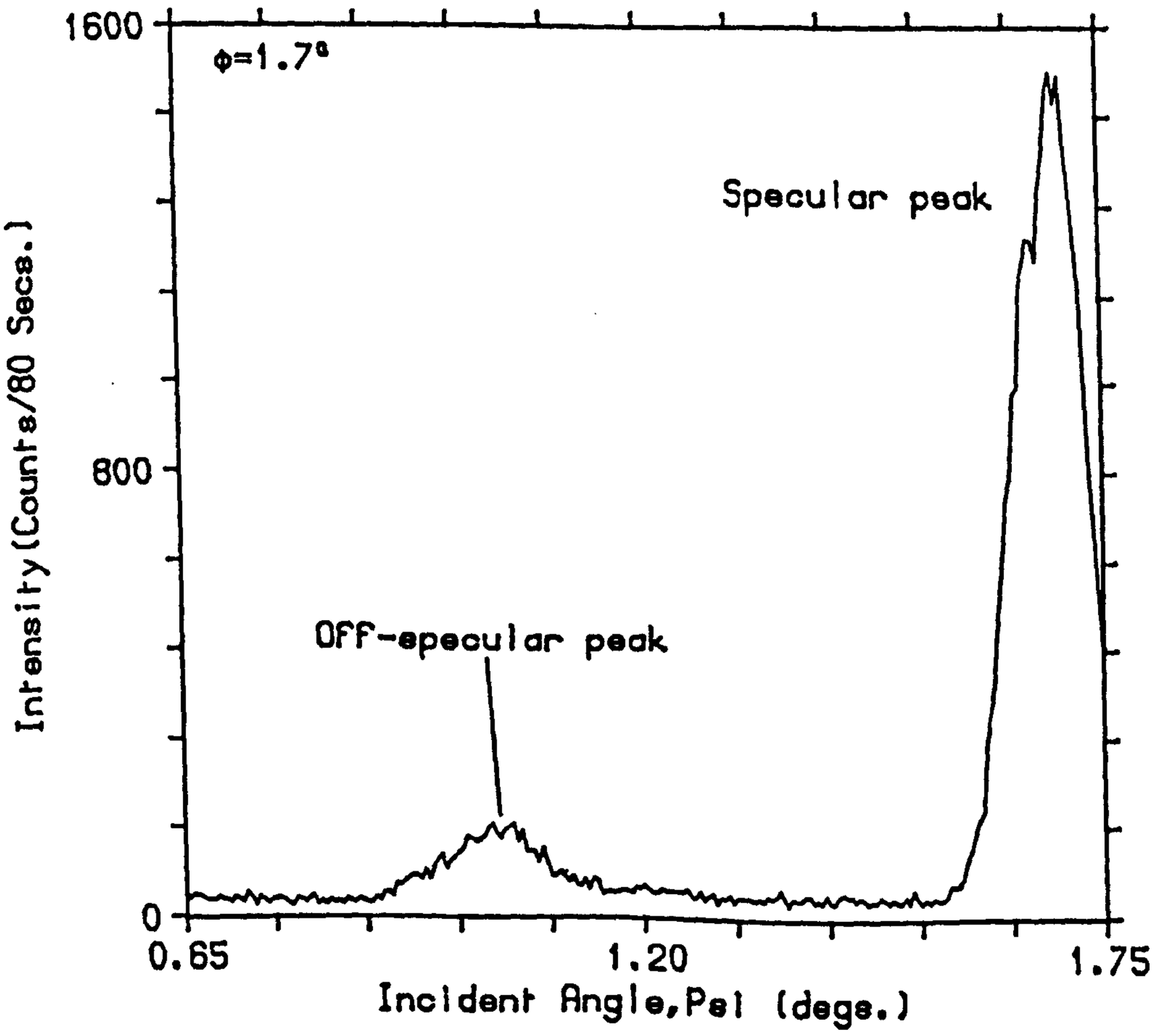

Figure 3.9. The intensity observed when scanning the scattering angle from a [1 0 0] Si slice. The count time is 80s/point and the results show the specularly reflected peak at 1.70° and an additional peak at $\psi_i+\psi_c=1.03°$.

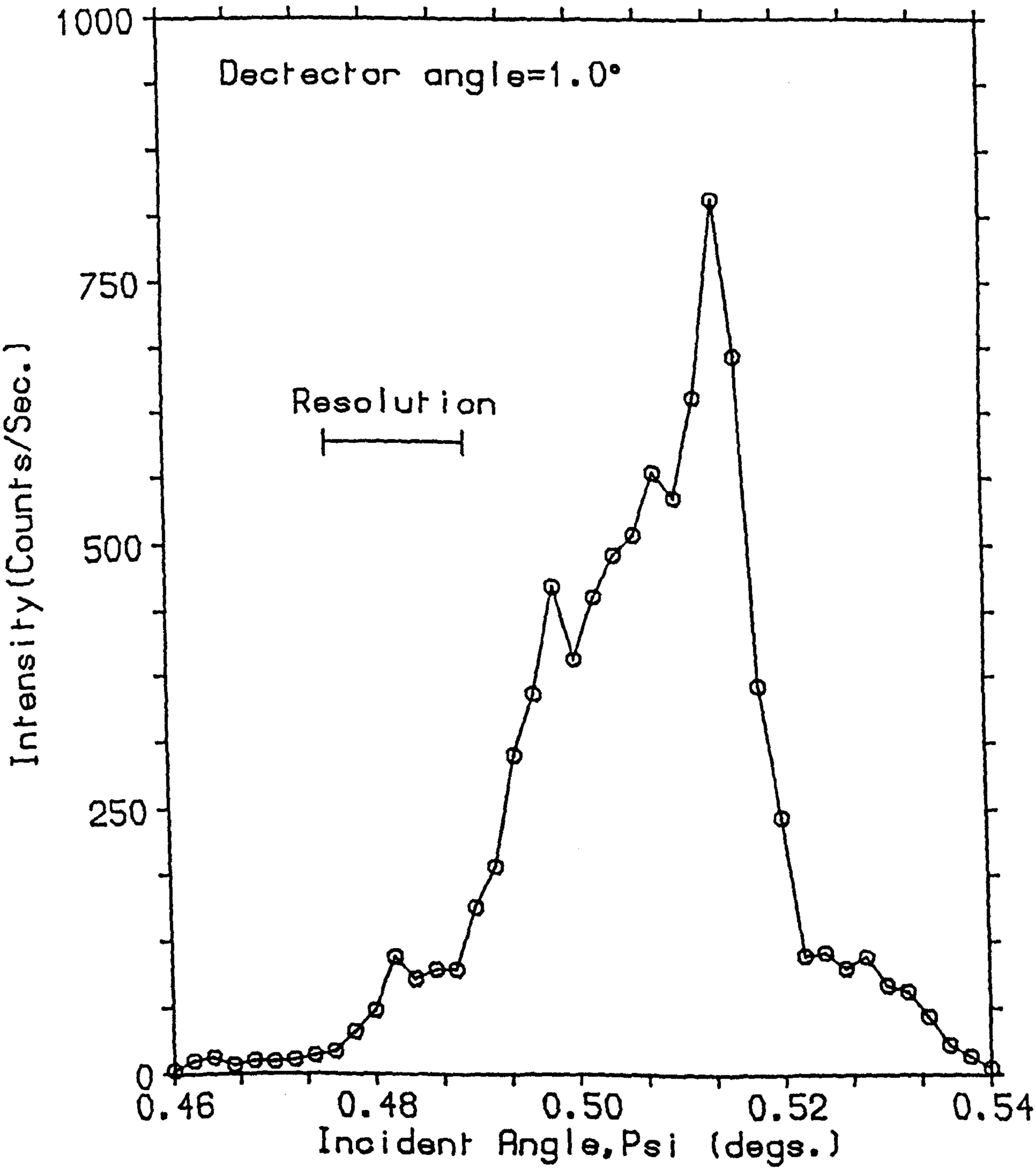

Figure 3.10. The intensity observed as a function of sample orientation (ψ) when $\varnothing$=1.03°. The width is much wider than the resolution and arises because the Si wafer is, macroscopically, not flat.

Secondly, it is found that semiconductor wafers in preparation for device fabrication can be, macroscopically, far from flat. The silicon wafers had a diameter of three inches and visual examination often revealed a dished or rippled surface on a millimetre length-scale. This departure from flatness is quite distinct from the microscopic surface roughness probed by the x-ray reflectivity measurements. For some nominal incident angle the sample presents a range of incident angles to the x-ray beam. This problem is overcome by using an analyser crystal which decouples the scattered direction from the position of the elements of the instrument. The measurement is then performed by rocking the sample, at a fixed scattering angle, to obtain the integrated intensity from all parts of the sample. This is performed at each scattering angle to obtain the reflectivity curve. Figure 3.10 shows a typical scan at a low scattering angle where a large part of the sample is illuminated. The features in the scattered intensity are a function of the macroscopic curvature of the wafer.

(3.2) Results and Analysis.

Figure 3.11 shows the reflectivity curve from the silicon sample which had been thermally oxidised, nominally to a thickness of 270 ±10Å. The oxide thickness was determined by ellipsometry measurements at the Microfabrication Facility, a technique sensitive to layers down to 100Å in thickness. Qualitatively the reflectivity results may be understood in the following way. The oscillations arise from the interference between waves reflected at the air/SiO_2 and the SiO_2/Si interfaces, with the period of the oscillations giving an accurate measure of the oxide thickness. The amplitude of these oscillations is determined by the electron density difference between the oxide layer and the bulk silicon crystal. Roughness at the air/oxide interface causes a general decrease in the reflectivity with increasing angle, whereas roughness at the Si/SiO_2 interface would damp the oscillations at higher angles. It must be stressed that roughness in this context means deviation from a step function change in electron density at an interface.

The simulation, also shown in figure 3.11, was calculated using the model described in Appendix II, with the parameters being varied in a least-squares way to obtain a good fit to the data. The starting parameters

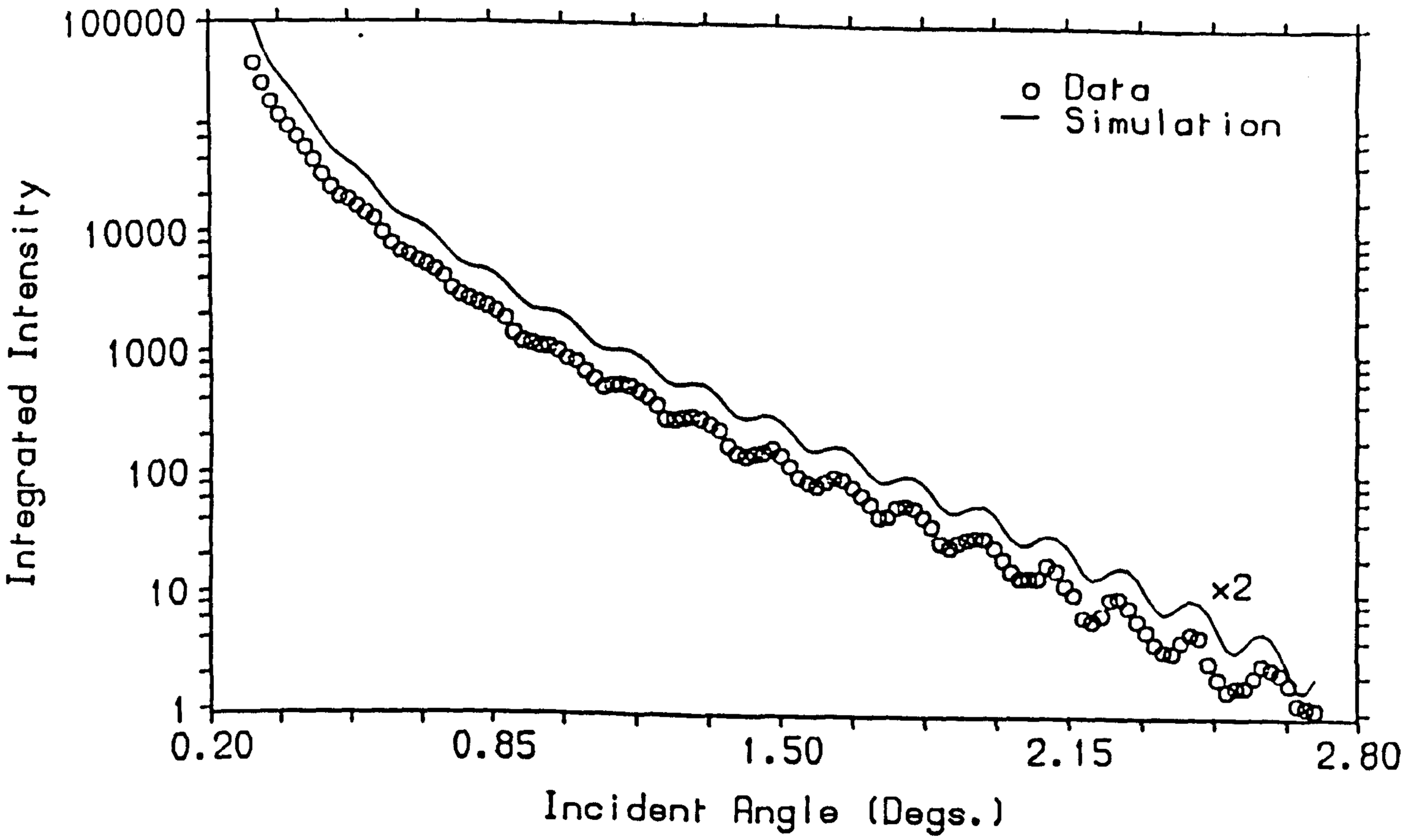

Figure 3.11. The reflectivity, plotted on a logarithmic scale against ψ for the thermally oxidised Si sample. The solid curve is calculated with the theory described in Appendix II and the parameters in Table 3.2.

	Thickness (Å)	ρ/ρ_s	Roughness σ (Å)
Layer 1	7.5±1.5	0.48±0.05	0.5±1.0
Layer 2 (SiO_2)	269±5	0.95±0.01	2.5±1.0
Substrate (Si)	—	1.0	4.1±1.0

Table 3.2. Parameters of the fit to the data in figure 3.11 using a two-layer model as described in Appendix II.

were the nominal values for Si and SiO_2 (Irene, 1987; Rochet, Rigo, Froment, d'Anterroches, Maillot, Roulet and Dufour, 1986), and the refined parameters are listed in table 3.2. The fits were performed with a variable overall scale parameter, A, because of the difficulty in collecting reliable data at very low angles of incidence. The results show that the reflectivity measurements can be interpreted well, using this simple model, and the calculated oxide thickness is in very good agreement with the value obtained by ellipsometry. The simple Gaussian roughness model (Appendix II; Névot and Croce, 1980) indicates a transition layer at the Si/SiO_2 interface approximately one monolayer thick, in agreement with the crystal truncation rod measurements from the previous section (Table 3.1). It is not possible to further characterise this interface, because the introduction of monolayers of non-stoichiometric oxides, $SiO_x (x < 2)$, into the model, has little effect on the calculated curve, due to the small density differences involved. However, the model does give a feel for the width of the transition region and also a measure of the sharpness of the oxide termination at the surface. This is also seen to be sharp with variations only over monolayer thicknesses. To obtain a good fit to the data it was necessary to introduce a second surface layer into the model at the air/oxide interface. The oscillations from this 7.5Å layer of low electron density cannot be observed directly, but its inclusion is necessary to reproduce the increasing fringe amplitude at higher angles. The nature of this layer, thought either to be a manifestation of surface roughness (Smirnov and Anokhin, 1980) or of surface contamination, was studied in the following set of experiments.

The reflectivity of the native oxide Si (1 0 0) wafer was measured and the results are shown in figure 3.12, with the fitting parameters in Table 3.3 again including the low density surface layer. The wafer was then immersed in distilled water for two hours and blow dried in nitrogen before the reflectivity measurements were repeated. A dramatic change in the reflectivity curve was observed (figure 3.13). In the model, the only major change in the refined parameters is an increase in the thickness of the upper layer from 8.5Å to 17.8Å, the density mismatch corresponding to that of water. In conjunction with the x-ray experiments, a Lambda 9 infrared/ultraviolet spectrometer, operating in reflection mode, was used to scan the samples over the wavelength range 2500 - 2900nm. Water has

Text cut off in original

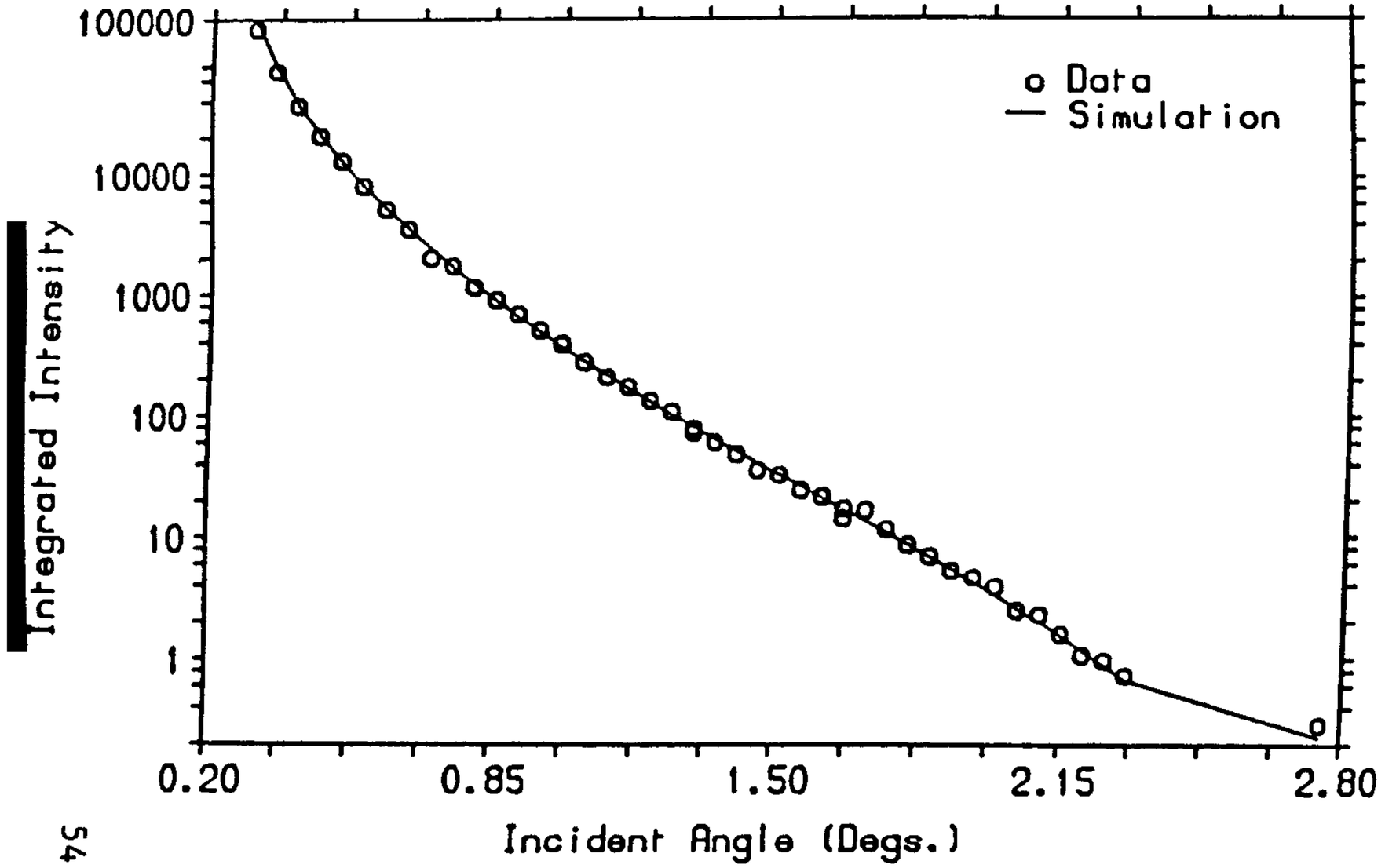

Figure 3.12. As for figure 3.11 for the native oxide Si sample. The fitting parameters are in Table 3.3.

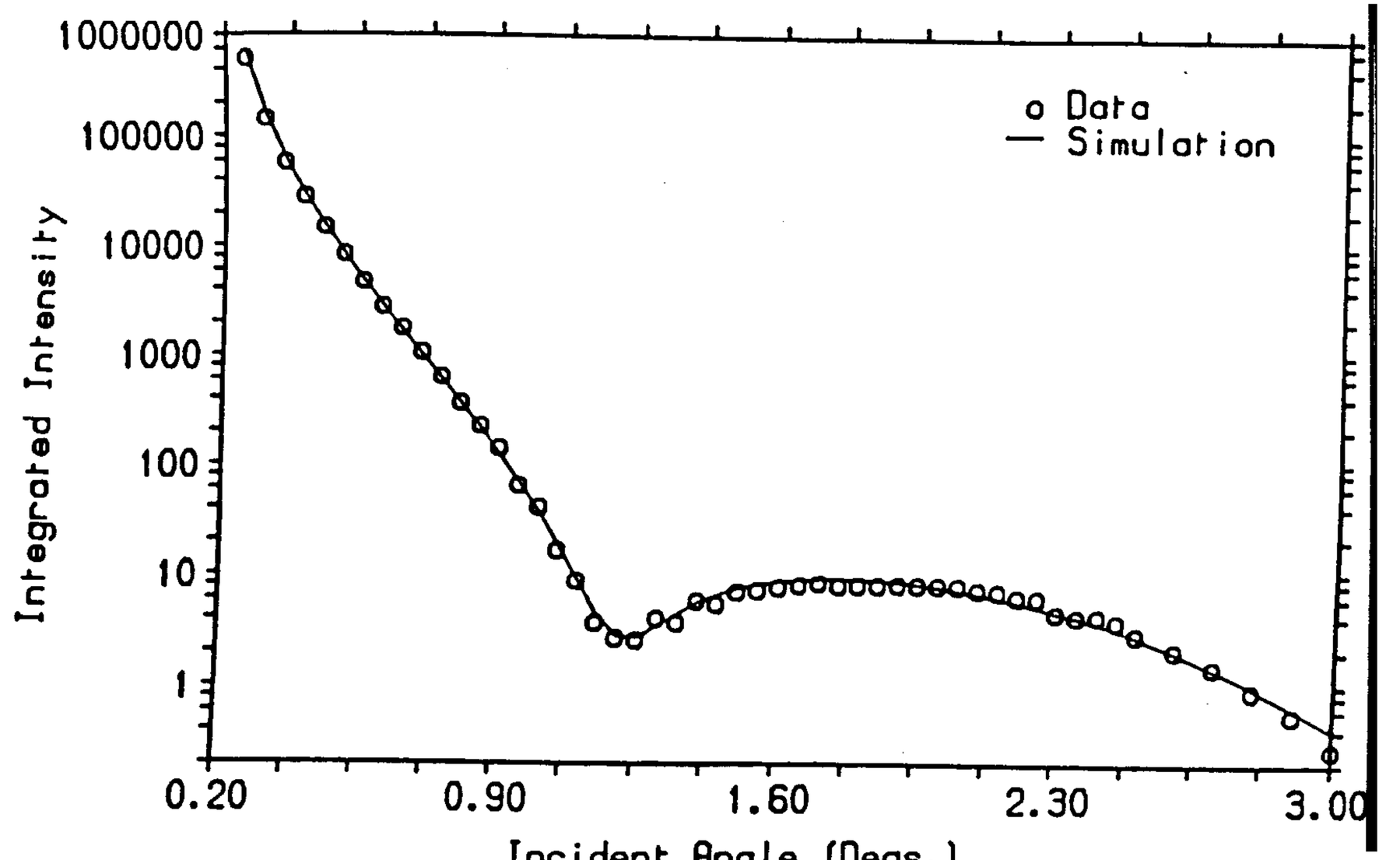

Figure 3.13. The reflectivity curve as in figure 3.12 but after the sample had been dipped in distilled water. The new parameter for calculating the solid line are shown in Table 3.3.

	d_1 (Å)	ρ_1/ρ_s	σ_1 (Å)	d_2 (Å)	ρ_2/ρ_s	σ_2 (Å)	σ_s (Å)
Native Oxide	8.4±2.0	.47±.05	2.3±1.5	16.0±4.0	.96±.01	3.1±1.0	3.8±2.0
Dipped in water	17.8±0.5	.49±.05	3.4±1.5	16.0±4.0	.96	3.1	4.2±2.0

Table 3.3. Parameters of the fits to the data in figure 3.12 and figure 3.13 using the same two-layer model.

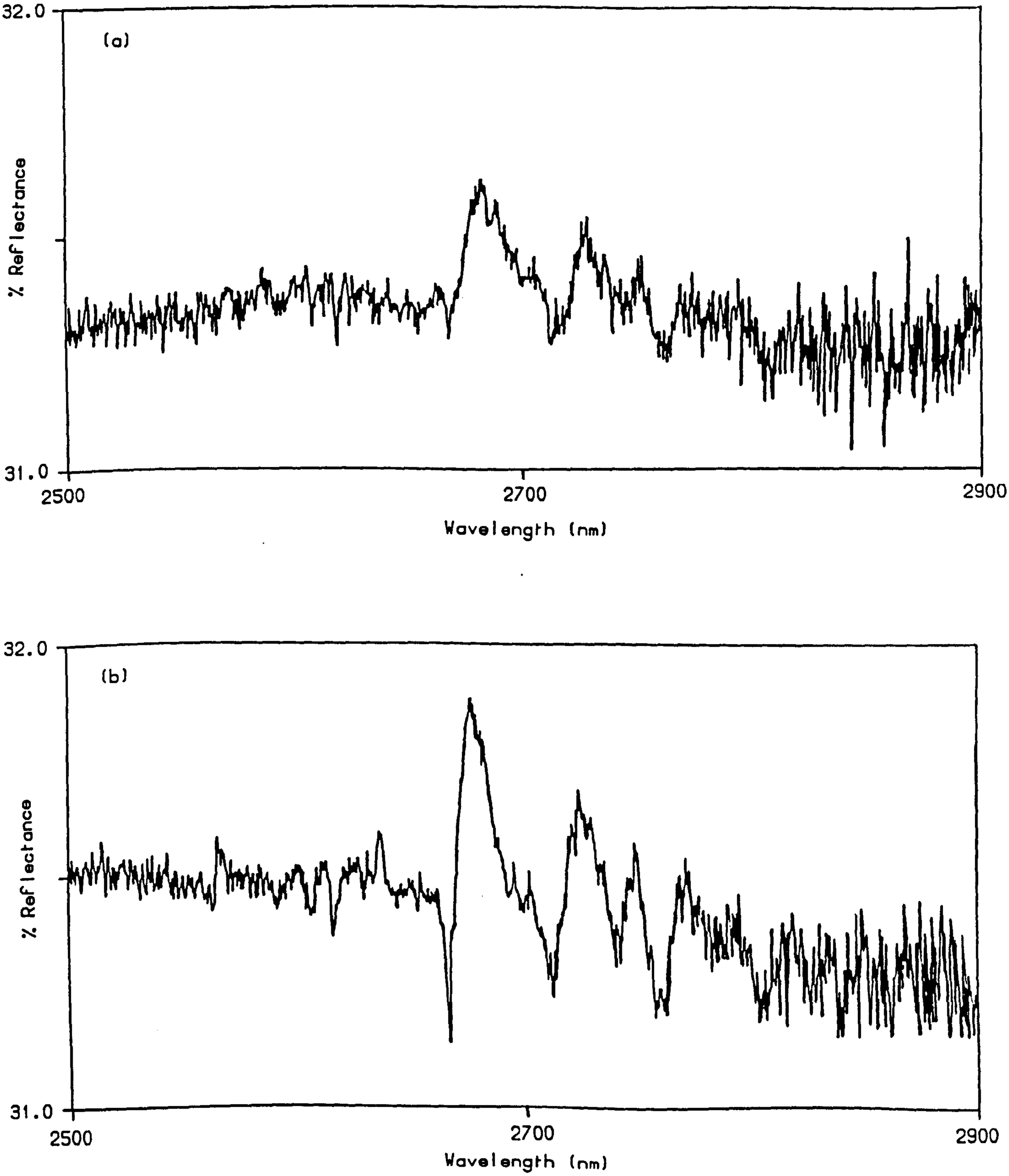

Figure 3.14. The measured IR/UV spectrum over the wavelength range 2500-2900nm for the native oxide Si sample (a) before and (b) after dipping in distilled water. After heating the sample the spectrum in (a) was again obtained.

a complicated absorption spectrum near 2700nm. Figure 3.14 shows the spectrum obtained for the wafer before and after dipping in distilled water. The increase in the peak around 2700nm was removed by heating the sample for two hours at 200°C in a vacuum oven. The x-ray reflectivity curve then also returned to the form of figure 3.12 with a slight reduction in the upper layer thickness, compared to the original fit parameters. Even with the sample maintained at high temperature under vacuum, a surface layer of 6Å was still required to fit the data. In all experiments, a consistent value for the thickness of the native oxide layer was obtained, showing that x-ray reflectivity is sensitive to very thin amorphous layers and provides measurements outside the range of other techniques.

Figure 3.15 shows similar measurements from a sample thermally oxidised for thirty minutes at 800°C, nominally to a depth of 50Å. Surprisingly, figure 3.15a was obtained without treating the wafer in any way and figure 3.15b was obtained after heating the wafer at 200°C in a vacuum oven. The results (Table 3.4) show a similar behaviour to Table 3.3, the native oxide measurements. Clearly the interpretation of reflectivity measurements depends critically on surface contamination and this may have caused the inconsistencies observed in previous results (Cowley and Ryan, 1987). Other workers (Pershan, 1989) have reported similar effects in reflectivity measurements, with ESCA (Electron Spectroscopy for Chemical Analysis) suggesting carbon contamination. Carbon is indistinguishable from water in a reflectivity measurement and could well explain the seemingly irremoveable layer at the sample surface. Experiments performed under UHV (ultra high vacuum) conditions, where detailed sample preparation is possible, may be the way to solve this problem. However, UHV equipment is expensive and time-consuming, making it impractical for obtaining quick and simple results.

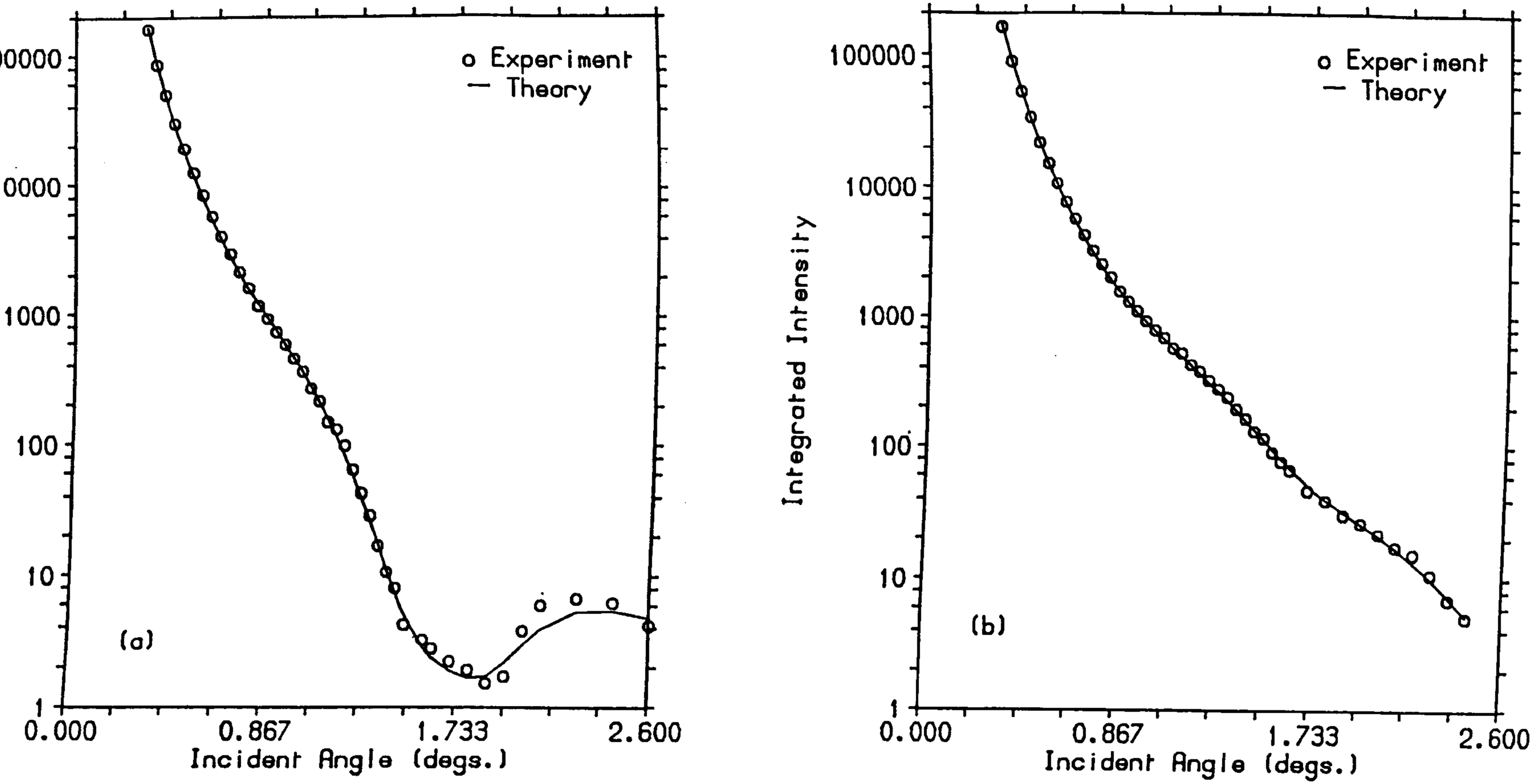

Figure 3.15. Reflectivity measurements from a Silicon slice oxidised nominally to a depth of 50Å, (a) without any treatment other than the manufacturers and (b) after heating in a vacuum oven. The parameters to the solid lines are in Table 3.4.

	d_1 (Å)	ρ_1/ρ_s	σ_1 (Å)	d_2 (Å)	ρ_2/ρ_s	σ_2 (Å)	σ_3 (Å)
Untreated wafer	12.8±1.0	.43±.10	<1	46.9±4.0	.98±.01	4.2±1.5	4.0±2.0
Heated wafer	5.3±3.0	.30±.10	<1	45.6±4.0	.97±.01	2.9±1.5	3.5±2.0

Table 3.4. Parameters of the fits to the data in figure 3.15, as discussed in the text.

4. Neutron Reflectivity

Reflectivity measurements using long-wavelength neutrons can be used to obtain structural information about surfaces, in the form of the scattering length profile as a function of depth (Hayter, Highfield, Pullman, Thomas and Penfold, 1981). At glancing angles the interaction of a neutron with a sample can be described by the index of refraction, n, given by (Goldberger and Seitz, 1947)

$$n^2 = 1 - \lambda^2 p/\pi \, , \; p = \Sigma N_i \langle b_i \rangle ,$$

where λ is the incident neutron wavelength, N_i is the number of atoms per unit volume and $\langle b_i \rangle$ is the mean scattering length for the material i. As in x-ray reflectivity, the effectiveness of the technique depends upon the differences in refractive index which occur as a function of depth into the sample. However, the refractive index for neutrons depends upon the scattering length, not the electron density, and this may be exploited for studying many materials.

There are two methods of measuring neutron reflectivity depending on the neutron source. The first is to vary the glancing angle at a constant neutron wavelength and is applicable only at reactor sources. The second, useful for both reactor and pulsed sources, is to use the time-of-flight (TOF) technique, where the glancing angle is kept constant and a range of wavelengths is measured. Such an instrument has been developed at the Rutherford Appleton Laboratory, using the ISIS pulsed neutron beam source. The instrument, CRISP (Critical reflection surface spectrometer), enables the reflectivity to be measured simultaneously by the TOF technique, whilst keeping the incident angle fixed, giving constant resolution and sample illumination (Penfold, Ward and Williams, 1987)

The measurements described here were performed during the commissioning stage of the instrument, on a Si/SiO_2 wafer, thermally oxidised to a thickness of 330Å. Data was collected at three angles of incidence, 0.3°, 0.6° and 1.5°and the wavelength spectrum at 0.3° is shown in figure 3.16. The Q range of each scan overlapped and they were normalised to give a continuous reflectivity curve over the whole range measured. This is illustrated in figure 3.17a together with a fit to the data using the theory described by Harwood, Messoloras, Stewart, Penfold and

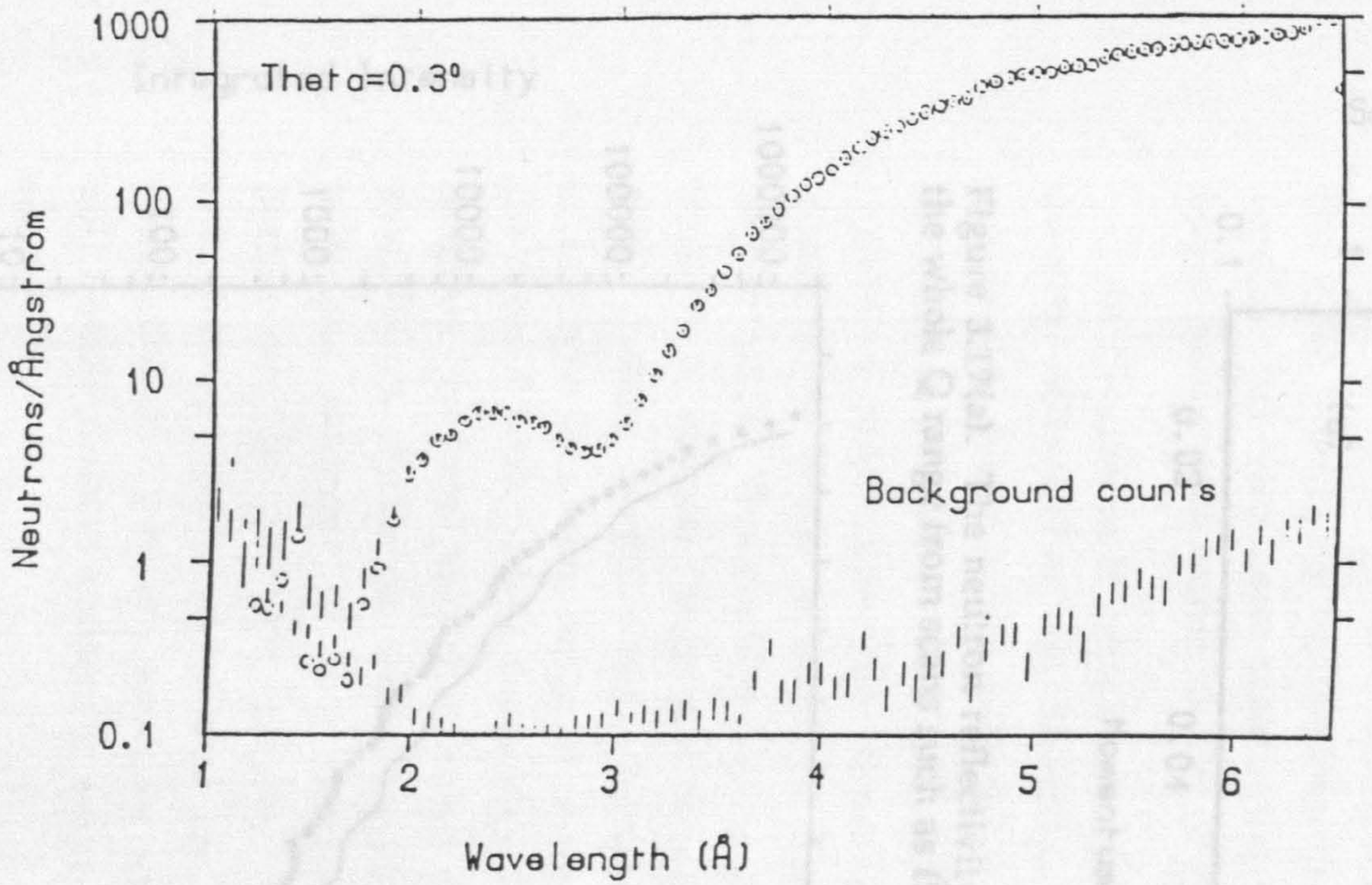

Figure 3.16. Wavelength spectrum of the scattered neutrons from a thermally oxidised silicon slice, at an incident angle 0.3°.

	d_1 (Å)	ρ_1/ρ_3	σ_1 (Å)	d_2 (Å)	ρ_2/ρ_3	σ_2 (Å)	σ_3 (Å)
X-ray	7.1±1.0	.51±.05	<1	329±5	.97±.01	1.0±1.0	3.5±2.0
Neutron	—	—	—	345±5	—	8.5±2.0	0.0

Table 3.5. Parameters obtained by neutron reflectivity and x-ray reflectivity measurements.

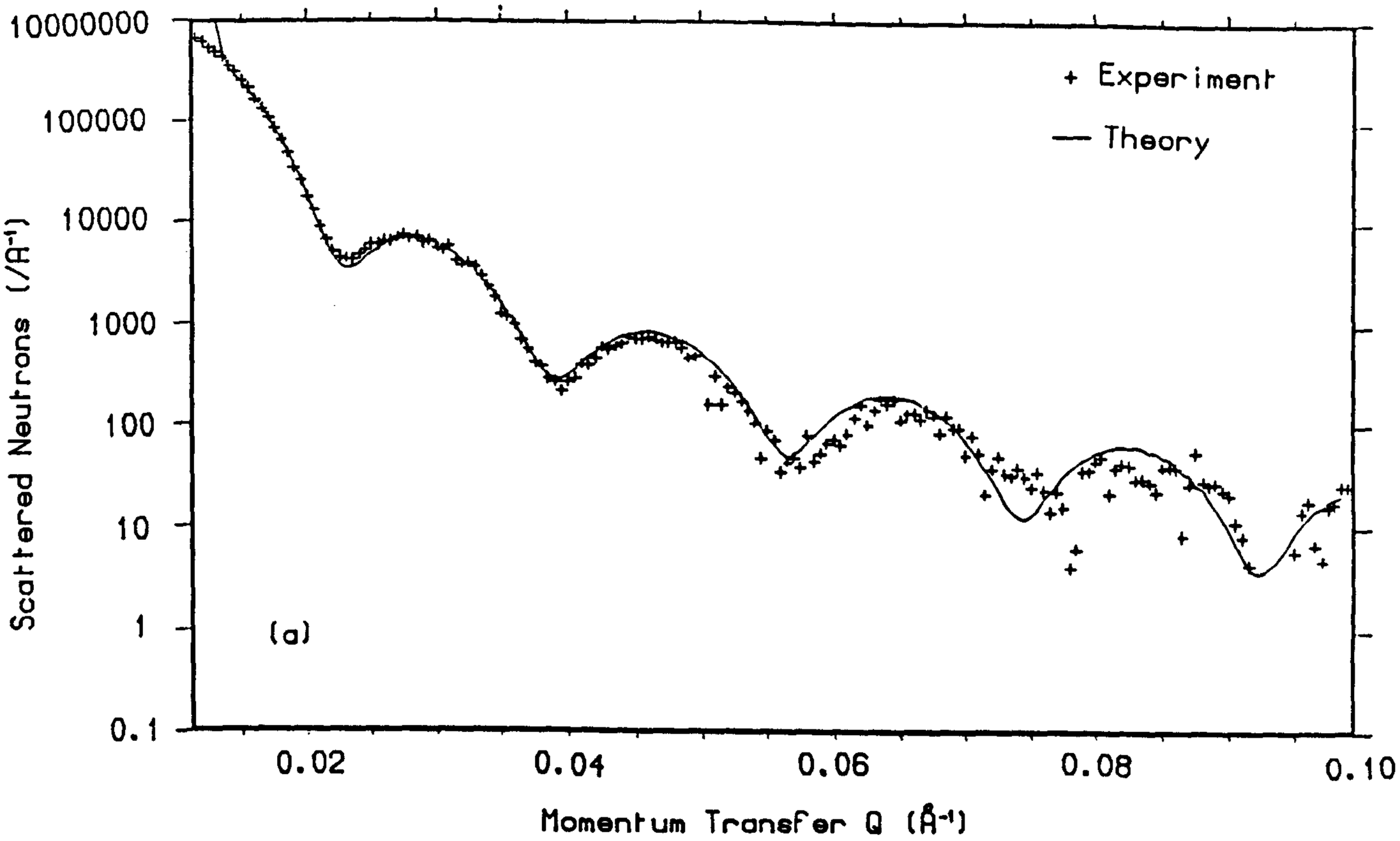

Figure 3.17(a). The neutron reflectivity curve, normalised to be continuous over the whole Q range from scans such as figure 3.16.

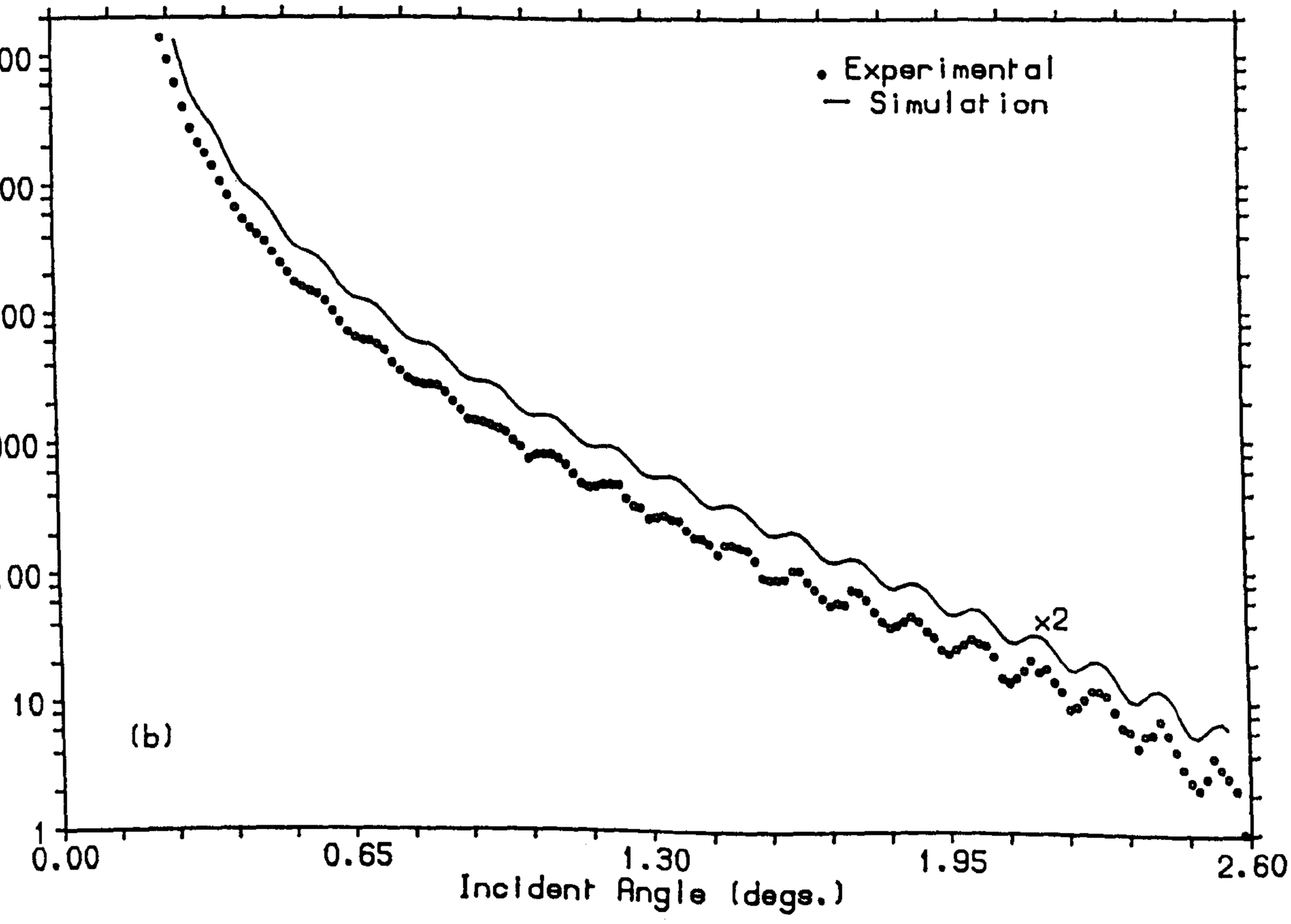

Figure 3.17(b). The equivalent x-ray reflectivity curve from the sample as in figure 3.17(a). The parameters to the solid lines, in both curves, according to the different theories, are shown in Table 3.5.

PAGE
NUMBERS
CUT OFF
IN
ORIGINAL

Ward (1988), in a least-squares fitting program available at the R.A.L. The main parameters to the theory are shown in Table 3.5, which includes the equivalent parameters measured by x-ray reflectivity, the curve shown in figure 3.17b. Ellipsometry measurements gave the thickness of the oxide to be 325 ±10Å, in excellent agreement with the x-ray results, but not the neutron results. The data in the neutron experiment has a momentum range approximately three times smaller than that in the x-ray experiment and consequently only four distinct fringes are observed. The discrepancy in the calculated thickness may be due to the variations allowed within this limited range. The same explanation may also account for the roughness values, which are calculated in the same way as the x-ray reflectivity values (Névot and Croce, 1980), but give different results. Sub-nanometer-scale roughnesses can only reliably be probed at larger momentum transfers, out of this neutron reflectivity range.

In conclusion it appears that, even in materials with small electron density mismatches, ie. Si/SiO_2, x-ray reflectivity has considerable advantages over neutron reflectivity for structural characterisation. X-ray sources are available which provide x-ray beams with intensities several orders of magnitude over those available with neutron sources, in addition to better control of instrumental and sample dependent backgrounds. This enables measurement over a much larger momentum transfer, or angular range, and thus provides a better probe of Ångstrom-scale surface irregularities. However, neutron reflectivity does have advantages in a wide range of problems. Isotopic substitution, in which the ratio of D_2O to H_2O, molecules with very different neutron scattering lengths, has been varied to solve phase problems in block copolymer monolayers (Richards, Qureshi and Thomas, 1988). Also, due to the magnetic moment of the neutron, reflectivity studies of surface magnetism in metallic glasses, magnetic multilayers and high-temperature superconductors are possible (Felcher, 1981). The installation of a position sensitive detector on CRISP is planned, and this will enable diffuse scattering away from the specular reflection to be studied.

CHAPTER FOUR

X-Ray Scattering from Single Quantum Well Semiconductor Heterostructures

1. Introduction

Heteroepitaxial crystal growth techniques, such as molecular beam epitaxy (MBE) and metal organic chemical vapour deposition (MOCVD), have made a tremendous impact on semiconductor physics and technology. The ability to grow thin crystalline layers, with a built-in strain determined by the composition, allows tailoring of the band structure and, therefore, the material's optoelectronic properties (Cho, 1971; "Heteroepitaxial Approaches in Semiconductors", 1989). As the active regions of heterostructure devices become smaller, their performance can be critically affected by interface roughness, as well as the usual degrading effects caused by unwanted impurities. It is therefore essential to develop analysis techniques capable of characterising these nanometer-scale epitaxial structures.

Double-crystal x-ray diffractometry is a well established method for the non-destructive characterisation of III-V semiconductor heterostructures (Bartels, 1983; Hill, Tanner, Halliwell and Lyons, 1985; Baumbach, Brühl, Rhan and Pietsch, 1988). As most III-V epitaxial layers are grown on [1 0 0] surface oriented substrates, 'rocking curve' measurements, in which the sample crystal is rotated through the Bragg condition, are usually performed on the [4 0 0] symmetric Bragg reflection. In addition to giving direct information about the lattice parameter mismatch in a material, analysis of the rocking-curve shapes can give information about layer thickness and compositional grading (Lyons and Halliwell, 1985). Rocking-curve analysis has also been used to study ion implantation in silicon (Kyutt, Petrashen and Sorokin, 1980). Simulation of the rocking-curves may be performed, using calculations based on the Takagi-Taupin formalism of the dynamical theory of x-ray diffraction (Taupin, 1964; Takagi, 1969), and various models have been used to explain results (Chu and Tanner, 1986; Bartels, Hornstra and Lobeek, 1986). The method has recently been adapted to operate in an

asymmetric scattering geometry (Tanner and Hill, 1986a; Pietsch and Borchard, 1987) enabling full characterisation of layers down to 1000Å in thickness (Tanner and Hill, 1986b). Simulations suggest that layers of the order of 350Å in thickness could be studied using only a conventional laboratory source of x-rays (Halliwell and Lyons, 1985).

Although double-crystal x-ray diffractometry has been extensively developed for semiconductor characterisation, desk-top instruments for use in on-line sample control are now available, comparatively little work has been done using a triple-crystal diffractometer. The addition of an analyser crystal, with the resulting decrease in the resolution volume, mean that in rocking-curve analysis longer count-times are required to achieve essentially the same results. This is a severe disadvantage if quick results are required for feedback into the sample growth process. However, for more detailed studies, the triple-crystal arrangement has several advantages over the conventional double-crystal technique. Macroscopic sample bend, which causes problems in the interpretation of rocking-curve measurements (Lum, Klingert, Bytsma, Glass, Macrander, Harris and Lamont, 1989; Chu, Macrander, Strege and Johnston, Jr, 1985), can easily be accounted for in a triple-crystal measurement (Cowley and Ryan, 1987; Chapter 3 of this thesis). Also, the improved wave-vector resolution of the triple-crystal instrument permits the observation of weak scattering, away from Bragg reflections, which is found to contain detailed structural information (Ryan, Hatton, Bates, Watt, Sotomayor-Torres, Claxton and Roberts, 1987). In the previous chapter it was shown that atomic-scale information could be obtained about the termination of the silicon lattice by analysis of the 'crystal truncation rod'. If the crystal lattice is terminated on both sides, as in a crystalline heteroepitaxial layer, the substrate Bragg peaks are accompanied by a series of interference fringes which modulate the crystal truncation rod intensities. In dynamical scattering theory these are known as Bragg-case Pendellösung fringes (Renninger, 1968; Batterman and Hildebrandt, 1968) and can yield information such as lattice mismatch, degree of crystalline perfection and layer thickness (Macrander and Strege, 1986). A second technique, x-ray reflectivity, can also give information about layer thickness and interface roughness and, although not sensitive to crystalline perfection, may give

an idea of sample composition through the electron density profile of the crystal (Chapter 3; Appendix II).

In this chapter, measurements of three different single-quantum-well semiconductor heterostructures, using the 'crystal truncation rod' and reflectivity techniques, are described. In section 2 it is shown how the two techniques may be combined to give consistent and complimentary results in the characterisation of a MBE-grown heterostructure. The x-ray reflectivity results are used in the interpretation of the truncation rod data to indirectly obtain information about a crystalline layer only 30Å thick. Section 3 describes crystal truncation rod measurements of a MOVPE-grown crystal in which scattering from a buried layer only 80Å in thickness is directly observed. In section 4 it is shown that reflectivity measurements can give a misleading guide to sample quality due to the technique's insensitivity to crystalline perfection. The final section summarises the experiments and results and indicates their possible importance in the field of semiconductor growth physics.

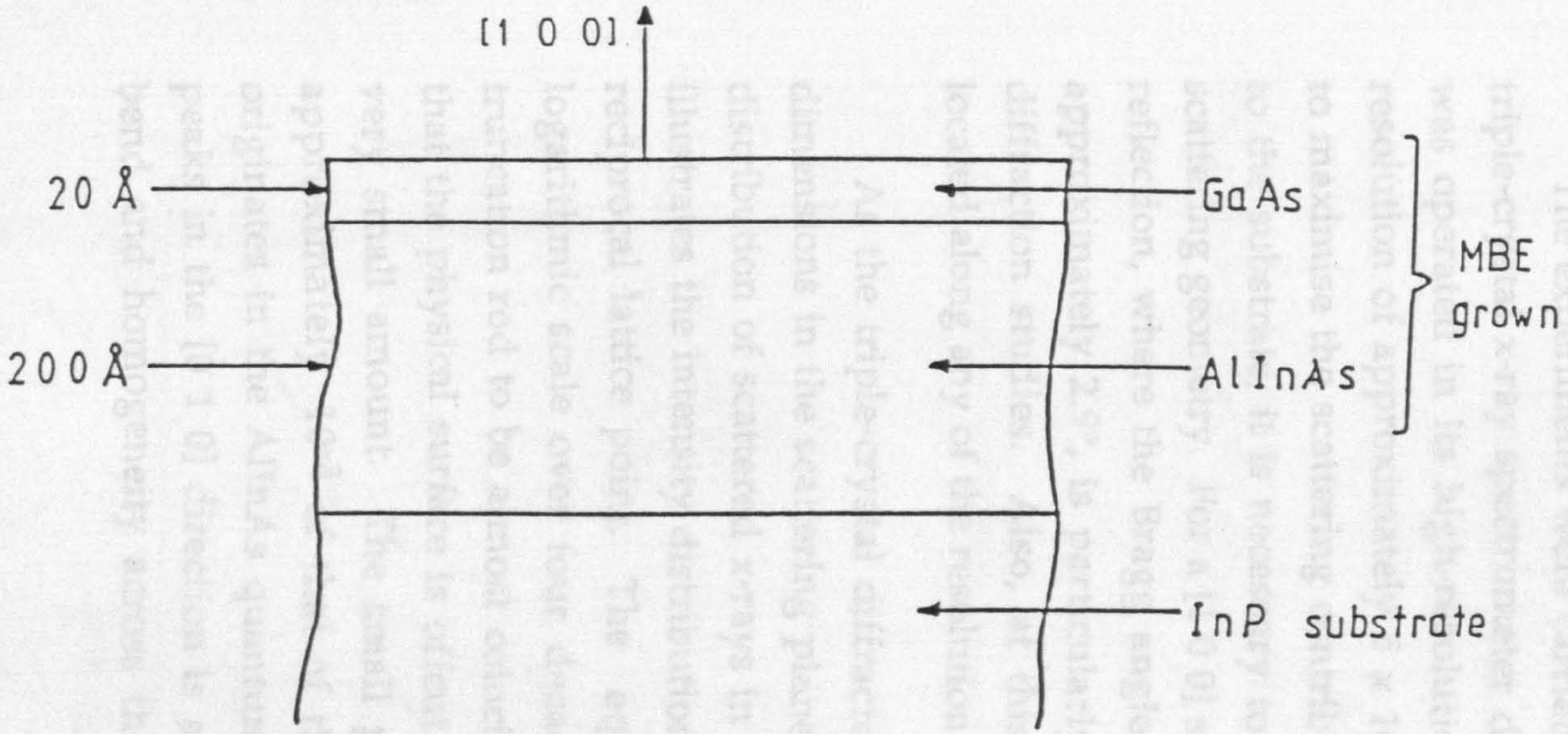

Figure 4.1. The sample crystal MV494, consists of a 20Å GaAs capping layer and a 200Å AlInAs quantum well epitaxially grown on [1 0 0] oriented InP. The layer thicknesses were estimated from the growth conditions.

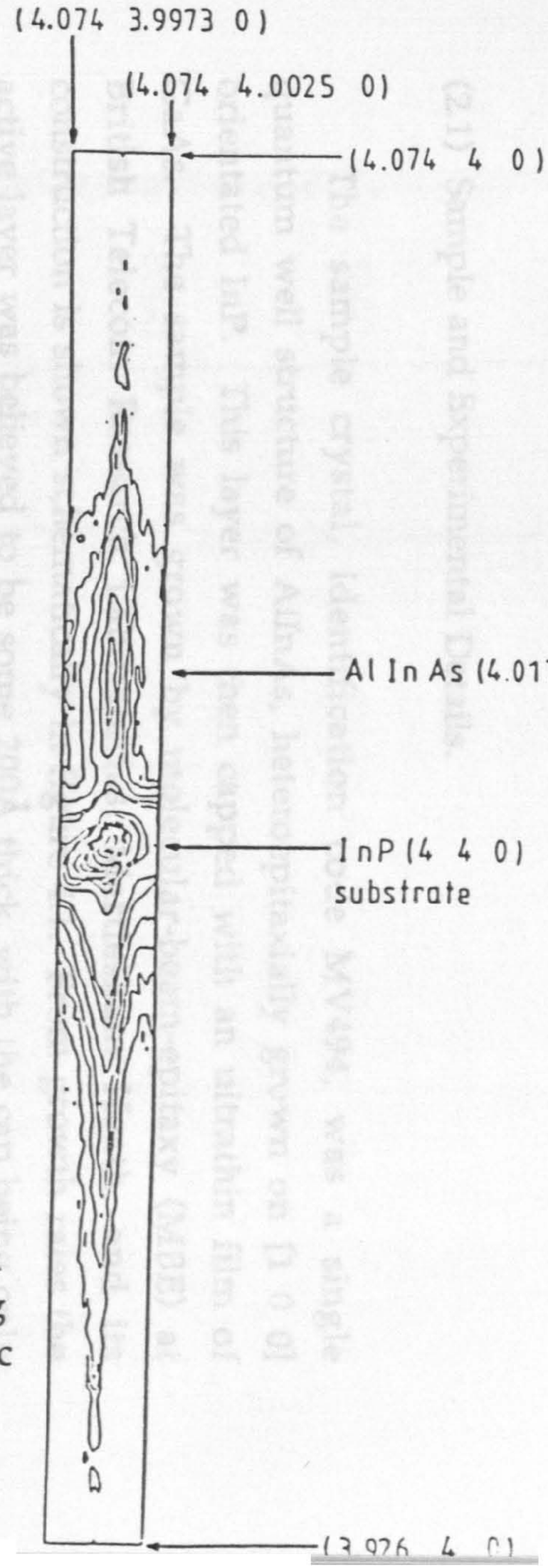

Figure 4.2. An isointensity contour plot of the observed x-ray scattering in the region of the InP (4 4 0) Bragg peak. The data are presented on a quasi- logarithmic scale over four decades of intensity.

2. Sample I - GaAs/AlInAs/InP

(2.1) Sample and Experimental Details.

The sample crystal, identification code MV494, was a single quantum well structure of AlInAs, heteroepitaxially grown on [1 0 0] orientated InP. This layer was then capped with an ultrathin film of GaAs. The sample was grown by molecular-beam-epitaxy (MBE) at British Telecom Research Laboratories, Martlesham Heath, and its construction is shown schematically in figure 4.1. From growth rates the active layer was believed to be some 200Å thick, with the cap being only 20Å thick.

The experiments were carried out at Edinburgh University using the triple-crystal x-ray spectrometer described in Chapter 2. The instrument was operated in its high-resolution configuration giving a wave-vector resolution of approximately 5×10^{-4}Å^{-1} in the scattering plane. In order to maximise the scattering contribution of the surface layers with respect to the substrate, it is necessary to adopt an extremely asymmetric Bragg scattering geometry. For a [1 0 0] surface orientated InP sample the (4, 4, 0) reflection, where the Bragg angle, θ_B is 47.75° and the incident angle is approximately 2.9°, is particularly suitable for glancing-incidence x-ray diffraction studies. Also, at this reflection, the surface normal is not located along any of the resolution degrading streaks.

As the triple-crystal diffractometer provides high-resolution in two dimensions in the scattering plane, it is possible to map out the intensity distribution of scattered x-rays in an area of reciprocal space. Figure 4.2 illustrates the intensity distribution for the sample around the InP (4, 4, 0) reciprocal lattice point. The equal-intensity contours are on a quasi-logarithmic scale over four decades of intensity and show the crystal truncation rod to be almost coincident with the [1 0 0] axis. This means that the physical surface is offcut from the crystallographic surface by a very small amount. The small peak at (4.0178, 4, 0) has an intensity approximately 10^{-3} of that of the substrate (4, 4, 0) Bragg peak, and originates in the AlInAs quantum well layer. The width of the Bragg peaks in the [0 1 0] direction is a measure of sample mosaicity, sample bend and homogeneity across the layer. Double-crystal rocking-curve

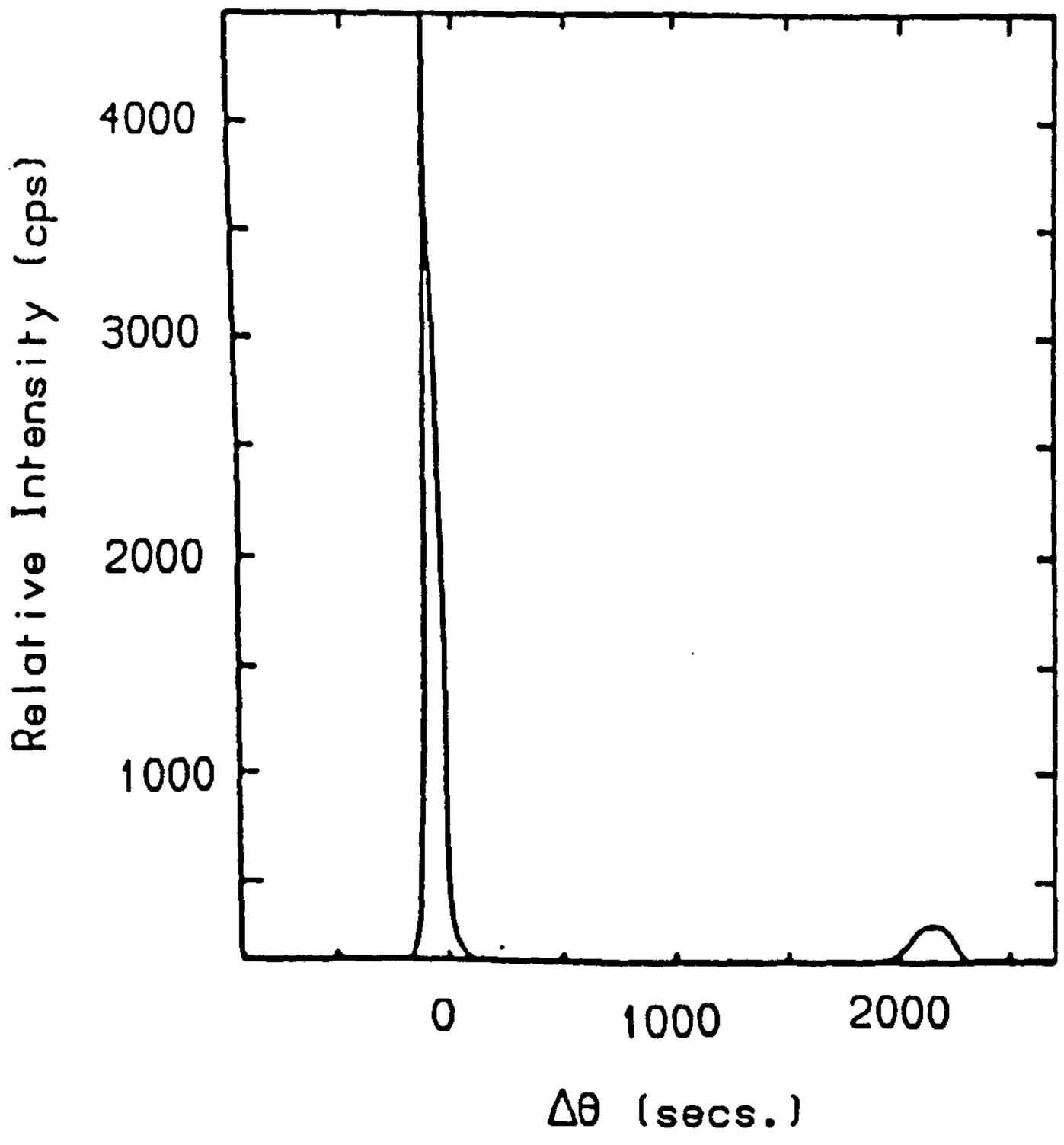

Figure 4.3. Experimental double crystal rocking curve. The count time was 80s/point spaced at 10.2 arc secs.

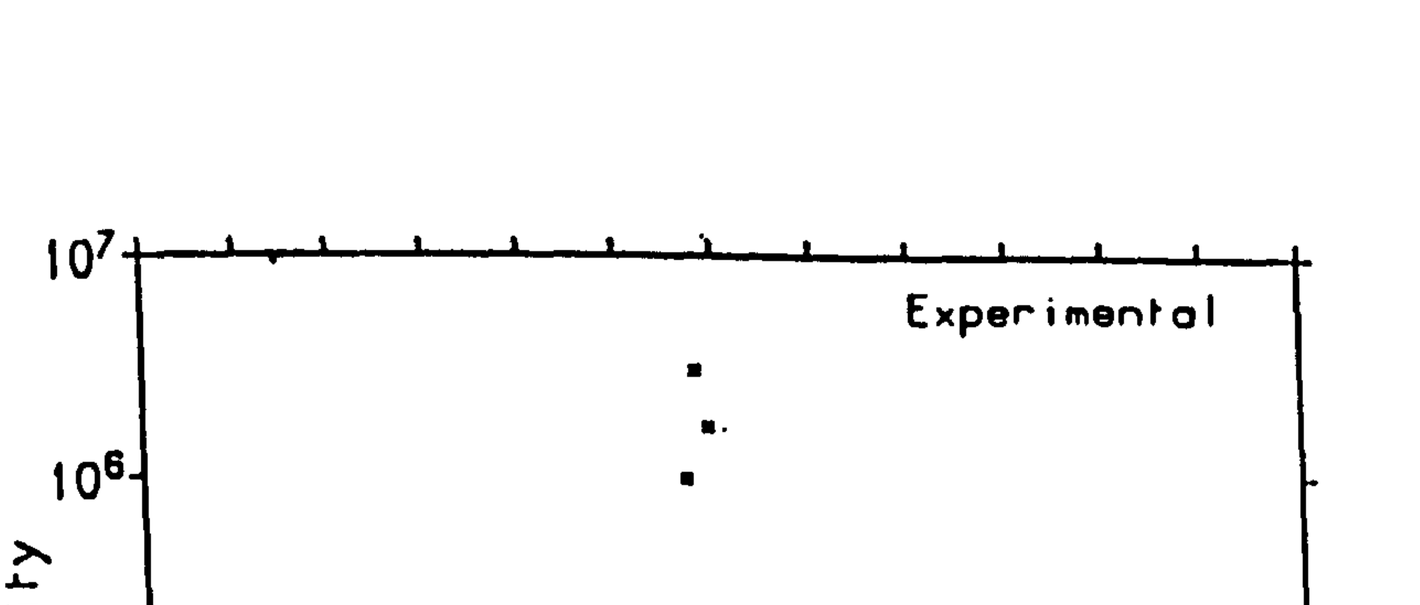

Figure 4.4. The intensity distribution along [1 0 0], the face normal direction through the InP (4 4 0) Bragg peak. The intensity is shown on a logarithmic scale.

measurements (figure 4.3) give a width of 50 seconds which is less than twice the simulated value. The epitaxial layer is thus of excellent crystalline quality. The presence of the secondary Bragg peak in figure 4.2 is more clearly seen in figure 4.4, which plots the integrated intensity along the face normal direction, over the scan range $q_\perp = \pm 0.075$ a*. The logarithmic scale over five orders of magnitude emphasises the weak scattering observed around the (4, 4, 0) Bragg peak. Comparison of the results in figures 4.4 and 4.3 shows that such extremely weak features can only be observed due to the enhanced sensitivity of the triple-crystal geometry and its improved signal to noise ratio. The Bragg peak positions and weak satellites, highlighted in figure 4.4, give an apparent lattice mismatch $(\frac{\Delta a}{a})$, between the tetragonally strained AlInAs layer and the InP substrate, of -4.45×10^{-3}, and are consistent with a layer thickness of approximately 225Å.

The sample was also examined using the specular x-ray reflectivity method, at glancing angles just above the critical angle for total external reflection. The refinements to the conventional x-ray reflectivity techniques and the precise experimental methods are described in detail in section 3 of Chapter 3. Results were obtained for values of the reflectivity R between 1 and 10^{-6} as a function of the scattering angle ϕ (for the specular reflection $\phi = 2\psi$, where ψ is the angle of incidence). As the calculated reflectivity (Appendix II) has a ψ^4 term in the denominator it is convenient to describe the results in terms of $T = R\psi^4$. This enables different features in the reflectivity curve to be more easily distinguished. The reflectivity data from the sample is plotted on a logarithmic scale of T versus incident angle in figure 4.5a. Fringes, arising from the 200Å AlInAs layer, are clearly seen, and the pattern is modulated by a larger period, corresponding to reflection from a thin surface layer.

(2.2) Theory and Analysis of Results.

(2.2.1) X-ray Reflectivity.

In the previous chapter it was shown that a simple two layer system (film on substrate) displays a steadily decreasing reflected intensity as the incident angle increases, with superimposed oscillations arising from the

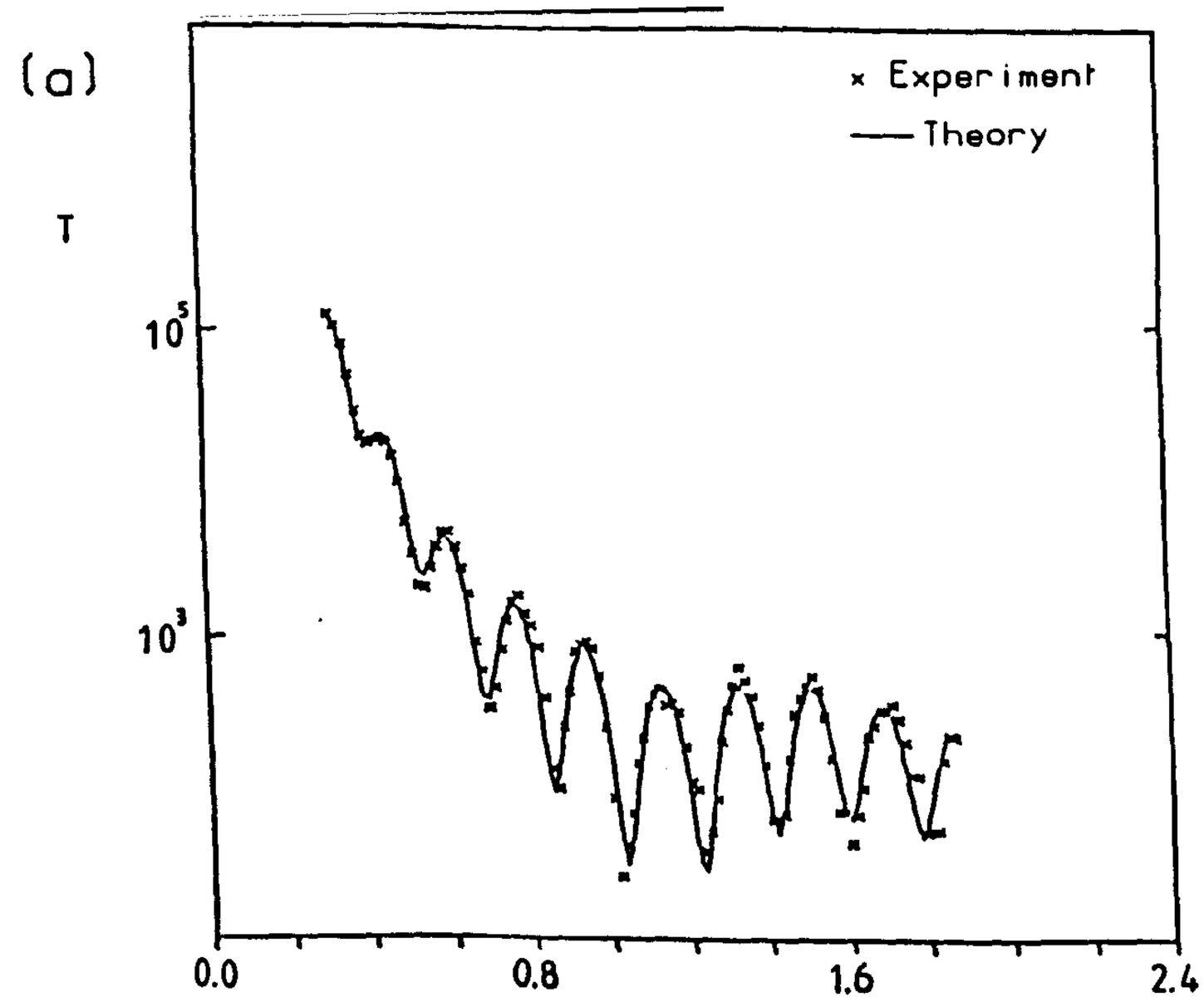

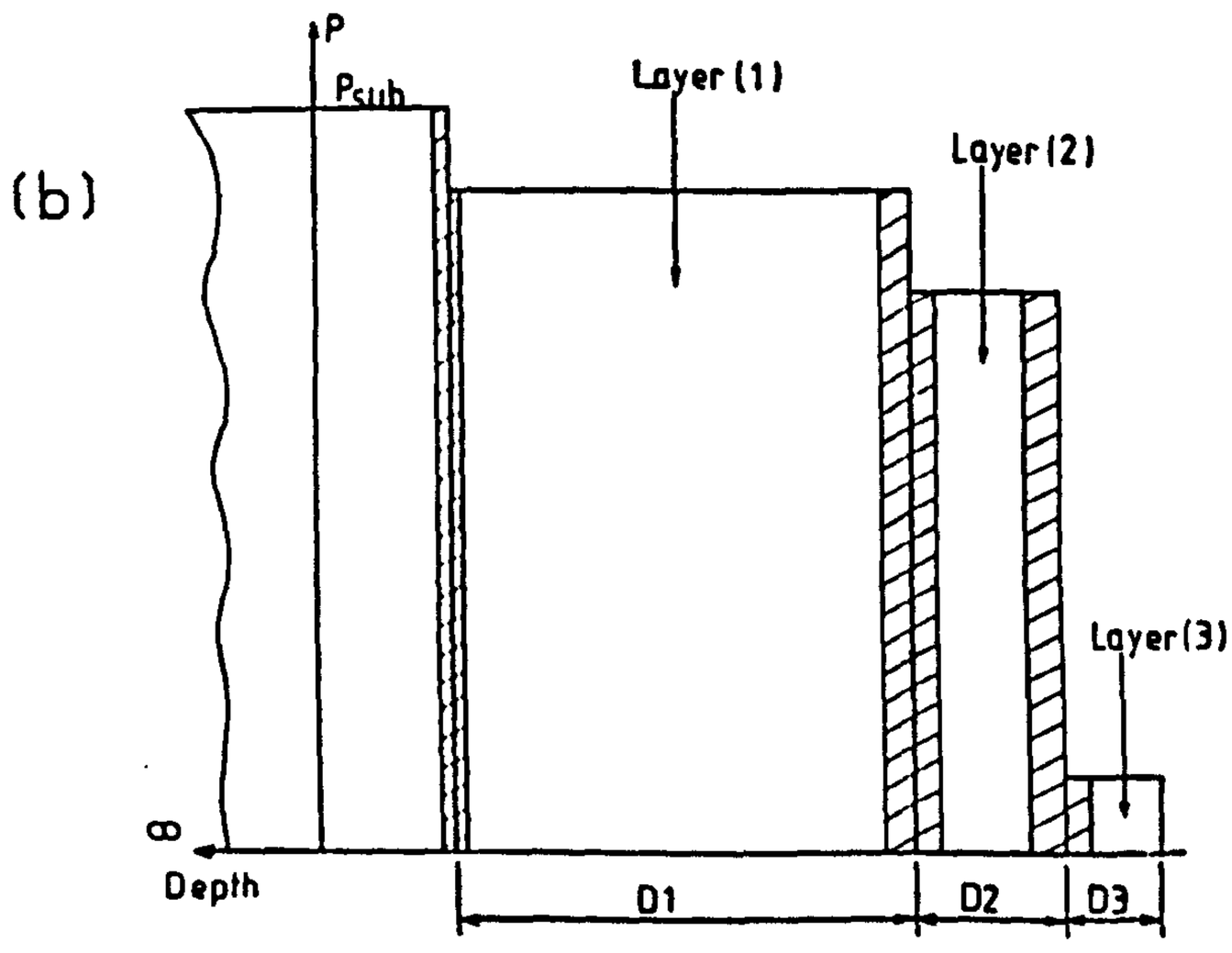

Figure 4.5(a). T, the reflectivity R multiplied by ψ^4, plotted on a logarithmic scale against ψ. The full curve gives the four-layer fit to the results, as described by the parameters in Table 4.1

(b). The electron density profile used for the calculated fit of figure 4.5(a).

	Thickness (Å)	ρ/ρ_s	Roughness σ (Å)
Layer 3	22.3±0.7	-0.90±.02	<1
Layer 2 (GaAs)	30.5±0.7	-0.24±.02	8.8±0.7
Layer 1 (AlInAs)	210.0±0.8	-0.11±.04	8.9±0.7
InP substrate	—	1.0	4.3±0.8

Table 4.1. Results of least-squares fit to the x-ray reflectivity data of figure 4.5(a).

interference between waves reflected from the first and second interfaces. The general form of the data in figure 4.5a suggests a more complex behaviour, characteristic of a number of layers. For a chosen model, the variable parameters of the theory (Appendix II) are fitted to the data using least-squares refinement. The fit to the data in figure 4.5a was obtained using the parameters listed in Table 4.1 in a model represented by figure 4.5b. Two thin surface layers, in addition to the 210Å of AlInAs (layer 1) are required to produce the fit. Layer 2 corresponds to the GaAs "capping layer" of thickness 30Å and there is an unexpected surface layer (layer 3) with a very low electron density. This is consistent with the measurements of the Si/SiO_2 wafers which indicated the dramatic effect that impurities, such as water, can have on the x-ray reflectivity curve. Reflectance infrared spectroscopic measurements (see section 3 of Chapter 3) of this sample showed complex absorption features at approximately 2700nm, corresponding to OH vibrations at or near the surface. It should be noted that the interfaces of the GaAs layer are rough (cf Table 3.2) and the low density suggests that oxygen may be present in the system.

(2.2.2) Crystal Truncation Rods.

X-ray diffraction from a layered structure consisting of "thin" crystalline sheets can be expressed as a sum of the contributions from each interface of each crystalline layer. In a one-dimensional model the amplitude contributions assume the general form

$$\pm A_0 G_j e^{i\underline{Q}\cdot\underline{r}_j} R_j Y_j (1 - e^{iQ_z a_j})^{-1} \qquad (1)$$

Ao is an amplitude constant and G_j is the usual unit cell structure factor. The phenomenological damping term Y_j can be written as $e^{-\mu_j t_j}$ and is dependent on the path length t_j of the x-rays in reaching the interface and the linear absorption coefficient μ_j of the propagation media. The phase term $e^{i\underline{Q}\cdot\underline{r}_j}$ is dependent on the position vector $\underline{r}_j$ of the layer, and the $(1 - e^{iQ_z a_j})^{-1}$ term generates the Bragg peaks arising from the periodic crystal lattice, with lattice parameter a_j parallel to Q_z along the surface normal. The roughness parameter R_j is given by

$$R_j = \exp\left[-\sigma_{pj}^2 \sin^2\left(\frac{Q_z a_j}{2}\right)\right] \qquad [2]$$

where σ_{pj}^2 is the variance of the Poisson random variables used to model the random surface crystalline roughness (Chrzan and Dutta, 1986). For small Q_z, σ_{pj}^2 can be directly compared with the equivalent reflectivity variance σ_n^2 with $\sigma_n^2 = \frac{a_j^2 \sigma_{pj}^2}{2}$. This kinematical scattering approach is justifiable when the layer thickness is a small fraction of the extinction length and is, therefore, valid for modelling the weak scattering arising in the tails of the substrate Bragg reflection. To model the intensity near to the Bragg condition would require a full dynamical calculation (Bartels and Nijman, 1978). However, the kinematical theory can readily be applied to the weak scattering features to obtain structural information in a simple and understandable way.

The observed x-ray scattering in figure 4.4 was simulated by assuming the heterostructure to consist of a semi-infinite substrate and two thin crystalline layers. The simulation shown in figure 4.6 is according to the parameters listed in Table 4.2. The values of the lattice parameter mismatch, and the thickness of the AlInAs (layer 1), obtained from the fit are considerably different from the parameters derived by inspection of the data. These differences arise from the interference effects, taking place between the x-rays diffracted from the different crystal layers, leading to false maxima and apparent peak shifting (Fewster, 1989a).

(2.3) Discussion of Results.

The fits to both the reflectivity and crystal truncation rods give the same crystalline layer thicknesses to within one unit cell, although the diffraction measurements are relatively insensitive to the thin capping layer (layer 2 of table 4.2). The major discrepancy between the values obtained lies in the nature of the internal interfaces. The reflectivity measurements suggest that the interfaces are rough, with a typical root-mean-square deviation of approximately 8Å. In contrast, the truncation rod measurements indicate that the crystal interfaces are relatively smooth with rms roughnesses of less than 1Å. However, in the scattering model, thin-noncrystalline layers were introduced between the crystal slabs (see table 4.2). The disordered regions will not contribute to the scattering around the Bragg peaks but will appear in the reflectivity

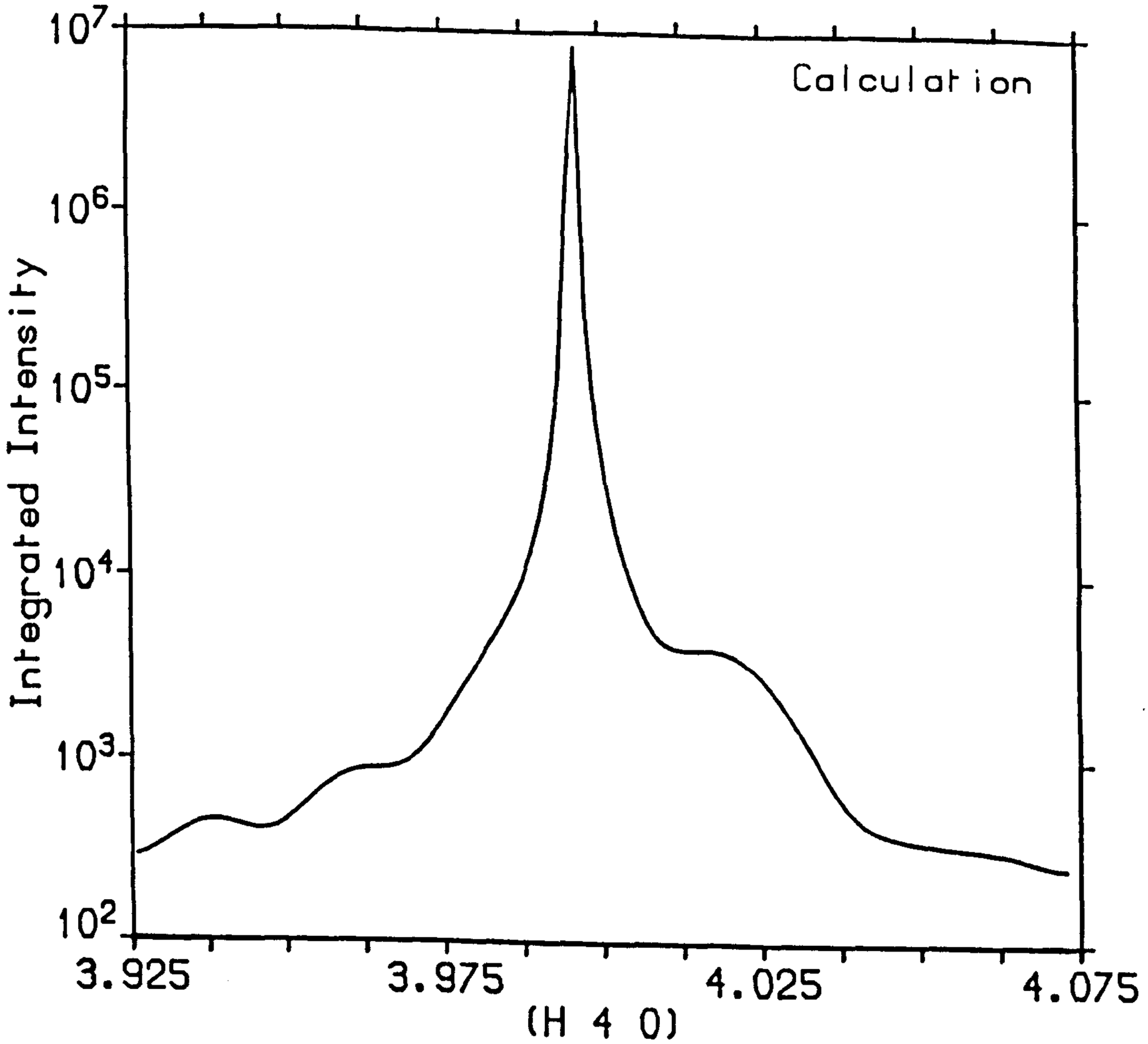

Figure 4.6. A least-squares fit to the crystal truncation rod data in figure 4.4 according to a kinematical scattering model and the parameters in Table 4.2.

	Thickness (Å)	$\Delta a/a_s$	Roughness σ (Å)
Layer 2 (GaAs)	29±1	$1.2\times10^{-3}\pm0.3\times10^{-3}$	<1
Disordered layer 2	15.0±0.5		
Layer 1 (AlInAs)	204.0±1.2	$-8.1\times10^{-3}\pm0.2\times10^{-3}$	1.0±0.7
Disordered layer 1	20±1		
InP substrate	—	1.0	2.5±0.8

Table 4.2. Results of least-squares fit to the (4 4 0) truncation rod of figure 4.4. The rms roughness values σ, have been expressed in angstroms to be compatible with the equivalent reflectivity roughness.

data as an additional rough contribution to the underlying crystalline layers. This can be seen by adapting the truncation rod model to include a loss of crystallinity at the crystalline interfaces.

As the distance from the interface increases, the probability of finding each crystal unit cell in the correct crystal plane becomes progressively smaller, and can be represented by the normalised Gaussian probability function

$$P(N) = (2\pi Na^2w)^{-1/2} \exp\left(\frac{-z^2}{2Na^2w}\right) \tag{3}$$

N is the crystal layer index within the disordered region and w is the disordering constant which governs the rate of decay. Ignoring absorption, the scattering from a general layer within the disordered region is proportional to the Fourier transform of the probability function

$$A_N = A_o G_j \int_{-\infty}^{\infty} P(N)\, e^{iQ_z z}\, dz \tag{4}$$

$$= A_o G_j \exp\left[-Q_z^2 Na^2 \frac{w}{2}\right]$$

If the surface region is n unit cells thick, with the crystalline interface at $\underline{r} = 0$, the complete scattering amplitude is given by

$$A = A_o G_j \left[\sum_{N=0}^{n-1} e^{iQ_z Na}\, e^{-Q_z^2 Na^2 w/2} + \sum_{N=0}^{-\infty} e^{iQ_z Na}\right] \tag{5}$$

Away from the Bragg peaks ($Q_z = 2n\pi/a$) this becomes

$$A = A_o G_j \left[\frac{\left[1 - e^{iQ_z na}\, e^{-Q_z^2 na^2 w/2}\right]}{\left[1 - e^{iQ_z a}\, e^{-Q_z^2 na^2 w/2}\right]} + (1 - e^{iQ_z a})^{-1}\right] \tag{6}$$

Close to the high indexed Bragg peaks, where Qz is large, the expression becomes

$$A = A_o G_j (1 - e^{iQ_z a})^{-1} \tag{7}$$

By comparison with equation (1) the effective interface is smooth and positioned at $\underline{r} = 0$, ie. the disordered system is not observed in the truncation rod measurement.

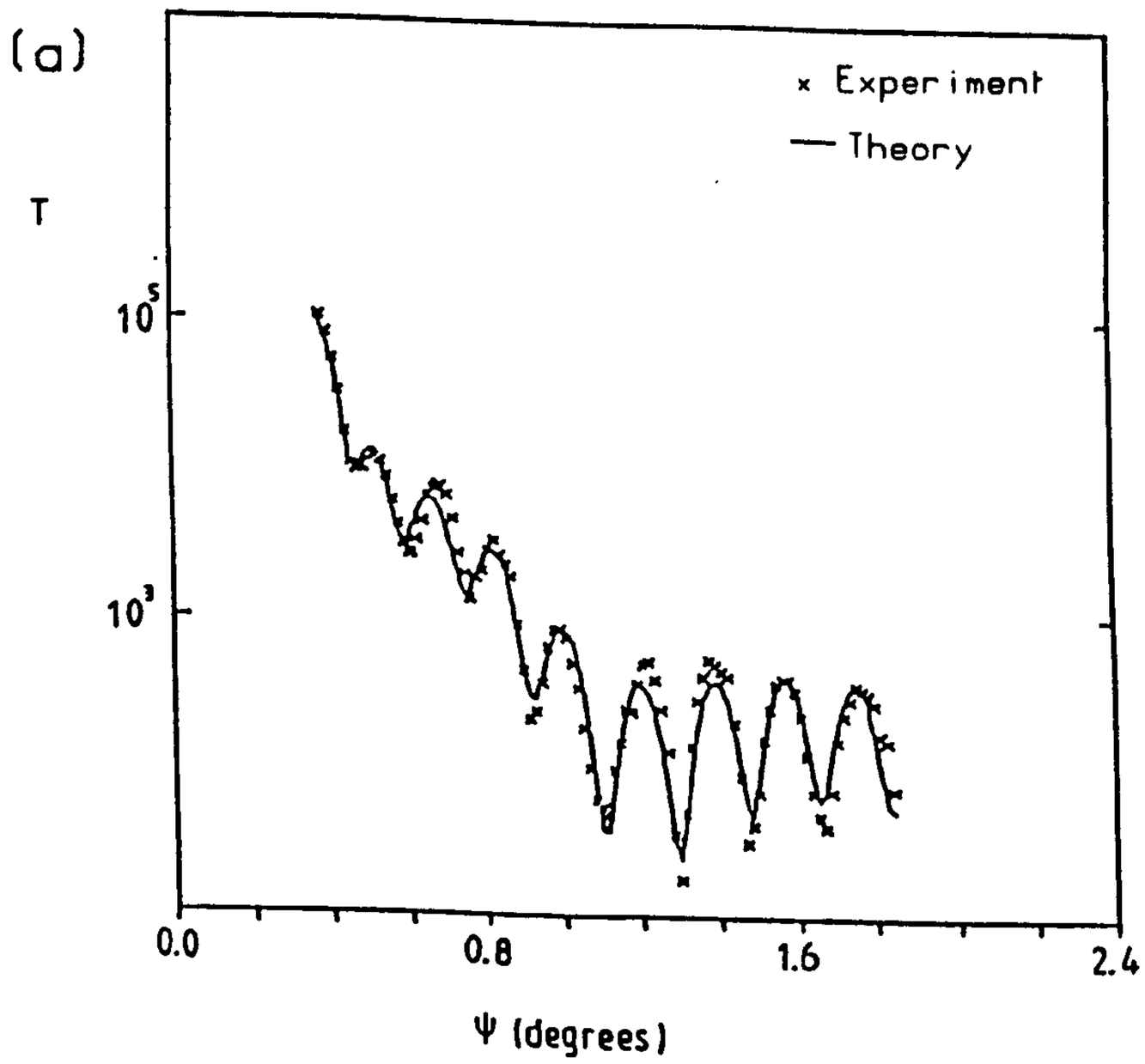

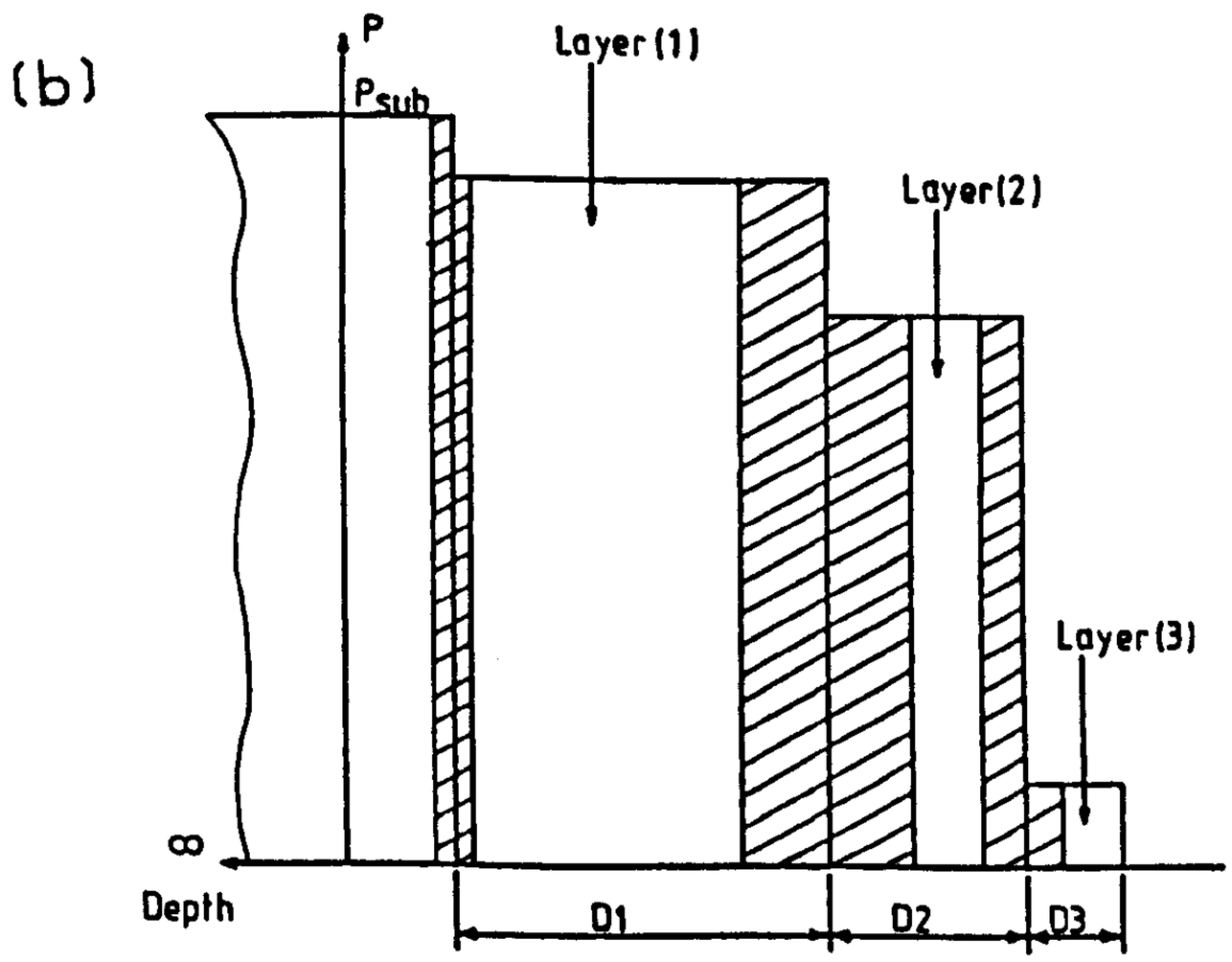

Figure 4.7.(a). T, the reflectivity R multiplied by ψ^4, plotted on a logarithmic scale, after baking of the sample in a vacuum oven. The dark line is the least-squares fit according to the parameters in Table 4.3.

(b) The electron density profile for the fit in Figure 4.7(a) shows how the layer thicknesses have changed after oxidation into the quantum well.

	Thickness (Å)	p/p_s	Roughness σ (Å)
Layer 3	23.1±0.7	-0.89±.02	<1
Layer 2 (GaAs)	45.4±0.8	-0.26±.02	9.3±0.7
Layer 1 (AlInAs)	197.0±0.9	-0.08±.04	20.3±0.8
InP substrate	—	1.0	4.0±0.8

Table 4.3. Results of least-squares fit to the x-ray reflectivity data of figure 4.7(a).

For reflectivity measurements $Q_z \rightarrow 0$, and assuming $\exp(-Q_z^2 na^2 w/2) \sim 1$, the expression becomes

$$A = -A_0 G_j e^{iQ_z na} e^{-Q_z^2 na^2 w/2} (1 - e^{iQ_z a})^{-1} \quad (8)$$

The effective interface has now moved to r = na, so that the system appears to be thicker, increasing by the thickness of the disordered region. In addition there is a roughness term $\exp(-Q_z^2 na^2 w/2)$ which is of the same form as the roughness term used in the reflectivity model (Appendix II), with $\sigma_n = (wna^2)^{1/2}$. A comparison of the results obtained by the different techniques now shows them to be in excellent agreement. The thicknesses of the disordered non-crystalline layers (Table 4.2) correspond to the Gaussian spreads of the interface roughnesses in the reflectivity model (Table 4.1).

Prompted by the evidence of absorbed water, reflectivity measurements were repeated after the sample had been heated at 200°C for two hours in an oven. The new reflectivity data are shown in figure 4.7a, and fitted with the same model, as in figure 4.7b. Table 4.3 shows that the fitted parameters are significantly different from those used to describe the original data. The AlInAs layer has decreased in thickness to 197Å, resulting in a proportional increase of layer 2. Considerable roughening of the interface between these layers indicates transfer across the boundary and it is concluded that the heating of the sample induced oxidation into the AlInAs layer. The heating process made little difference to the topmost layer (layer 3), which indicates a stable contaminate or, possibly, that this may be a manifestation of surface roughness. Perfect fits to the reflectivity data were not possible, due perhaps to the presence of a graded electron density which would not be ideally represented by the model used.

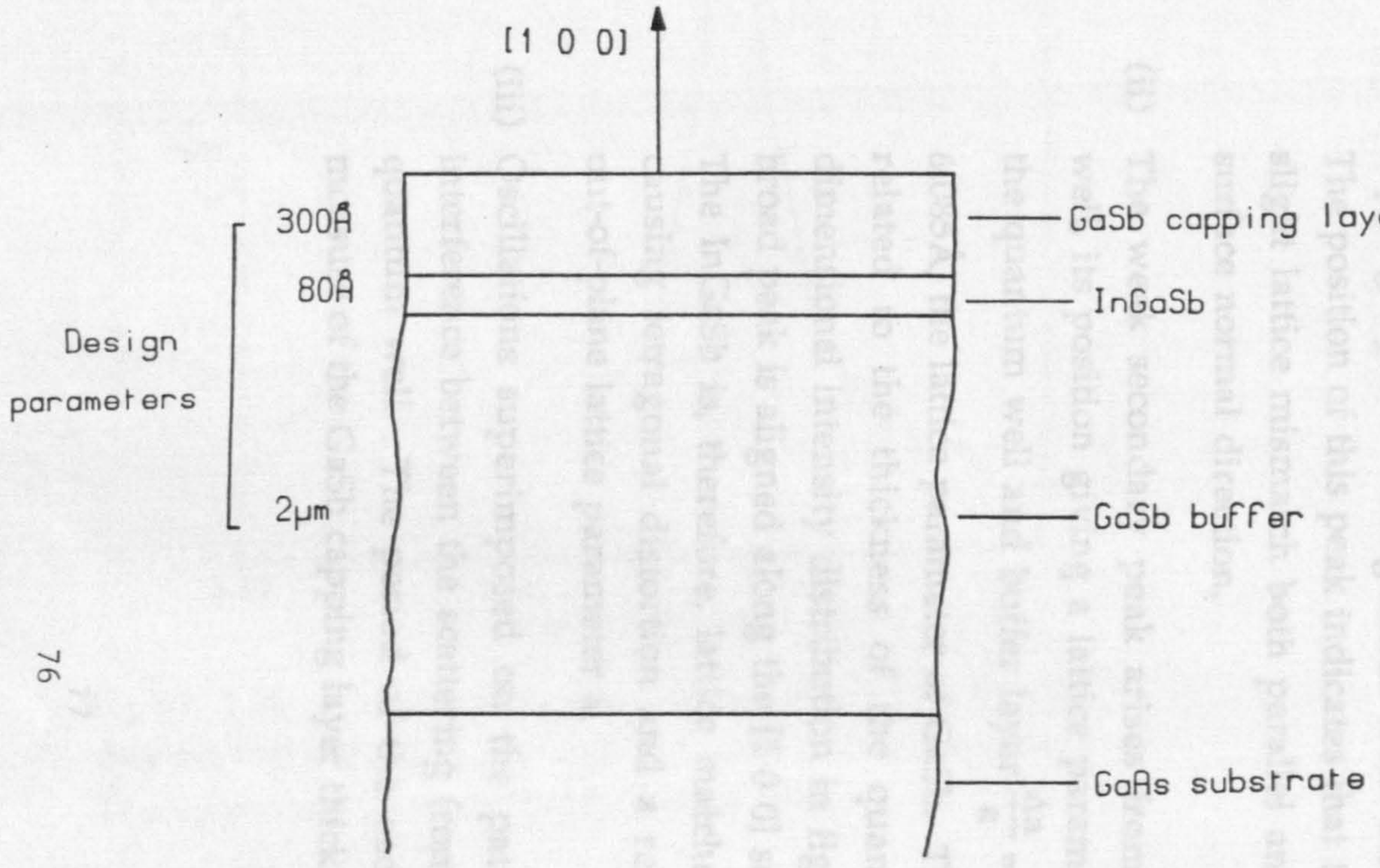

Figure 4.8. A schematic illustration of the sample crystal grown by MOCVD at Oxford University on [1 0 0] oriented GaAs.

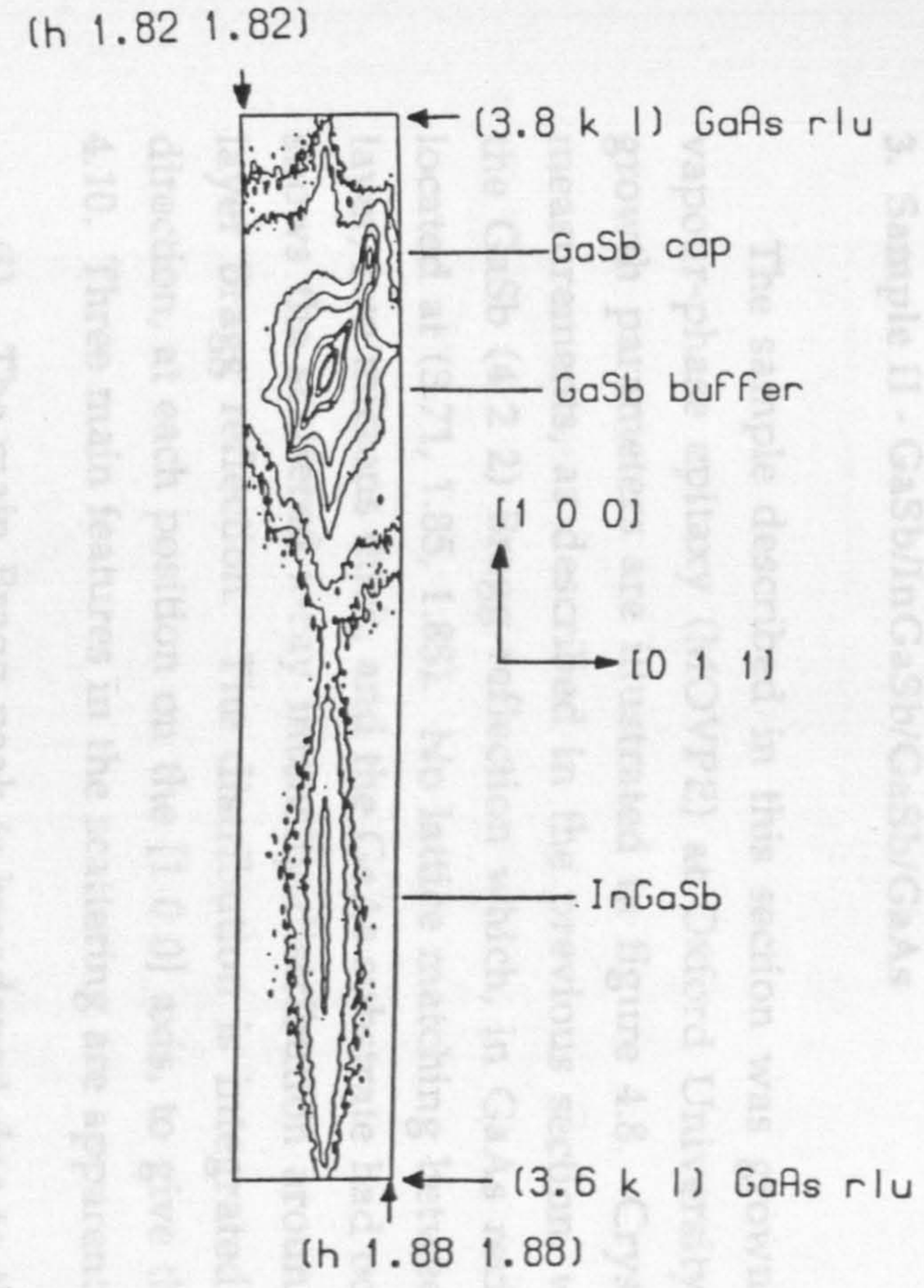

Figure 4.9. An isointensity contour plot of the observed x-ray scattering in the region of the GaSb (4 2 2) Bragg reflection.

3. Sample II - GaSb/InGaSb/GaSb/GaAs

The sample described in this section was grown by metal organic vapour-phase epitaxy (MOVPE) at Oxford University and the nominal growth parameters are illustrated in figure 4.8. Crystal truncation rod measurements, as described in the previous section, were taken around the GaSb (4 2 2) Bragg reflection which, in GaAs reciprocal space, was located at (3.71, 1.85, 1.85). No lattice matching between the GaSb buffer layer, two microns thick, and the GaAs substrate had occurred. Figure 4.9 shows the scattered x-ray intensity distribution around the GaSb buffer layer Bragg reflection. The distribution is integrated along the [0 1 1] direction, at each position on the [1 0 0] axis, to give the results in figure 4.10. Three main features in the scattering are apparent:

(i) The main Bragg peak is broadened due to the presence of the almost lattice matched GaSb capping layer. In fact, from figure 4.9, it is seen that a well defined peak arising from the GaSb capping layer is distinguished from the main Bragg reflection. The position of this peak indicates that the layer has acquired a slight lattice mismatch both parallel and perpendicular to the surface normal direction.

(ii) The weak secondary peak arises from the InGaSb quantum well, its position giving a lattice parameter mismatch between the quantum well and buffer layer $\frac{\Delta a}{a} = 18.6 \times 10^{-3}$, where a = 6.085Å, the lattice parameter of GaSb. The width of this peak is related to the thickness of the quantum well. The two-dimensional intensity distribution in figure 4.9 shows that this broad peak is aligned along the [1 0 0] surface normal direction. The InGaSb is, therefore, lattice matched in the surface plane causing tetragonal distortion and a resultant increase in the out-of-plane lattice parameter a.

(iii) Oscillations superimposed on the pattern are the effects of interference between the scattering from the capping layer and quantum well. The period of the oscillations gives a direct measure of the GaSb capping layer thickness.

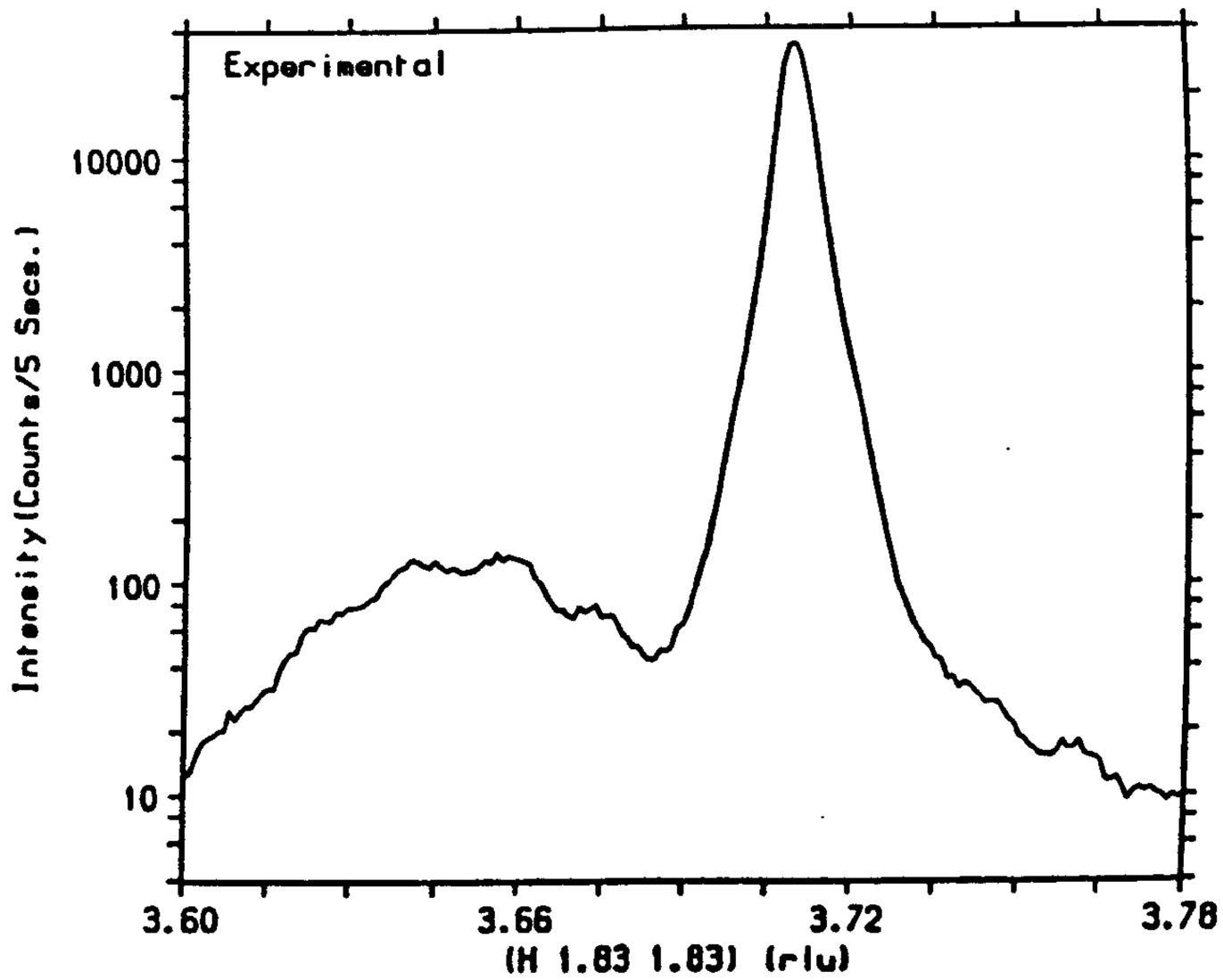

Figure 4.10. The intensity distribution along [1 0 0], the face normal direction, through the GaSb (4 2 2) Bragg peak. The x axis is in GaAs reciprocal lattice units.

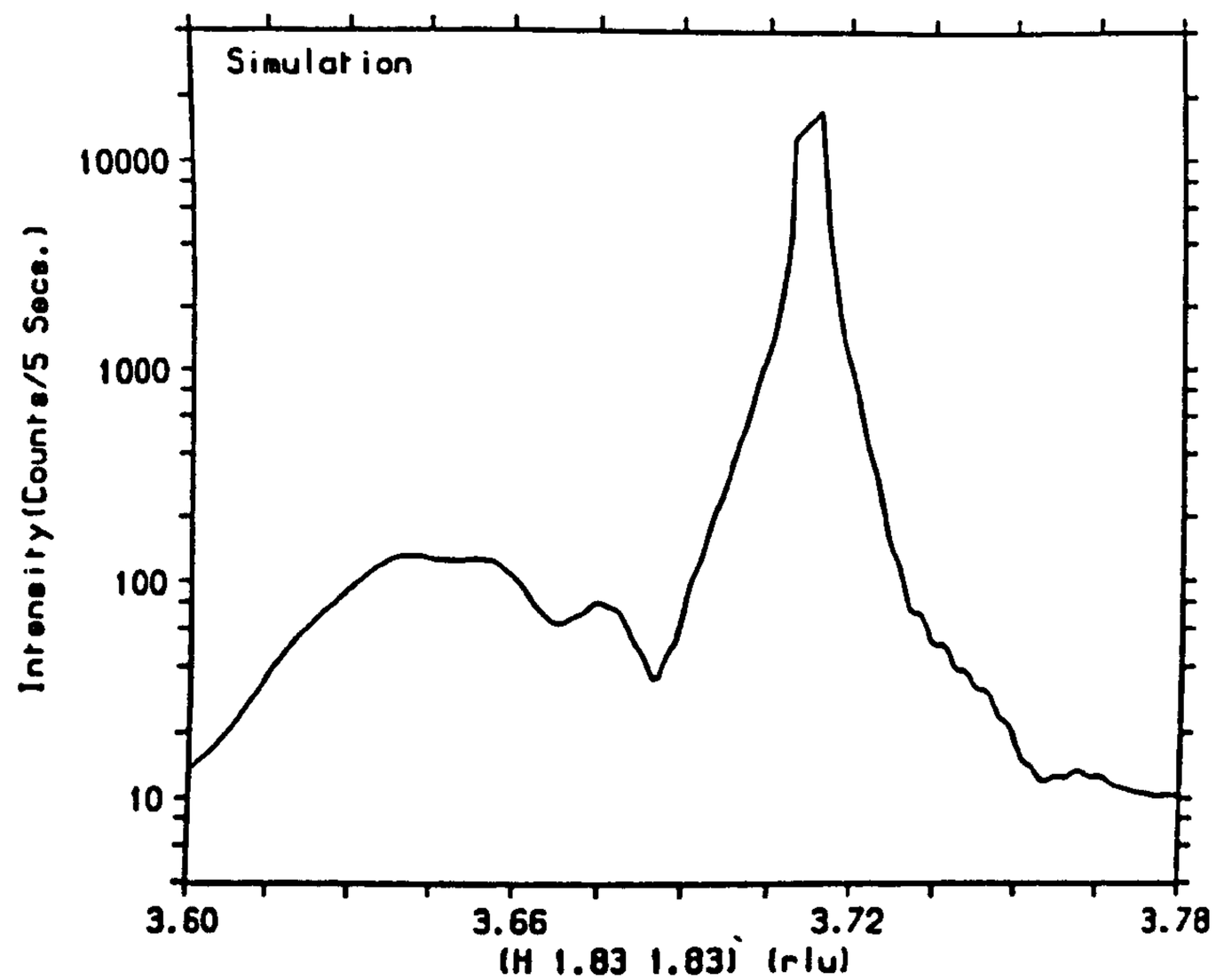

Figure 4.11. A least squares fit to the data in figure 4.10 according to the parameters in Table 4.4.

	Thickness (Å)	$\Delta a/a_s$	Roughness σ (Å)
Layer 1 (GaSb)	268±6	$0.8\times10^{-3}\pm0.2\times10^{-3}$	19±4
Layer 2 (InGaSb)	93±4	$18.6\times10^{-3}\pm0.7\times10^{-3}$	27±5
GaSb buffer	—	a_s=6.085Å	34±5

Table 4.4. Results of least-squares fit to the (4 2 2) truncation rod of figure 4.10.

The experimental results were simulated using the kinematical scattering model described in detail in the previous section. The essential parameters of the theory were varied in a least-squares fit to the data, beginning at their nominal values, and refining to the values shown in Table 4.4. No amorphous regions between the crystalline layers were included in the model. Apart from the unavoidable discrepancy in the region of the Bragg reflection, the simulation accurately reproduces the features of the scattered intensity (figure 4.11). The results are in reasonable agreement with the nominal growth parameters but very large values of rms roughness were required for the fit. The physical credibility of these values was reinforced when x-ray reflectivity measurements of the sample were attempted.

At angles greater than the critical angle, no significant specular scattering was observed. The scattering was dominated by a very large off-specular signal, its angular position governed by the equation

$$\phi = \psi + \psi_c$$

where ϕ is the scattering angle, ψ is the incident angle and ψ_c is the critical angle for total external reflection. This result is characteristic of a very disordered system (Petrashen, Korev, Chukhovskii and Degrtyarev, 1983; Sinha, Sirota, Garoff and Stanley, 1988) and supports the results of the crystal truncation rod experiment. The reflectivity technique is very sensitive to roughness, particularly at the sample surface, and in this case it was impossible to obtain a reflectivity curve. Other crystals, also grown by MOVPE, showed visual evidence of islanding and similar problems in obtaining reflectivity measurements were experienced. Due to the very small angles involved in the reflectivity experiments, a much larger area of the crystal is illuminated than in the truncation rod experiment and, therefore, macroscopic islanding would have a greater effect on the reflectivity results. However, if this is the case, the truncation rod measurements indicate that an average structure, possibly within the islands, is maintained, with a crystalline form corresponding to the nominal structure.

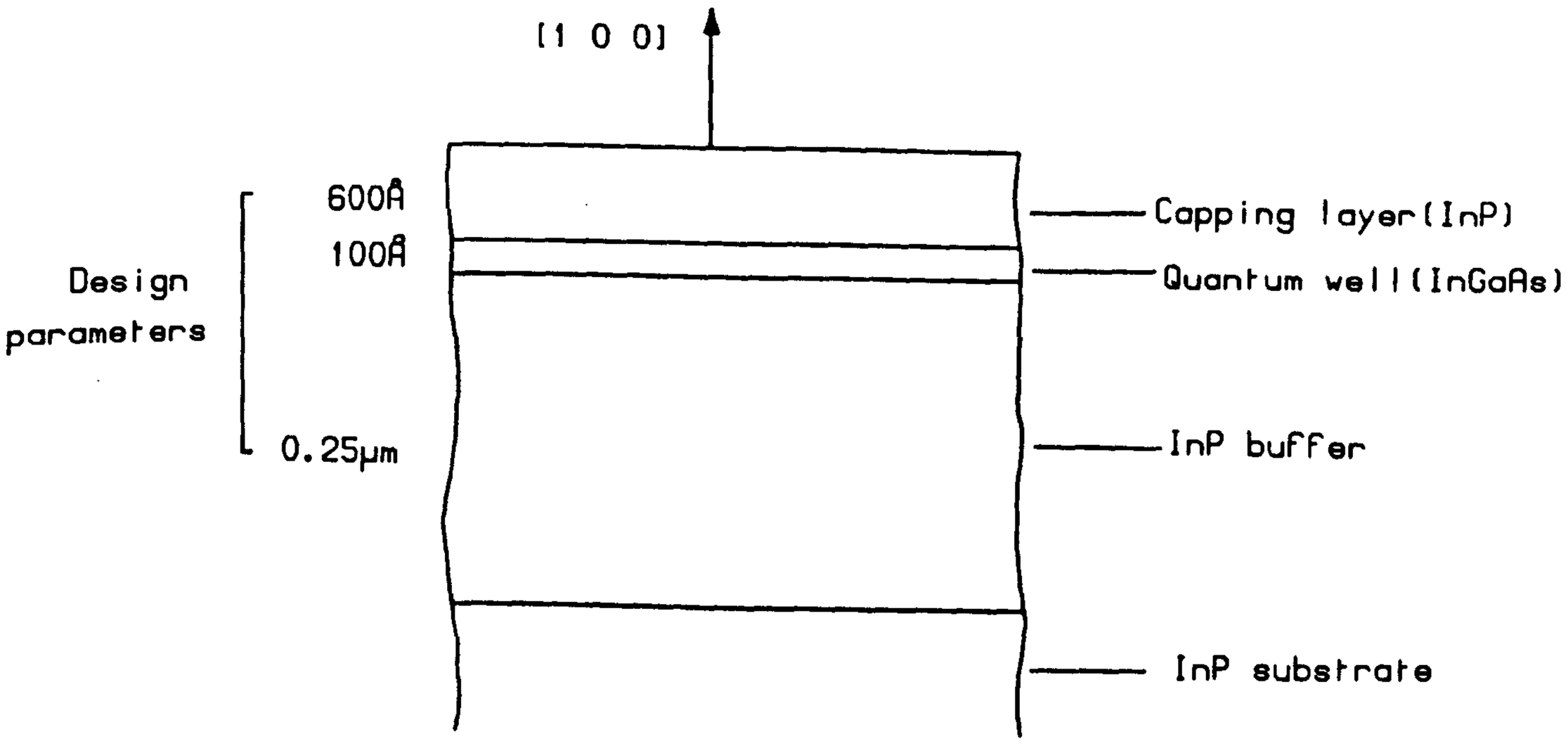

Figure 4.12. A schematic illustration of the sample crystal PMB251 grown by MBE at Sheffield University. The thickness parameters shown were estimated from growth rates.

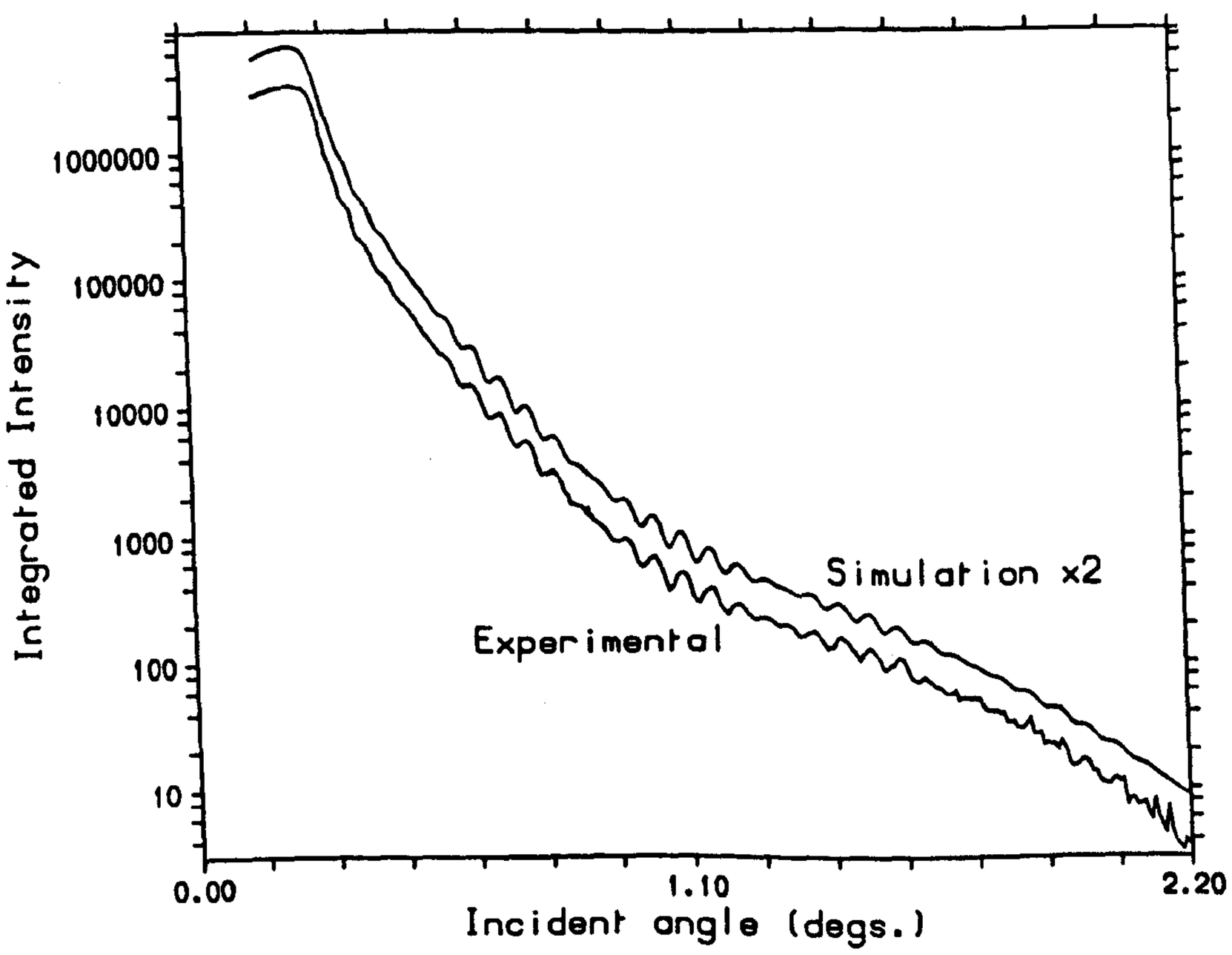

Figure 4.13. The specularly reflected intensity, plotted on a logarithmic scale, as a function of incident angle ψ, for the sample PMB251. The solid line is the calculated fit to the data according to the parameters in Table 4.5.

4. Sample III - InP/InGaAs/InP

The experiments described in this section were performed on a sample crystal, identification code PMB251, grown by MBE using the VG 80H reactor at Sheffield University. From growth rates, the InP cap was expected to be about 600Å thick, with the single buried layer of InGaAs being only 100Å thick. The nominal structure of the device is schematically illustrated in figure 4.12.

X-ray reflectivity measurements of the sample were taken, according to the method described in section 2, using the triple-crystal diffractometer in its high-resolution mode of operation. After background correction and normalisation procedures (Chapter 3), the results are represented by the full curve in figure 4.13. At very small angles of incidence a region of total reflection occurs, with the slight tail-off of intensity towards lower angles being due to the limited sample size. Above the critical angle, high frequency fringes arising from the 600Å capping layer are clearly seen, and the interference between these and fringes from the 100Å layer produces the beats observed. In addition the pattern appears to be modulated by a very low frequency oscillation, corresponding to reflection from a thin surface layer.

These observations are confirmed by the least-squares refined fit to the data, also shown in figure 4.13, and calculated according to a four-layer model with the parameters in Table 4.5. The fit is displaced by an order of magnitude from the data in order to show the excellent agreement between theory and experiment. For the purpose of the calculation it was assumed that the InP buffer layer, 0.25 microns thick, and the InP substrate formed an effectively infinite homogeneous substrate. Any electron density difference between the two materials would be very small, and oscillations from a layer 0.25 μm thick occur with a reciprocal space frequency which is several times smaller than the resolution of the instrument. The parameters agree almost exactly with their nominal values, with the interface roughnesses indicating transition widths between layers of 1-2 monolayers in thickness. The large-scale oscillation is reproduced by the introduction of a 26Å thick surface layer of a lower density material, possibly an oxide. The agreement between theory and experiment clearly demonstrates that the

	Thickness (Å)	ρ/ρ_s	Roughness σ (Å)
Layer 1 (surface)	26±1	-0.12±.02	6±1
Layer 2 (InP)	603±6	-0.002±.01	6±2
Layer 3 (InGaAs)	103±4	0.11±.04	6±4
InP substrate	—	1.0	4±3

Table 4.5. Results of least-squares fit to the reflectivity data of figure 4.13, using a three-layer model.

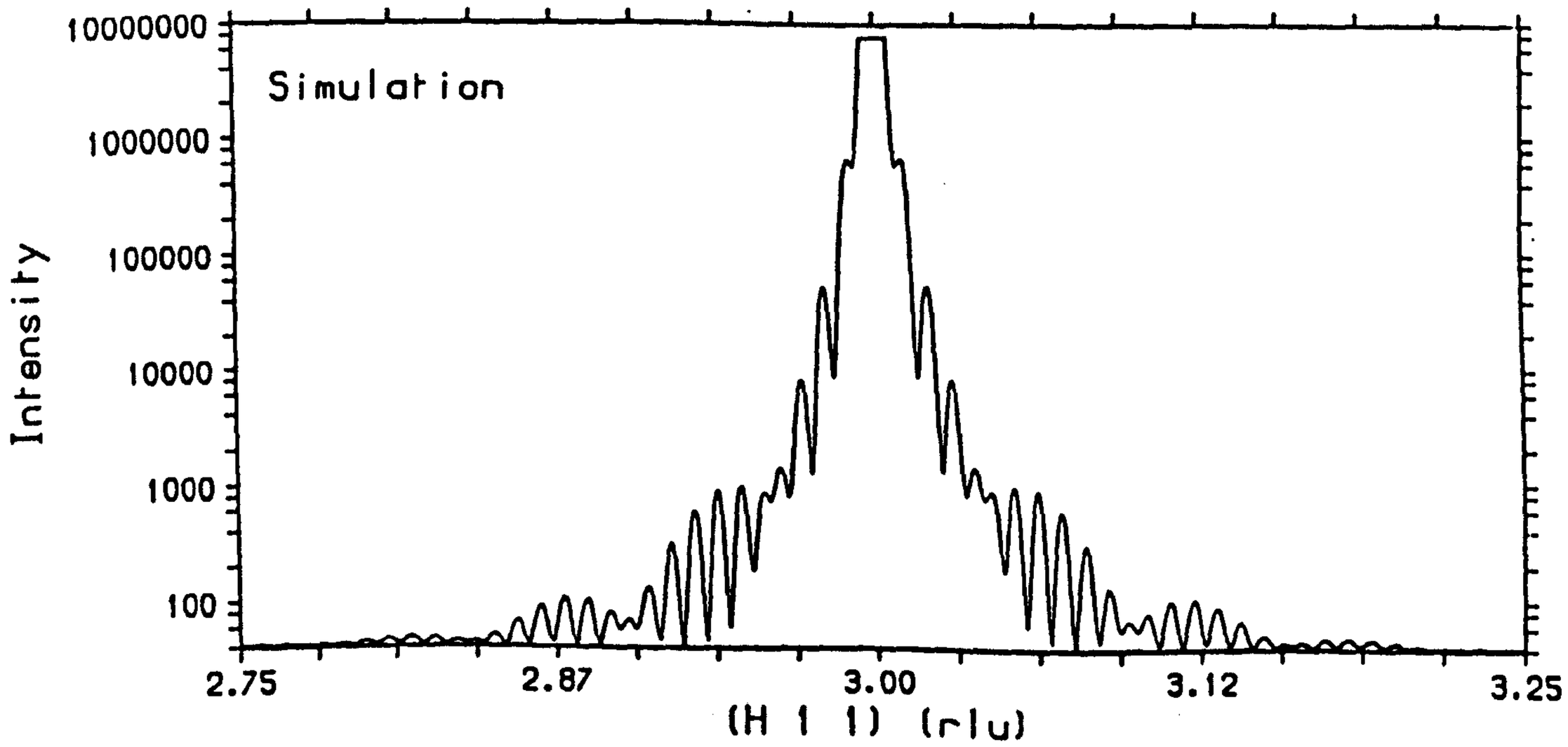

Figure 4.14. A simulation of the scattered distribution around the InP (311) Bragg reflection, as expected from the measured x-ray reflectivity parameters and assuming perfect crystalline quality, and no lattice mismatch.

reflectivity model, which treats the sample as a series of homogeneous, dielectric slabs, is an excellent approximation in the case of MBE-grown semiconductor heterostructures.

Using the parameters obtained from the reflectivity calculation, the expected results from the crystal truncation rod experiment were simulated using the kinematical theory described in section 2. The simulation, figure 4.14, was performed under the assumption that there was no lattice mismatch between any of the layers in the structure. Lattice mismatch would cause a shifting of intensity to one side of the Bragg peak, without altering the basic interference pattern. With this simulation in mind, measurements of the crystal truncation rod were taken around the InP (3 1 1) Bragg reflection and the results, in the form of an intensity contour map and its integrated profile, are shown in figure 4.15. A number of surprising details are revealed, which conflict with the initial picture given by the reflectivity results.

The obvious asymmetry around the Bragg reflection is due to a large strain in the system, causing an increase in the out-of-plane lattice parameters of the deposited layers. The period of the interference fringes indicates scattering from a crystalline layer approximately 500Å thick, 100Å smaller than the expected thickness. This is presumably due to the presence of non-crystalline layers around the strained interfaces. Also, the lateral offset (0 ξ ξ) between the Bragg peak and the centre of the crystal truncation rod is evidence that the layers are not lattice matched in the surface place, i.e. the strain has not been entirely removed by tetragonal distortion, as it was in the two previous samples studied. Indeed, measurements on a number of Bragg reflections showed that the in-plane distortions were highly anisotropic, suggesting that, by performing experiments in a two-dimensional scattering plane, only a projection of the scattered intensity was being measured. This was supported by an inability to simulate the data, despite using a variety of models to represent the non-crystallinity present in the system. The reflectivity measurements are not sensitive to the crystalline perfection of the sample and consequently give a misleading interpretation of its quality.

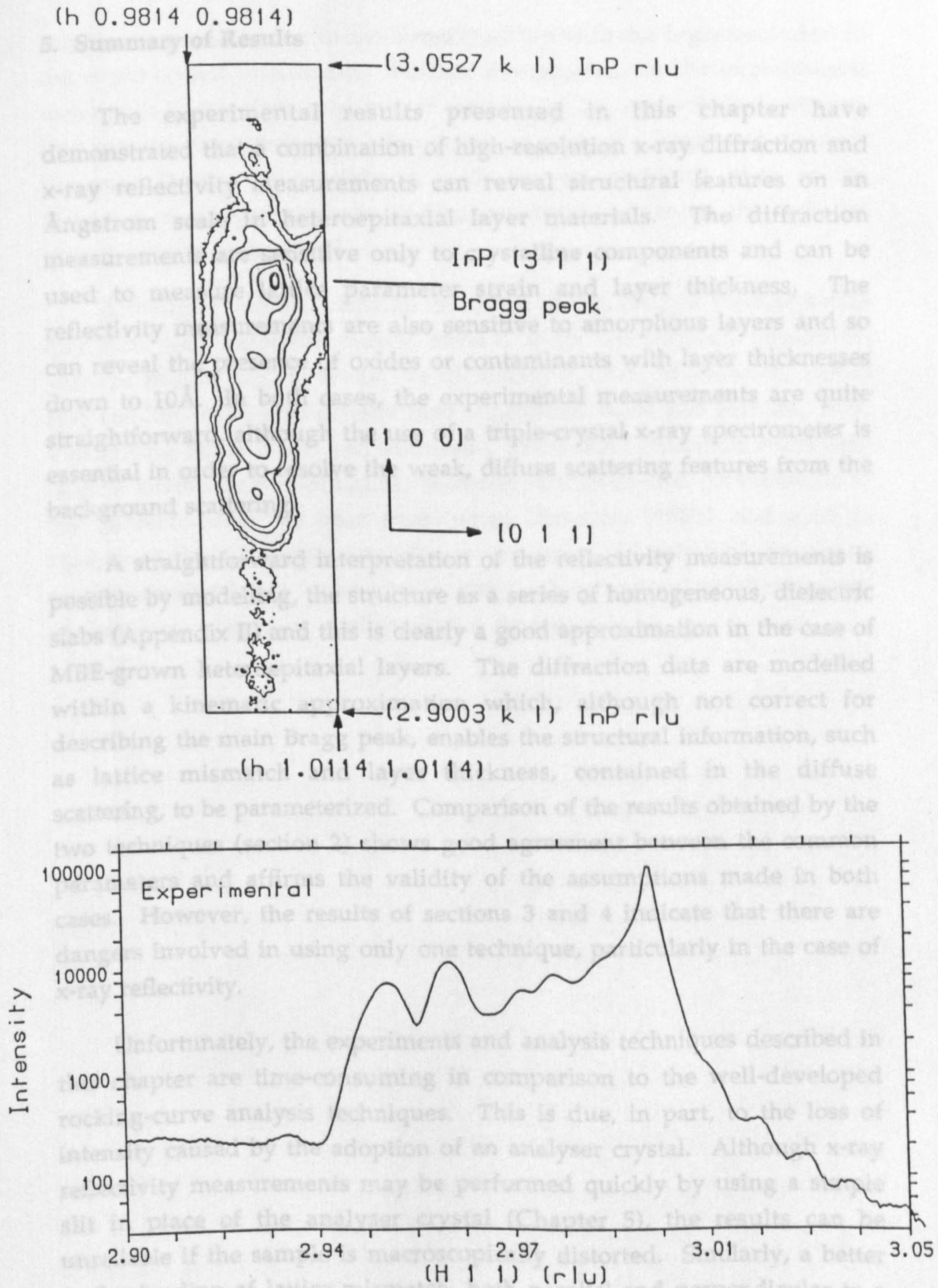

Figure 4.15. The measured scattered x-ray distribution about the InP (3 1 1) Bragg reflection and the integrated intensity distribution corresponding to the simulated profile in figure 4.14. The discrepancy between the two distributions is described in the text.

5. Summary of Results

The experimental results presented in this chapter have demonstrated that a combination of high-resolution x-ray diffraction and x-ray reflectivity measurements can reveal structural features on an Ångstrom scale in heteroepitaxial layer materials. The diffraction measurements are sensitive only to crystalline components and can be used to measure lattice parameter strain and layer thickness. The reflectivity measurements are also sensitive to amorphous layers and so can reveal the presence of oxides or contaminants with layer thicknesses down to 10Å. In both cases, the experimental measurements are quite straightforward, although the use of a triple-crystal x-ray spectrometer is essential in order to resolve the weak, diffuse scattering features from the background scattering.

A straightforward interpretation of the reflectivity measurements is possible by modelling, the structure as a series of homogeneous, dielectric slabs (Appendix II) and this is clearly a good approximation in the case of MBE-grown heteroepitaxial layers. The diffraction data are modelled within a kinematic approximation which, although not correct for describing the main Bragg peak, enables the structural information, such as lattice mismatch and layer thickness, contained in the diffuse scattering, to be parameterized. Comparison of the results obtained by the two techniques (section 2) shows good agreement between the common parameters and affirms the validity of the assumptions made in both cases. However, the results of sections 3 and 4 indicate that there are dangers involved in using only one technique, particularly in the case of x-ray reflectivity.

Unfortunately, the experiments and analysis techniques described in this chapter are time-consuming in comparison to the well-developed rocking-curve analysis techniques. This is due, in part, to the loss of intensity caused by the adoption of an analyser crystal. Although x-ray reflectivity measurements may be performed quickly by using a simple slit in place of the analyser crystal (Chapter 5), the results can be unreliable if the sample is macroscopically distorted. Similarly, a better understanding of lattice mismatch, both parallel and perpendicular to a sample surface, is obtained if the diffracted intensity can be mapped out in

sample reciprocal space, in the detail possible with the high-resolution of the triple-crystal instrument. Further development in the experimental techniques is therefore required, if they are to be used routinely for on-line growth characterisation. However, as part of a long-term research program, it may be possible to study several problems, such as the influence of stepped surfaces and surface irregularities on the epitaxial growth process (Vlieg, 1988).

Although the measurements described in this chapter were of single quantum well heterostructures, several more complicated structures, such as multiquantum wells (Vandenburg, Hamm, Macrander, Parish and Temkin, 1986) and superlattices (Kashihara, Kase and Harada, 1986; Vardanyan, Manoukyan and Petrosyan, 1985) would provide interesting studies for the x-ray techniques. Recently, a four-crystal, six-reflection x-ray diffractometer has been constructed (Fewster, 1986b), and used to study a variety of complex multilayer structures. Clearly high-resolution x-ray scattering has a major part to play in the structural characterisation of these new, thin-layer semiconductor devices.

CHAPTER FIVE

An X-ray Reflectivity Study of the Photo-dissolution of Silver in Chalcogenide Glasses.

1. Introduction

In 1966 Kostychin, Mikhailovskya and Romanenko observed that when thin films of amorphous As_2S_3 deposited on silver substrates were illuminated, the silver metal diffused into the chalcogenide. Initially the phenomenon was considered to be limited to the near-interface region and was known as photo-doping. Further investigation showed that large amounts of the metal could participate in the process, with the silver concentration in the chalcogenide being much higher than that achieved by doping, and so the process became known as photo-dissolution. Since this discovery a wide variety of light-induced changes has been observed in amorphous chalcogenides, such as photo-darkening (de Neufville, Moss and Ovshinksy, 1973) and photo-crystallisation (Ovshinsky and Klose, 1972), and a review of these phenomena has been given by Tanaka (1981).

The incorporation of silver into a chalcogenide glass markedly changes many of its physical properties, in particular causing a drastic reduction of the solution rates in dry and wet chemical etchants (Chang and Chen, 1978; Yoshikawa, Ochi, Nagai and Mizushima, 1976). This means that, after exposure to light, silver/glass samples can be developed in an alkali or plasma etched to produce a relief image. Photo-sensitive chalcogenide systems therefore have great potential as photo-resists for micro-lithography in the fabrication of integrated circuits (Tai, Ong and Vadimsky, 1982). Photo-dissolution can also be stimulated by electrons, x-ray or ion beams, as well as by light, opening up the possibility of manufacturing high-resolution devices of great technological importance.

Figure 5.1 shows a schematic illustration of a photo-dissolution experiment. The sample is made by thermal evaporation onto a glass substrate and consists of a thin layer of silver (100-1000Å thick) on top of a layer of chalcogenide an order of magnitude thicker. When illuminated

by light, the silver diffuses into the chalcogenide at a rate much higher than normal thermal diffusion. Various methods have been developed to study the reaction kinetics, measuring either the amount of silver remaining on the surface or the thickness of the reaction product, by optical transmission (Mizuno, Tanaka and Kikuchi, 1973; Chatani, Shimizu, Kokado and Inoue, 1977) and resistance measurements (Goldschmidt and Rudman, 1976; Yaji and Kurita, 1983). However, the interpretations of these experiments implicitly assumed the presence of a well-defined reaction product layer. The distribution of silver after photo-dissolution has been studied by Rutherford backscattering (Goldschmidt, Bernstein and Rudman, 1977), Raman scattering (Ewen, Taylor, Firth and Owen, 1983) and Extended X-ray Absorption Fine Structure (EXAFS) (Greaves, Elliott, Gladden and Spence, 1987). Several models, capable of describing various aspects of the photo-dissolution process have been proposed (Street and Mott, 1975; Kastner, Adler and Fritzsche, 1976; Ishikawa and Kikuchi, 1980; Janai, 1981) and a more general treatment, considering the effect as a radiation-enhanced solid-state reaction has recently been given (Kluge, 1987).

Despite the abundance of experimental work performed on the silver/chalcogenide system, a complete understanding of the structural evolution during the photo-dissolution process has not been achieved. This is due to the insensitivity of many of the probing techniques to the detailed microscopic structure.X-ray reflectivity is very sensitive to the microscopic structure at the surface of a sample (see Chapters 3 and 4 of this thesis) and has been used to study subjects such as antiferroelectric surface layers in liquid crystals (Gramsbergen, de Jeu and Als-Nielsen, 1986) and capillary waves on the surface of simple liquids (Braslau, Pershan, Swislow and Ocko, 1988). X-ray reflectivity has also been used to study diffusional alloying in polycrystalline thin-film couples (Wagendristel, Bangert and Tonsern, 1979; Wagendristel, Schurz, Ehrmann-Falkenau and Bangert, 1980). In these experiments the x-ray reflectivity in the region of the critical angle for total reflection was examined as a function of alloy growth, allowing the determination of alloy composition and growth rates for these processes.

The work described in this chapter is the application of x-ray scattering techniques to determining the structural properties of the

photo-dissolution process in thin-film silver/chalcogenide systems. Section 2 describes measurements of the diffraction signal from the polycrystalline silver film, which may be used to monitor the disappearance of the silver layer as a function of illumination time (Rennie and Elliott, 1985). This technique was initially used to study diffusion in metal multilayers (Du Mond and Youtz, 1940; Dinklage and Frerichs, 1963; Dinklage, 1967). In conjunction with the x-ray reflectivity measurements, it is then possible to build up a detailed microscopic picture of the reaction process. Section 3 contains x-ray scattering measurements of an optical diffraction grating created by etching a sample in which an image of the grating had been produced by photo-dissolution. Using a simple kinematical scattering theory it is possible to simulate the results obtained. Such analysis may have widespread use in solving a variety of surface structural problems.

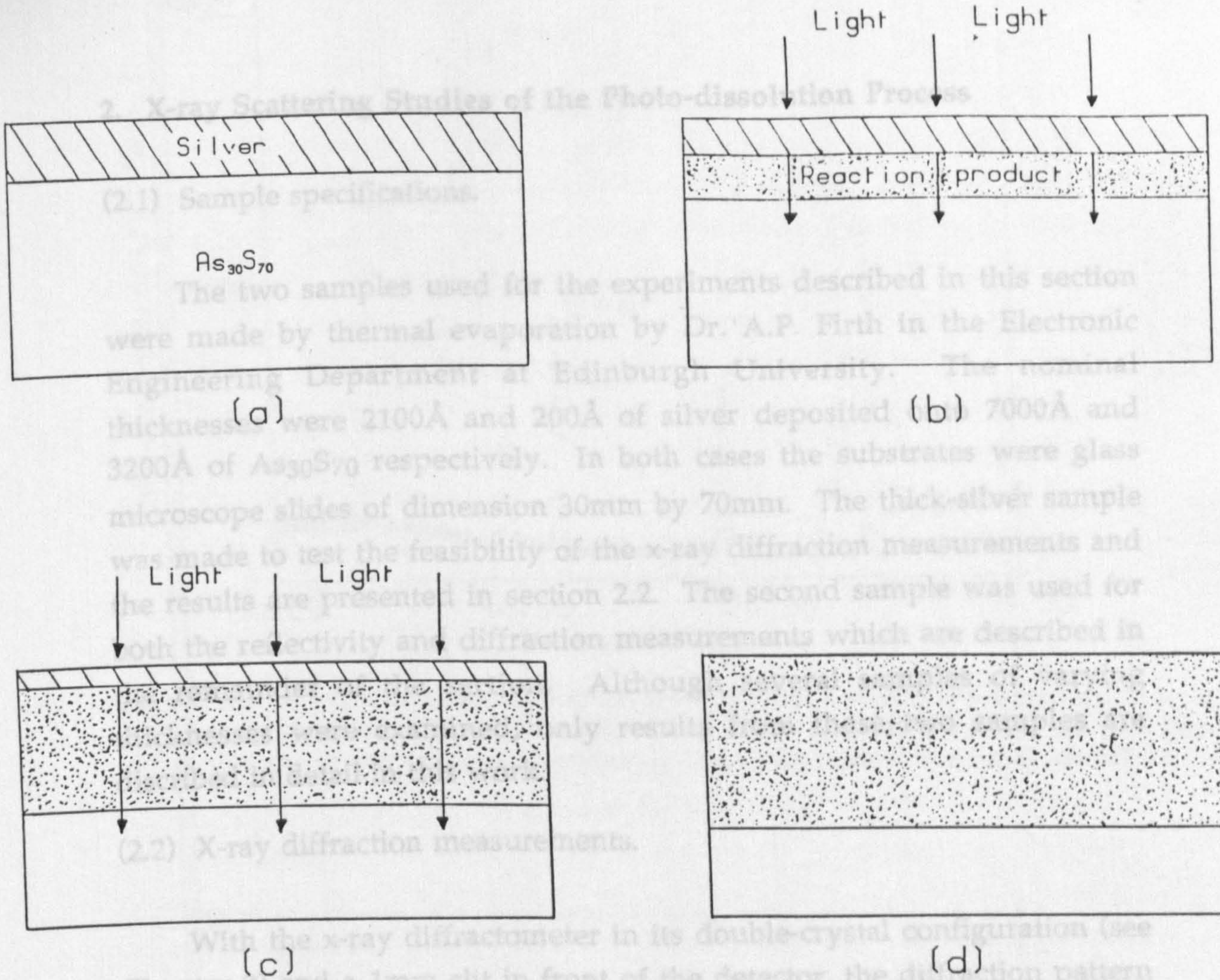

Figure 5.1. Schematic illustration of the photo-dissolution of a metal in a chalcogenide glass.

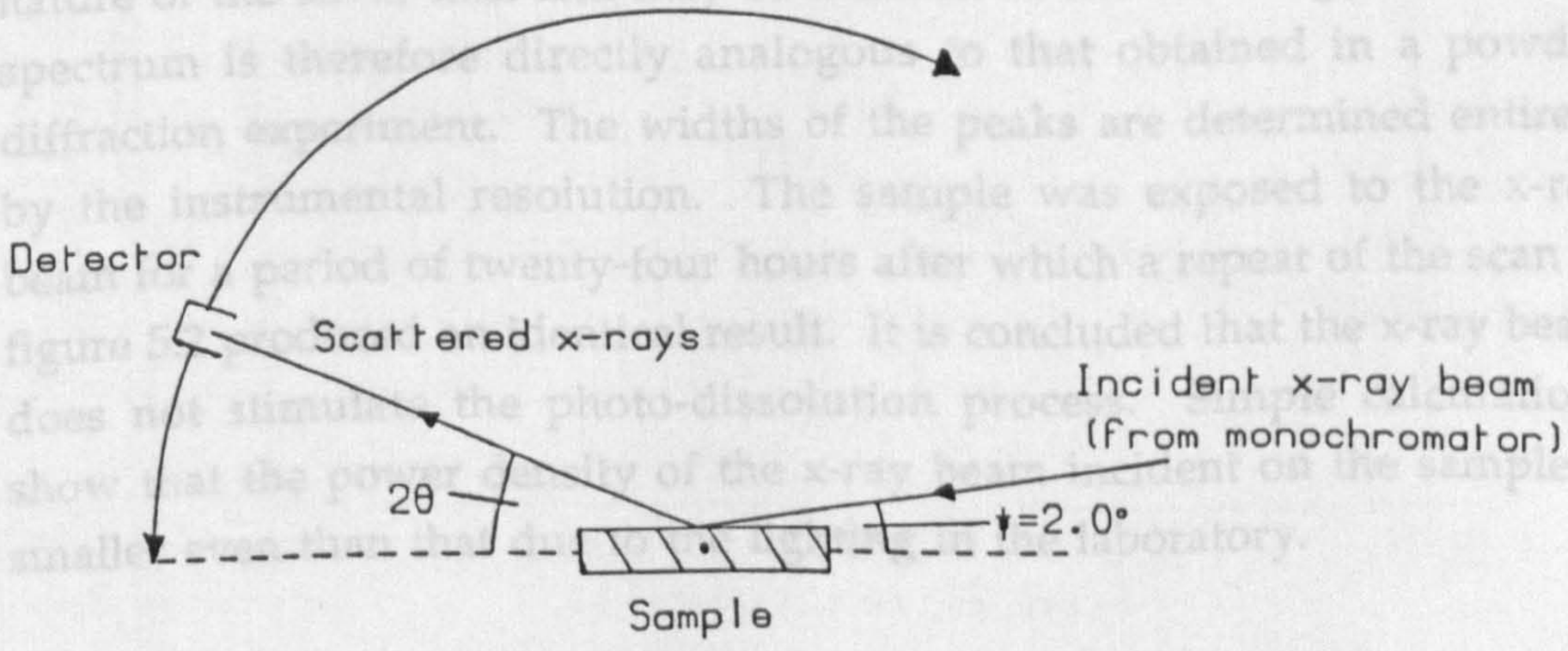

Figure 5.2. Schematic illustration of the experimental configuration for a 2-θ scan. A 1mm slit is placed in front of the detector.

2. X-ray Scattering Studies of the Photo-dissolution Process

(2.1) Sample specifications.

The two samples used for the experiments described in this section were made by thermal evaporation by Dr. A.P. Firth in the Electronic Engineering Department at Edinburgh University. The nominal thicknesses were 2100Å and 200Å of silver deposited onto 7000Å and 3200Å of $As_{30}S_{70}$ respectively. In both cases the substrates were glass microscope slides of dimension 30mm by 70mm. The thick-silver sample was made to test the feasibility of the x-ray diffraction measurements and the results are presented in section 2.2. The second sample was used for both the reflectivity and diffraction measurements which are described in the remainder of the section. Although several samples of varying thicknesses were examined, only results from these two samples are discribed in detail in this work.

(2.2) X-ray diffraction measurements.

With the x-ray diffractometer in its double-crystal configuration (see Chapter 2) and a 1mm slit in front of the detector, the diffraction pattern in figure 5.3 was obtained by scanning the detector arm (commonly referred to as a 2-θ scan) over a large angular range. This process is schematically illustrated in figure 5.2. The incident angle of the x-rays on the sample was fixed at $\psi = 2.0°$, giving an approximate 'beam footprint' measuring 5mm by 5mm, the vertical dimension being fixed by the pre-sample slit. The peaks in the spectrum arise due to the polycrystalline nature of the silver film and may be indexed as shown in figure 5.3. The spectrum is therefore directly analogous to that obtained in a powder diffraction experiment. The widths of the peaks are determined entirely by the instrumental resolution. The sample was exposed to the x-ray beam for a period of twenty-four hours after which a repeat of the scan in figure 5.2 produced an identical result. It is concluded that the x-ray beam does not stimulate the photo-dissolution process. Simple calculations show that the power density of the x-ray beam incident on the sample is smaller even than that due to the lighting in the laboratory.

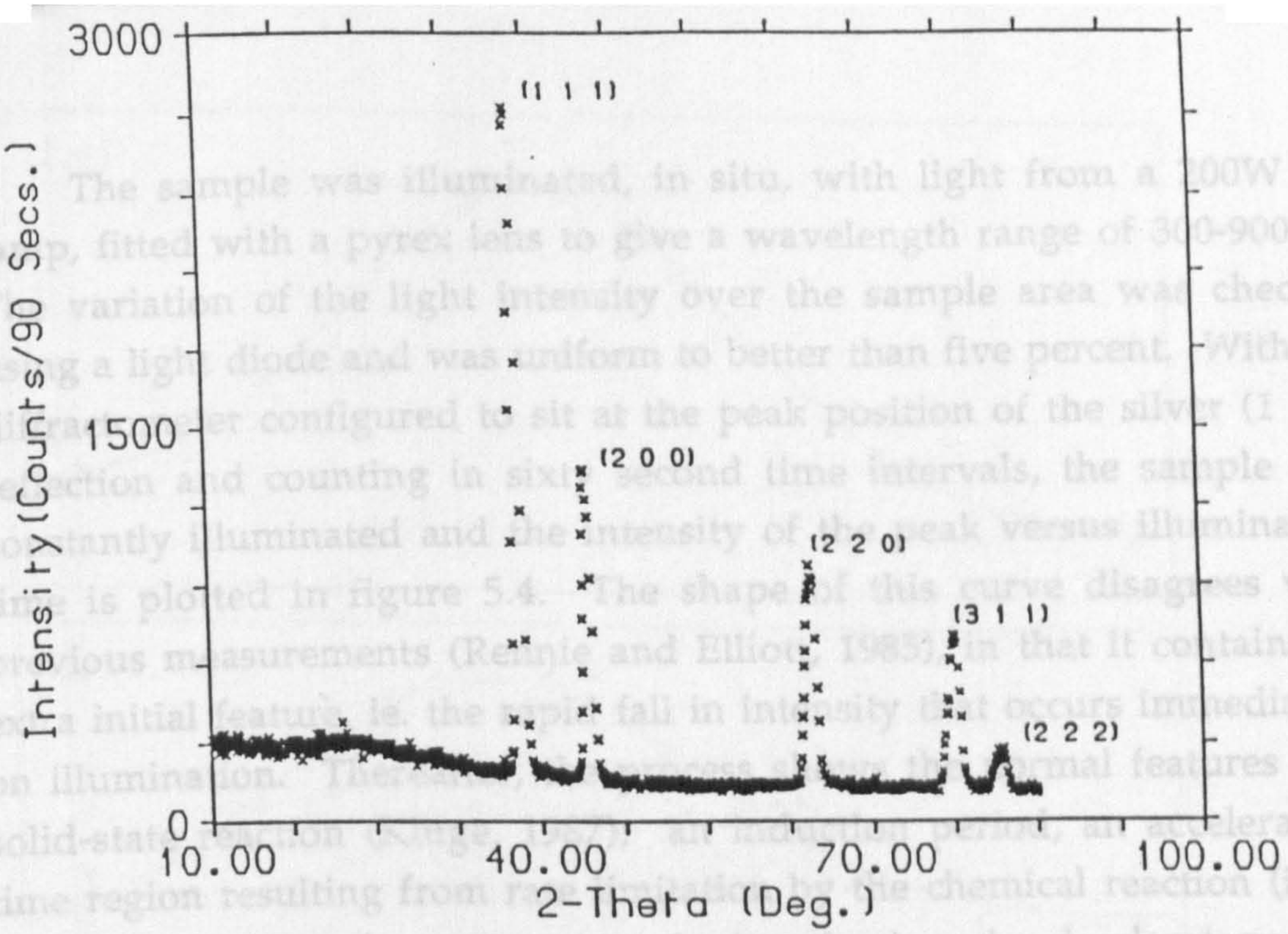

Figure 5.3. X-ray diffraction spectrum from the thick-silver/chalcogenide sample and an incident angle ψ=2.0°. The count time was 90 seconds/point. The diffraction peaks are indexed according to the silver lattice parameter, d=2.359Å.

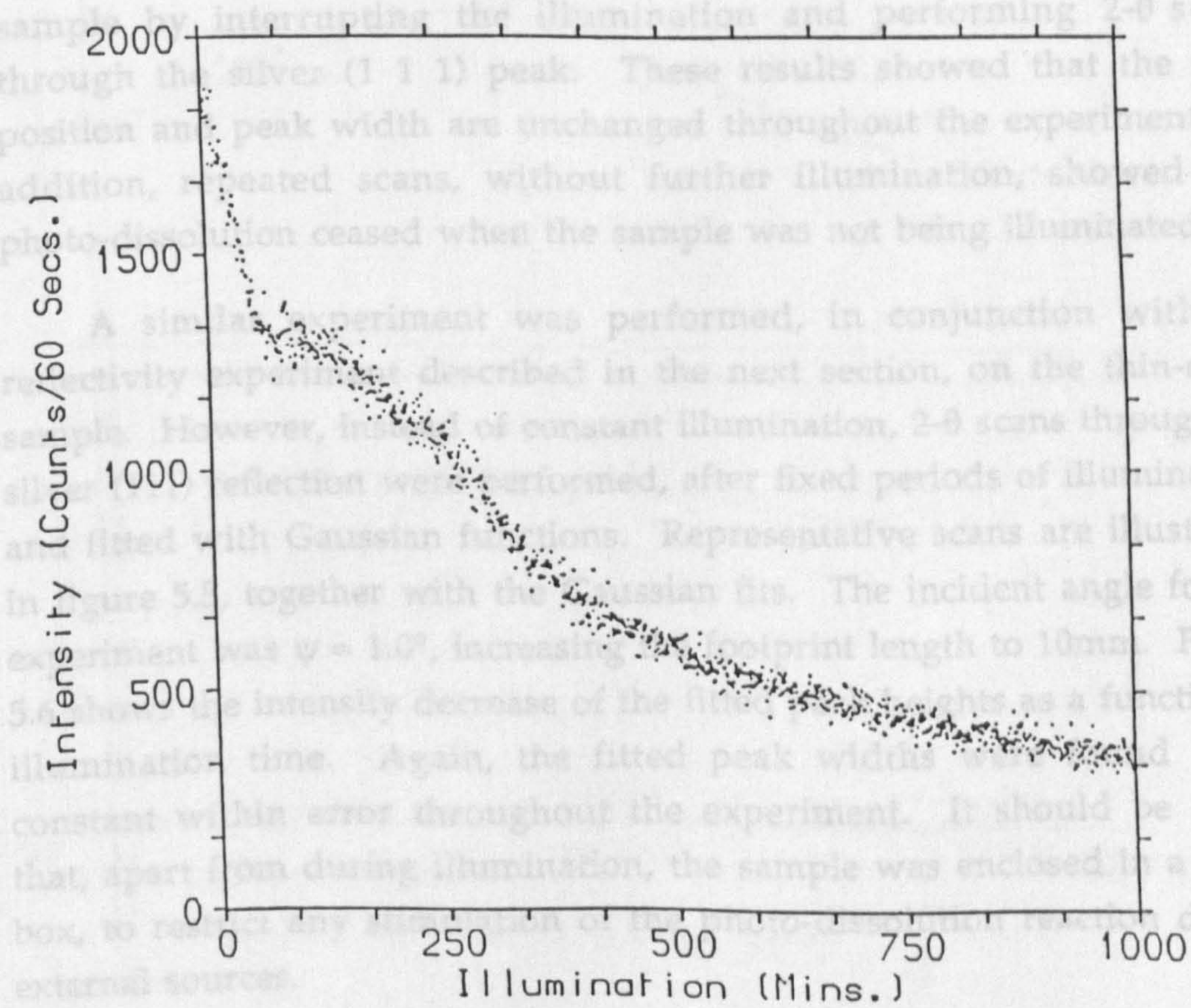

Figure 5.4. Variation in the peak intensity of the silver (1 1 1) reflection in figure 5.3 as a function of illumination time. The counttime was 60 seconds/point and the Hg lamp was used on a low intensity setting to facilitate the measurement.

The sample was illuminated, in situ, with light from a 200W Hg lamp, fitted with a pyrex lens to give a wavelength range of 300-900nm. The variation of the light intensity over the sample area was checked using a light diode and was uniform to better than five percent. With the diffractometer configured to sit at the peak position of the silver (1 1 1) reflection and counting in sixty second time intervals, the sample was constantly illuminated and the intensity of the peak versus illumination time is plotted in figure 5.4. The shape of this curve disagrees with previous measurements (Rennie and Elliott, 1985), in that it contains an extra initial feature, ie. the rapid fall in intensity that occurs immediately on illumination. Thereafter, the process shows the normal features of a solid-state reaction (Kluge, 1987); an induction period, an acceleratory time region resulting from rate limitation by the chemical reaction (ionic and electronic transfer processes at the interface), and a deceleratory time region due either to exhaustion of the silver layer or rate limitation by the physical transport processes of the reactants through the product layer. Possible explanations for the unexpected initial phase will be discussed in the next section. A control experiment was performed on a similar sample by interrupting the illumination and performing 2-θ scans through the silver (1 1 1) peak. These results showed that the peak position and peak width are unchanged throughout the experiment. In addition, repeated scans, without further illumination, showed that photo-dissolution ceased when the sample was not being illuminated.

A similar experiment was performed, in conjunction with the reflectivity experiment described in the next section, on the thin-silver sample. However, instead of constant illumination, 2-θ scans through the silver (111) reflection were performed, after fixed periods of illumination, and fitted with Gaussian functions. Representative scans are illustrated in figure 5.5, together with the Gaussian fits. The incident angle for the experiment was $\psi = 1.0°$, increasing the footprint length to 10mm. Figure 5.6 shows the intensity decrease of the fitted peak heights as a function of illumination time. Again, the fitted peak widths were found to be constant within error throughout the experiment. It should be noted that, apart from during illumination, the sample was enclosed in a black box, to restrict any stimulation of the photo-dissolution reaction due to external sources.

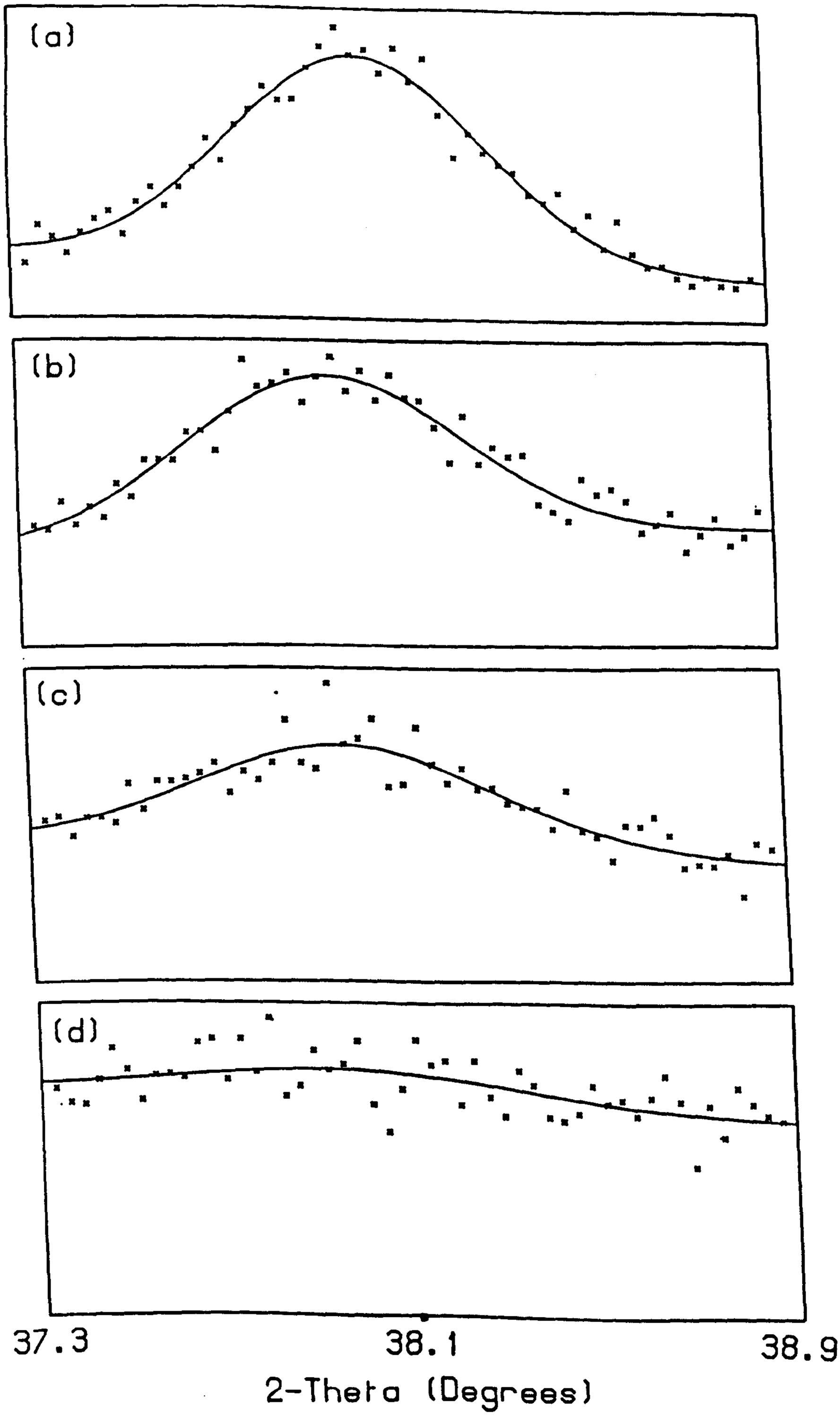

Figure 5.5. 2-θ scans through the silver (1 1 1) reflection after illumination time (a) 0 seconds (b) 160 seconds (c) 280 seconds and (d) 320 secs. The range of the vertical axis is adjusted in each scan and the count time was 90 seconds/point.

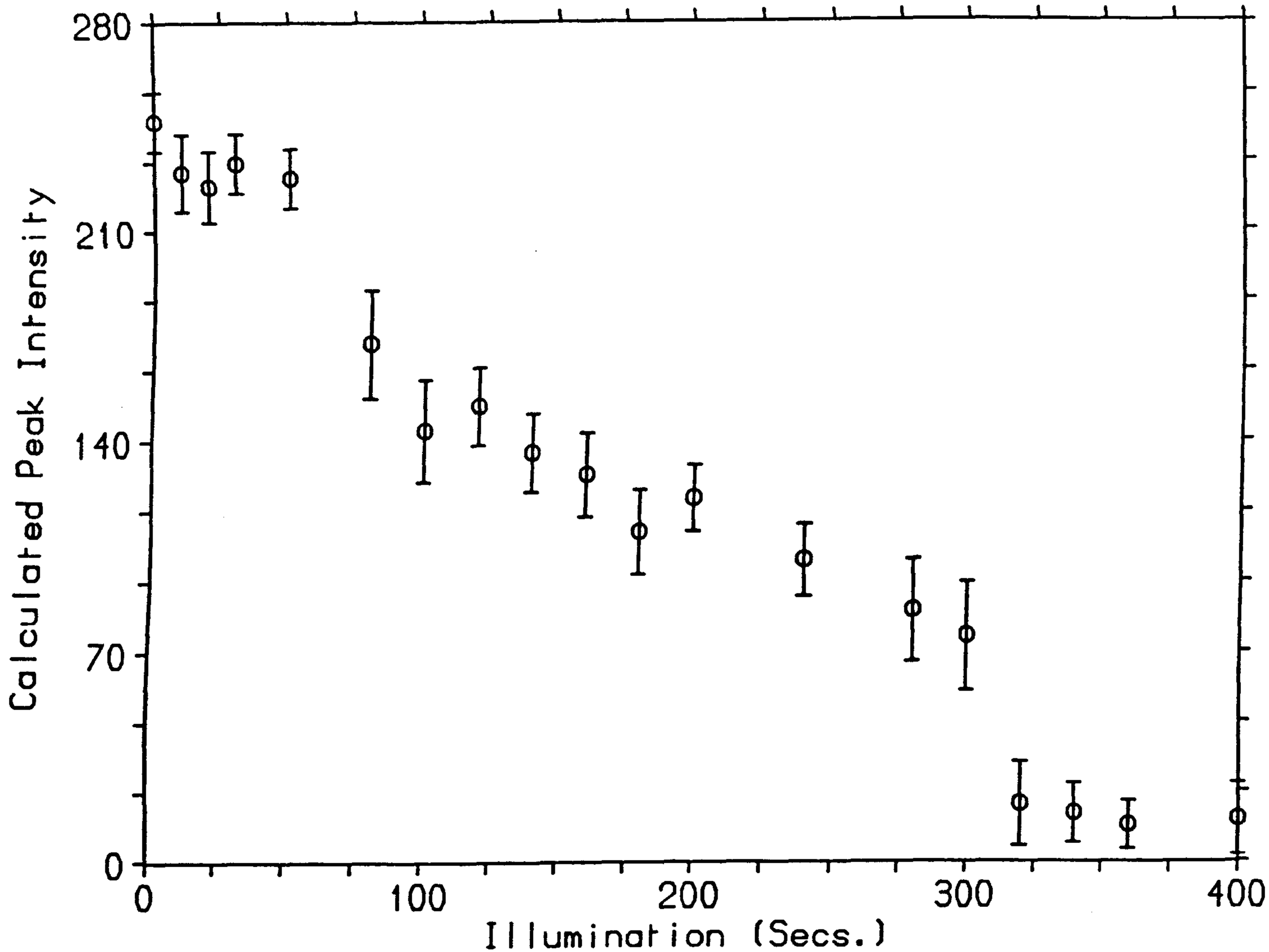

Figure 5.6. Variation in the fitted peak intensity of the silver (1 1 1) reflection for the thin silver sample. The points are background subtracted.

Several other samples were examined at a variety of stages during the photo-dissolution process and at no time were any additional peaks in the diffraction spectrum observed. It can be concluded that the reaction product is amorphous, containing no crystalline phases (Ewen, Taylor, Firth and Owen, 1983).

(2.3) X-ray reflectivity measurements.

Chapters 3 and 4 of this thesis have shown how x-ray reflectivity measurements may be used to obtain a detailed picture of the electron density profile as a function of depth into a sample. However, for measurements using a triple-crystal arrangement these experiments necessarily take a long time and this is undesirable for the study of a dynamic process such as photo-dissolution. Section 5 of chapter 2 explained that, providing a sample was of sufficient macroscopic quality, x-ray reflectivity measurements could be performed in the double-crystal diffractometer configuration, utilising a small slit in front of the detector, and yielding exactly the same results (see figure 2.18). For this reason, the reflectivity measurements described in this section were performed using a double-crystal arrangement, with a 0.15mm slit defining the angular acceptance range of the detector. The average time taken to record a reflectivity curve was approximately one and a half hours. A check of sample quality was performed at various stages during photo-dissolution, by rocking the crystal (ψ scan) at a fixed detector angle, and with the diffractometer in its triple-crystal configuration. As explained in chapter 3, such a scan contains information on the macroscopic quality of the sample.

Figure 5.7 is the reflectivity curve from the nominally 200Å silver/3200Å $As_{30}S_{70}$ sample prior to illumination and figure 5.8 is the corresponding ψ scan, at a detector angle ϕ = 1.0°, as described above. Figure 5.8 shows the sample to be of good macroscopic quality, the diffuse peaks are the so-called 'off-specular' peaks (Yoneda, 1963; Andreev, 1985) and were easily resolved from the main peak even in the double-crystal diffractometer configuration. These peaks are significantly smaller than the main specular reflection. The fit to the data in figure 5.7 was performed using the Parratt formulation described in Appendix II and yielded the parameters in table 5.1. A top-hat function, with a width

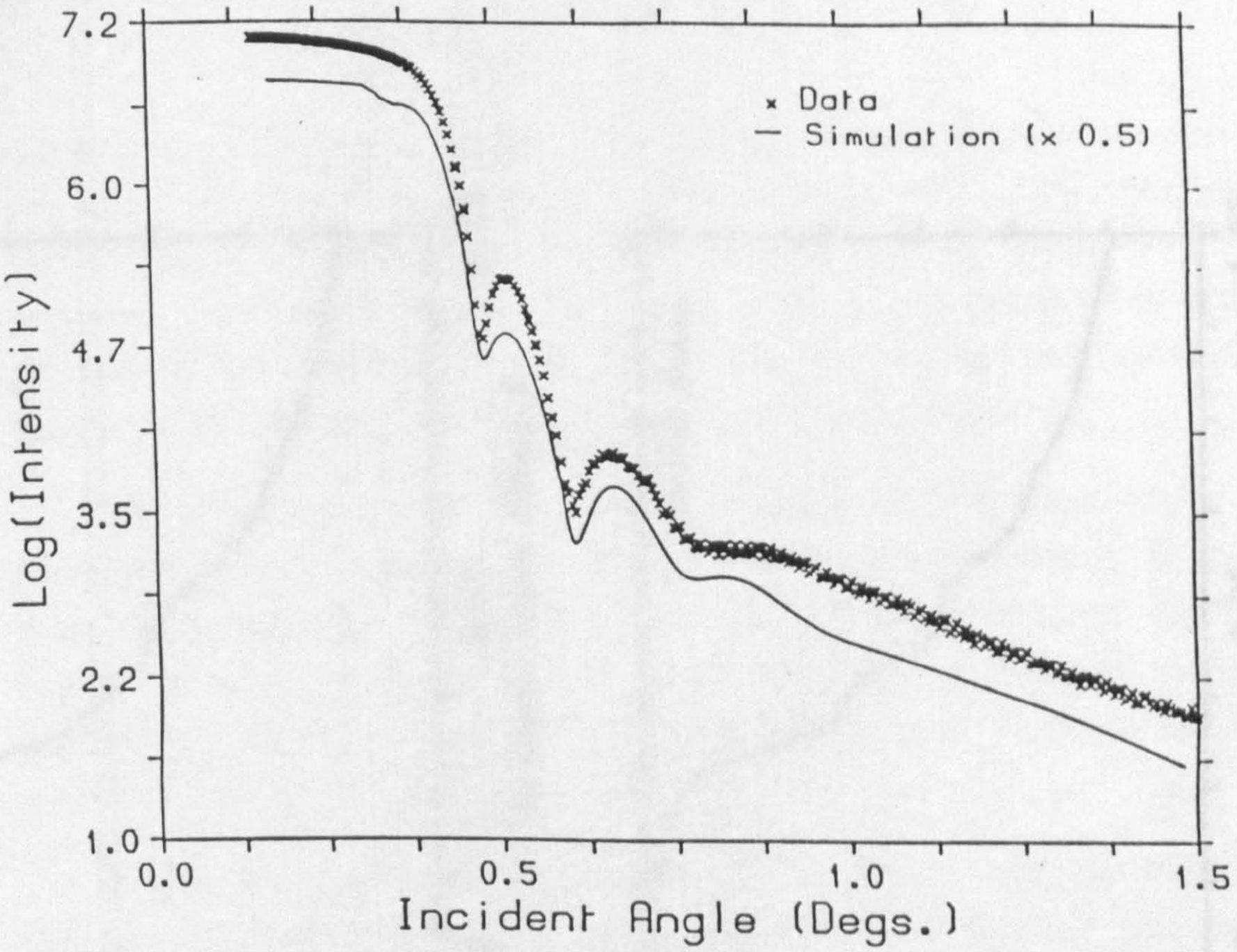

Figure 5.7. Reflectivity curve from the sample prior to illumination, plotted on a logarithmic scale against ψ. The simulation is displaced for clarity and is according to the parameters in Table 5.1.

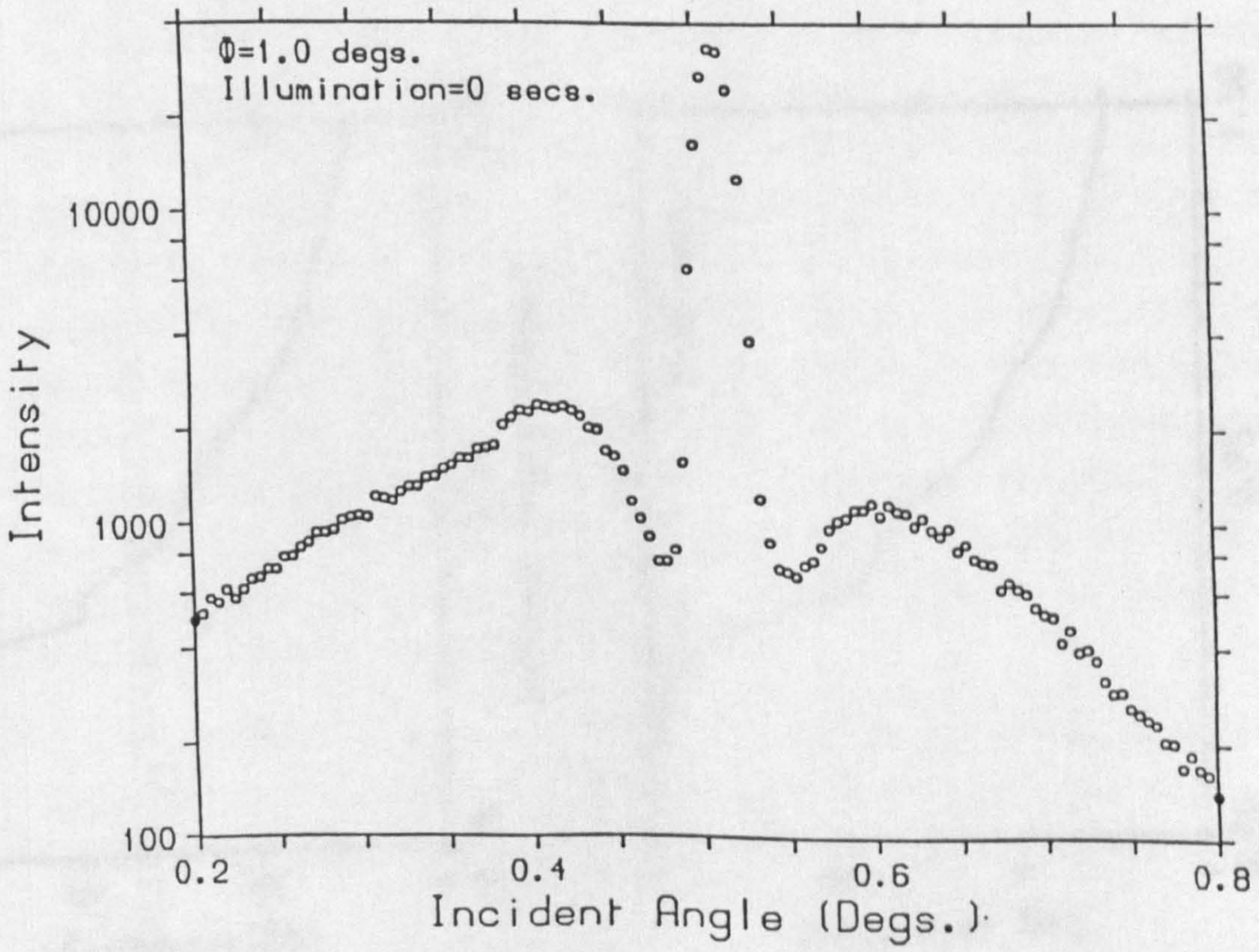

Figure 5.8. Triple-crystal ψ scan prior to illumination. The specular peak is resolution limited, showing the sample to be of good macroscopic quality. The additional peaks are manifestations of the 'off-specular' reflection at $\theta_i \approx 0.4°$ and $\theta_{exit} \approx 0.4°$.

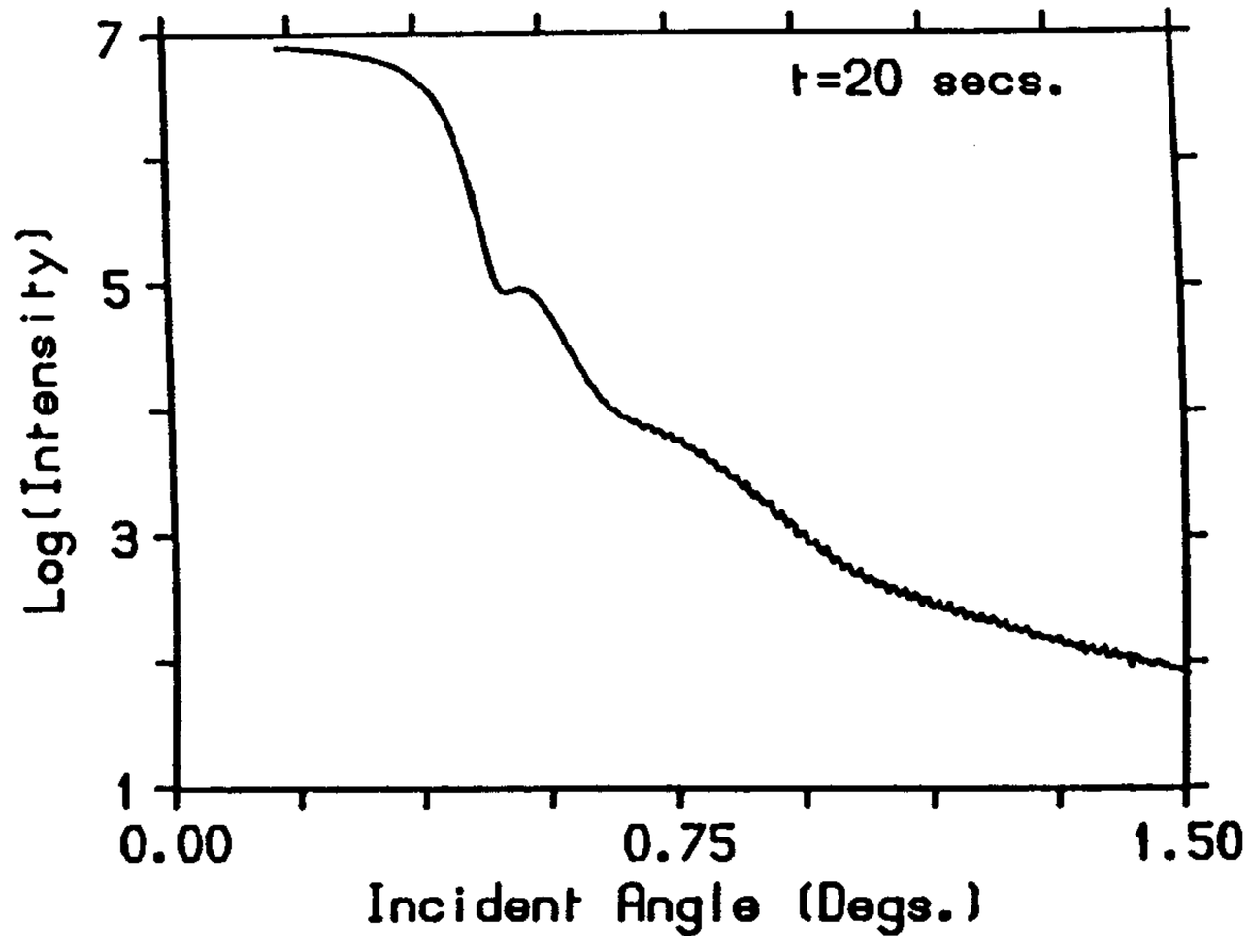

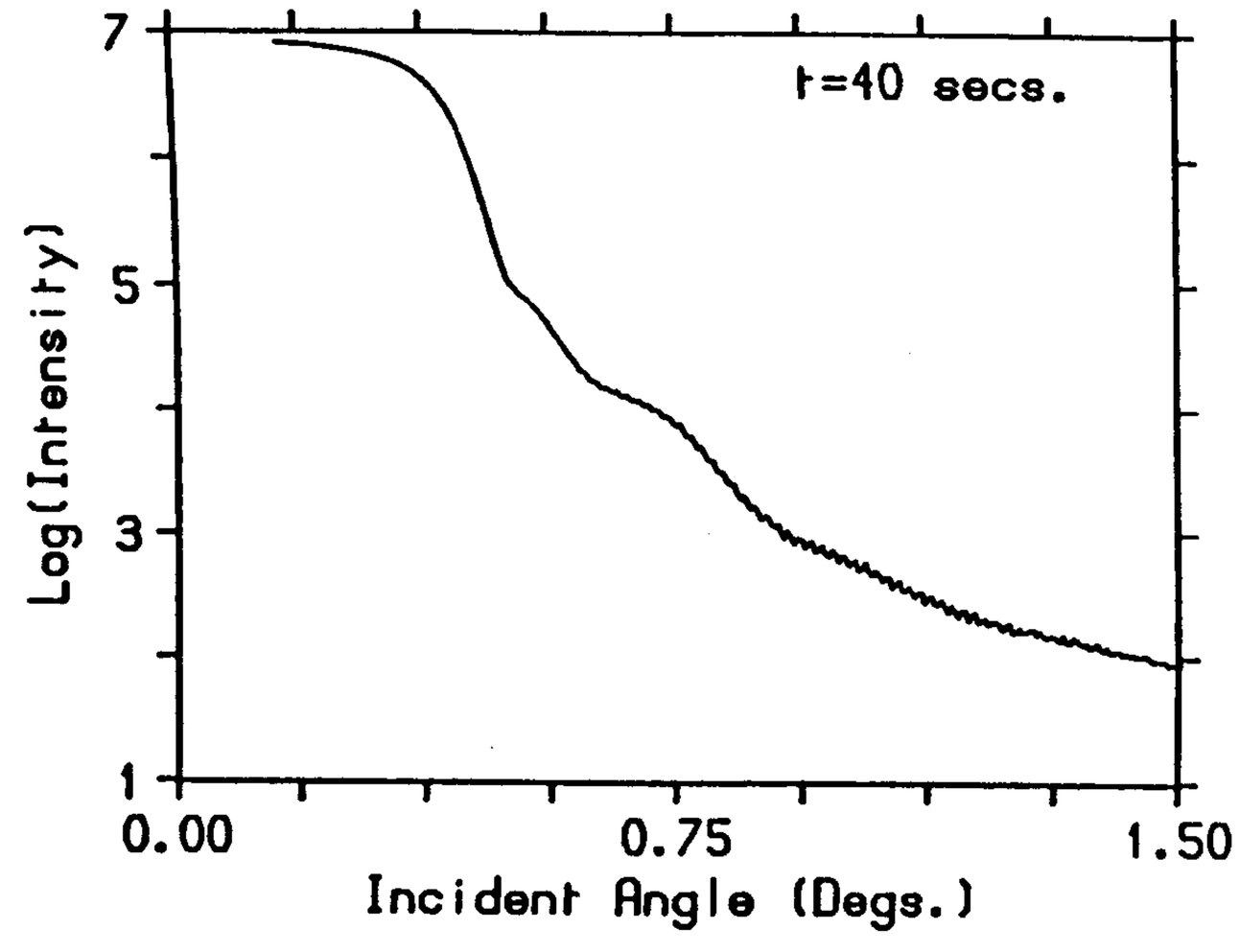

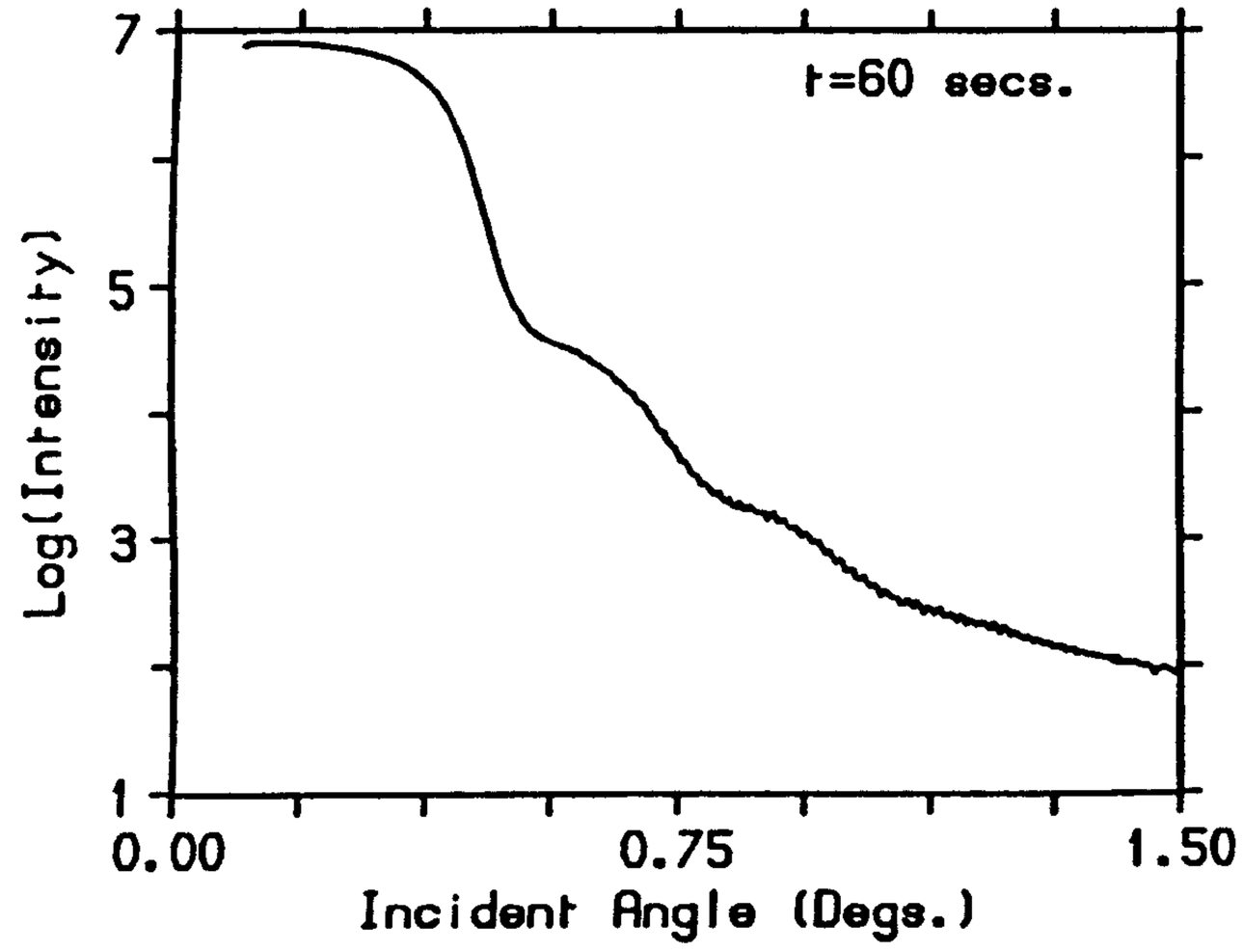

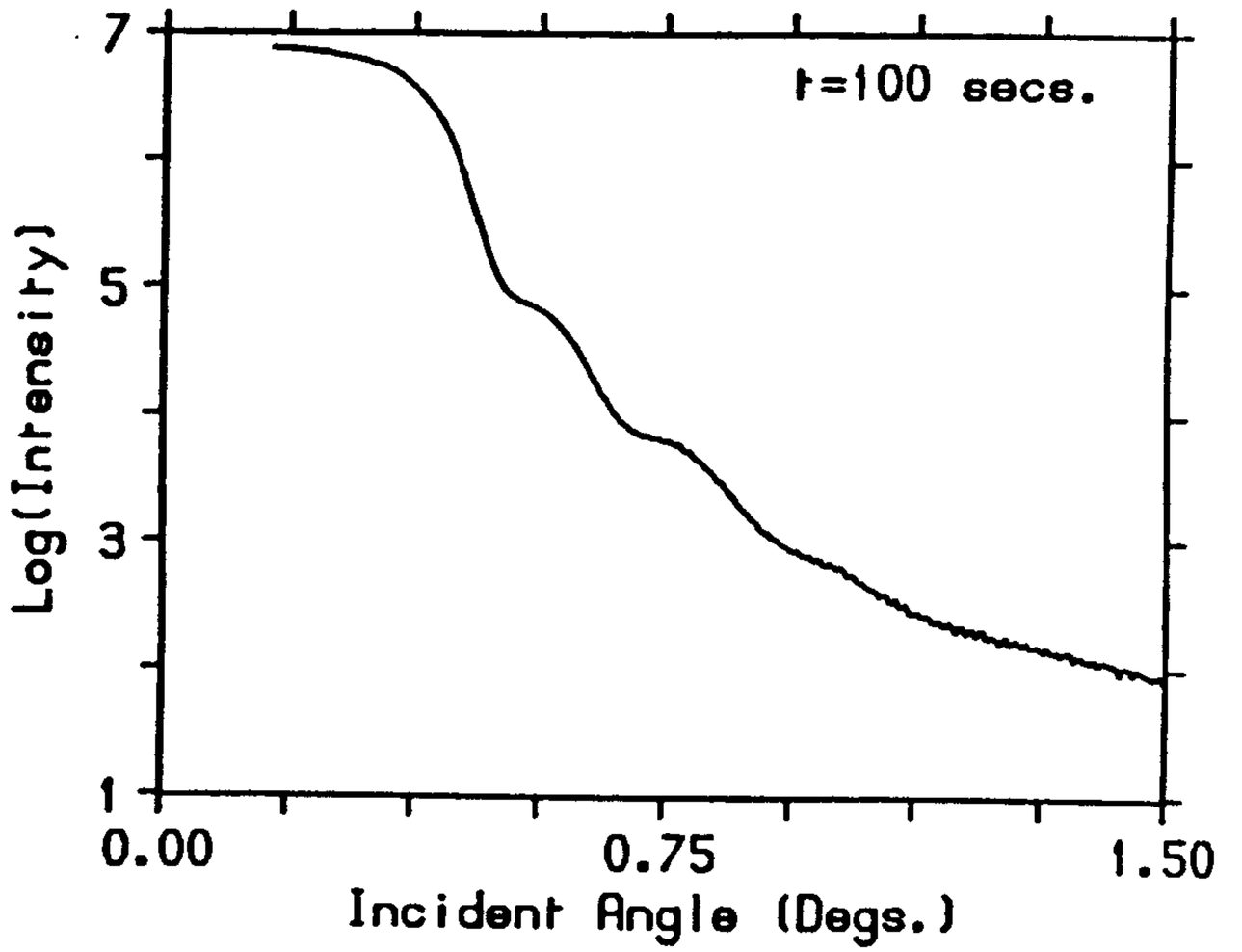

Figures 5.9. Double-crystal reflectivity curves as a function of illumination time, t. No significant new oscillation, caused by a well-defined reaction product layer, is observed. Attempted simulations of the data are discussed in detail in the text.

defined by the angular acceptance range of the slit, was convoluted with the data as an approximation to the resolution, effectively blurring the high frequency fringes which are expected from the thick $As_{30}S_{70}$ film. In addition to the silver layer, a thin extra layer, is also required in order to produce a reasonable fit to the data. The parameters indicate that the surface of the crystal is rough, probably due to oxidation.

The experiment was performed by illuminating the sample for a fixed period and then repeating the reflectivity measurements, diffraction peak measurements (figures 5.5 and 5.6) and in some cases the triple-crystal ψ scan, as in figure 5.8. The reflectivity results at increasing illumination times are shown in figures 5.9 up to an illumination time t = 100 seconds.

Beginning with the parameters in table 5.1 and introducing a reaction product layer into the reflectivity model, an attempt was made to fit the reflectivity curves by varying the interface roughnesses, composition and thickness of the reaction product layer. This would be according to the model of photo-dissolution schematically illustrated in figure 5.1. The approximate density of the reaction product layer was known from optical measurements (Firth, 1987). Attempts at fitting successive reflectivity curves by varying the expected parameters were unsuccessful, and only when the density of the silver layer was varied could reasonable fits to the curves be achieved. Qualitatively this is seen in the reduction in amplitude of the fringes originating in the silver layer. Although a slight reduction in the thickness of the silver appears to be observed, there is no new oscillation superimposed on the pattern, as expected if a well-defined product layer is formed. The silver is known to combine in a ratio of 3:1 with the chalcogenide, so a reduction in the thickness of the silver layer would generate a product layer with a thickness of approximately four times this reduction. No effect of this is seen in the first 100 seconds of illumination time, although the diffraction measurements in figure 5.6 indicate that a significant quantity of crystalline silver has reacted.

As no well defined product layer appears to be forming in the initial stages of photo-dissolution, it is possible that the silver moves into the chalcogenide under a diffusion-type process. This would create a

	Thickness (Å)	ρ/ρ_s	Roughness σ (Å)
Layer 1 (oxide)	23±3	0.7±0.3	5.4±1.0
Layer 2 (silver)	184±10	4.3±0.5	23.6±3.0
Layer 3 ($As_{30}S_{70}$)	3200 (fixed)	1.3 (fixed)	6.1±2.0
Substrate (glass)		1.0	33.0±10.0

Table 5.1. Results of least-squares fit to the reflectivity data of figure 5.7, using a three-layer model and the Parratt formulation of scattering theory described in Appendix II.

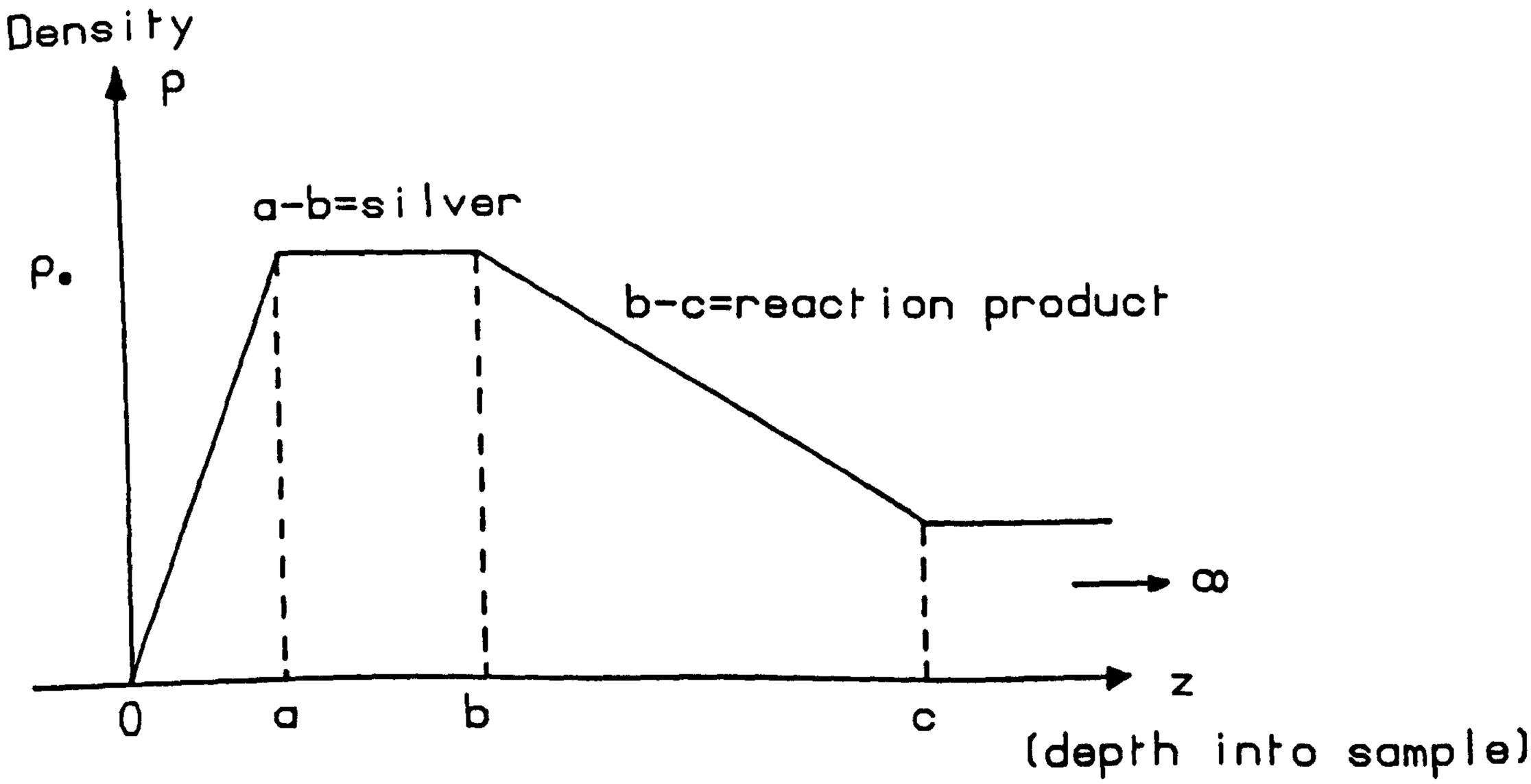

Figure 5.10. A graded density profile of the sample as used for calculations of the reflectivity using the 'master formula'. This would represent a diffusion type process in the sample.

gradually varying electron density profile, conflicting with the reflectivity model of discrete, homogeneous dielectric slabs. Although it is possible to break down such a gradient into a series of discrete steps in order to perform an exact calculation (Pomerantz and Segmüller, 1980), it is more convenient to use the kinematical scattering model described in Appendix II. Using the 'master formula'

$$\frac{R(Q_z)}{R_F(Q_z)} = \left|-iQz\int\rho(z)e^{iQ_zz}dz\right|^2$$

with the density model in figure 5.10, a series of reflectivity curves according to a variation in the parameters of figure 5.10 were simulated, but comparison with the data still showed poor agreement in fitting consecutive profiles with physically realistic parameters. Reflectivity depends solely on the electron density $\rho(z)$ averaged over the surface plane directions, and so it must be possible to fit the data with an electron density, $\rho(z)$, function. However, there is much ambiguity in choosing a function to fit the data unless many of the parameters, in this case the silver, chalcogenide and reaction product densities, can be fixed. Without varying these parameters or complicating the model by introducing several additional layers, no reasonable fits to the data could be obtained.

As the illumination time increases beyond t = 100 seconds a layer appears to be forming, as indicated by the fringes in figures 5.11 which go to higher frequency with increasing illumination time. This indicates the thickening of a layer in the sample until, at t = 320 seconds, the frequency of the fringes is 3-4 times that of the frequency observed in the initial reflectivity curve. It therefore appears that a well-defined reaction product layer has formed, with a thickness slightly smaller than that expected after complete exhaustion of the silver. At t = 320 seconds the diffraction measurements (figures 5.6) indicated that the silver layer was exhausted, but illumination was continued up to t = 600 seconds. This extra illumination caused the disappearance of the fringes in the reflectivity data.

Before considering a model of photo-dissolution it is interesting to examine the ψ scans that were performed at t = 80, 160, 240 and 600 seconds. These are illustrated in figures 5.12. At t = 80 seconds the scattered distribution is identical to figure 5.8. The spectrum consists of a

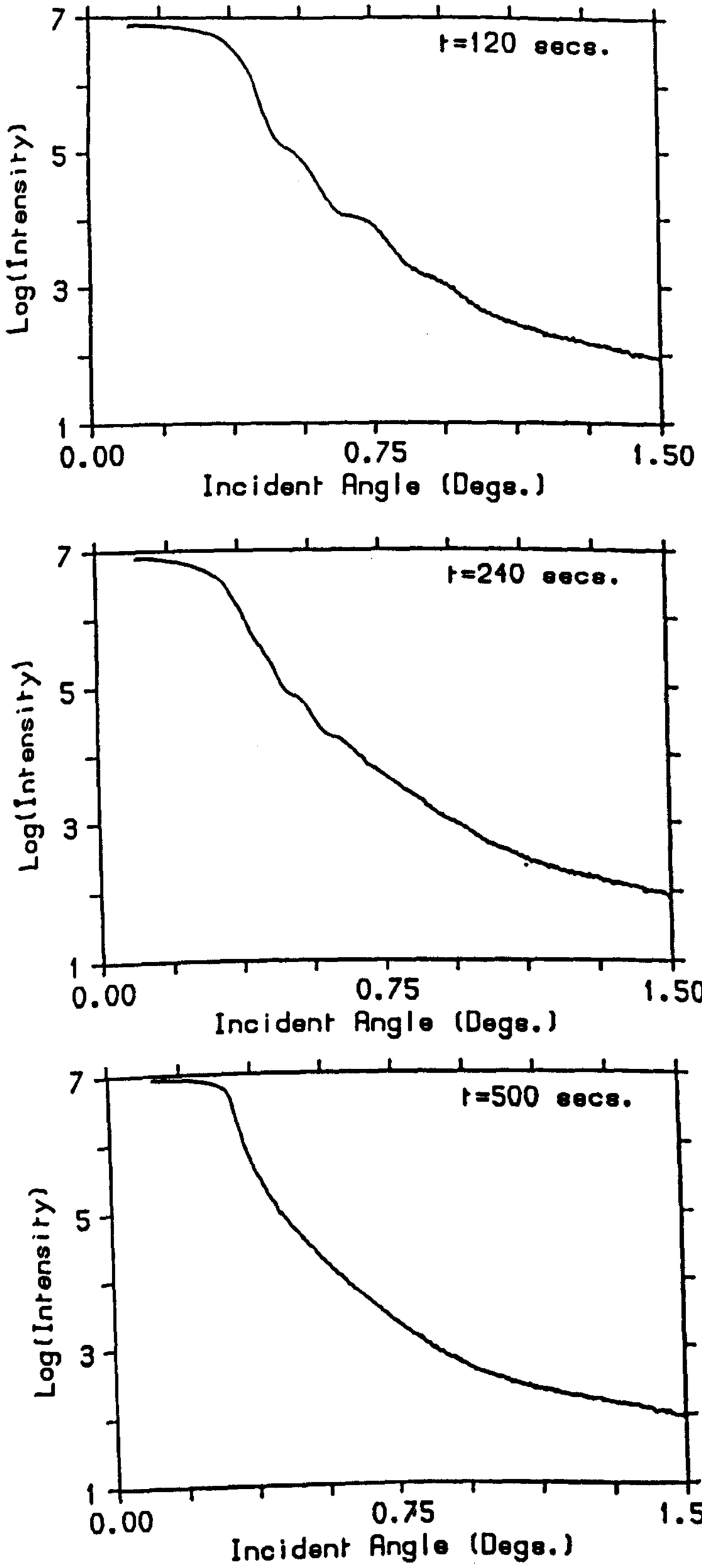

Figures 5.11. Double-crystal reflectivity curves as a function of illumination time, t, up to the conclusion of the experiment. Oscillations of higher frequency are seen to appear up to t=320 seconds. At this point the diffraction measurements (figure 5.6) indicate that most of the silver layer has photo-dissolved. Further illumination causes these fringes to disappear.

resolution-limited specular component and two off-specular peaks. These off-specular peaks occur when the incident angle or the scattering angle with respect to the surface are equal to the critical angle of the sample material. Their behaviour can be described within the Distorted-Wave Born Approximation to scattering theory, as explained in chapter 3. These features are enhanced by departure from an average electron density in the sample, for example, surface roughness or sample defects (Sinha, Sirota, Garoff and Stanley, 1988). At t = 160 seconds and in subsequent scans there is a diffuse component, as well as the specular component, in the distribution. Indeed, at t = 160 seconds and t = 240 seconds, it is conceivable that there are two diffuse components in the spectrum. This is not a manifestation of the off-specular reflection, which can only occur at angles less than or equal to the critical angle of silver (ψ_c=0.4°), and is clearly resolved in figure 5.8. Figure 5.13 shows a two-dimensional map of the scattered x-rays in the region of the specular reflection, at t = 320 seconds. The $Q_\perp$ axis, wave-vector transfer perpendicular to the surface normal, is expanded by 100 to show the details of the distribution. The separation of the off-specular peaks is clearly seen, as is the broad diffuse component, centred on the specular peak, and showing an increase in width as $Q_{||}$ increase.

Although there is insufficient data to attempt a complete analysis of the mechanism causing the diffuse scattering, it is interesting to look for similar features in other experimental work. Low-energy electron diffraction (LEED) has been used to examine the growth of steps on surfaces during crystal deposition and this is known to give a diffuse component to the diffracted beam (Henzler, 1984; Lent and Cohen, 1984; Pukite, Lent and Cohen, 1985). A random distribution, such as that which occurs in an islanding process, gives rise to similar scattering distributions to those of figures 5.12 (Kruger, Savage and Lagally, 1989). Andrews and Cowley (1985) calculated the scattering that arises from correlated fluctuations in the surface position, due to, for example, a frozen-in surface acoustic wave or a step surface, and this also produced a diffuse component to the scattered spectrum. The appearance of the diffuse component in figures 5.12 therefore suggests that preferential structure, such as islands, are forming in the sample surface during the photo-dissolution reaction. The results are analogous to small-angle scattering

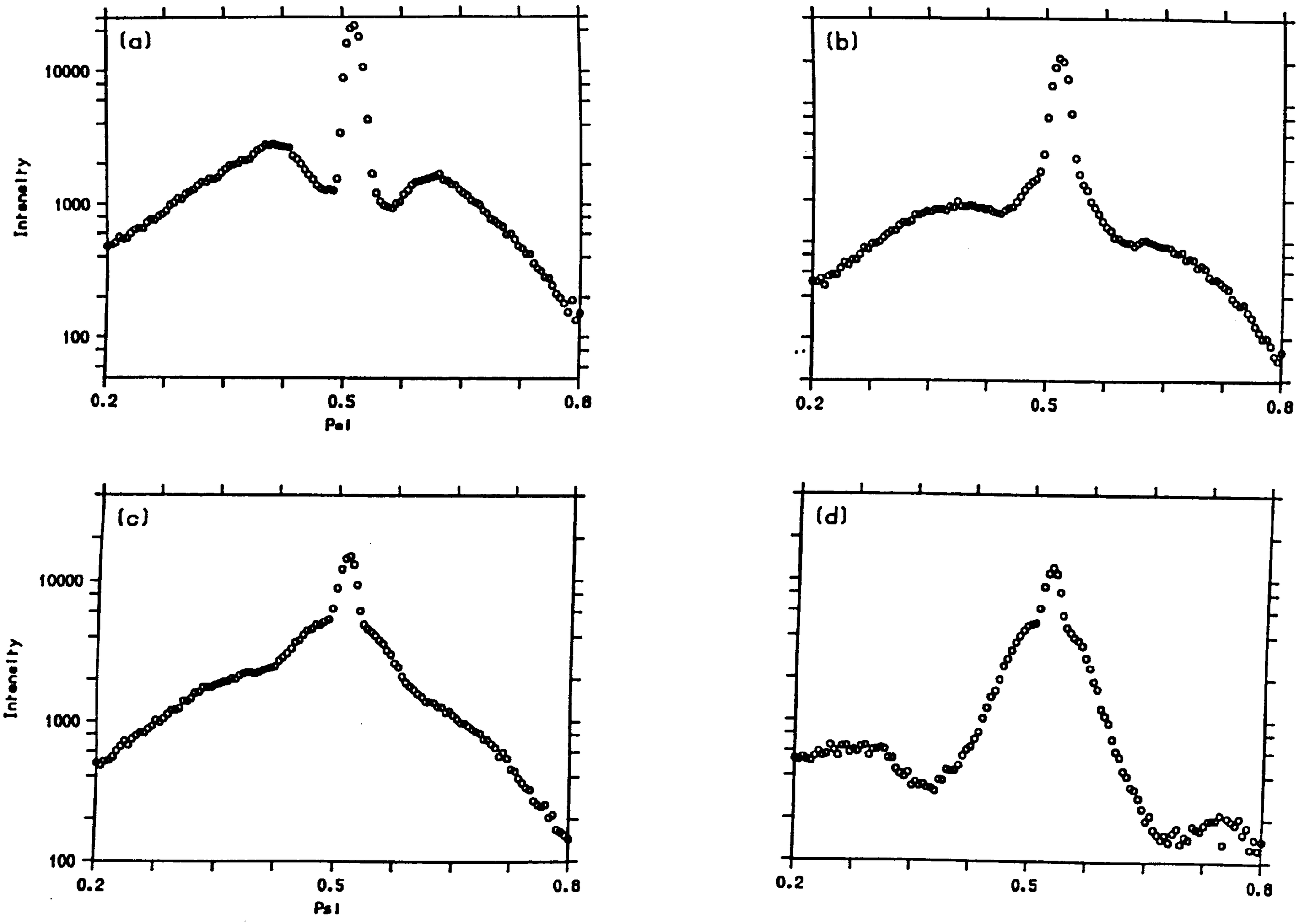

Figure 5.12. Triple-crystal ψ scans as in figure 5.8 at illumination times (a) t =80 seconds (b) t = 160 seconds (c) t = 240 seconds and (d) t = 600 seconds. In addition to the specular peak a diffuse component in the spectrum is also observed. This is not caused by the 'off-specular' reflection.

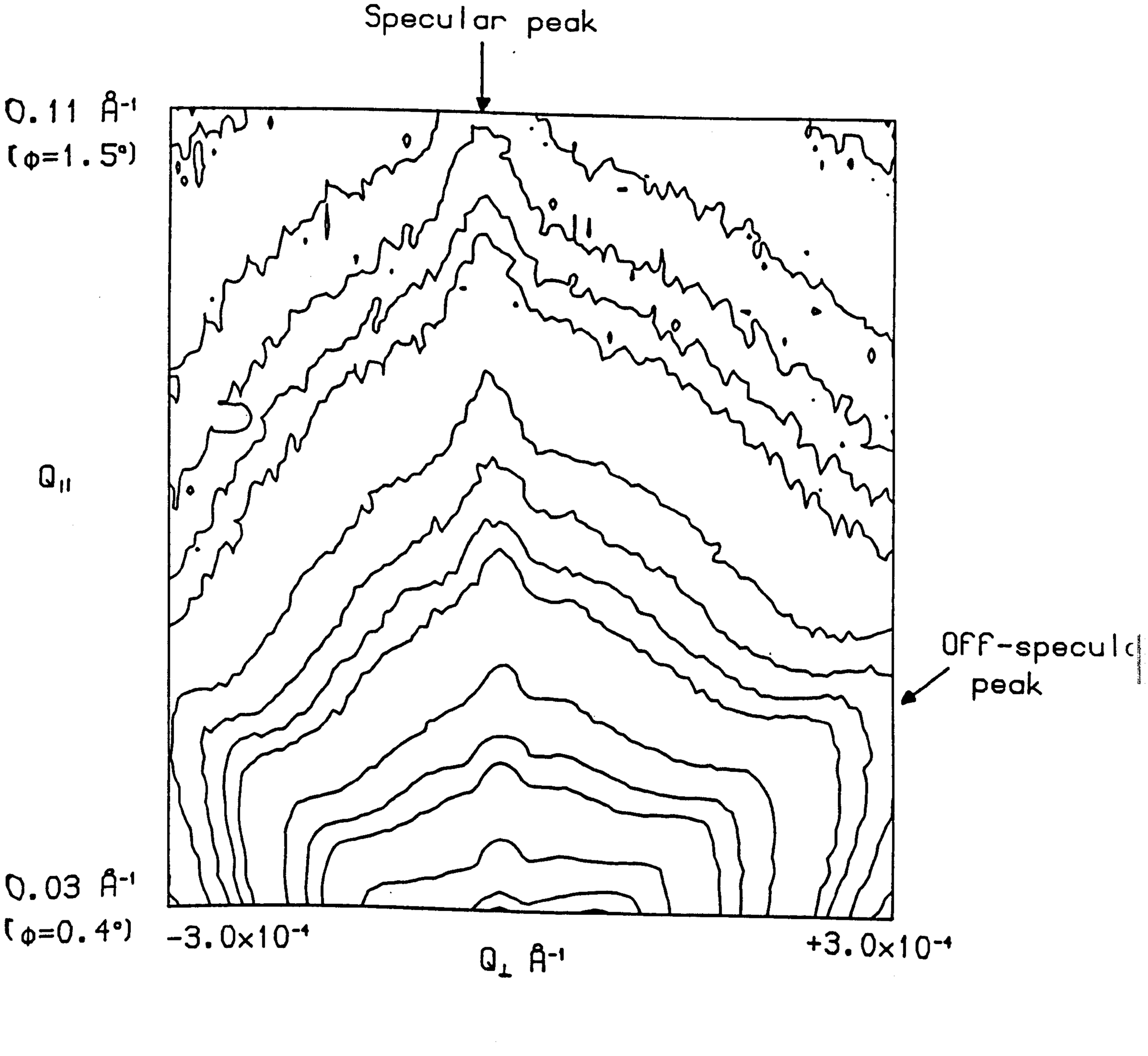

Figure 5.13. An isointensity contour plot of the observed x-ray scattering in the region of the specular reflection. The $Q_\perp$ axis is expanded by 100 to show the main features of the distribution. Peaks due to the off-specular reflection are seen to separate at low $Q_\parallel$.

experiments from clusters, where the width of the scattering (in the $Q_\perp$ direction) is directly related to the cluster size.

(2.4) A structural model for photo-dissolution.

The inability to obtain reliable fits to the reflectivity data using the model for photo-dissolution shown in figure 5.1 indicates that a more disordered process is occurring. This is supported by the appearance of a diffuse component in the scattered intensity, appearing between t = 80 seconds and t = 160 seconds, when, from figure 5.6, approximately half of the silver has photo-dissolved. Even after prolonged exposure, t = 600 seconds, there is still a large diffuse component. From the x-ray reflectivity data it appears that during the initial stages of photo-dissolution (figures 5.9) no well-defined product layer is formed, although when the silver layer has been exhausted (t = 320 seconds) there is strong evidence of a reaction product layer (figure 5.11), with a thickness which is similar to the expected value predicted from its composition. This layer disappears with increasing illumination.

On the basis of these experimental results, the structural model of the photo-dissolution process, illustrated in figure 5.14 is proposed. Initially photo-dissolution occurs through grain boundaries or voids in the silver film, causing a decrease in the electron density of the silver layer and forming uneven areas of reaction product. This is a slow process due to the limited area of silver available for reaction, hence the observed induction period (t≈50 seconds) in figure 5.6. As the reaction proceeds at a quicker rate silver islands are formed, causing the diffuse scattering which appears at this stage. Simultaneously, the reaction product layer begins to even out, giving rise to the oscillations in the reflectivity curves (figures 5.11). At t = 320 seconds, the diffraction measurements indicate that most of the silver has disappeared, and the presence of a thick, well-defined product layer is indicated in the reflectivity data. Silver, or possibly silver-oxide islands remain at the surface, causing the diffuse scattering in figures 5.12. Upon further illumination, silver in the reaction product layer moves into the unreacted chalcogenide region in a diffusion-type process, thus destroying the sharpness of the reaction product/chalcogenide interface. Evidence of this secondary process has been seen in optical measurements (Ewen,

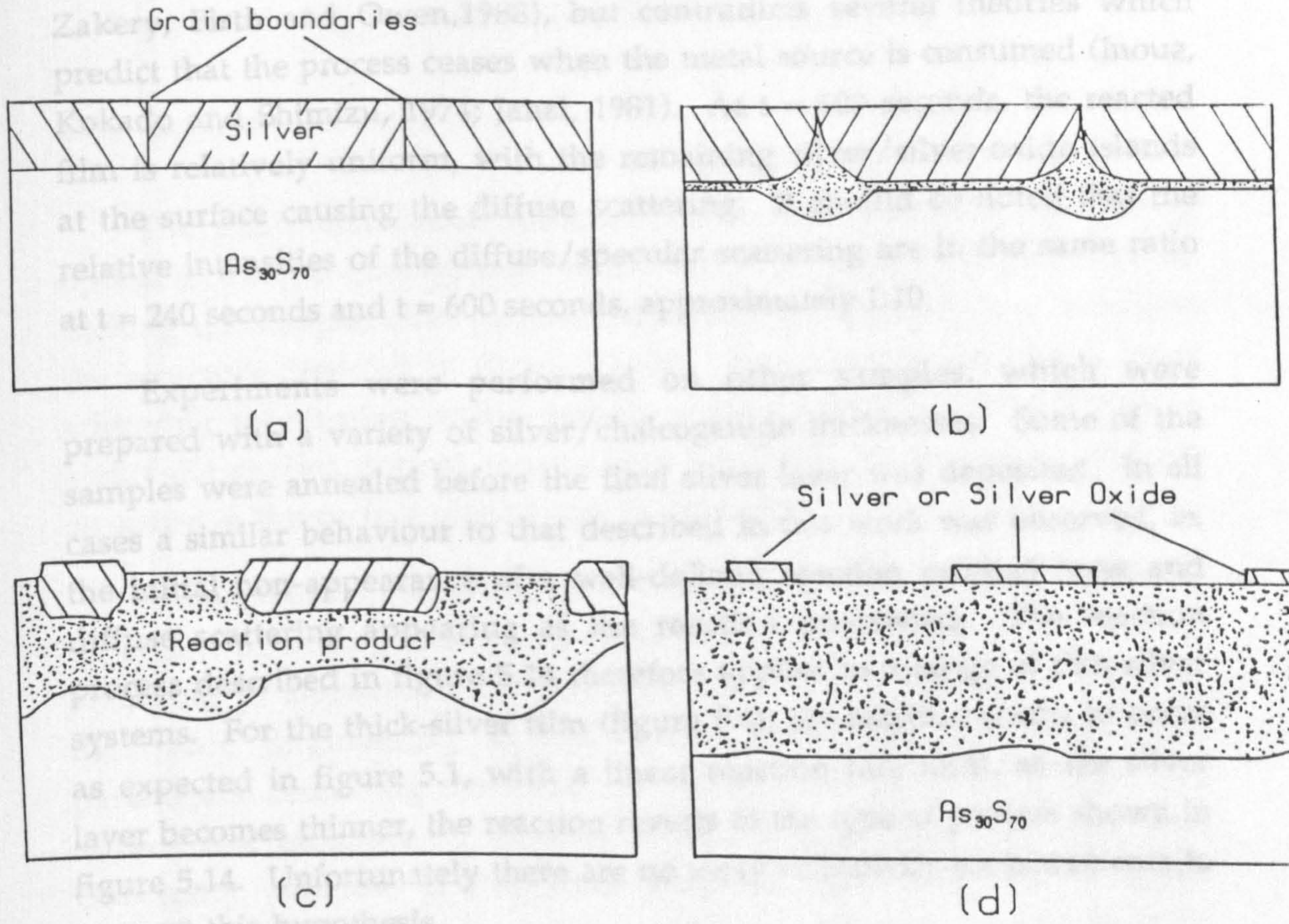

Figure 5.14. A schematic illustration of the proposed evolution of the photo-dissolution process. The figures correspond to the experimental results at (a) t = 0 seconds (b) t = 60 seconds (c) t = 160 seconds (d) t =320 seconds and (e) t = 600 seconds. The link between the experimental results and this model is described in section (2.5).

Zakery, Firth and Owen,1988), but contradicts several theories which predict that the process ceases when the metal source is consumed (Inoue, Kokado and Shimizu, 1974; Janai, 1981). At t = 600 seconds, the reacted film is relatively uniform, with the remaining silver/silver-oxide islands at the surface causing the diffuse scattering. It should be noted that the relative intensities of the diffuse/specular scattering are in the same ratio at t = 240 seconds and t = 600 seconds, approximately 1:10.

Experiments were performed on other samples, which were prepared with a variety of silver/chalcogenide thicknesses. Some of the samples were annealed before the final silver layer was deposited. In all cases a similar behaviour to that described in this work was observed, ie. the initial non-appearance of a well-defined reaction product layer and diffuse scattering appearing as the reaction proceeded. The reaction process described in figure 5.14 therefore applies to a range of thin-silver systems. For the thick-silver film (figure 5.4), the reaction seems to occur as expected in figure 5.1, with a linear reaction rate until, as the silver layer becomes thinner, the reaction reverts to the type of process shown in figure 5.14. Unfortunately there are no x-ray reflectivity measurements to support this hypothesis.

In conclusion, the x-ray measurements indicate that photo-dissolution in thin silver/chalcogenide films procedes through an islanding process. When the silver layer has been exhausted a well-defined reaction product layer is present, which is then destroyed in a secondary diffusion-type reaction. These results are important, if high-resolution micro-lithography is to be successful in producing devices with nanometer-scale features. Although the measurements are incomplete, for example a full study of the diffuse scattering would be interesting, the complimentary information obtained from the three x-ray techniques helps to create a microscopic structural picture of the photo-dissolution reaction.

3. X-ray Scattering from an Optical Diffraction Grating

(3.1) Experimental details.

The photo-dissolution reaction is an ideal process for preparing optical diffraction gratings and the method is illustrated in figure 5.15 (a). Etching the sample, after photo-dissolution has occurred, then produces the structure depicted in figure 5.15(b). Using grazing-incidence x-ray scattering to examine such a sample should provide information both about the surface normal composition (10-1000Å in thickness), and the structure in the surface plane (~μm in thickness).

A thin film sample, nominally 700Å silver/2000Å $As_{30}S_{70}$, deposited on a glass microscope slide, was made into an optical diffraction grating, according to the method illustrated in figure 5.15, in the Department of Electronic Engineering at Edinburgh University. The nominal parameters describing the structure are shown in figure 5.15(b). The sample was mounted on the triple-crystal diffractometer at Edinburgh University with the grating lines perpendicular to the plane of the incident and scattered x-ray beams. With the instrument operating in its high-resolution configuration (see Chapter 2), measurements of the x-ray scattering in the region of the specular reflectivity rod were collected, for incident angles of between 0.2 degrees and 1.6 degrees. These results are represented by the intensity contour map, figure 5.16, over the range $Q_{||} = .071Å^{-1}$-$.171Å^{-1}$, $Q_{\perp} = \pm 2.5 \times 10^{-4}Å^{-1}$, where $Q_{||}$ is the wave-vector transfer parallel to the surface normal and $Q_{\perp}$ is the wave-vector transfer in the plane of the sample. In addition to the specular reflection, $Q_{\perp}=0$, there are satellite reflections of the first and second order on either side of the specular peak. These are more clearly seen in figure 5.17, which is a ψ scan ($Q_{\perp}$ scan) at a fixed detector angle $\phi = 2.0°$ ($Q_{||} = 0.142Å^{-1}$). Details of the diffractometer arrangement and resolution are given in chapter 2.

(3.2) Simple scattering model.

If it can be assumed that any scattering out of the plane nominally defined by the incident and diffracted beams is integrated over by the detector, then the scattering problem becomes two-dimensional, as

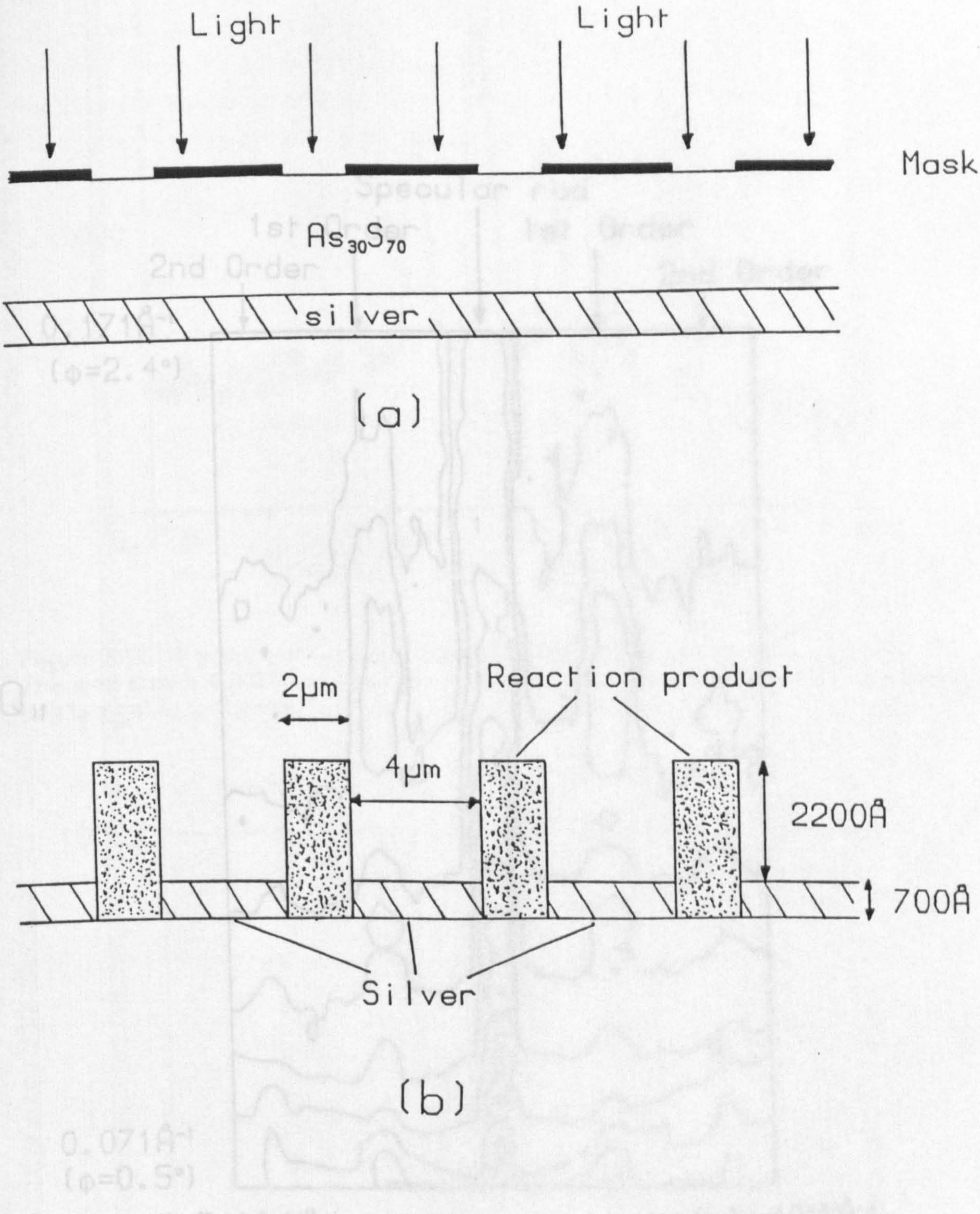

Figure 5.15 (a). A schematic illustration of the manufacturing process of optical diffraction gratings using photo-dissolution. The structure is initially deposited by thermal evaporation onto a glass microscope slide. The ideal result is illustrated in (b) after etching of the sample to remove any unreacted chalcogenide. The nominal parameters for the device studied in this work are shown.

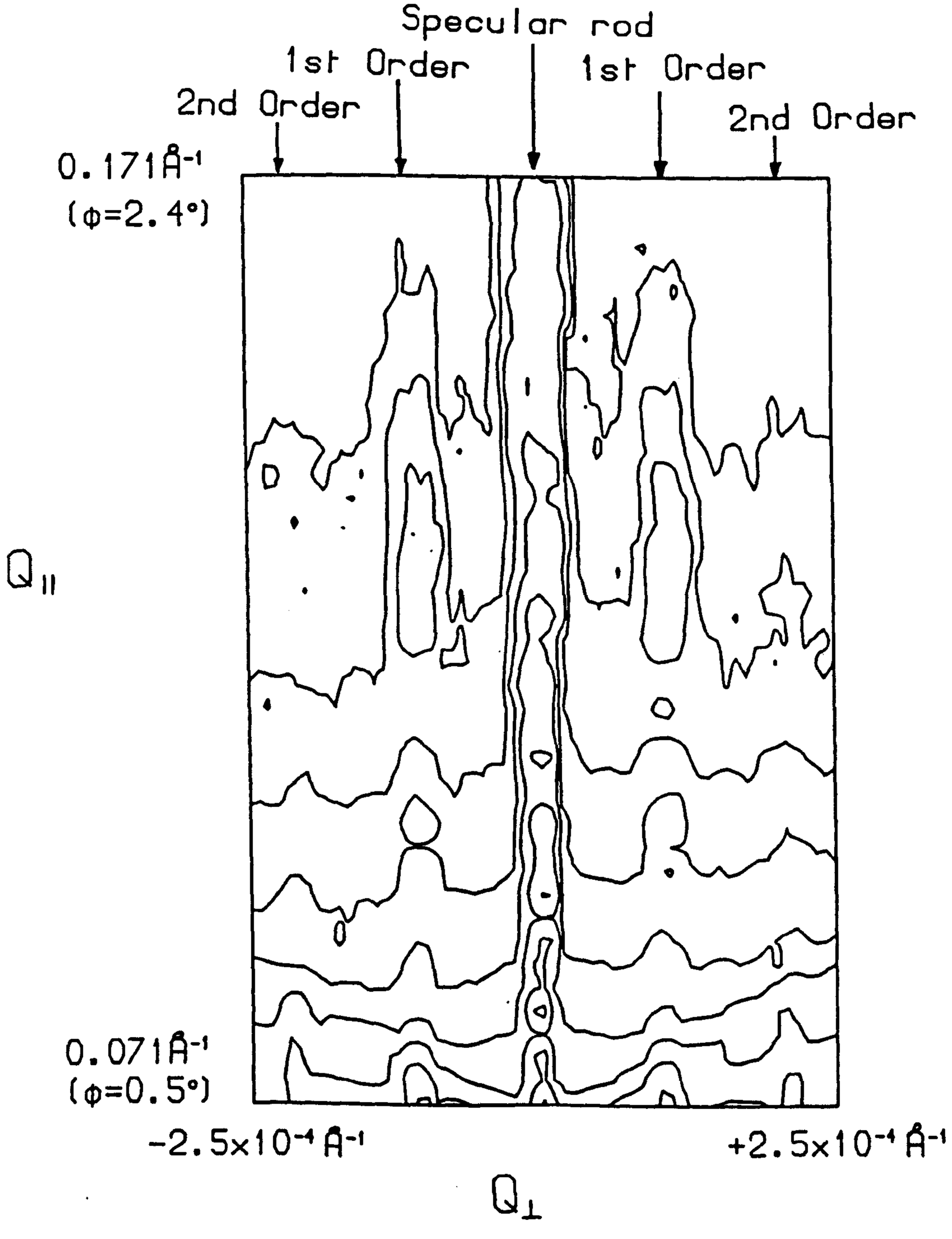

Figure 5.16. The distribution of scattered x-rays in the region of the specular reflection, between detector angles Ø=0.5° and Ø=2.4°. In addition to the specular reflection, $Q_\perp$=0, lines of scattering corresponding to first and second order diffraction maxima are also observed. A typical slice across this distribution (a $Q_\perp$ or ψ scan) is shown in Figure 5.17.

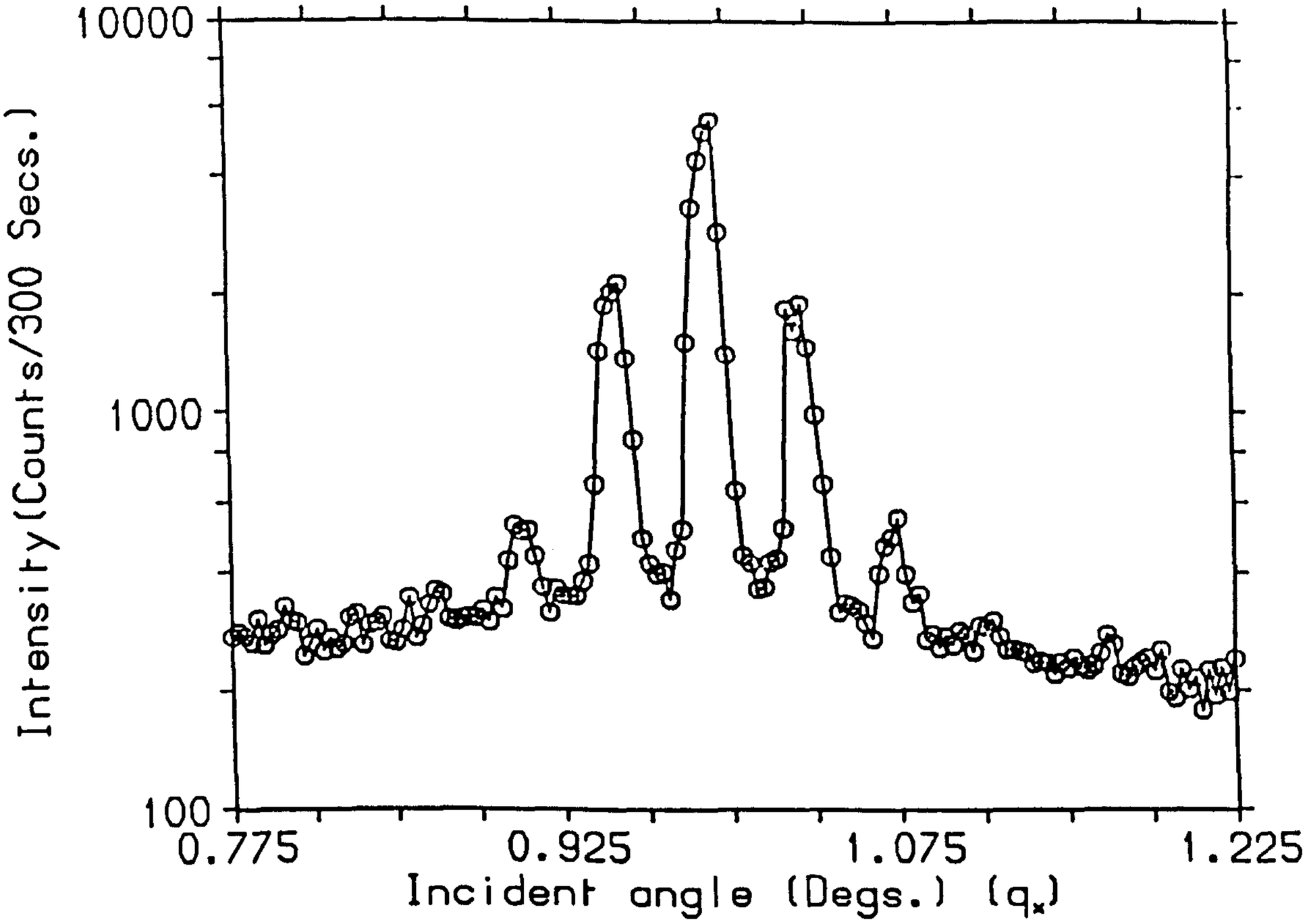

Figure 5.17. A ψ scan, or $Q_\perp$ scan, across the distribution in figure 5.16, at ∅=2.0°. The step size is 0.003° and the data is plotted on a logarithmic scale. The solid line is a guide to the eye.

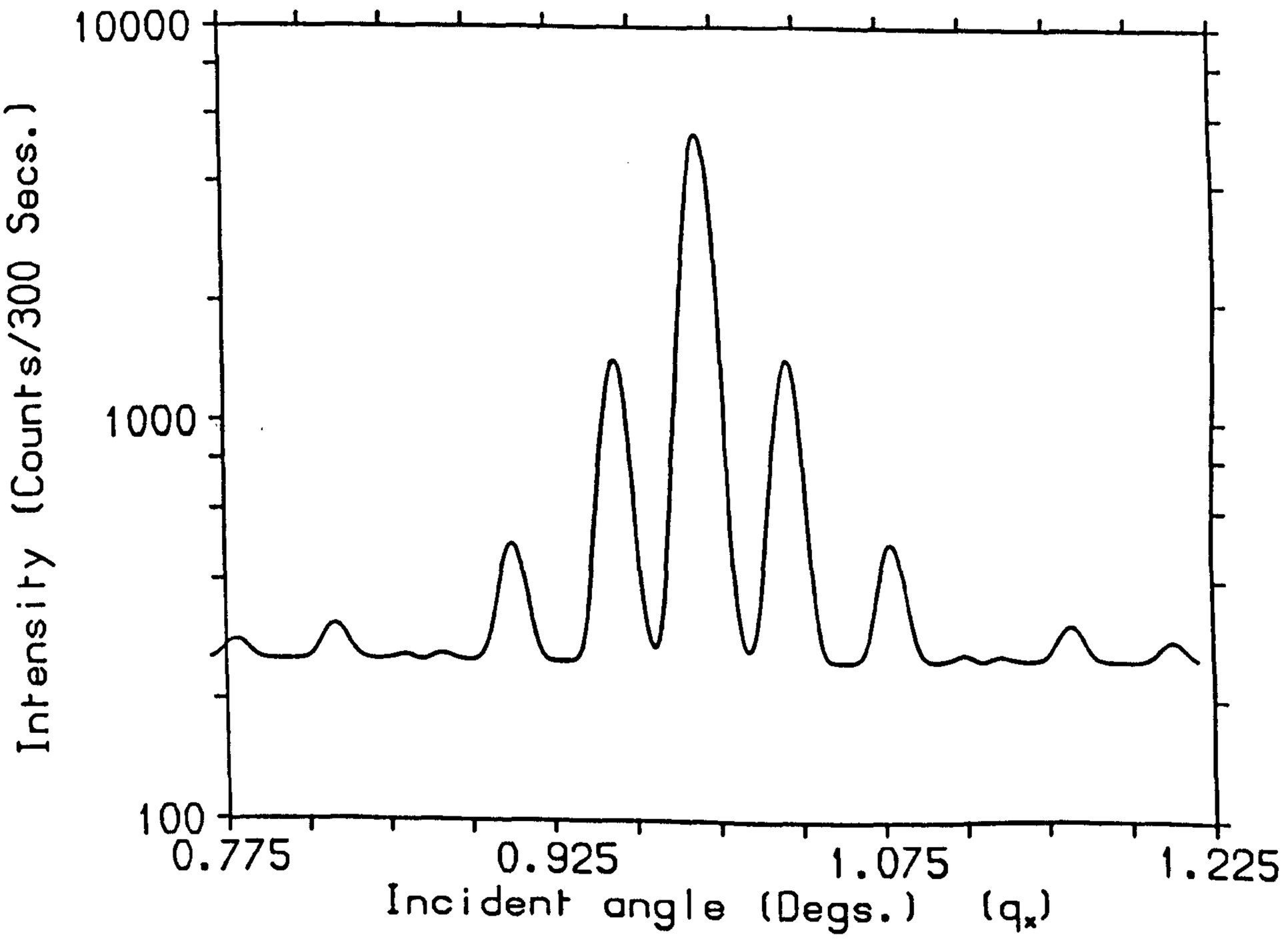

Figure 5.18. A simulation of the data in figure 5.17, according to the model in figure 5.19 and the nominal parameters in Table 5.2.

illustrated in figure 5.19. Provided that only scattering away from the critical angle for total-external-reflection is considered, then the problem can be formulated within a kinematic scattering theory (Appendix I). The scattered amplitude can be written as (see figure 5.19)

$$A(q_x, q_z) = A_0 \times \sum_{n=-\infty}^{\infty}$$

$$\left\{ \int_{n(d+s)}^{n(d+s)+d} \rho_1 \exp(iq_x x)dx \int_{-t_1}^{0} \exp(iq_z z)dz + \right.$$

$$\int_{n(d+s)+d}^{(n+1)(d+s)} \rho_2 \exp(iq_x x)dx \int_{-t_1}^{-t_1+t_2} \exp(iq_z z)dz + \qquad (1)$$

$$\left. \int_{n(d+s)}^{(n+1)(d+s)} \rho_3 \exp(iq_x x)dx \int_{-\infty}^{-t_1} \exp(iq_z z)dz \right\}$$

where A_0 is an amplitude constant and absorption corrections and area corrections have been ignored. In the terminology of figure 5.16 $q_x = Q_\perp$ and $q_z = Q_{||}$. The integrals in equation (1) may be solved to give

$$A(q_x q_z) = A_0 \left\{ \frac{\rho_1}{q_x q_z} [\exp(-iq_z t_1) - 1][\exp(iq_x d) - 1] \right.$$

$$+ \frac{\rho_2}{q_x q_z} \exp(-iq_z t_1)[1 - \exp(iq_z t_2)] \exp(iq_x d)[\exp(eq_x s) - 1] \qquad (2)$$

$$\left. + \frac{\rho_3}{q_x q_z} \exp(-iq_z t_1)[1 - \exp(iq_x (d+s))] \right\}$$

$$\times \sum_{n=-\infty}^{\infty} \exp[iq_x n(d+s)]$$

The infinite sum becomes

$$\frac{\sin[(N+1/2)\, q_x (d+s)]}{\sin\left(\frac{q_x (d+s)}{2}\right)} \quad N \to \infty \qquad (3)$$

The rapid oscillations in the numerator are averaged out and the denominator results in a delta function condition

$$\delta\left(q_x - \frac{2n\pi}{(d+s)}\right) \qquad (4)$$

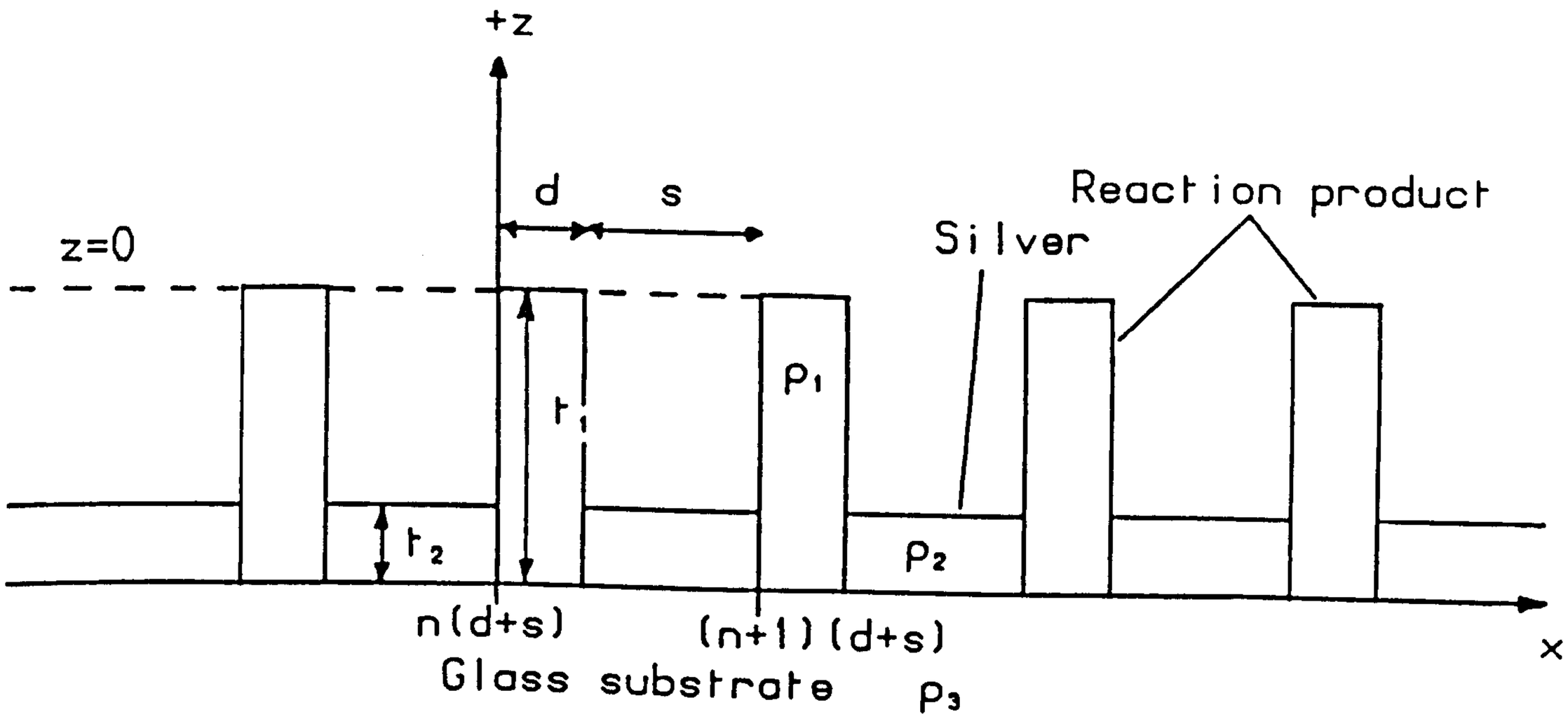

Figure 5.19. The simple model used for the kinematic scattering theory described in section (3.2).

Relative density	$\rho_1=2$	d=20000Å
	$\rho_2=5$	s=40000Å
	$\rho_3=1$	t_1=2800Å
Roughness	σ_x=2000Å	t_2=780Å

Table 5.2. Parameters for the calculation of figure 5.18 in the model of figure 5.19.

The scattered intensity is given by

$$I(q_x,q_z) = |A(q_x,q_z)|^2 \qquad (5)$$

which provides an intensity factor for the scattering, at the positions determined by the delta function. An overall uncertainty in the position of the interfaces may be represented by multiplying $A(q_x,q_z)$ by the fourier transform of the probability function, P(x), describing this uncertainty. If the interfaces are distributed randomly about their mean positions, according to a Gaussian function characterised by a width σ, then the scattered intensity in equation (5) is multiplied by a Debye-Waller type term $\exp(-q_x^2\sigma^2)$.

Replacing the delta function conditions by Gaussian functions, with widths given by the instrumental resolution and heights determined by equation (5), enables a scattered distribution to be calculated, and this is shown in figure 5.18, according to the nominal parameters of figure 5.15(b), and with an uncertainty in position given by σ=2000Å. The full parameters are shown in Table 5.2. The calculated profile gives a reasonable description of the experimental results, despite there being no adjustable parameters apart from a scaling factor.

Although the simple scattering model appears to be a reasonable approximation, if the $Q_{||}$ (or q_z) dependence of the diffraction peaks is investigated, then the model is seen to be incomplete. Figure 5.20 shows the q_z dependence of the zeroth order, first order and second order satellites. The symmetry related satellites show identical behaviour to their partners. In the zeroth order satellite, or specular beam, oscillations originating in the silver layer, the frequency giving a thickness of approximately 750Å, are clearly seen. The thickness of the photodoped region is expected to be 2500-3000Å, and this is too thick to be observed within the resolution of the instrument. In contrast to the zeroth order, the first order satellite is modulated by a second period. The frequency of this oscillation suggests a structure with a thickness of approximately 130Å. Data at the low q_z end of the spectrum, ie close to the critical angle, are unreliable due to the effect of the 'off-specular' reflection. In equation (2) there is no coupling between the q_x and q_z terms. Consequently the q_z

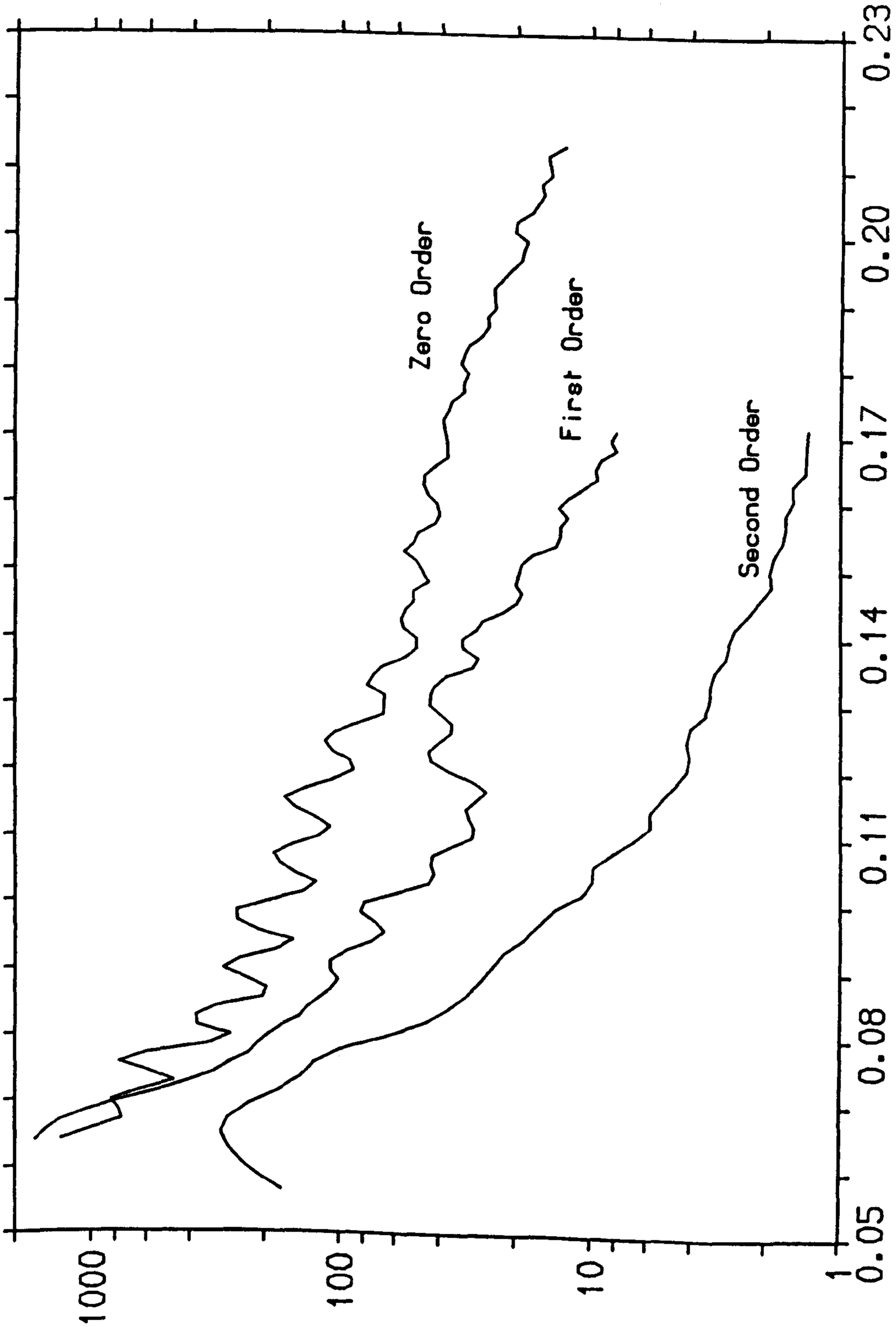

Figure 5.20. The measured Q_z dependence of the zero, first and second order satellites of figure 5.16. The results are obtained by integrating across the line of scattering and subtracting a background count in each case. Their behaviour is not explained within the simple scattering model.

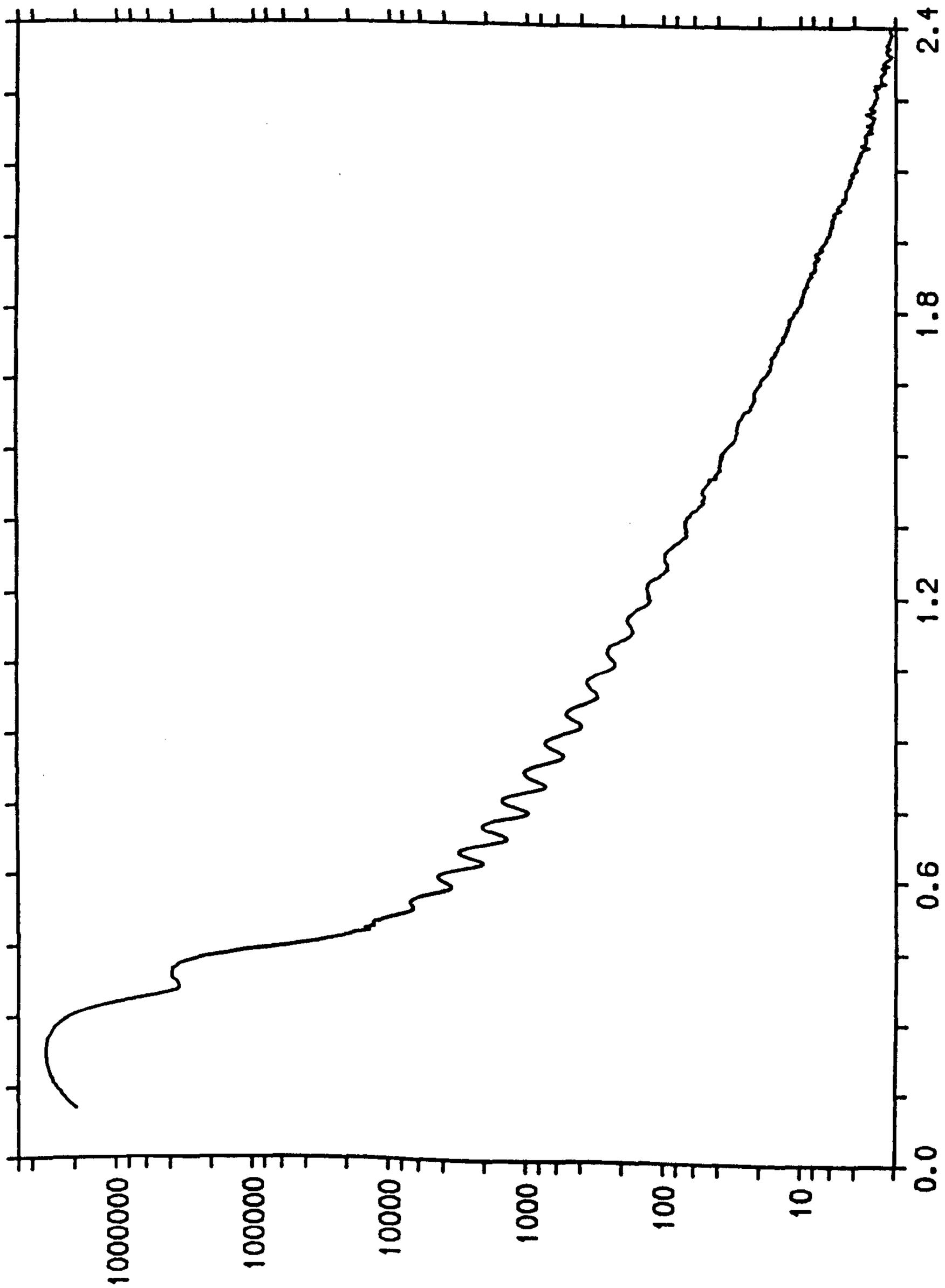

Figure 5.21. Double-crystal reflectivity curve of the diffraction grating after rotation by 90°. The incident and scattered x-rays now travel along the lines of the diffraction grating. Only one oscillation in the data is observed.

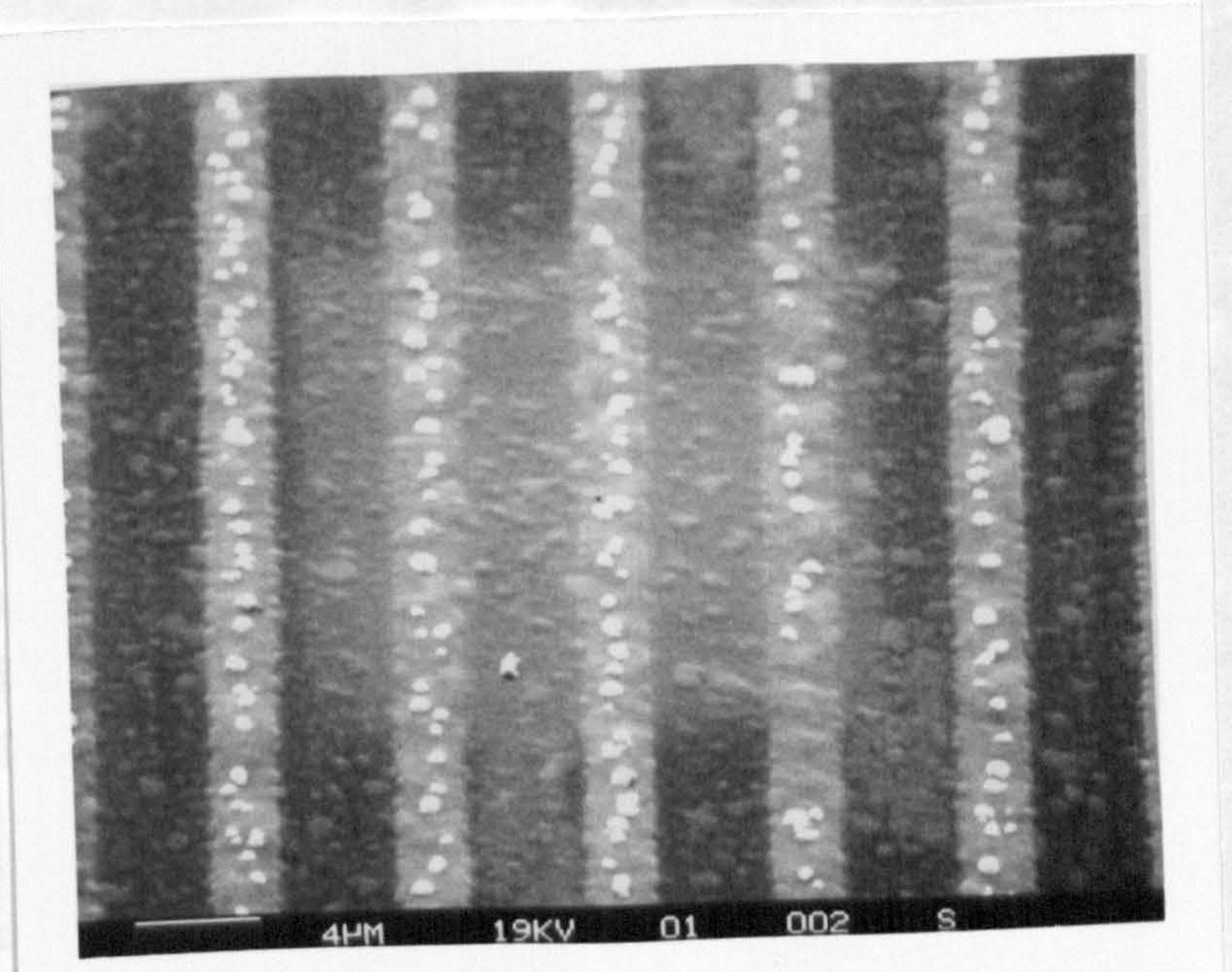

(a)

(b)

Figure 5.22. Scanning electron microscope (SEM) pictures of the sample taken at (a) normal incidence and (b) arbitrary glancing incidence.

dependencies of the diffraction maximae are identical apart from an overall scale factor. This is clearly not the case experimentally (figure 5.20) and a more complicated model of the structure is required.

The sample was rotated by 90°, and a reflectivity measurement as described in section 2 was performed to give the reflectivity curve of figure 5.21. With the sample in this position, the measurements are insensitive to the grating structure, but will merely sample an average of the structure in the surface normal direction. The results are similar to the zeroth order satellite in figure 5.20, indicating the presence of the silver layer, but not that of any additional thinner layer.

Scanning electron microscopy (SEM) measurements were also taken from the sample, using a Cambridge 5150 spectrometer in the Department of Electronic Engineering at Edinburgh University. The results are represented by figure 5.22(a), taken at normal incidence, and figure 5.22(b), taken at an arbitrary grazing incidence. In figure 5.22(a) the period of the structure is seen to be in good agreement with the predicted 6 μm period. However, there is an unexpected feature, the white blobs running along each line of the diffraction grating, corresponding to scattering from a highly reflecting substance at the surface. In the grazing incidence photograph this substance causes a projecting shadow effect, the black islands appearing on the grating line surface. Although not giving an accurate measure of thicknesses, figure 5.22(b) provides an indication of the grating profile. This shows that the grating is not sharp-edged as in figure 5.15(b), but that the line profile has smoothed edges.

(3.3) A more detailed scattering model.

The behaviour of the first-order satellite in figure 5.20 suggests that there is a lengthscale in the sample of approximately 130Å. As this feature is not observed in the zeroth order satellite, or in the reflectivity curve of the sample when it is rotated by 90°, it must be concluded that this lengthscale is not present in the structure in the form of a well-defined layer. The SEM measurements show unexpected features which are probably caused by excess silver at the surface of the grating. During the photo-dissolution reaction in sample preparation, illumination was continued for a prolonged period to ensure that the silver layer was fully

reacted. As the chalcogenide/silver ratio was low, this may have caused crystalline silver to be formed at the surface (Maruno and Kawaguchi, 1975; Firth, Ewen, Owen and Huntley, 1985). This silver would not form a layer of uniform thickness, as illustrated by the SEM measurements, but is more likely to form as droplets.

A new, more complicated model of the diffraction grating is illustrated in figure 5.23. This includes the smearing of the line interfaces and crudely approximates the silver droplets, to a triangular one-dimensional form, in order to simplify the mathematics. The scattered amplitude is now calculated as before, except that some integrals are complicated by the dependency of z on x. For example, the integral for the first section in figure 5.23 is written

$$\int_{n(d+2l+s)}^{n(d+2+s)+l} \exp(iq_x x)dx \qquad \int_{-t_1}^{-t_1+t_2+\frac{(t_1-t_2)}{l}[x-n(d+2l+s)]} \exp(iq_z z)dz \qquad (6)$$

with the result of additional terms occurring in the integral with respect to x. However, the mathematics is simple and the final expression is

$$A(q_x, q_z) = A_0 \times \sum_{n=-\infty}^{\infty} \exp[iq_x n(d+2l+s)] \quad \times$$

$$\left[\frac{\rho_1}{q_z}\exp(-iq_z t_1) \times\left[\frac{1}{\left(q_x+\frac{q_z(t_1-t_2)}{l}\right)}\left[1-\exp[i(lq_x+q_z(t_1-t_2))]\right]+\frac{1}{q_x}\left[\exp(iq_x l)-1\right]\right]\right.$$

$$+\frac{\rho_1}{q_x q_z}\left[\exp(-iq_z t_1)-1\right]\exp(iq_x l)\left[\exp(-iq_x d)-1\right]$$

$$\left.+\frac{\rho_1}{q_z}\exp[iq_x(l+d)]\times\left[\frac{1}{\left(q_x+\frac{q_z(t_1-t_2)}{l}\right)}\left[1-\exp[i(q_x l-q_z(t_1-t_2))]\right]+\frac{\exp(-iq_z t_1)}{q_x}\left[\exp(iq_x l)-1\right]\right]\right]$$

$$+\frac{\rho_2}{q_x q_z}\exp(-iq_z t_1)\exp[iq_x(2l+d)]\left[1-\exp(iq_z t_z)\right]\left[\exp(iq_x s)-1\right]$$

$$+ \frac{\rho_3}{q_x q_z} \exp(-iq_z t_1)\left[1 - \exp\left[iq_x(d + 2l + s)\right]\right]$$

$$+ \frac{\rho_2}{iq_z} \exp\left[iq_x\left(l + \frac{d}{2}\right)\right]\left\{\frac{1}{i\left(q_x + \frac{q_z t_3}{a}\right)}\left[\exp(iq_z t_3) - \exp(-iq_x a)\right]\right.$$

$$\left. - \frac{1}{i\left(q_x - \frac{q_z t_3}{a}\right)}\left[\exp(-iq_z t_3) - \exp(-iq_x a)\right]\right\}$$

$$+ \frac{\rho_2}{iq_z} \exp\left[iq_x\left(l + \frac{d}{2}\right)\right]\left\{\frac{1}{i\left(q_x - \frac{q_z t_3}{a}\right)}\left[\exp(iq_x a) - \exp(iq_z t_3)\right]\right.$$

$$\left.\left. - \frac{1}{i\left(q_x + \frac{q_z t_3}{a}\right)}\left[\exp(iq_x a) - \exp(-iq_z t_3)\right]\right\}\right| \qquad (7)$$

The infinite sum now gives the delta function condition as before

$$\delta\left(q_x - \frac{2n\pi}{(d+2l+s)}\right) \qquad (8)$$

Equation (7) now has coupling terms between q_x and q_z, unlike equation (2), and these represent the correlation between the x and z directions in the model.

Silver is a strong absorber of x-rays and so, some form of absorption correction must be included in the model. The differences in the angles between the satellite reflections in the diffraction pattern are small, and the effects of absorption in each case will be similar. Absorption cannot be the cause of the differences in the q_z dependencies of the diffraction maximae observed in figure 5.20. To consider all of the possible paths that an incident and scattered x-ray may take to reach a point in the material is a complicated problem, and detracts from the simplicity of the model. The x dependence of the absorption correction is therefore ignored, and it is assumed that x-rays reaching a certain depth, z, in the sample undergo attenuation as determined by the average structure. For example, the scattering from the reaction product is attenuated by a factor

$$\exp\left[\frac{-\mu_2 a t_3}{(d + 2l + s)}\right] \exp\left[\frac{(d + l)}{(d + 2l + s)}\mu_1 \eta z\right] \qquad (9)$$

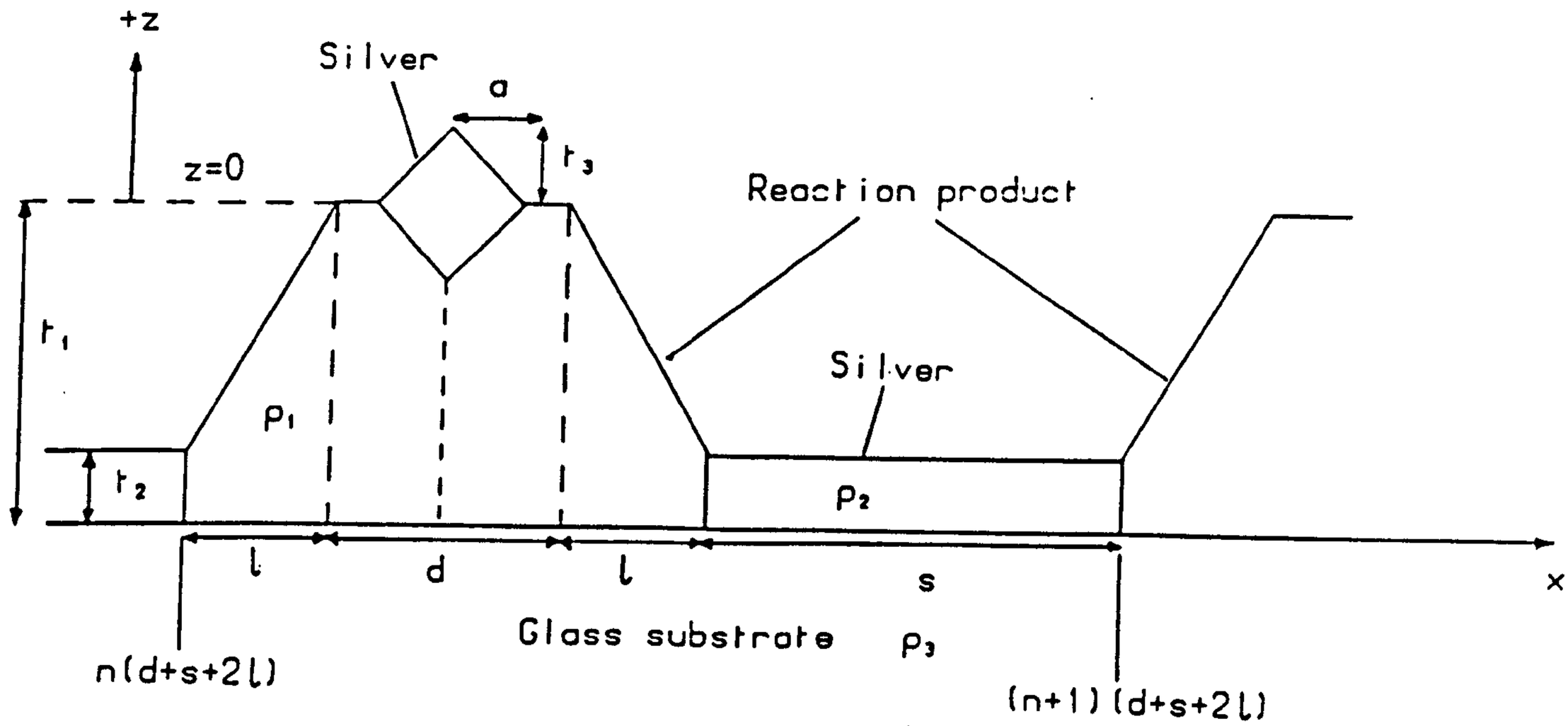

Figure 5.23. The more complicated model used for the kinematic scattering theory described in section(3.3). The extra features observed by SEM are included in simple approximations.

Relative density ρ_1=1.5	Absorption coeff. $\mu_1=4.0\times10^{-6}$Å^{-1}
ρ_2=6	$\mu_2=8.0\times10^{-6}$Å^{-1}
ρ_3=1	$\mu_3=1.0\times10^{-6}$Å^{-1}
d=18000Å	Uncertainty in x σ_x=5000Å
s=36000Å	Uncertainty in z σ_z=3Å
l=3000Å	
a=5000Å	σ_a=5000Å
t_1=2200Å	σ_{t_1}=30Å
t_2=780Å	σ_{t_2}=15Å
t_3=120Å	σ_{t_3}=15Å

Table 5.3. Parameters for the calculation of figure 5.24 in the model of figure 5.23.

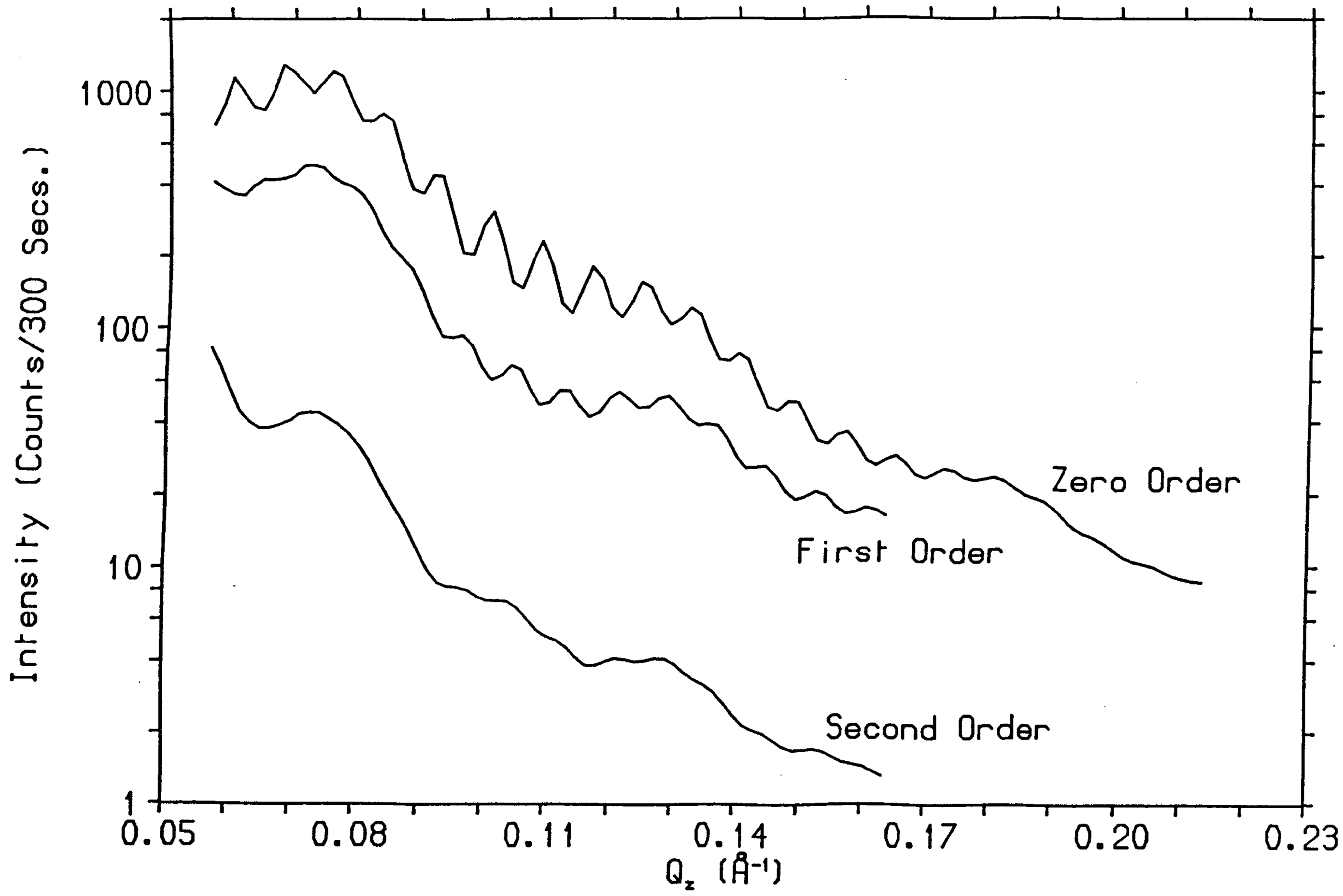

Figure 5.24. Simulation of the Q_z dependence of the diffraction maximae, as measured in figure 5.20, according to the model of figure 5.23 and the parameters in Table 5.3.

where μ_1 and μ_2 are the linear absorption coefficients of the reaction product and silver layers respectively, and

$$\eta = \left(\frac{1}{\sin\theta_i} + \frac{1}{\sin\theta_e}\right) \tag{10}$$

with θ_i being the angle of incidence and θe the angle of exit with respect to the sample surface. Similar corrections are applied to the other terms in the scattering amplitude. Roughness can be incorporated into the model by giving Gaussian distributions to the thicknesses t_1. t_2, t_3. Also, the SEM photographs show that the position of the silver droplets varies, and this is incorporated by multiplying the respective amplitude terms by a Debye-Waller-type factor $\exp\left[\frac{-q_x^2\sigma_a^2}{2}\right]$, as described earlier, in addition to the uncertainties in the overall position of the interfaces in the x and z directions.

The calculated scattering for the zeroth order, first order and second order satellites is shown in figure 5.24, according to the parameters in table 5.3. The calculations were corrected by some angular factors as discussed in chapter 2, but there are no adjustable scale factors between the different orders. There are too many approximations in the theory to invite direct comparison with the experimental data, but, it can be seen that the general features of the scattering in figure 5.20 are reproduced.

(3.4) Conclusions.

The aim of the experimental work described in this section was to see if x-ray reflectivity measurements, at grazing angles of incidence, could provide detailed information about modulated surface structures, in this case an optical diffraction grating produced by the photo-dissolution/etching process. Although there is limited success in describing the observed results, application of the simple theory is complicated by the necessary absorption corrections. This manifests itself in the relative insensitivity of the calculated profile to departures from the ideal structure (compare figures 5.23 and 5.15(b)). This problem can be overcome by recourse to a semi-dynamical theory (Andreev, Akhmanov and Ponomarev, 1986) but the solutions are not mathematically simple.

Structure at the surface of the sample, assumed to be silver droplets, can have a dramatic effect on the observed x-ray scattering and this may be of particular interest in future studies.

The results in this section are of a preliminary nature, and a range of applications of similar methods, to study a variety of systems, is anticipated. Detailed measurements of capillary waves on the surfaces of simple liquids have already been performed (Braslau, Pershan, Swislow, Ocko and Als-Nielsen, 1988). Simple systems, such as surface acoustic wave (SAW) devices, in which wavelengths of 6μm with amplitudes of 15Å are achievable, have been studied by neutron diffraction (Hamilton, Klein, Opat and Timmins, 1987) and x-ray reflectivity would provide a detailed probe of the SAW properties. Similarly, the effect of laser radiation on the surface of materials, would be another interesting example. As was shown in section 2, information on islanding processes, already a subject of intense study by electron diffraction, can be obtained using grazing-incidence x-ray scattering . Although x-ray reflectivity measurements are complicated by departures from ideal structures, it seems clear that further development of the technique and more sophisticated analysis procedures will enable a wide range of physical problems to be studied.

Conclusions

Surface sensitive x-ray and neutron scattering is finding increasing application in a wide range of surface physics and structural problems. The recent advances in sample growth techniques, and the parallel development of high-resolution diffractometers utilising intense x-ray sources, has enabled the microscopic properties of surfaces and interfaces to be probed. In this rapidly expanding field it is now possible, using ultra-high vacuum techniques and synchrotron radiation, to observe, in situ, the behaviour of a monolayer of material as it is deposited on a substrate.

The principle aim of this thesis was to explore the possible applications of x-ray scattering techniques, such as x-ray reflectivity and crystal truncation rod scattering, in surface structural characterisation. Experiments were performed using a high-resolution triple-crystal x-ray diffractometer and without recourse to complicated sample environmental control, such as ultra-high vacuum apparatus.

Reflectivity results from the Si/SiO_2 wafer illustrated the dramatic effects that contaminant surface layers, such as water, can have on the reflectivity curve. This demonstrates the sensitivity of the technique to the properties of a sample surface. In addition, crystal truncation rod scattering was used to probe the crystalline properties of the Si/SiO_2 interface, showing the interfacial region to extend over no more than three monolayers. An extension of these measurements would enable a detailed structural model of the interface to be derived.

The combination of these two x-ray scattering techniques was shown to yield complementary information in the study of single quantum well semiconductor heterostructures. In both cases, interpretation of the experimental results was seen to be quite straightforward. The diffraction results were interpreted within a kinematical scattering theory whereas, in the reflectivity theory, modelling the structure as a series of homogeneous, dielectric slabs was seen to be a good approximation in the case of materials grown by molecular-beam-epitaxy.

Such a simple approximation was not found to be appropriate in analysing reflectivity measurements performed during the photo-

dissolution reaction in silver/chalcogenide systems. The structural evolution of this reaction was seen to exhibit a complex time dependence as a result of islanding processes within the structure. Although, not capable of providing an exact quantative analysis, x-ray reflectivity and diffuse scattering measurements were shown to contain a wealth of information, and an application of the techniques in a wide range of problems is anticipated.

Clearly then, the techniques described in this thesis have a major part to play in the understanding of the physics of surfaces. The developments in sample growth and environmental control techniques promise to open up a range of both old and new problems in this exciting field.

Appendix I - Kinematical Scattering Theory for Surfaces

This description of kinematical scattering theory was given by Professor R.A. Cowley in a lecture course at Edinburgh University during 1987/88.

Within the Born approximation, ie. assuming that in the scattering process the perturbation on the incident wave is small, the measured quantity in an x-ray experiment, the partial differential cross-section, is given by

$$\frac{d^2\sigma}{dEd\eta} = |f(\underline{Q})|^2\left(\frac{e^2}{mc^2}\right)^2 (\underline{\mu}_o.\underline{\mu}_s)^2\, S(\underline{Q},\omega) \qquad (1)$$

where $f(\underline{Q})$ is the atomic form factor, $\left(\frac{e^2}{mc^2}\right)$ is the classical electron radius, $(\underline{\mu}_o.\underline{\mu}_s)^2$ is the Lorentz polarisation factor $1/2(1 + \cos 2\theta)$ and $S(\underline{Q},\omega)$ is the Van Hove correlation function. Equation (1) assumes a rigid atom approximation in order to separate out the form factor, $f(\underline{Q})$, from the structure factor contained in $S(\underline{Q},\omega)$. The correlation function $S(\underline{Q},\omega)$ is given by

$$S(\underline{Q},\omega) = \left\langle\left\langle \sum_l \exp(-i\underline{Q}.\underline{r}(l)) \sum_{l'} \exp(-i\underline{Q}.\underline{r}(l'))\right\rangle\right\rangle$$

$$\times\, \delta(\hbar\omega + E_m - E_n) \qquad (2)$$

where the bracket notation $\langle\langle\ldots\ldots\rangle\rangle$ represents the statistical sum over all of the states of the system, m and n, and the δ-function represents energy conservation.

By introducing the density operator

$$\rho(\underline{r}) = \sum_l \delta(\underline{r} - \underline{r}(l)) \qquad (3)$$

and its Fourier transform (defined without normalisation factors)

$$\rho(\underline{Q}) = \int \rho(\underline{r}) \exp(i\underline{Q}.\underline{r})d\underline{r}$$

$$= \sum_l \exp(i\underline{Q}.\underline{r}(l)) \qquad (4)$$

and assuming elastic scattering, equation (2) may be rewritten as

$$S(\underline{Q}) = \left\langle\left\langle \rho(\underline{Q})\, \rho(-\underline{Q})\right\rangle\right\rangle \tag{5}$$

Consider now a flat, crystalline surface as defined in figure AI.1. Taking one dimension for l, and an attenuation between planes $\mu = \frac{2a\mu_0}{\sin\psi}$, where μ_0 is the linear absorption coefficient, equation (4) becomes

$$\rho(Q) = \sum_{l=0}^{\infty} \exp\,(iQ_z la - \mu l)$$

$$= \frac{1}{1 - \exp\,(iQ_z a - \mu)} \tag{6}$$

The scattering is then given by

$$S(Q) = \frac{b^2}{\left[1 - \exp\,(iQ_z a - \mu)\right]\left[1 - \exp\,(-iQ_z a - \mu)\right]} \tag{7}$$

where b^2 represents the constants in equation (1) and a is the lattice parameter of the crystal in the z direction, as shown in figure AI.1. Assuming that the wave-vector transfer is close to a Bragg reflection, ie Q_z = $G_z + q_z$, where G_z is a reciprocal lattice vector, the exponential can be expanded to give

$$S(Q) = \frac{b^2}{(-iq_z a + \mu)\,(iq_z a + \mu)} = \frac{b^2}{(q_z a)^2 + \mu^2} \tag{8}$$

ie the Bragg reflection has $\frac{1}{q_z^2}$ tails, perpendicular to the surface in reciprocal space. This result is also derived in the dynamical theory of x-ray diffraction (Zachariasen, 1945), which implicitly includes the effect of surfaces.

If the crystal is assumed to be infinite in the x and y directions, the sums over Q_x and Q_y give delta functions, $\delta(q_x)$, $\delta(q_y)$, and a factor proportional to the area of illumination ie $\frac{A_B}{\sin\psi}$, where A_B is the cross-sectional area of the incident beam. The scattered intensity is then given by

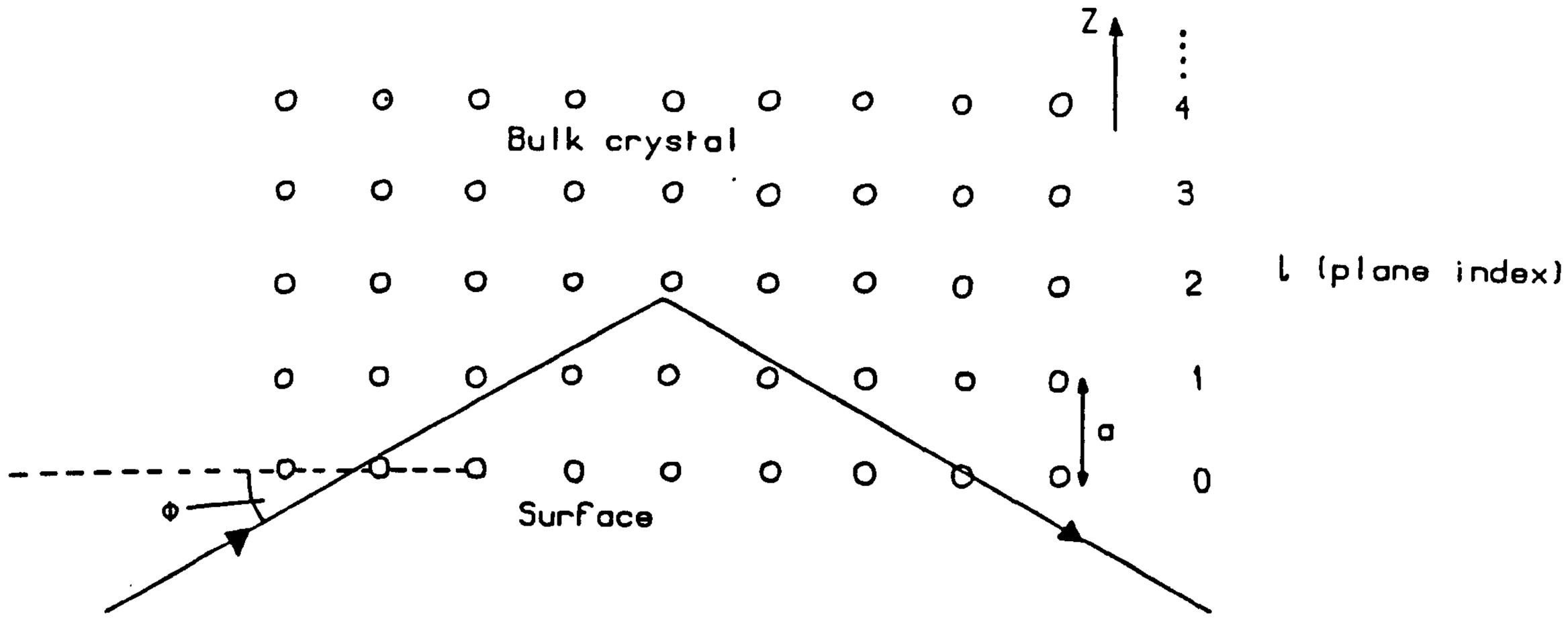

Figure AI.1. One-dimensional model used to describe the surface scattering from a crystal.

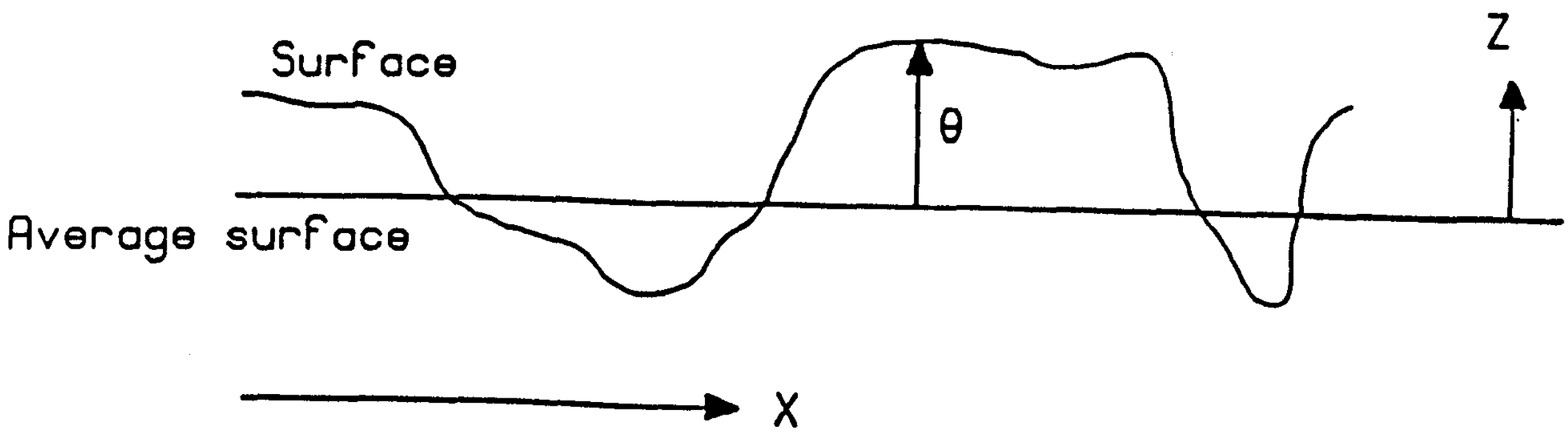

Figure AI.2. Surface roughness may be represented by a displacement θ(x,y) about a mean value.

$$I(Q) \propto \frac{A_B b^2}{\sin\psi\left[(q_z a)^2 + \mu^2\right]}\ \delta(q_x)\ \delta(q_y) \tag{9}$$

Given the finite resolution function of an x-ray spectrometer, this is a rod in reciprocal space, hence the term 'crystal truncation rod'. For an asymmetric reflection, the scattered intensity is identical, with the $\frac{1}{q_z^2}$ tails perpendicular to the surface and the attenuation factor modified to

$$\mu = a\mu_0\left(\frac{1}{\sin\psi} + \frac{1}{\sin\psi_e}\right) \tag{10}$$

ψ_e being the exit angle of the beam with respect to the crystal surface.

The effects of a slight surface roughness may be modelled by assuming that the displacement of the surface θ, from an average value, varies with the position (x,y) in the plane (see figure AI.2). The scattering equation, ignoring absorption corrections, now becomes

$$S(\underline{Q}) = \frac{b^2}{(q_z a)^2}\int\langle \exp\left[iq_z(\theta_1 - \theta_2)\right]\exp\left[iq_{||}\,.\,\underline{P}\right]\rangle\, d\underline{P} \tag{11}$$

where $\underline{P}$ is the position vector (x,y), $\underline{q}_{||} = (q_x, q_y)$ and $\underline{P} = \underline{P}_1 - \underline{P}_2$ with $\theta_1 = \theta(\underline{P}_1)$, $\theta_2 = \theta(\underline{P}_2)$. In order to evaluate this expression it is necessary to know the correlation function of θ_1 and θ_2. However, a simple approximation is to assume that θ_1 is independent of θ_2 and given by a Gaussian, ie $\langle\theta_1^2\rangle = \theta_0^2$. Equation (11) becomes

$$S(\underline{Q}) = \frac{b^2}{(q_z a)^2}\ \exp\left(-\theta_0^2 q_z^2\right)\ \delta(q_{||}) \tag{12}$$

The exponential term is like a Debye-Waller factor causing the $\frac{1}{q_z^2}$ tails to fall off more rapidly, at a rate proportional to the roughness value θ_0. This expression is not particularly suitable for describing a crystal as it assumes that the probability distribution is random on an atomic scale. Other roughness models, including the effects of in-plane correlation, have been dealt with in detail by several authors (Andrews and Cowley, 1985; Robinson, 1986; Held, Jordan-Sweet, Horn, Mak and Birgeneau, 1987; Wong and Bray, 1988).

This appendix is not intended to be a rigourous derivation of kinematical scattering theory but contains the pertinent concepts and

equations relating to the origin of the 'crystal truncation rod'. It therefore provides much of the basis for the work in this thesis. A detailed description of the kinematical theory is given by James (1949) and alternative derivations of the surface scattering may be found in the work of Robinson (1986), Vlieg (1988) and Feidenhans'l (1989).

Appendix II - X-Ray Reflectivity Theory

The theory of x-ray reflectivity outlined below follows the recursion formalism developed by Parratt (1954), with some minor modifications to include the effects of interface roughness. The basis of this treatment is the Maxwell theory (Compton and Allison, 1935) applied to a series of parallel boundary planes on which x-rays undergo multiple reflection and refraction.

Consider the system, illustrated in figure AII.1, with an electromagnetic wave incident on a plane surface at a grazing angle ψ. The incident wave generates a reflected and a diffracted wave at the interface, with the diffracted wave doing likewise at the next interface and so on. In the nth lamina the wave in the incident direction is characterised by the vector of its electric fieldstrength

$$E_n(x,z,t) = E_{no} \exp\left[i(\omega t - k_{nx}x - k_{nz}z)\right] \quad (1)$$

where x and z are the directions shown, $\omega/2\pi$ is the radiation frequency and E_{no} is the amplitude of the wave. The components of the wavevector can be approximated

$$k_{nx} \approx k_{(n-1)x} \approx k_1 \quad (2)$$

$$k_{nz} \approx k_1 (\psi^2 - 2\delta_n - 2i\,\beta_n)^{1/2} = k_1 f_n \quad (3)$$

In equation (3) $(\delta_n + i\beta_n)$ is the complement of the complex index of refraction, with the real part given by the Lorentz theory of light scattering (Compton and Allison, 1935)

$$\delta_n = \frac{N_n e^2}{2\varepsilon_0 m_e \omega^2} \quad (4)$$

where N_n is the electron density of the material and the other symbols have their usual meaning. In a handy approximation (Wagendristel, Schurz, Ehrmann-Falkenau and Bangert, 1980) equation (4) can be written as

$$\delta_n = 1.36 \times 10^{-9} \lambda_0^2 \rho_n \quad (5)$$

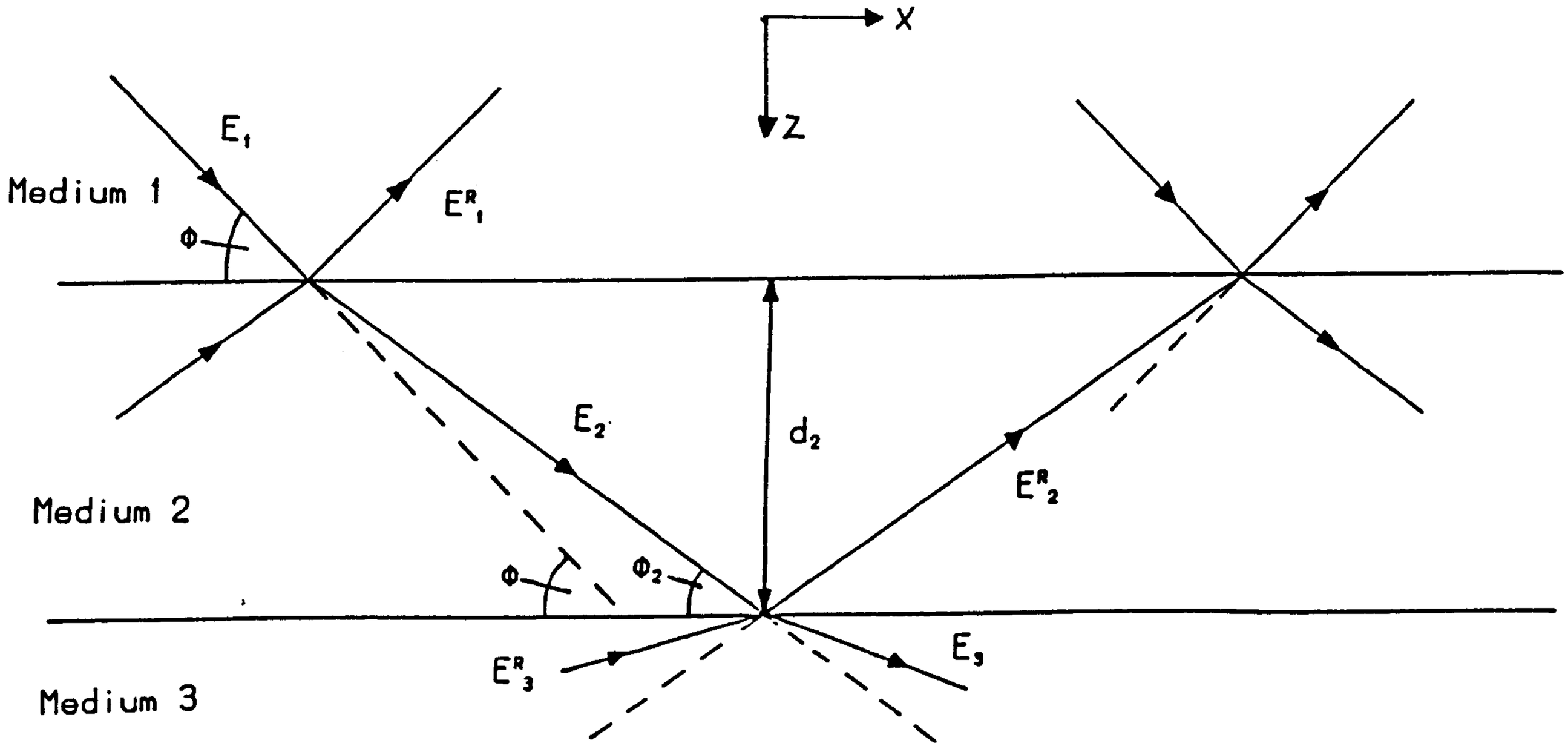

Figure AII.1. Schematic illustration of reflection and refraction for stratified homogeneous media.

where λ_0 is the vacuum x-ray wavelength (Å) and ρ_n is the mass density (kgm^{-3}). The complex component β_n is given by

$$\beta_n = \frac{\mu_n \lambda_0}{4\pi} \tag{6}$$

where μ_n is the linear absorption coefficient of the x-rays. Beams travelling in the direction of reflection are also represented by equation(1) but the signs of the amplitude E_{no} and the wavevector k_{nz} are reversed. These waves are marked with the subscript r in the following equations. The components of both the electric vector and the magnetic vector, parallel to the boundary plane, must be the same in consecutive media n-1,n (figure AII.1), thus yielding the boundary conditions

$$a_{n-1} E_{n-1} + a_{n-1}^{-1} E_{n-1,r} = a_n^{-1} E_n + a_n E_{n,r} \tag{7}$$

$$(a_{n-1} E_{n-1} - a_{n-1}^{-1} E_{n-1,r}) f_{n-1} k_1 = (a_n^{-1} E_n - a_n E_{n,r}) f_n k_1 \tag{8}$$

where the values of the vectors at the boundary are expressed by their values E_n, $E_{n,r}$ in the middle of the adjacent laminae multiplied by the amplitude factor

$$a_n = \exp\left[-ik_1 f_n \frac{d_n}{2}\right] \tag{9}$$

where d_n is the thickness of the nth lamina.

The solution of equations (7) and (8) is obtained by dividing their difference by their sum, resulting in the recursive formula

$$R_{n-1,n} = a_{n-1}^4 \left[\frac{R_{n,n+1} + F_{n-1,n}}{R_{n,n+1} F_{n-1,n} + 1}\right] \tag{10}$$

where

$$R_{n,n+1} = a_n^2 \left[\frac{E_{n,r}}{E_n}\right] \tag{11}$$

and the Fresnel coefficient of reflection is given by

$$F_{n-1,n} = \frac{f_{n-1} - f_n}{f_{n-1} + f_n} \tag{12}$$

Roughness is most simply incorporated into the model by assuming a random Gaussian form (Névot, Pardo and Corno, 1988) whereby each interface reflectivity, $R_{n-1,n}$, is multiplied by a factor

$$\exp\left\{\frac{-1}{2}\left[\left(\frac{4\pi\sigma_n}{\lambda_0}\right)\sin\psi\right]^2\right\} \tag{13}$$

correcting the misprint in Ryan and Cowley (1987). σ_n is the root-mean-square value of the roughness for the layer n.

Equation (10) is solved by setting $R_{N,N+1} = 0$, for the substrate layer which is regarded as semi-infinite, and carrying out N recursive calculations to obtain $R_{1,2}$. The ratio of reflected to incident intensity is determined by taking the product of $R_{1,2}$ with its complex conjugate. It should be noted that the expressions are derived only for the σ component of polarisation. However, within the approximations made, particularly the small angles of incidence, no distinction needs to be made between the σ and π components of polarisation (Parratt, 1954; Underwood and Barbee, 1981).

In x-ray reflectivity curve simulation, a model, containing a finite number of different layers, must be selected to represent the sample. Each layer is characterised by four parameters; thickness d_n, mass density ρ_n, linear absorption coefficient μ_n and roughness at the topmost interface σ_n. In practice, μ_n and ρ_n can often be deduced from known values, allowing them to be fixed in parameter refinement. However, in the case of complicated structures a unique representation of the sample may not be possible in which case interpretation of the results becomes ambiguous. It must also be noted that a determination of the incident intensity, needed to normalise the data, is difficult to obtain due to the way in which focusing occurs on reflection from the sample crystal. For this reason, when calculating fits to the data, a variable scale parameter is used to represent the incident beam intensity (Cowley and Ryan, 1987).

Although the method described above has the advantage of being exact, taking both refraction and absorption properly into account, there are many cases where the approximation of the electron density profile to a series of homogeneous, dielectric slabs obscures the physical reality of the structure. Despite this, Pomerantz and Segmüller (1980) have used

the method to describe the reflectivity of a multilayer Langmuir-Blodgett film of manganese stearate ($MnSt_2$), approximating the electron density of the molecule by four boxes, and allowing each molecule to slightly overlap in an eleven-layer system. However, an alternative "kinematical" theory of reflectivity has been derived (Als-Nielsen, 1989), which relates the measured reflectivity to the electron density profile in a more transparent way.

This theory constructs a normalized density profile $\rho(z)$ of the sample, in which the substrate density $\rho_s=1$. If $\rho(z)$ is a step function, ie zero for $z<0$ and unity for $z>0$, the reflected intensity follows the Fresnel law (Born and Wolf, 1975)

$$R_F(\psi) = \left[\frac{(\psi - \psi')}{(\psi + \psi')}\right]^2 , \psi > \psi_c \tag{14}$$

where ψ is the incident angle and ψ' is the angle of the beam inside the material, determined by its refractive index. For $\psi >> \psi_c$ equation (14) is readily expanded to give the simple result

$$R_F(\psi) = \left[\frac{2\psi}{\psi_c}\right]^{-4}, \; R_F(Q) = \left[\frac{2Q}{Q_c}\right]^{-4} \tag{15}$$

where Q is the wavevector transfer given by

$$Q = \frac{4\pi}{\lambda_0} \sin\psi \tag{16}$$

By constructing a "missing-length" argument, Als-Nielsen (1989) derives a 'master formula' relating I(Q) and $\rho(z)$

$$\frac{I(Q)}{I_F(Q)} = \left| \int \rho'(z) \exp(iQz) dz \right|^2 \tag{17}$$

where $\rho'(z)$ denotes the gradient of $\rho(z)$. The details of the derivation are not included here. This alternative treatment of x-ray reflectivity is well suited to modelling graded interfaces between materials, where the approximation of a discrete step in the electron density is a poor one (Braslau, Deutsch, Pershan, Weiss, Als-Nielsen and Bohr, 1985; Pershan, Braslau, Weiss and Als-Nielsen, 1987). The treatment is analogous in many ways to the surface scattering theory described in Appendix I.

References

Afanas'ev A.M., Alexsandrov P.A., Fanchenko S.S., Chaplanov V.A. and Yakimov S.S., Acta Cryst. A42, 116 (1986)

Afanas'ev A.M., Alexsandrov P.A., Imanov R.M., Lomov A.A. and Zavyalova A.A., Acta Cryst. A40, 352 (1984)

Als-Nielsen J., in 'Handbook of Synchrotron Radiation', vol. 3, (North Holland, Amsterdam) (1989)

Andreev A.V., Sov. Phys. Usp. 28, 70 (1985)

Andreev A.V., Akhamov S.A. and Ponomarev Y.V., Bull. Acad. Sci. USSR, Phys. Ser. (USA), 50, 156 (1986)

Andreeva M.A., Borisova S.F. and Stepanov S.A., Phys. Chem. Mech. Surfaces, 4, 951 (1986)

Andrews S.R. and Cowley R.A., J. Phys. C, 18, 6427 (1985)

Andrews S.R. and Cowley R.A., J. Phys. C, 19, 615 (1986)

Aspnes D.E. and Theeten J.B., J. Electrochem. Soc. 127, 1359 (1980)

Barrett N.T., Greaves G.N., Pizzini S. and Roberts K.J., Surf. Sci., submitted for publication (1989)

Bartels W.J., J. Vac. Sci. Technol. B1, 338 (1983)

Bartels W.J., Hornstra J. and Lobeek D.J.W., Acta Cryst. A42, 539 (1986)

Bartels W.J., and Nijman W., J. Cryst. Growth, 44, 518 (1978)

Batterman B.W., Phys. Rev. A133, 759 (1964)

Batterman B.W. and Cole H., Rev. Mod. Phys. 36, 681 (1964)

Batterman B.W., and Hildebrandt G, Acta Cryst. A24, 150 (1968)

Baumbach T, Brühl H.G., Rhan H. and Pietsch U., J. Appl. Cryst. 21, 386 (1988)

Beaumont J.H. and Hart M., J. Phys. E, 7, 823 (1974)

Bindell J. and Wainfan N., J. Appl. Cryst. 3, 503 (1970)

Binnig G, Rohrer H., Gerber Ch., and Weibel E., Phys. Rev. Lett. 50, 120 (1983)

Bjerrum-Møller H and Nielsen M, 'Instrumentation for Neutron Inelastic Scattering Research', p. 49 (Vienna: International Atomic Energy Agency) (1969)

Bohr J., Feidenhans'l R., Nielsen M., Toney M., Johnson R.L. and Robinson I.K., Phys. Rev. Lett. 54, 1275 (1985)

Born M., and Wolf E., 'Principles of Optics' (Pergamon, New York) (1975)

Braslau A., Deutsch M., Pershan P.S., Weiss A.H., Als-Nielsen J. and Bohr J., Phys. Rev. Lett. 54, 114 (1985).

Braslau A., Pershan P.S., Swislow G., Ocko B.M. and Als-Nielsen J., Phys. Rev. A38, 2457 (1988)

Chang M.S., and Chen J.T., Appl. Phys. Lett. 33, 892 (1978)

Chatani K., Shimizu I., Kokado H. and Inoue E., Jap. J. Appl. Phys. 16, 389 (1977)

Chesser N.J. and Axe J.D., Acta Cryst. A29, 160 (1973)

Cho A.Y., J. Vac. Sci. Technol. 8, 531 (1971)

Chrzan D. and Dutta P., J. Appl. Phys. 59, 1504 (1986)

Chu S.N.G., Macrander A.T., Strege K.E., and Johnston W.D., J. Appl. Phys. 57, 249 (1985)

Chu X and Tanner B.K., Appl. Phys. Lett. 49, 1773 (1986)

Compton A.H., Phil. Mag. 45, 1121 (1923)

Compton A.H. and Allison S.K., 'X-rays in Theory and Experiment', (New York: Van Nostrand) (1935)

Cooper M.J. and Nathans R., Acta Cryst. 23, 357 (1967)

Cowley R.A., Acta Cryst. A43, 825 (1987)

Cowley R.A. and Ryan T.W., J. Phys. D, 20, 61 (1987)

Croce P. and Névot L., J. Appl. Cryst. 7, 125 (1974)

Daillant J., Benattar J.J., Bosio L. and Leger L., Europhys. Lett. 6, 431, (1988)

Darwin C.G., Phil. Mag. 27, 315, 675 (1914)

Dederichs P.H., Phys. Rev. B4, 1041 (1971)

de Neufville J.P., Moss S.C. and Ovshinsky S.R., J. Non. Cryst. Solids, 13, 191 (1973)

Dev B.N., Materlik G., Johnson R.L., Kranz W. and Funke P., Surf. Sci. 178, 1 (1986)

Dietrich S and Wagner H., Phys. Rev. Lett. 51, 1469 (1983)

Dinklage J., J. Appl. Phys. 38, 3781 (1967)

Dorner B., Burkel E., Illini Th and Peisl J., Z. Phys. B, 69, 179 (1987)

Du Mond J. and Youtz J., J. Appl. Phys. 11, 357 (1940)

Eisenberger P., Alexandropolous N.G. and Platzmann P.M., Phys. Rev. Lett. 28, 1519 (1972)

Eisenberger P. and Marra W.C., Phys. Rev. Lett. 46, 1081 (1981)

Ewen P.J.S., Taylor W., Firth A.P. and Owen A.E., Phil. Mag. B, 48, 45 (1983)

Ewen P.J.S., Zakery, A., Firth A.P. and Owen A.E., Phil. Mag. B, 57, 1 (1988)

Feidenhans'l R., PhD Thesis, Risø National Laboratory (1986)

Feidenhans'l R., Surf. Sci. Rep. 10, 105 (1989)

Felcher G.P., Phys. Rev. B 24, 1595 (1981)

Fewster P.F., in 'Heteroepitaxial Approaches in Semiconductors: Lattice Mismatch and its Consequences', p. 278, Electrochem. Soc. (1989a)

Fewster P.F., J. Appl. Cryst. 22, 64 (1989b)

Firth A.P., private communication (1987)

Firth A.P., Ewen P.J.S., Owen A.E. and Huntley C.M., SPIE, 539, 160 (1985)

Fukuhara A. and Takano Y., J. Appl. Cryst. 10, 287 (1977)

Fuoss P.H., Norton L.J., Brennan S. and Fischer-Colbrie A., Phys. Rev. Lett. 60, 600 (1988)

Gartstein E., Acta Cryst., submitted for publication (1989)

Gibbs D., Moncton D.E., D'Amico K.L., Bohr J. and Grier B.H., Phys. Rev. Lett 55, 234 (1985)

Gibbs D., Ocko B.M., Zehner D.M. and Mochrie S.G.J., Phys. Rev. B38, 7303 (1988)

Goldschmidt D., Bernstein T. and Rudman P.S., Phys. Stat. Sol. (a) 41, 283 (1977)

Goldschmidt D. and Rudman P.S., J. Non. Cryst. Solids, 22, 229 (1976)

Gramsbergen E.F., de Jeu W.H. and Als-Nielsen J., J. de Physique, 47, 711 (1986)

Greaves G.N., Elliott S.R., Gladden L.F. and Spence C.A., Proc. Int. Conf. on Effects of Modes of Formation on the Structure of Glass, Vanderbilt Univ. USA (1987)

Grunthaner F.J. and Grunthaner P.J., Mater. Sci. Rep. 1, 65 (1986)

Grunthaner F.J., Grunthaner P.J., Vasquez R.P., Lewis B.F., Maserjian J. and Madhukar A., Phys. Rev. Lett. 43, 1683 (1979)

Guentert O.J., Phys. Rev. 138, A 732 (1965a)

Guentert O.J., J. Appl. Phys. 36, 1361 (1965b)

Hamilton W.A., Klein A.G., Opat G.I. and Timmins P.A., Phys. Rev. Lett. 58, 2770 (1987)

Harada J and Kashiwagura N, J. de Physique, in press (1989)

Harwood N.M., Messoloras S, Stewart R.J., Penfold R. and Ward R.C., Phil. Mag. 58, 217 (1988)

Hayter J.B., Highfield R.R., Pullman B.J., Thomas R.K. and Penfold J., J. Chem. Soc. Faraday Trans. I, 77, 1437 (1981)

Held G.A., Jordan-Sweet J.L., Horn P.M., Mak A. and Birgenau R.J., Phys. Rev. Lett. 59, 2075 (1987)

Henzler M., Appl. Phys. A, 34, 205 (1984)

Herman F. and Kasowski R.V., J. Vac. Sci. Technol. 19, 395 (1981)

Heteroepitaxial Approaches in Semiconductors: Lattice Mismatch and its Consequences, Electrochem. Soc. (1989)

Hill M.J., Tanner B.K., Halliwell M.A.G. and Lyons M.H., J. Appl. Cryst. 18, 446 (1985)

Himpsel F.J., McFeely F.R., Taleb-Ibrahimi A., Yarmoff J.A. and Hollinger G., Phys. Rev. B38, 6084 (1988)

Hollinger G. and Himpsel F.J., Appl. Phys. Lett. 44, 93 (1984)

Iida A. and Kohra K., Phys. Stat. Sol. (a), 51, 533 (1979)

Inoue E., Kokado H. and Shimizu I., Jap. J. Appl. Phys. 43, 101 (1974)

Irene E.A., Phil. Mag. B, 55, 131 (1987)

Ishikawa R. and Kikuchi M., J. Non-Cryst. Solids, 35-36, 1061 (1980)

James R.W., 'The Optical Principles of the Diffraction of X-Rays', (G. Bell and Sons, London) (1949)

Janai M., Phys. Rev. Lett. 47, 726 (1981)

Jona F., Strozier J.A. and Yang W.S., Rept. Progr. Phys. 45, 527 (1982)

Kapp D.S. and Wainfan N., Phys. Rev. 138, A1490 (1965)

Kashihara Y., Kase T. and Harada J., Jap. J. Appl. Phys. 25, 1834 (1986)

Kashihara Y., Kawamura K., Kashiwagura N. and Harada J., Jap. J. Appl. Phys., 26, L1029 (1987)

Kashihara Y., Kimura S. and Harada J., Surf. Sci. 214, 477 (1989)

Kashiwagura N., Kashihara Y., Sakata M., Harada J., Wilkins S.W. and Stevenson A.W., Jap. J. Appl. Phys. 26, L2026 (1987)

Kastner M., Adler D. and Fritzsche H., Phys. Rev. Lett. 37, 1504 (1976)

Kiessig H., Ann. der Physik, 10, 769 (1931)

Kluge G., Phys. Stat. Sol. (a), 101, 105 (1987)

Kortright J.B., J. de Physique, in press (1989)

Kostychin M.T., Mikhailovskya E.V. and Romanenko P.F., Sov. Phys. Sol. Stat. 8, 451 (1966)

Kruger D.W., Savage D.E. and Lagally M.G., Phys. Rev. Lett. 63, 402 (1989)

Kyutt R.N., Petrashen P.V. and Sorokin L.M., Phys. Stat. Sol. (a), 60, 381 (1980)

Lee P.A., Citrin P., Eisenberger P. and Kincaid B.M., Rev. Mod. Phys. 53, 769 (1981)

Lent C.S., and Cohen P.I., Surf. Sci. 139, 121 (1984)

Lomov A.A., Zaumseil P. and Winter U., Acta Cryst. A41, 223 (1985)

Lu B.C. and Rice S.A., J.Chem. Phys. 68, 5558 (1978)

Lum R.M., Klingert J.K., Bylsma R.B., Glass A.M., Macrander A.T., Harris J.D. and Lamant M.G., in 'Heteroepitaxial Approaches in Semiconductors: Lattice Mismatch and its Consequences', p. 183. Electrochem. Soc. (1989)

Lyons M.H. and Halliwell M.A.G., Inst. Phys. Conf. Ser. 76, 445 (1985)

Macrander A.T. and Strege K.E., J. Appl. Phys. 59, 442 (1986)

Marra W.C., Eisenberger P. and Cho A.Y., J. Appl. Phys. 50, 6927 (1979)

Marra W.C., Fuoss P.H., Eisenberger P., Phys. Rev. Lett. 49, 1169 (1982)

Martens G. and Rabe P., J. Phys. C, 14, 1523 (1981)

Maruno S. and Kawaguchi T., J. Appl. Phys. 46, 5312 (1975)

Melroy O.R., Toney M.F., Borges G.L., Samant M.G., Kortright J.G., Ross P.N. and Blum L., Phys. Rev. B38, 10962 (1988)

Mizuno H., Tanaka K. and Kikuchi M., Sol. Stat. Commun. 12, 999 (1973)

Névot L. and Croce P., J. Appl. Cryst. 8, 304 (1975)

Névot L. and Croce P., Revue Phys. Appl. 15, 761 (1980)

Névot L., Pardo B. and Corno J., Revue Phys. Appl. 23, 1675 (1988)

Nigam A.N., Phys Rev. 138, A1189 (1965)

Norris C., private communication (1989)

Norris C., Taylor J.S.G., Moore P.R. and Harris N.W., to be published (1987)

Ocko B.M. and Mochrie S.G.J., Phys. Rev. B38, 7378 (1988)

Ohdomari I., Akatsu H., Yamakoshi Y. and Kishimoto K., J. Appl. Phys. 62, 3751 (1987)

Ourmazd A., Taylor D.W., Rentschler J.A. and Bevk J. Phys Rev. Lett. 59, 213 (1987)

Ovshinsky S.R. and Klose P.H., J. Non-Cryst. Solids, 8-10, 892 (1972)

Pardo B., Megademini T. and André J.M., Revue Phys. Appl. 23, 1579 (1988)

Parish W., Hart M., Erickson C.G., Masciocci N. and Huang T.C., Adv. X-ray Anal. 29, 243 (1986)

Parratt L.G., Phys. Rev. 95, 359 (1954)

Penfold J., Ward R.C. and Williams W.G., J. Phys. E, 20, 1411 (1987)

Pershan P.S., private communication (1989)

Pershan P.S., Braslau A, Weiss A.H. and Als-Nielsen J., Phys. Rev. A35, 4800 (1987)

Petrashen P.V., Korev E.K., Chukhovskii F.N. and Degrtyarev Y.L., Sov. Phys. Sol. Stat. 25, 695 (1983)

The Physics of SiO_2 and its Interfaces, edited by Sokrates T. Pantelides, (Pergamon, New York) (1978)

Pick M.A., Bickmann K., Potahl E., Zwoll K. and Wenzl H., J. Appl. Cryst. 10, 450 (1977)

Piecuch M., Revue Phys. Appl. 23, 1727 (1988)

Pietsch U. and Borchard W., J. Appl. Cryst. 20, 8 (1987)

Pomerantz M. and Segmüller A., Thin Solid Films, 68, 33 (1980)

Pukite P.R., Lent C.S. and Cohen P.I., Surf. Sci. 161, 39 (1985)

Pynn R., Fujii Y. and Shirane G., Acta Cryst. A39, 38 (1983)

Rennie J.H.S. and Elliott S.R., J. Non-Cryst. Solids, 77-78, 1161 (1985)

Renninger M., Acta Cryst. A24, 143 (1968)

Robinson I.K., Phys. Rev. Lett. 50, 1145 (1983)

Robinson I.K., Phys. Rev. B33, 3830 (1986)

Robinson I.K., in 'Handbook on Synchrotron Radiation', vol. 3, (North-Holland, Amsterdam) (1989)

Robinson I.K.,Kuk Y. and Feldman L.C., Phys. Rev. B29, 4762 (1984)

Robinson I.K., Waskiewicz W.K., Tung R.T. and Bohr J., Phys. Rev. Lett. 57, 2714 (1986)

Richards R.W., Quereshi M.S. and Thomas R.K., ISIS Report (1988)

Rochet F., Rigo S., Froment M., d'Anterroches C., Maillot C., Roulet H. and Dufour G., Phil. Mag. B55, 309 (1987)

Rosen D.L., Brown D., Gilfrich J. and Burkhalter P, J. Appl. Cryst. 21, 136 (1988)

Rovinskii B.M., Sinaiskii V.M. and Sidenko V.I., Sov. Phys. Sol. State, 14, 340 (1972)

Ryan T.W., PhD Thesis, University of Edinburgh. (1986)

Ryan T.W., Hatton P.D., Bates S., Watt M., Sotomayor-Torres C., Claxton P.A. and Roberts J.S., Semicond. Sci. Technol. 2, 241 (1987)

Sauro J.P., Bindell J. and Wainfan N., Phys. Rev. 143, 439 (1966)

Sauro J.P., Fankuchen I. and Wainfan N., Phys. Rev. 132, 1544 (1963)

Shen Q., Blakely J.M., Bedzyk M.J. and Finkelstein K.D., Phys. Rev. B40, 3480 (1989)

Sinha S.K., Sirota E.B., Garoff S. and Stanley H.B., Phys. Rev. B38, 2297 (1988)

Smirnov L.A. and Anokhin S.B., Opt. Spectrosc. 48, 315 (1980)

Spiller E., Revue Phys. Appl 23, 1687 (1988)

Street A. and Mott N.F., Phys Rev. Lett. 35, 1293 (1975)

Tai K.L., Ong E. and Vadimsky R.G., Proc. Electrochem. Soc. 82-89, 9 (1982)

Takagi S., J. Phys. Soc. Japan, 26, 1239 (1969)

Tanaka K., in 'Fundamental Physics of Amorphous Semiconductors', ed. F. Yonezawa (Berlin: Springer-Verlag) (1981)

Tanner B.K. and Hill M.J., J. Phys. D., 19, L229 (1986a)

Tanner B.K. and Hill M.J., Adv. X-ray Analysis, 29, 337 (1986b)

Taupin D., Bull. Soc. Fr. Min. Cryst. 87, 469 (1964)

Torrance K.E. and Sparrow E.M., J. Opt. Soc. Am. 57, 1105 (1967)

Underwood H. and Barbee T.W., Appl. Opt. 20, 3027 (1981)

Vandenburg J.M., Hamm R.A., Macrander A.T., Panish M.B. and Temkin H., Appl. Phys. Lett. 48, 1153 (1986)

van der Veen J.F., Surf. Sci. Rep. 5, 199 (1986)

Vardanyan D.M., Manoukyan H.M. and Petrosyan H.M., Acta Cryst. A41, 218, 222 (1985)

Vineyard G.H., Phys. Rev. B26, 4146 (1982)

Vlieg E., PhD Thesis, FOM-Institute for Atomic and Molecular Physics, Amsterdam (1988)

Vlieg E., Fischer A.E.M.J., van der Veen J.F., Dev B.N. and Materlik G., Surf. Sci. 178, 36 (1986)

Vlieg E., van der Gon A.W., van der Veen J.F., Macdonald J.E. and Norris C., Surf. Sci. 209, 100 (1989)

Wagendristel A., Bangert H. and Tonsern W., Surf. Sci. 86, 68 (1979)

Wainfan N. and Parratt L.G., J. Appl. Phys. 31, 1331 (1960)

Wagendristel A., Schurz H., Ehrmann-Falkenau E. and Bangert H., J.Appl.Phys. 51, 4808 (1980)

Wainfan N., Scott N.J. and Parratt L.G., J. Appl. Phys. 30, 1604 (1959)

Warren B.F. and Clarke J.S., J. Appl. Phys. 36, 324 (1965)

Wolcryz M. and Lukaszewich, J. Appl. Cryst. 15, 406 (1982)

Wollschläger J. and Henzler M., Phys. Rev. B39, 6052 (1988)

Wong P. and Bray A.J., Phys. Rev. B37, 7751 (1988)

Yaji T. and Kurita S., J. Appl. Phys. 54, 647 (1983)

Yoneda Y., Phys. Rev. 131, 2010 (1963)

Yoshikawa A., Ochi O., Nagai H. and Mizushima Y., Appl. Phys. Lett. 29, 677 (1976)

Zachariasen W.H., 'Theory of x-ray diffraction in crystals', (New York: Wiley) (1945)

Zaumseil P. and Winter U., Phys. Stat. Sol. (a), 73, 455 (1982)

From: ADVANCES IN X-RAY ANALYSIS, Vol. 31
Edited by Charles S. Barrett, John V. Gilfrich, Ron Jenkins,
John C. Russ, James W. Richardson, Jr. and Paul K. Predecki
(Plenum Publishing Corporation, 1988)

GRAZING INCIDENCE X-RAY SCATTERING STUDIES OF SINGLE QUANTUM WELLS

S.Bates, P.D.Hatton, C.A.Lucas and T.W.Ryan*

Department of Physics, University of Edinburgh
Mayfield Rd., Edinburgh, U.K.

and

S.J.Miles and B.K.Tanner

Department of Physics, University of Durham
South Rd., Durham, U.K.

ABSTRACT

X-ray scattering techniques at grazing incidence have been used to characterize single quantum well hetero-structures. Double- and triple-axis diffractometry has been used to determine lattice mismatch and layer thickness of a 250Å thick layer of AlInAs grown by MBE on an InP substrate and capped by a 45Å GaAs layer. Reflectivity measurements in the triple-crystal mode permit accurate measurement of individual layer thicknesses, relative electron density and interface roughnesses on the Ångstrom level.

INTRODUCTION

Over the past decade X-ray double axis diffractometry has become widespread for the characterization of heteroepitaxial layers of III-V compounds for optical communications devices[1]. The technique provides, (non-destructively), data on layer thickness, composition, uniformity and perfection necessary to meet the increasingly high tolerances demanded of electro-optic devices. Rocking curve analysis of single, thick layers can be performed at a very rudimentary level and such analysis is often adequate for on-line quality control. In graded[2,3] or multiple layers of which at least two are of the same composition[4,5] the rocking curves become much more complex and computer simulation is necessary for interpretation[1,3].

As most III-V device structures are grown on (001) wafers, the 004 reflection with CuK radiation is readily accessible and most practitioners use this symmetric Bragg

*Now at Philips I&E, Lelyweg 1, 7602 EA, Alemlo, Netherlands

geometry exclusively for epilayer characterization. However, for layers less than 0.2 um thickness, the layer peaks become extremely broad and of low intensity, making analysis difficult and data collection times long. Use of highly asymmetric reflections with glancing incidence angle provide a means of reducing the extinction distance and hence penetration depth of the X-rays. The result is both an increase in layer intensity and a sharpening of the layer rocking - curve peaks from sub-micron layers[4,6]. Using synchrotron radiation to tune wavelength over an extensive range, Hill and Tanner[7] showed that for layers typically 0.25 um thick such sharp, intense peaks could be obtained, in very good agreement with theoretical predictions across the whole wavelength range.

Triple-crystal diffractometry on the other hand is not in such extensive use and only recently has it been used for epilayer characterization. In the highly asymmetric geometry it has been exploited to determine layer thickness, composition and internal-interface roughness of a buried layer only 230Å thick[8].

As early as 1931, Kiessig[9] showed that measurements of reflectivity of surfaces at angles close to the region of total external reflection gave information on the variation of electron density below the surface. Using a triple-crystal diffractometer to measure specular reflectivity at grazing incidence, Cowley and Ryan[10] showed that the thickness and interface roughness of amorphous films on semiconductor crystals could be determined experimentally. Recently, we have shown[11] that the combination of glancing-incidence diffraction and specular reflectivity measurements on a heterostructure composed of layers less than about 200Å thick could yield structural information on layers as thin as 20Å. In this paper we compare the data obtained on such a structure by glancing incidence diffractometry and specular reflection measurements using both double and triple-crystal techniques. The additional information inherent in the triple crystal configuration is highlighted.

EXPERIMENTAL DETAILS

All experiments reported here were performed on a wedge-shaped specimen from a disc consisting of a layer of AlInAs of nominal thickness 200Å grown by MBE on a (001) oriented InP wafer; the layer being capped by about 20Å of GaAs.

Double-crystal diffractometry was performed at Durham on a prototype of the Bede Model 150 diffractometer. The 044 reflection was used with CuK radiation which has an incidence angle of 2.9°; the reference reflection being the 044 from a highly perfect InP crystal cut parallel to (011). Thus all double-crystal experiments were performed in the (+-) parallel geometry which is non-dispersive in energy and highly sensitive to lattice strain. The instrumental angular resolution was 0.1 arc secs. At the sample, the beam size was about 0.25mm in the incidence plane by 1mm perpendicular to this plane. All double-crystal data was taken after the

specimen had been heated to 200°C for 2 hours[11] while the triple crystal data given here was taken prior to heating.

Triple-crystal diffractometry was performed on the diffractometer built at Edinburgh based on a Huber 430/440 goniometer with a GEC Avionics GX21 rotating anode X-ray generator[12]. Reference and analyser were (111) cut Ge crystals used in symmetric Bragg geometry giving a wavevector resolution in the scattering plane of 5 x 10^{-4}Å^{-1}, corresponding to an angle of about 25 secs.

GLANCING-ANGLE DIFFRACTOMETRY

Double-crystal diffractometry

Figure 1(a) shows a rocking curve recorded close to the specimen edge, the corresponding simulation[2] using the Takagi-Taupin dynamical theory equations being shown in Fig.1(b). This simulation assumes abruptly flat interfaces and uniform composition through the layers. The experimental substrate peak width was 50 secs. compared with 30 secs. predicted in the simulation. This arises as a result of the curvature of the wafer due to mismatch in lattice parameters of substrate and layer or to mounting strains. In order to match these peak widths, a 50 secs. change in incidence angle across the beam area had to be convoluted into the simulation of Fig.1(b). Curvature affects both width and relative height of the layer peak, both increasing with increasing curvature. In order to fit the experimental layer peak width of 204 secs and relative height, an additional tilt of 2° had to be added to the incidence angle, reducing the asymmetry. This could have arisen from misalignment of the [110] direction on mounting, which is not corrected by the tilt optimization. From the fitting we deduce that the mismatch is -4785 p.p.m. which corresponds to 45.21% In with a layer thickness 355Å. In order to match exactly the layer peak shape a non-

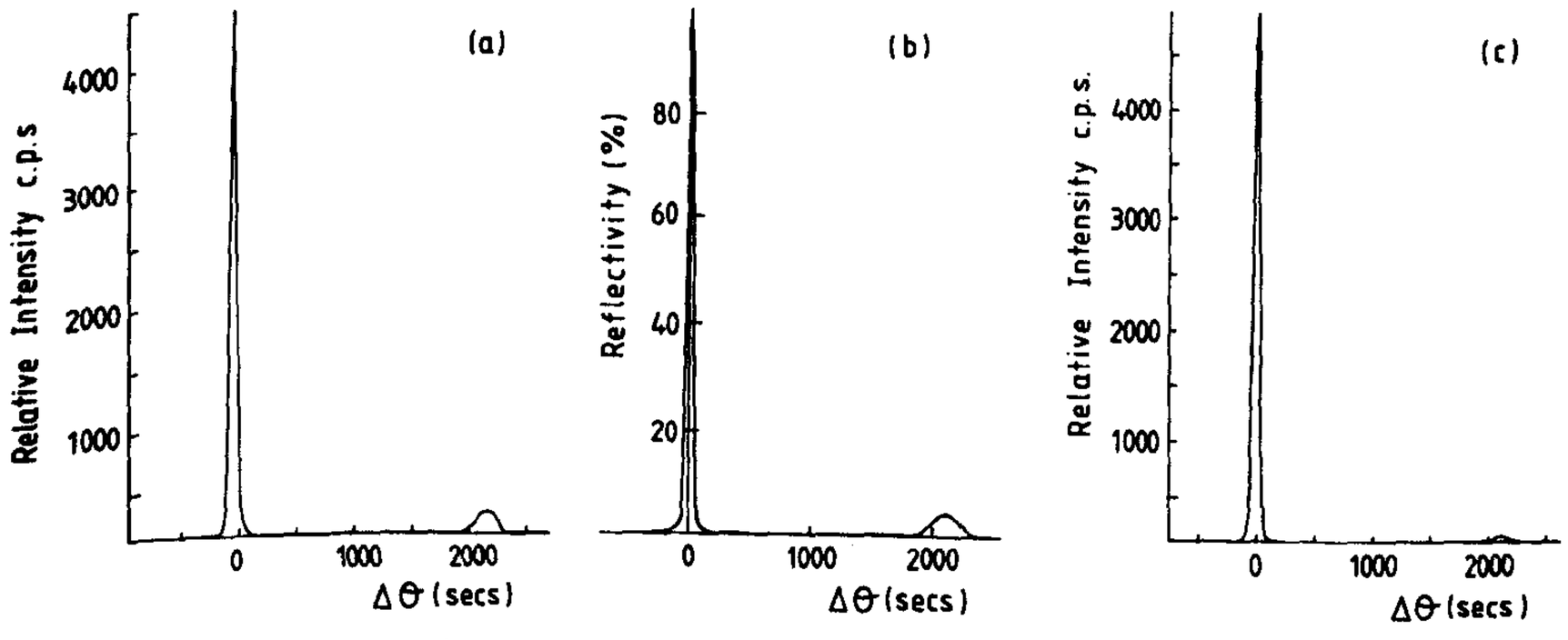

Fig.1 (a) Experimental double crystal rocking curve taken near wafer edge, (b) dynamical theory simulation, (c) experimental rocking curve near wafer centre. 80s count time per data point spaced 10.2 arc sec.

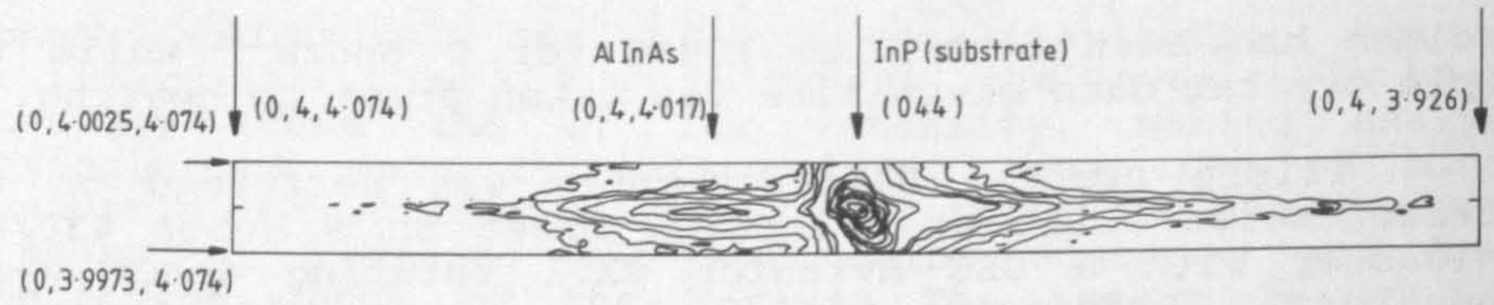

Fig.2 Equal intensity contour plot of scattering around the 044 reciprocal lattice point for the AlInAs on InP specimen.

uniform composition must be assumed. No structure associated with the GaAs capping layer could be clearly distinguished and the thickness of this was taken to be 50Å in the simulations. The layer is far from uniform across the wafer and Fig. 1(c) shows a rocking curve taken near the specimen centre, where it is seen that peak heights, widths and separation differ markedly from Fig. 1(a). Here the mismatch is -4630 p.p.m. (45.43% In) and layer thickness 200Å.

Triple-crystal diffractometry

The variation in thickness and composition across the wafer makes a one-to-one correlation between double- and triple-crystal data impossible. Our triple-crystal instrument provides additional information principally as a result of the high signal-to-noise ratio but also the removal of the effects of specimen curvature by use of the analyser. In a triple-crystal diffraction experiment, specimen and analyser are scanned to produce a two-dimensional map of scattered intensity in an area of reciprocal space determined by the incidence plane. Figure 2 shows a typical plot of equal-intensity contours on a quasi-logarithmic scale over four decades of intensity. The effect of instrumental resolution and aberrations on the plots has been discussed by Ryan[12].

In order to compare with the double-crystal rocking curves, the intensity data must be integrated parallel to (010). Figure 3(a) shows this intensity plotted on a true logarithmic scale and Fig.3(b) shows a least-squares fit to

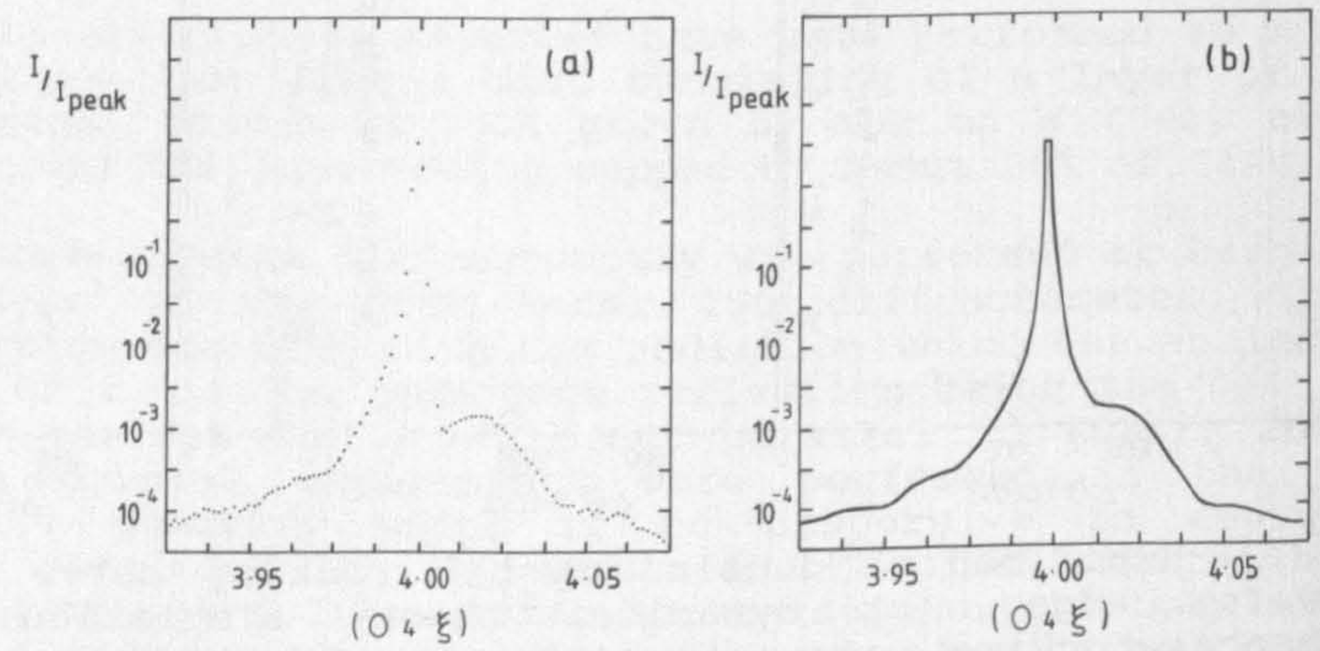

Fig.3 Intensity distribution parallel to [001] through the InP 044 Bragg peak (a) experimental, (b) simulation.

Table 1. Layer thickness, r.m.s. roughness and mismatch data used in the fit of Fig. 3

Layer	ThicknessÅ	r.m.s. roughnessÅ	mismatch (ppm)
GaAs	29±0.4	<1	600±150
Disordered	15±0.5	-	-
AlInAs	204±0.4	1.0±0.7	-4050±100
Disordered	20±1.0	-	-
InP substrate	-	2.5±1.0	-

the data, using the parameters given in Table 1 in a kinematical theory. Note the necessary inclusion of two disordered layers at the interfaces and surface roughnes. The thickness of the very thin capping layer and surface roughness parameters are determined from the diffuse scattering along the crystal "truncation rod" far from the reciprocal lattice point. Although insensitive to exact value, the oscillations at the 10^{-4} level are determined by the GaAs cap thickness.

REFLECTIVITY MEASUREMENTS IN TRIPLE-CRYSTAL MODE

Use of an analyser crystal to define the direction and wavelength of the scattered beam enables the effects of diffuse scattering to be eliminated and the effect of wafer curvature is removed. Full experimental details are to be found in Cowley and Ryan[10]. For angles of incidence just above the critical angle for total external reflection, oscillations in the reflectivity are observed (Fig.4) resulting from the surface layer structures. As the reflectivity is determined by electron density, and not the long-range order, amorphous layers contribute to the reflectivity in the same way as crystalline layers.

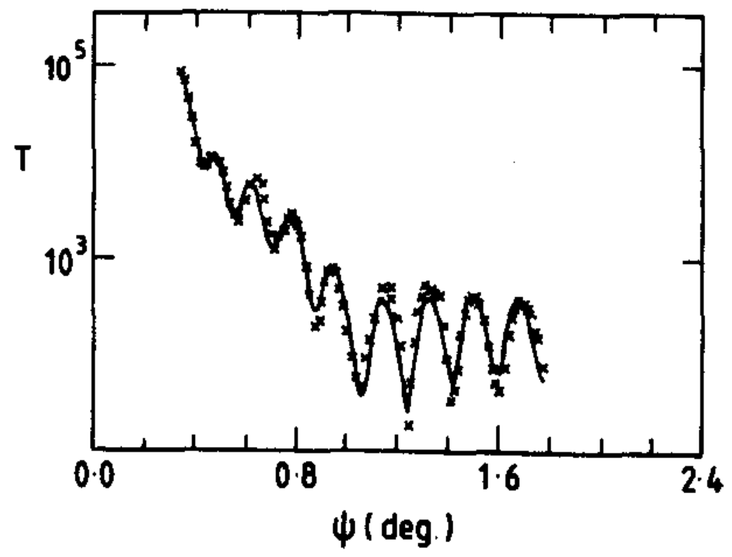

Figure 4. Plot of the product of reflectivity and (scattering angle)^4 versus incidence angle. Crosses are experimental data points, solid line is a least-squares fit to theory[11].

Table 2 Parameters used for least-squares fit to the data in Fig.4

Layer	Thickness(Å)	r.m.s.roughness(Å)	Fractional electron density change
Water	22.3±0.7	< 1.0	-0.90±0.02
GaAs	30.5±0.7	8.8±0.6	-0.24±0.02
AlInAs	210.0±0.8	8.9±0.7	-0.11±0.04
InP substrate	-	4.2±0.8	0

DISCUSSION

Both double-and triple-axis diffractometry can be used to provide thickness and composition data in layers less than 200Å thick. Provided that a proportional counter with a narrow energy window is used, there appears to be similar quality data to be gained from the two techniques (see also[3]). In the double-crystal method, wafer curvature must be determined from the substrate peak width and included in fitting the layer peak. The effects of curvature are absent in triple crystal diffractometry which also provides 2D information on the scattering in reciprocal space. In reflectivity measurements the triple-crystal mode is far superior to the double-crystal mode as both diffuse scatter and wafer curvature are eliminated. Reflectivity measurements in double-crystal mode with a 100um slit before the detector gave similar quality data but only over a restricted range of scattering angles because of the increased background. For III-V films over 100Å thick, electron density and film thickness can be determined but the triple-crystal data is needed for determination of interface roughness.

REFERENCES

1. B.K.Tanner, Double Crystal X-ray Diffraction and Topography, in: "Analysis for the development of microelectronic devices",M. Grasserbauer and H.Werner,eds., Wiley, Chichester.
2. M.J.Hill, B.K.Tanner, M.A.G.Halliwell and M.H.Lyons, Simulation of X-ray double crystal rocking curves of multiple and inhomogeneous epitaxial layers, J. Appl. Cryst.,18 (1985) 446
3. B.M.Paine,Materials analysis with X-ray rocking curves, Mat. Res. Soc. Symp. Proc. 69 (1986) 39
4. B.K.Tanner and M.J.Hill, X-ray double crystal diffractometry of multiple and very thin heteroepitaxial layers, Adv. X-ray Anal. 29 (1986) 337
5. X.Chu and B.K.Tanner, Interference effects in double crystal X-ray rocking curves of GaAlAs/GaAs laser structures Appl. Phys. Letts. 49 (1986) 1773
6. M.A.G.Halliwell and M.H.Lyons, Double crystal diffractometry of III-V semiconductor device structures, Inst. Phys. Conf. Ser. 76 (1985) 445
7. M.J.Hill and B.K.Tanner, Double axis X-ray diffractometry at glancing angles J. Phys. D: Appl. Phys. 19 (1986) L229
8. T.W.Ryan, P.D.Hatton, S.Bates, M.Watt, C.Sotomayor-Torres, P.A Claxton a J.S.Roberts, X-ray scattering from a single-quantum-well Semicond. Sci. Technol. 2 (1987) 241
9. H.Kiessig, Interferenz van Röntgenstrahlen an dünnen schichten Ann. Physik 10 (1931) 715
10. R.A.Cowley and T.W.Ryan, X-ray scattering studies of thin films and surfaces, J.Phys.D:Appl. Phys. 20 (1987) 61
11. C.A.Lucas, P.D.Hatton, S.Bates, T.W.Ryan, S.J.Miles and B.K. Tanner, Characterization of nanometer-scale epitaxial structures by grazing incidence X-ray diffraction and specular reflectivity, J. Appl. Phys. submitted
12. T.W.Ryan, Ph.D. Thesis, Edinburgh University (1986)

+Work supported by the Science & Engineering Research Council

Acta Cryst. (1989). A45, 416–422

The Resolution Function of an X-ray Triple-Crystal Diffractometer: Comparison of Experiment and Theory

BY C. A. LUCAS, E. GARTSTEIN AND R. A. COWLEY

Department of Physics, University of Edinburgh, Mayfield Road, Edinburgh EH9 3JZ, Scotland

(*Received* 28 *June* 1988; *accepted* 16 *January* 1989)

Abstract

The resolution function of an X-ray triple-crystal diffractometer on a rotating-anode source has been studied both experimentally and theoretically. Three different experimental configurations were used, with perfect germanium, distorted germanium and pyrolytic graphite as monochromator and analyser, leading to changes in the resolution of two orders of magnitude. The results are compared with a Gaussian description of the resolution function and it is found that this describes the width of the central part with an accuracy of better than 25%. The wings of the resolution in the high-resolution mode show the effect of the non-Gaussian resolution elements but these are reproduced by a full numerical convolution theory of the resolution function.

I. Introduction

With the availability of intense X-ray sources, such as high-brilliance rotating-anode generators and synchrotron radiation sources, the triple-crystal X-ray diffractometer has found increasing use in high-resolution diffraction experiments. The ability to probe the reciprocal space of a sample crystal with a momentum resolution as small as 10^{-4} Å^{-1} has led to new results in the study of phase transitions (*e.g.* Ryan, Nelmes, Cowley & Gibaud, 1986) and of surfaces and interfaces (*e.g.* Andrews & Cowley, 1985; Robinson, 1986; Cowley & Ryan, 1987). However, even when using perfect crystals as monochromator and analyser, a thorough understanding of the instrumental resolution is required in order to measure quantitatively the nature of the scattered intensity in an experiment. In addition, a detailed knowledge of the resolution function in wave-vector space can enable the measurement of relatively weak diffuse scattering from critical fluctuations or surfaces, without interference from the strong scattering arising from the Bragg reflection (Andrews & Cowley, 1986).

Although the resolution function of a neutron three-axis spectrometer has been dealt with, both theoretically and experimentally, by several authors (Cooper & Nathans, 1967; Stedman, 1968; Bjerrum-Møller & Neilsen, 1970; Chesser & Axe, 1973), the corresponding calculation for an X-ray diffractometer has received comparatively little attention. The use of nearly perfect crystals for monochromator and analyser in the X-ray case means that their scattering must be described by dynamical diffraction theory (Zachariasen, 1945; Batterman & Cole, 1964). Reflection from a perfect crystal is then governed by the characteristic long-tailed asymmetric form of the Darwin profile, and not by the Gaussian form, assumed for the case of mosaic crystals, and used in the neutron scattering calculations. Unlike the Gaussian approximation, which may be solved largely analytically, convolution of these non-Gaussian profiles requires a complex numerical integration. Pynn, Fujii & Shirane (1983) have applied the formalism of Bjerrum-Møller & Neilsen (1970) to the case of the perfect-crystal X-ray diffractometer, and calculated the central part of the resolution function. They compared their calculations with experimental measurements of the peak shapes of the Bragg reflections from perfect germanium and silicon crystals and found good agreement. Recently Cowley (1987), following a suggestion by Pynn *et al.* (1983), approximated the results of the dynamical theory by a Gaussian, enabling the central part of the resolution function to be obtained analytically in terms of relatively simple expressions. It was hoped that, after convolution with other resolution elements, the calculations would be sufficiently accurate to allow a straightforward analysis of experimental results, and an easier planning of new experiments.

In this paper we report on further studies of the resolution function of a triple-crystal X-ray diffractometer with a rotating-anode source. Measurements of the resolution function of the diffractometer have been performed with three different sets of monochromator and analyser crystals; perfect germanium, distorted germanium and pyrolytic graphite. Measurements for a variety of different wave-vector transfers are described in § II, and these are compared with the widths calculated using the Gaussian approximation in § III. The tails of the resolution are far from Gaussian in form when perfect crystals are used for monochromator and analyser. This is because their scattering is described by the Darwin curve which has $1/\theta^2$ wings, rather than the more rapidly decreasing Gaussian wings assumed in the

0108-7673/89/060416-07$03.00

Table 3. *Calculated and experimental atomic thermal tensors*

(*exp.*) Experimental (Brock & Dunitz, 1982; Mason, 1964); (*a*) without charges; (*b*) with charges.

$$T(\mathbf{H}) = \exp\left[-2\pi^2 \sum_i \sum_j U_{ij} a_i^* a_j^* H_i H_j\right],$$

$$\mathbf{H} = (hkl)(\text{Å}^2 \times 10^4).$$

	U_{11}	U_{22}	U_{33}	U_{12}	U_{13}	U_{23}
Naphthalene (92 K)						
C(1) (exp.)	165	202	140	14	94	2
(*a*)	179	211	131	13	85	−4
(*b*)	172	209	133	15	83	−4
C(2)	136	138	157	−9	85	−25
	148	151	137	−7	68	−27
	136	147	140	−7	65	−28
C(3)	100	110	144	6	79	3
	100	113	126	2	56	−3
	92	107	129	2	56	−3
C(4)	128	113	183	−1	102	15
	138	132	168	−3	84	16
	129	126	175	−1	87	18
C(5)	166	179	187	18	127	40
	169	192	162	17	101	38
	165	189	168	22	105	41
Anthracene (290 K)						
C(1)	680	820	582	13	367	−62
	682	1078	703	66	358	−12
	594	1075	640	26	331	−57
C(2)	495	585	497	−21	239	−65
	596	786	694	−2	292	−110
	505	786	644	−30	276	−138
C(3)	376	447	531	−4	239	−3
	396	557	651	2	228	−36
	346	551	599	−5	223	−51
C(4)	397	445	557	−11	252	−87
	426	504	710	−39	244	−34
	369	497	659	−36	245	−44
C(5)	361	445	540	−24	236	59
	383	550	679	−1	241	21
	342	541	623	1	239	9
C(6)	474	613	625	32	279	−87
	541	758	809	−15	347	122
	488	744	742	−6	342	102
C(7)	653	864	617	34	374	171
	643	1057	789	56	400	157
	583	1044	713	43	380	116

should be made, at least in the general case and with present-day potentials.

We acknowledge the Spanish CAICYT for financial support of this work. Thanks are due to a referee for many helpful comments.

References

BONADEO, H. & BURGOS, E. (1982). *Acta Cryst.* **A38**, 29-33.

BORN, M. & HUANG, K. (1954). *Dynamical Theory of Crystal Lattices*. Oxford: Clarendon Press.

BROCK, C. & DUNITZ, J. (1982). *Acta Cryst.* **B38**, 2218-2228.

BUSING, W. R. (1972). *Acta Cryst.* **A28**, S252-S253.

CALIFANO, S., RIGHINI, R. & WALMSLEY, S. H. (1979). *Chem. Phys. Lett.* **64**, 491-494.

CHAPLOT, S. L., LEHNER, N. & PAWLEY, G. S. (1982). *Acta Cryst.* **B38**, 483-487.

CRIADO, A. & MARQUEZ, R. (1988). *Acta Cryst.* **A44**, 76-78.

DELLA VALLE, R. G., FRASCASSI, P. F., RIGHINI, R. & CALIFANO, S. (1983). *Chem. Phys.* **74**, 179-195.

DORNER, B., BOKHENKOV, E. L., CHAPLOT, S. L., KALUS, J., NATKANIEC, I., PAWLEY, G. S., SCHMELZER, U. & SHEKA, E. F. (1982). *J. Phys. C*, **15**, 2353-2365.

EWALD P. P. (1921) *Ann. Phys. (Leipzig)*, **64**, 253.

FILIPPINI, G. (1985). *J. Mol. Struct.* **130**, 117-124.

FILIPPINI, G. & GRAMACCIOLI, C. M. (1986). *Acta Cryst.* **B42**, 605-609.

FILIPPINI, G., GRAMACCIOLI, C., SIMONETTA, M. & SUFFRITTI, G. B. (1973). *J. Chem. Phys.* **59**, 5088-5101.

FILIPPINI, G., GRAMACCIOLI, C., SIMONETTA, M. & SUFFRITTI, G. B. (1976). *Acta Cryst.* **A32**, 259-264.

FILIPPINI, G., GRAMACCIOLI, C., SIMONETTA, M. & SUFFRITTI, G. B. (1978). *Mol. Phys.* **35**, 1659-1667.

FILIPPINI, G., SIMONETTA, M. & GRAMACCIOLI, C. M. (1984). *Mol. Phys.* **51**, 445-459.

GAMBA, Z. & BONADEO, H. (1981). *J. Chem. Phys.* **75**, 5059-5066.

GAMBA, Z. & BONADEO, H. (1982). *J. Chem. Phys.* **76**, 6215-6220.

GRAMACCIOLI, C. M. & FILIPPINI, G. (1983). *Acta Cryst.* **A39**, 784-791.

GRAMACCIOLI, C. M. & FILIPPINI, G. (1985). *Acta Cryst.* **A41**, 356-361, 361-365.

GRAMACCIOLI, C. M., FILIPPINI, G. & SIMONETTA, M. (1982). *Acta Cryst.* **A38**, 350-356.

HIRSHFELD, F. L. & MIRSKY, K. (1979). *Acta Cryst.* **A35**, 366-370.

JINDAL, V. K. & KALUS, J. (1983). *J. Phys. C*, **16**, 3061-3080.

JINDAL, V. K., KALUS, J., BOKHENKOV, E. L., CHAPLOT, S. L., DORNER, B., NATKANIEC, I., PAWLEY, G. S. & SHEKA, E. F. (1982). *J. Phys. C*, **15**, 7283-7294.

KROON, P. & VOS, A. (1978). *Acta Cryst.* **A34**, 823-824.

LEHMANN, M. S. & PAWLEY, G. S. (1972). *Acta Chem. Scand.* **26**, 1996-2004.

LIFSON, S. & WARSHEL, A. (1968). *J. Chem. Phys.* **49**, 5116-5129.

LINK, K. H., GRIMM, H., DORNER, B., ZIMMERMANN, H., STILLER, H. & BLECKMANN, P. (1985). *J. Phys. Chem. Solids*, **46**, 135-142.

LONSDALE, K. & MILLEDGE, J. (1961). *Acta Cryst.* **14**, 59-61.

MASON, R. (1964). *Acta Cryst.* **17**, 547-555.

MULLIKEN, R. S. (1955). *J. Chem. Phys.* **23**, 1833-1840, 1841-1846.

NATKANIEC, I., BOKHENKOV, E. L., DORNER, B., KALUS, J., MACKENZIE, G. A., PAWLEY, G. S., SCHMELZER, U. & SHEKA, E. F. (1980). *J. Phys. C*, **13**, 4265-4283.

NETO, N., RIGHINI, R., CALIFANO, S. & WALMSLEY, S. H. (1978). *Chem. Phys.* **29**, 167-179.

PAWLEY G. S. (1972). *Phys. Status Solidi B*, **39**, 475-487.

PAWLEY, G. S. & CYVIN, S. J. (1970). *J. Chem. Phys.* **52**, 4073-4077.

PAWLEY, G. S., MACKENZIE, G. A., BOKHENKOV, E. L., SHEKA, E. F., DORNER, B., KALUS, J., SCHMELZER, U. & NATKANIEC, I. (1980). *Mol. Phys.* **39**, 251-260.

PAWLEY, G. S. & YEATS, E. A. (1969). *Acta Cryst.* **B25**, 2009-2013.

RASTOGI, A., ANDERSON, A. & LEECH, J. W. (1979). *Can. J. Phys.* **57**, 2120-2125.

SCHOMAKER, V. & TRUEBLOOD, K. N. (1968). *Acta Cryst.* **B24**, 63-76.

SHEKA, E. F., BOKHENKOV, E. L., DORNER, B., KALUS, J., MACKENZIE, G. A., NATKANIEC, I., PAWLEY, G. S. & SCHMELZER, U. (1984). *J. Phys. C*, **17**, 5893-5914.

VENKATARAMAN, G. & SAHNI, V. C. (1970). *Rev. Mod. Phys.* **42**, 409-470.

WILLIAMS, D. E. (1967). *J. Chem. Phys.* **47**, 4680-4684.

WILLIAMS, D. E. & COX, S. R. (1984). *Acta Cryst.* **B40**, 404-417.

WILLIAMS, D. E. & STARR, T. L. (1977). *Comput. Chem.* **1**, 173-177.

WILLIS, B. T. M. & PRYOR, A. W. (1975). *Thermal Vibrations in Crystallography*. Cambridge Univ. Press.

Gaussian theory. An understanding of these tails is essential if measurements are to be performed close to the Bragg reflections. In § II we present a qualitative description of the origin of these tails or streaks (Ryan, 1986). A quantitative description necessarily requires a numerical convolution over the different resolution elements. A computer program for doing such convolutions has recently been written (Gartstein, 1989) to calculate not only the central part of the resolution function, but also the wings down to the 10^{-3} level. In § III we compare the results of these calculations with the measurements and find very satisfactory agreement between experiment and theory. The results are discussed in a final section.

II. Experiments and results

1. *The experiments*

The experiments were performed at Edinburgh University using a triple-axis X-ray diffractometer based on a Huber 430/440 goniometer, and utilizing a GEC Avionics GX21 rotating-anode X-ray generator with a copper target. Cu $K\alpha_1$ X-rays (λ = 1·54051 Å, $\Delta\lambda$ = 0·00058 Å) were used, and the focal spot of the rotating-anode tube was a vertical line of height 3 mm and width 0·3 mm, viewed at a take-off angle of 6°. Fig. 1 shows a schematic picture of a triple-crystal X-ray diffractometer in the (+, −, +) configuration. This arrangement, in which $\theta_M = \theta_A \neq \theta_S$, was used throughout the experiments. A variable-width slit, immediately in front of the monochromator crystal, was used to limit the angular range of the X-ray beam incident on the monochromator and hence, for the germanium crystals, to eliminate the $K\alpha_2$ line. The monochromator was at a distance of 200 mm from the source. An additional slit, placed between the monochromator and sample crystals, limited the vertical divergence of the X-rays and ensured that the incident beam was fully intercepted by the sample. No other collimators were present between the monochromator crystal and the detector. The detector was a proportional counter with about 1·5 keV FWHM energy resolution at 8 keV.

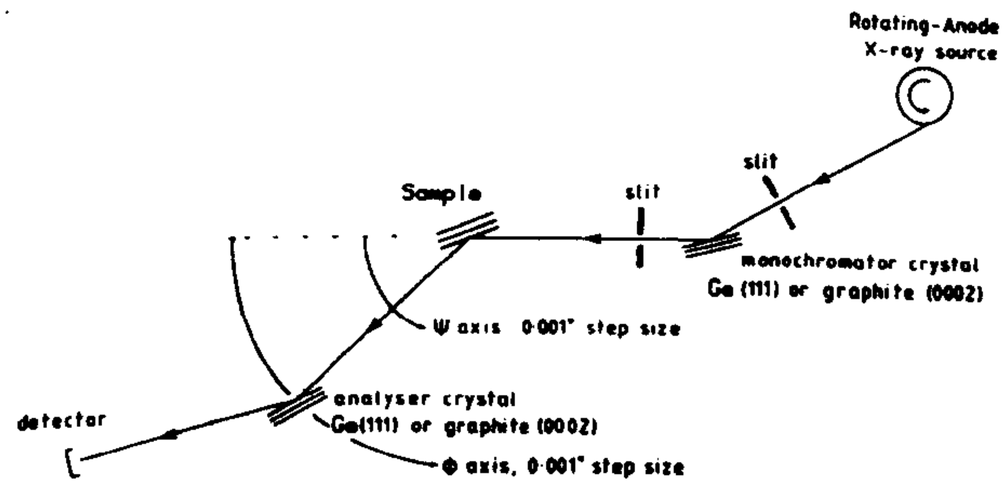

Fig. 1. Schematic diagram of a triple-crystal X-ray diffractometer.

Three different sets of crystals were used for the monochromator and analyser:

(1) *High resolution.* The 111 reflections of perfect germanium crystals were used for both monochromator and analyser. These reflections have a Darwin width of $4{\cdot}3 \times 10^{-3}$ °.

(2) *Intermediate resolution.* The 111 reflections from poor-quality germanium crystals were used as monochromator and analyser. These crystals had a measured mosaic spread (FWHM) of about 0·021°.

(3) *Low resolution.* The (0002) planes of pyrolytic graphite (Union Carbide UCAR grade ZYA) were used as monochromator and analyser. These crystals have a mosaic structure with an approximately Gaussian distribution of orientations and a mosaic spread of 0·4 (1)° (FWHM).

These three arrangements then provide for changes in the resolution of the diffractometer by two orders of magnitude.

Unfortunately the resolution function of the diffractometer cannot be measured directly, especially in its high-resolution mode, because the scattering from the sample is not a delta function in reciprocal space. Clearly the sample must be a material which has a perfect crystal structure, with a fairly large number of reciprocal-lattice points to enable the theory to be tested over a range of wave-vector transfers. We chose to use single crystals of InP or GaAs, grown in wafer form for use as substrates for the MBE growth of semiconductor heterostructures. The wafer had the [100] axis perpendicular

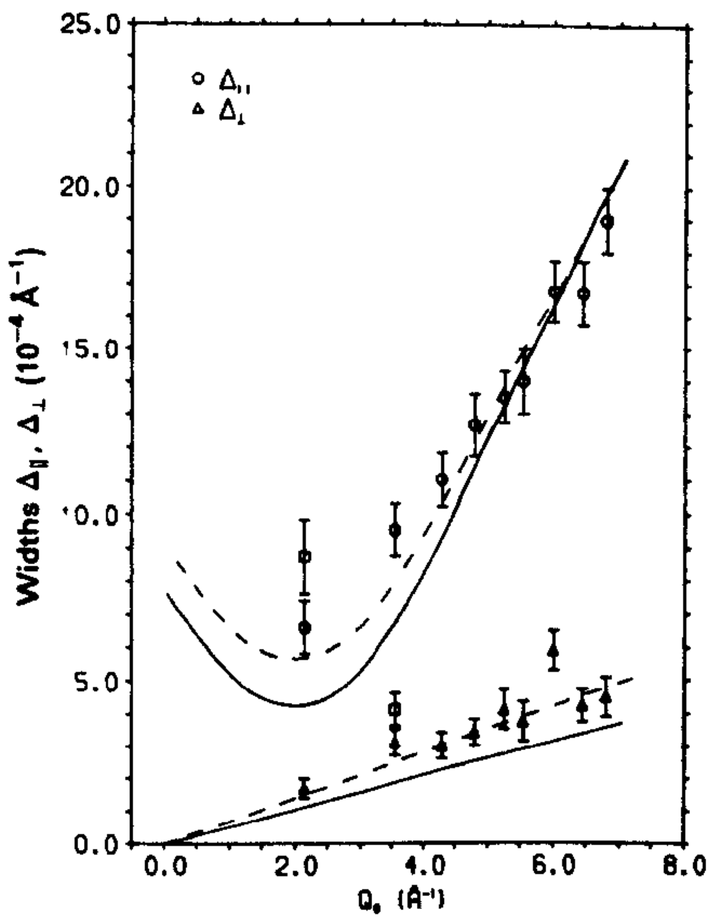

Fig. 2. The widths of the resolution function for the high-resolution mode with perfect germanium monochromator and analyser. The experimental results have been corrected for the Darwin width of the InP sample (circles). The correction is smaller than the error bars except for two low-Q points where the uncorrected data are shown by squares. The solid line is the calculated width using the theoretical Darwin width of Ge (111) planes and the dotted line is calculated with the Darwin width increased by 33%.

to the surface plane and was etched to remove any surface damage. The sample was oriented in an extended face geometry on the diffractometer, with either a [001] or [01$\bar{1}$] axis vertical and perpendicular to the scattering plane. Clearly the Darwin width of the InP or GaAs crystal has an effect on the observed scattering, especially in the high-resolution configuration. In this case in comparing experiment and theory it is necessary to incorporate the effect of the Darwin widths; this is described in § III.

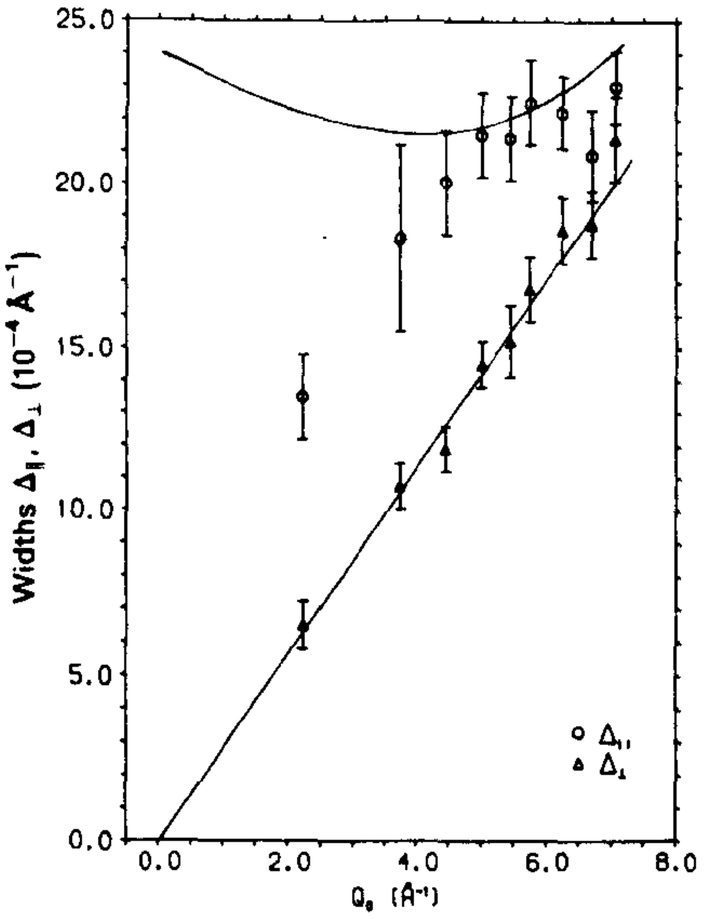

Fig. 3. The widths of the resolution function with the distorted Ge monochromator and analyser. The solid lines are the Gaussian theory with each Ge crystal having a mosaic width of 0·023°.

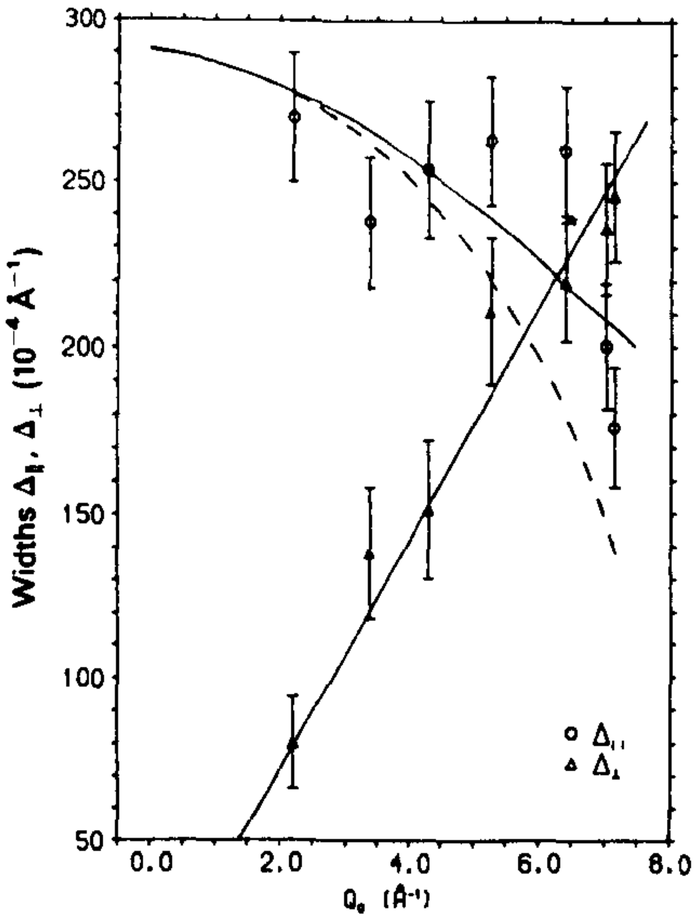

Fig. 4. The width of the resolution function with the pyrolytic-graphite monochromator and analyser. The dotted curve is the Gaussian theory with $\Delta\lambda/\lambda = 3{\cdot}5 \times 10^{-4}$ and mosaic 0·29°, while the solid curve has $\Delta\lambda/\lambda = 2{\cdot}5 \times 10^{-3}$.

For each experimental arrangement, the resolution function was measured in the transverse ($\delta Q_\perp$) and longitudinal ($\delta Q_\parallel$) directions by rocking the sample (a ψ scan in the notation of Fig. 1) or by scanning the sample and analyser arm in a ratio of 1:2 ($\psi - \varphi = 2\psi$ scan). The ψ and φ axes had an angular precision of better than 0·001°. These measurements were performed for the InP 200, 400 and 600 symmetric reflections and for the 311, 422, 511 and 622 asymmetric reflections. The crystal was then rotated by 45° in the surface plane, enabling additional measurement at the 420, 440 and 620 Bragg reflections. For all the asymmetric reflections both shallow and deep entry angles of incidence were used, to study, for example, both the 311 and 3$\bar{1}\bar{1}$ reflections. The results of these experiments are shown in Figs. 2–4.

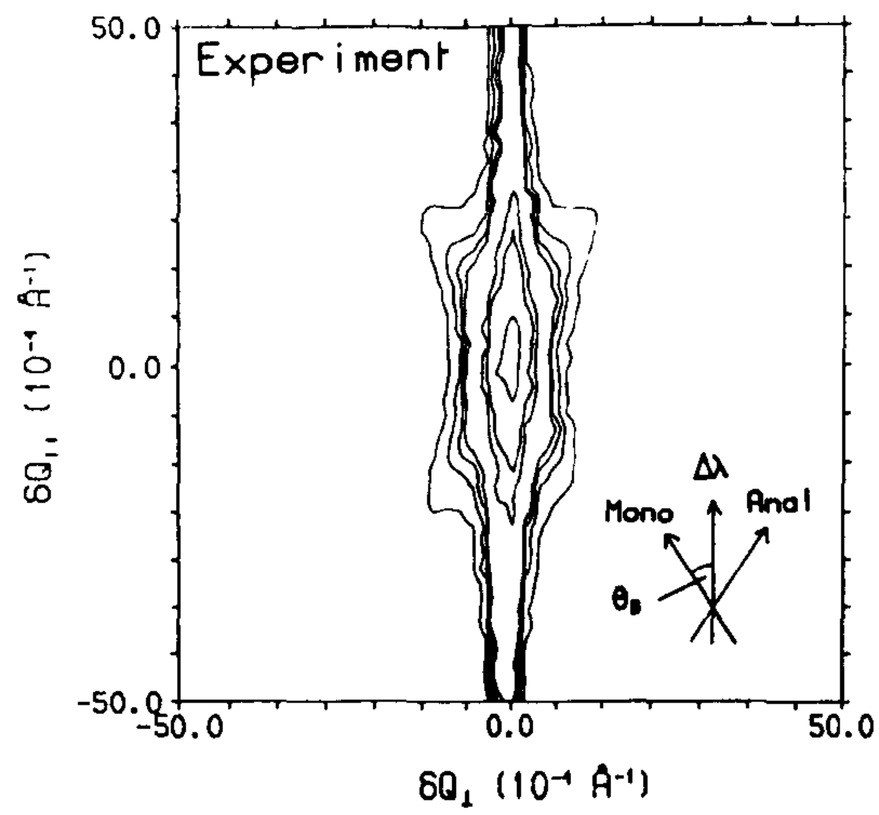

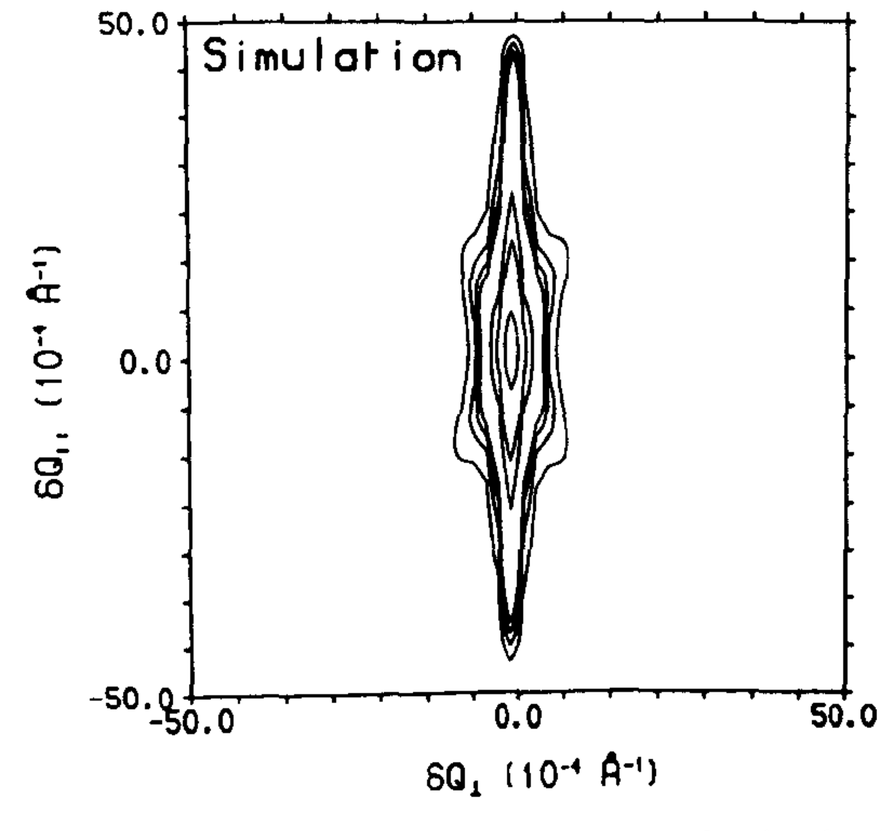

Fig. 5. A contour map of the scattered intensity in the high-resolution configuration around the InP 400 reflection as measured and as calculated by the convolution theory. The figure shows the directions of monochromator, analyser, and $\Delta\lambda$ streaks. The contour levels are 0·5, 0·1, 0·05, 0·01, 0·0075, 0·005 and 0·0025 of the peak intensity. The Bragg angle for this reflection, θ_B, is ~31·6°.

In addition to the measurements of the half-widths, a detailed study was made of the intensity distribution of the scattered X-rays around several of the Bragg reflections in the high resolution mode. The results are presented as contour maps with contours down to the 0·25% level in Figs. 5–7.

2. *Qualitative description of the resolution*

The high-resolution measurements shown in Figs. 5–7 are initially unexpected, in that the shape of the contours varies with their intensity level. The contours down to the 5% level are within error simple ellipses with the principal axes oriented parallel and perpendicular to the wave-vector transfer. This is as expected on the basis of the Gaussian theory of the resolution function (Cowley, 1987). The lower contours have a much more complex shape (Figs. 5–7), and these shapes cannot be explained by the Gaussian theory. These effects arise because the resolution-determining elements, the line width of the source, and the reflectivities of the perfect monochromator and analyser crystals, are not described by Gaussians but have larger wings dependent upon the square of the deviation from the nominal ray. As a result of this there are streaks corresponding to rays which pass through the central part of all except one of the resolution elements. Following the work of Ryan (1986) we now consider the location of these streaks in reciprocal space as an effect of each of the resolution elements in turn.

(*a*) *The monochromator.* The Darwin curve describing the reflectivity of the monochromator has $1/\delta\theta_M^2$ tails and these give rise to deviations in the direction of the incident beam. As illustrated in Fig. 8, if the angle of scattering at the sample is φ these then give rise to streaks at an angle $\varphi/2$ to the wave-vector transfer. Since the $1/\delta\theta^2$ tails arise from the surface scattering (Andrews & Cowley, 1985; Robinson, 1986) their effect can be reduced by using a monochromator with a rough surface, but the crystal structure must then remain perfect if the resolution is not to be degraded. If the monochromator is a mosaic

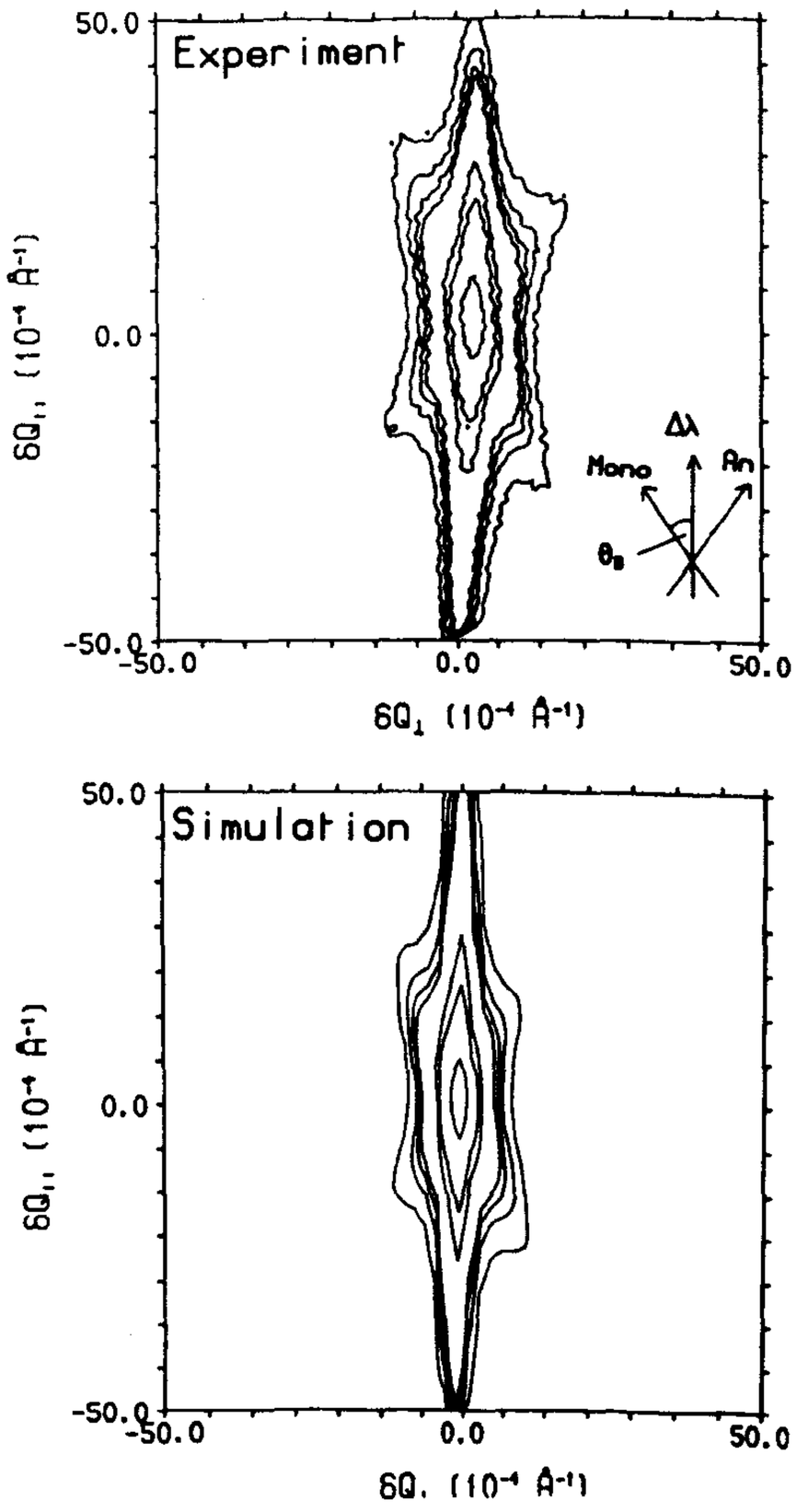

Fig. 6. The InP 420 reflection in the same representation as Fig. 5.

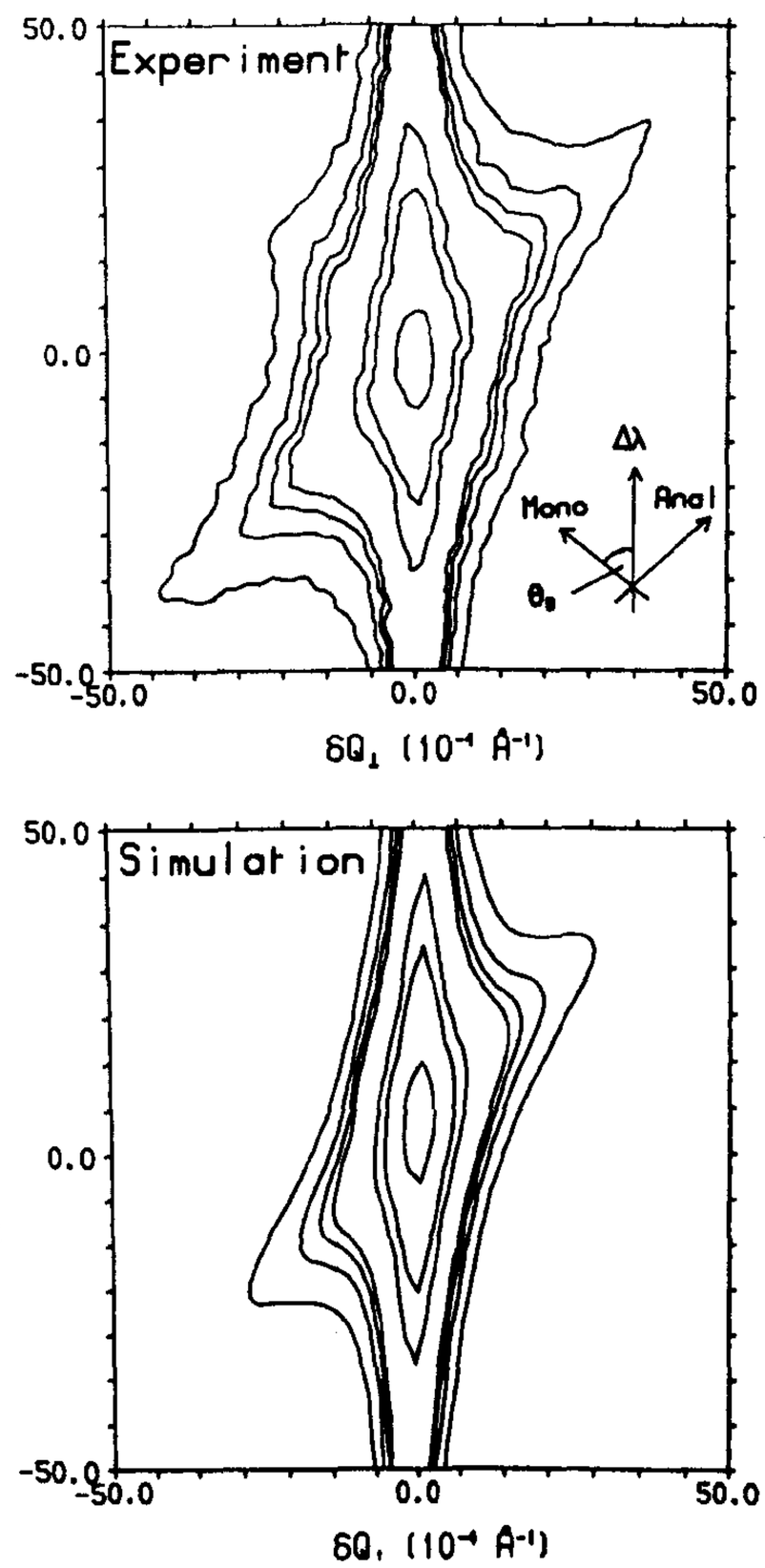

Fig. 7. The InP 4$\bar{4}$0 reflection in the same representation as Fig. 5.

crystal with different mosaic domains this may produce a similar streak with a form which reflects the mosaic structure.

(*b*) *The analyser.* The effect of the Darwin curve of the analyser is to allow deviations in the direction of the scattered beam, and so produces a streak perpendicular to that direction. As shown in Fig. 8, this is at an angle of $-\varphi/2$ to the wave-vector transfer. Experimentally it is usually found that this streak is more intense than that arising from the monochromator. Both of these streaks are clearly visible in Figs. 5–7.

(*c*) *The wavelength spread.* The characteristic line in the X-ray spectrum has a Lorentzian form, with $(1/\Delta\lambda)^2$ tails. Furthermore it is superimposed on the continuous spectrum which has $\sim 10^{-3}$ of the intensity of the characteristic line. For measurements at low levels of intensity it is then essential to understand the effects of the spread in incident wavelength. Experimentally the spread in wavelengths is reduced by a slit in front of the monochromator and the detailed shape of the effect of the wavelength spread depends critically on the positioning of this slit.

The effect of different wavelengths from a very small spot on the rotating anode is to give, after reflection on the monochromator, a beam whose direction depends on the wavelength or wave vector as shown in Fig. 8. For a triple-crystal spectrometer in the focusing configuration of Fig. 1, the change in the wave vector δk results in a change in the wave-vector transfer

$$\delta Q_{\parallel} = \delta k(2\tan\varphi/2 - \tan\theta_M - \tan\theta_A)\cos\varphi/2$$

$$\delta Q_{\perp} = \delta k(\tan\theta_M - \tan\theta_A)\sin\varphi/2.$$

In the usual symmetric case with $\theta_M = \theta_A$, this shows that the spread in wavelength is along the wave-vector transfer. As is well known, focusing occurs if the scattering angle $\varphi = 2\theta_M = 2\theta_A$.

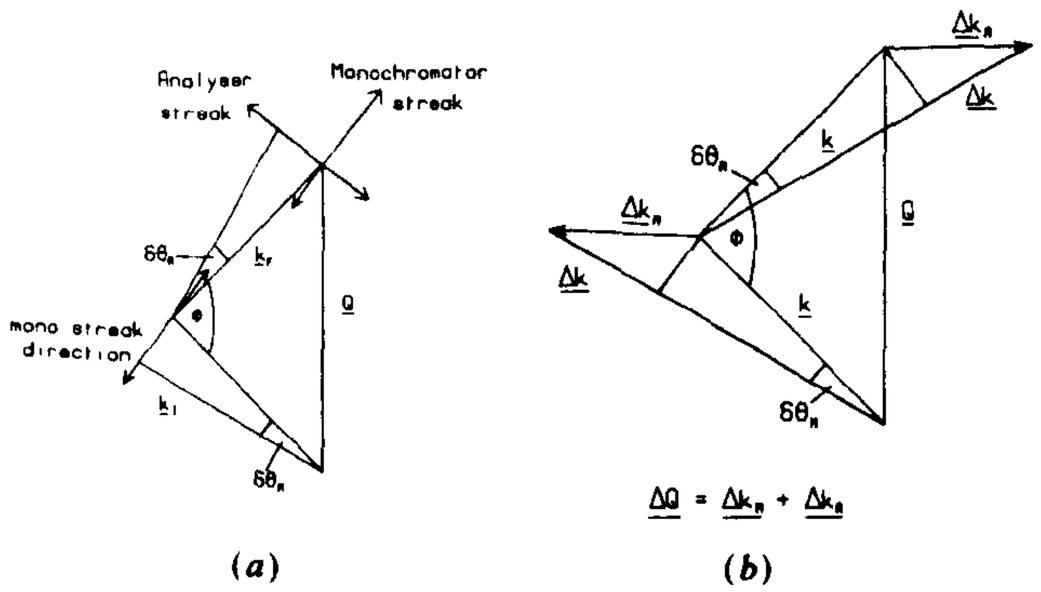

Fig. 8. The origin of the streaks in the wings of the resolution function. (*a*) The direction of the monochromator and analyser streaks. (*b*) The effect of a wavelength spread.

(*d*) *The specimen.* An ideal extended-face sample also has its reflectivity given by the Darwin curve, with $(1/\delta q)^2$ tails resulting from the surface scattering. Consequently the sample Bragg reflection is broadened in reciprocal space perpendicular to the extended face of the crystal in real space. For symmetric reflections, for which the wave-vector transfer is perpendicular to the sample surface, it is then impossible to distinguish between the $\Delta\lambda$ and specimen streaks unless the reflection is one with no wavelength dispersion. However, for asymmetric reflections the specimen and $\Delta\lambda$ streaks are in different directions.

In Figs. 5–7 the directions of the different streaks are clearly seen, and support the predictions of the simple theory given above. If the contour maps are extended to lower levels then these streaks become even more prominent.

III. Comparison with theory

1. *Gaussian theory*

The Gaussian theory of the resolution function is derived by assuming that all the resolution elements can be described by Gaussian response functions (Cowley, 1987). The theory then predicts that the resolution function is an ellipsoid in reciprocal space, with its principal axes parallel and perpendicular to the wave-vector transfer. Furthermore the theory gives explicit and relatively simple expressions for the widths of the resolution function.

In Fig. 2 we show the longitudinal and transverse widths of the resolution function as a function of wave-vector transfer. These were calculated using the theoretical Darwin width for the monochromator and analyser of $4{\cdot}3 \times 10^{-3}$ °. The experimental results were measured as described in § II, and corrected for the Darwin width of the InP sample crystal. The correction was calculated by using the Gaussian formalism and convoluting the calculated resolution function with a Gaussian representing the sample Darwin width. Except for the two reflections at the smallest wave-vector transfers, 200 and 311, the resulting corrections were smaller than the error bars. For these two points both the uncorrected widths and corrected widths are shown in Fig. 2. The experimental results are clearly in reasonable agreement with the theory, especially in view of the fact that there are no adjustable parameters in the theoretical calculations. Nevertheless the calculated transverse widths are approximately 75% of the measured ones and the minimum in the longitudinal widths at 2 Å^{-1} is also too small. Both of these features are largely dependent on the germanium Darwin widths of the monochromator and analyser, whereas the longitudinal widths for wave vectors $Q = 5$–$7\ \text{Å}^{-1}$, which are largely dependent on the wavelength spread, give excellent agreement between theory and experiment.

Consequently we also show in Fig. 2 calculations with the Darwin width increased to $5{\cdot}7\times10^{-3}$°. There is then very satisfactory agreement between the calculations and experiment.

There are two possible reasons why the agreement is better with a larger-than-theoretical Darwin width. It may be that the germanium is not perfect, but has a small mosaic width in addition to the Darwin width. Alternatively, it may be that the Gaussian approximation underestimates the width because the Darwin curve is not of a Gaussian form. The convolution of two equal-width Gaussians gives a Gaussian of width $\sqrt{2}$ larger than a single Gaussian, whereas the convolution of two Lorentzians gives a curve of twice the width. The larger width may then result from the inadequacy of the Gaussian approximation to the Darwin curve. Evidence against this latter suggestion is provided by the numerical convolution theory described in the next section. The widths calculated with this theory are also too small, suggesting that the reason for the discrepancy is that the germanium monochromator and analyser crystals are not perfect.

The results of the experiments performed with poor-quality germanium monochromator and analyser and a GaAs sample are shown in Fig. 3. In this case corrections for the Darwin width of GaAs are negligible. The widths were calculated by adjusting the mosaic widths of the monochromator and analyser, and a good description of the transverse widths was obtained when these both had a width of 0·023°, as shown in Fig. 3. The measured mosaic spread of the monochromator crystal was 0·021°. The longitudinal widths are then in good agreement with experiment for wave vectors greater than 4 Å^{-1}, but at smaller wave vectors the observed widths are significantly smaller than those calculated. We do not understand the origin of this discrepancy.

In Fig. 4 we show the results obtained with the pyrolytic-graphite monochromator and analyser together with the InP sample. The mosaic spread of the graphite crystals was found by adjusting the calculated transverse widths to give agreement with experiment when $\eta_M = 0{\cdot}29°$. Calculations of the longitudinal width were then made with a wavelength spread equal to the width of the $K\alpha_1$ line, shown by the dotted line, and with $\Delta\lambda/\lambda = 2{\cdot}5\times10^{-3}$, the separation between the $K\alpha_1$ and $K\alpha_2$ lines. These calculations clearly give a good description of the experimental results.

2. *The convolution theory*

The reflectivity of perfect crystals is described by the Darwin curve rather than a Gaussian curve and therefore a detailed description of the resolution function of a triple-crystal X-ray diffractometer requires a convolution of Darwin profiles. This was first performed by Pynn *et al.* (1983) but they considered only the central part of the resolution function. The calculations have now been extended by Gartstein (1989) to obtain a more detailed form of the intensity distribution around Bragg reflections. We shall not repeat the details of the calculations here but merely comment that accurate numerical calculations require a careful treatment of the different rays in the diffractometer, leading to quite lengthy numerical convolutions.

Calculations were performed to compare with the observed scattering for three reflections, 400, 420 and 44$\bar{0}$, taking into account the Darwin widths of the InP sample. The results are shown as contour maps in Figs. 5–7, with the same contour levels as those plotted for the experiment. Clearly there is reasonable agreement between experiment and theory, although the experimental results are slightly broader in the direction perpendicular to the wave-vector transfer.

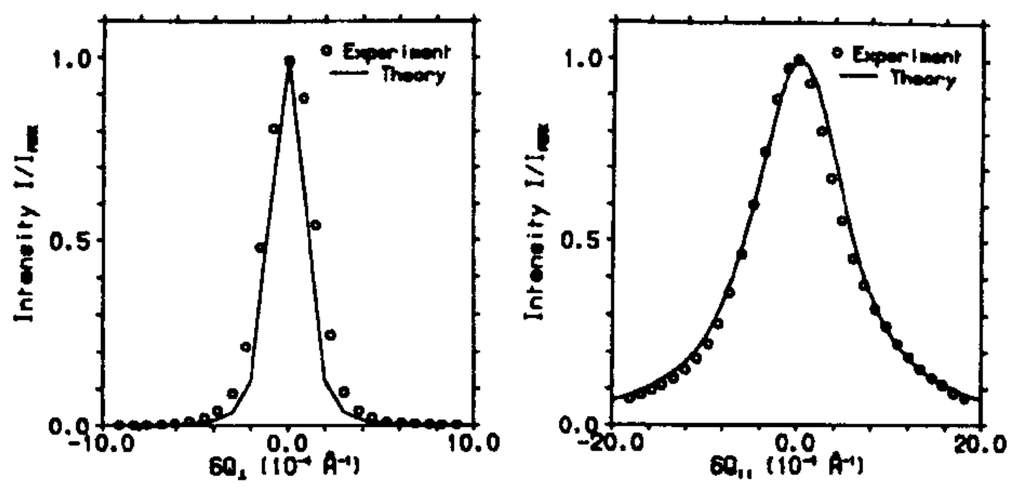

Fig. 9. The longitudinal and transverse profiles through the InP 400 reflection as measured and as calculated with the convolution theory using the nominal Darwin-width values for the high-resolution configuration.

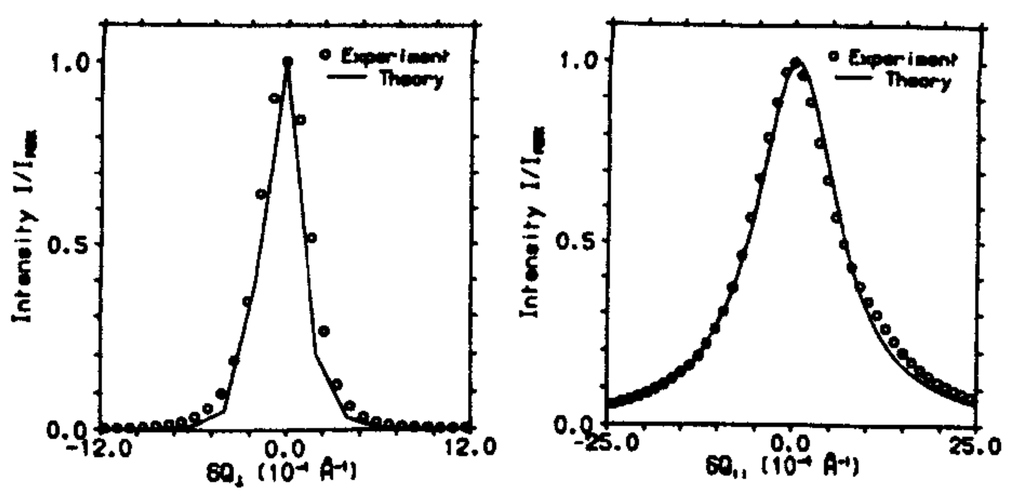

Fig. 10. The InP 420 reflection as for Fig. 9.

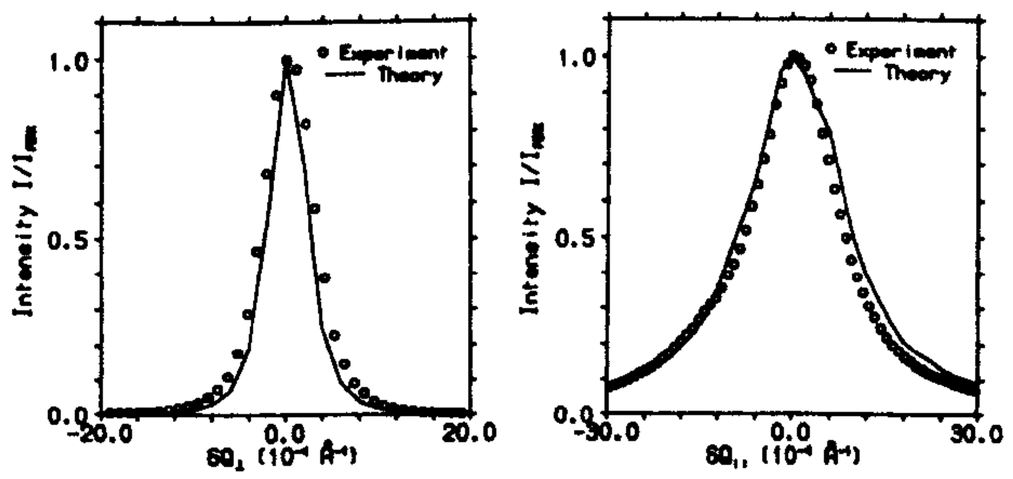

Fig. 11. The InP 44$\bar{0}$ reflection as for Fig. 9.

An alternative comparison is of the longitudinal and transverse scans through the centres of the Bragg reflections, and these are shown in Figs. 9–11. The theoretical transverse widths are systematically smaller than the measured widths by about 20%, in reasonable agreement with the discrepancy between the Gaussian theory and the measured transverse widths shown in Fig. 2. The longitudinal widths for the 400 and 420 reflections are in good agreement with experiment but the calculation for the $44\bar{0}$ reflection is slightly broader than expected. This may be due to a reduction in the wavelength spread caused by the positioning of the pre-monochromator slit in the experiment.

IV. Concluding remarks

In this paper we have presented a detailed theoretical and experimental study of the resolution function of a triple-crystal X-ray diffractometer based on a rotating-anode source. Two different theories are compared with the experimental results.

In the Gaussian approximation theory, analytic and relatively simple expressions are used to calculate the widths of the central part of the resolution function. The comparison with experiment shows that the theory predicts the widths with an accuracy of better than 25% for a variety of different diffractometer configurations. The accuracy is improved if the Darwin widths of the monochromator and analyser crystals are adjusted to fit the data at one wave-vector transfer.

A more complicated theory, involving numerical convolution of the Darwin profiles, enables the detailed form of the resolution function to be calculated in the high-resolution configuration. This theory not only successfully describes the central part of the resolution function, but also the qualitative features of the scattered intensity away from the Bragg peak. The streaks, which appear at low intensity levels, are caused by the asymmetric form of the monochromator and analyser response functions. A simple account of the origin and direction of the streaks is given in § II.2. Unfortunately a detailed description requires a full knowledge of the monochromator and analyser response functions. These depend critically on the surface roughness of the crystals which is not usually controlled in an experiment.

We are grateful for the technical support of H. Vass, and for the financial support of the Science and Engineering Research Council.

References

ANDREWS, S. R. & COWLEY, R. A. (1985). *J. Phys. C*, **18**, 6427–6439.
ANDREWS, S. R. & COWLEY, R. A. (1986). *J. Phys. C*, **19**, 615–635.
BATTERMAN, B. & COLE, H. (1964). *Rev. Mod. Phys.* **36**, 681–717.
BJERRUM-MØLLER, H. & NIELSEN, M. (1970). *Instrumentation for Neutron Inelastic Scattering Research*, pp. 49–76. Vienna: International Atomic Energy Agency.
CHESSER, N. J. & AXE, J. D. (1973). *Acta Cryst.* A**29**, 160–169.
COOPER, M. J. & NATHANS, R. (1967). *Acta Cryst.* **23**, 357–367.
COWLEY, R. A. (1987). *Acta Cryst.* A**43**, 825–836.
COWLEY, R. A. & RYAN, T. W. (1987). *J. Phys. D*, **20**, 61–68.
GARTSTEIN, E. (1989). In preparation.
PYNN, R., FUJII, Y. & SHIRANE, G. (1983). *Acta Cryst.* A**39**, 38–46.
ROBINSON, I. K. (1986). *Phys. Rev. B*, **33**, 3830–3836.
RYAN, T. W. (1986). PhD thesis. Univ. of Edinburgh, Scotland.
RYAN, T. W., NELMES, R. J., COWLEY, R. A. & GIBAUD, A. (1986). *Phys. Rev. Lett.* **56**, 2704–2707.
STEDMAN, R. (1968). *Rev. Sci. Instrum.* **39**, 878–883.
ZACHARIASEN, W. H. (1945). *Theory of X-ray Diffraction in Crystals*. New York: Wiley.

Acta Cryst. (1989). A**45**, 422–427

Distortion of the Zeroth-Order Laue-Zone Pattern Caused by Dislocations in a Silicon Crystal*

BY JIANGUO WEN, RENHUI WANG AND GANGHUA LU†

Department of Physics, Wuhan University, 430072 *Wuhan, People's Republic of China*

(*Received* 7 *November* 1988; *accepted* 18 *January* 1989)

Abstract

The effect of dislocations in a silicon single crystal on the zeroth-order Laue-zone (ZOLZ) pattern in large-angle convergent-beam electron diffraction (LACBED) has been studied experimentally. It is found that edge dislocations cause the ZOLZ pattern to be compressed or elongated and screw dislocations cause it to be dislocated. This phenomenon is the consequence of opposite shifts of the two halves of the Tanaka pattern, separated by the shadow image of the dislocation line along directions **b** and $-\mathbf{b}$ of the Burgers vector. The shift direction of each half

* Project supported by the National Natural Science Foundation of China.

† Also with Laboratory of Atomic Image of Solids, Institute of Metal Research, Academia Sinica, 110015 Shenyang, People's Republic of China.

0108-7673/89/060422-06$03.00

An alternative comparison is of the longitudinal and transverse scans through the centres of the Bragg reflections, and these are shown in Figs. 9–11. The theoretical transverse widths are systematically smaller than the measured widths by about 20%, in reasonable agreement with the discrepancy between the Gaussian theory and the measured transverse widths shown in Fig. 2. The longitudinal widths for the 400 and 420 reflections are in good agreement with experiment but the calculation for the $44\bar{0}$ reflection is slightly broader than expected. This may be due to a reduction in the wavelength spread caused by the positioning of the pre-monochromator slit in the experiment.

IV. Concluding remarks

In this paper we have presented a detailed theoretical and experimental study of the resolution function of a triple-crystal X-ray diffractometer based on a rotating-anode source. Two different theories are compared with the experimental results.

In the Gaussian approximation theory, analytic and relatively simple expressions are used to calculate the widths of the central part of the resolution function. The comparison with experiment shows that the theory predicts the widths with an accuracy of better than 25% for a variety of different diffractometer configurations. The accuracy is improved if the Darwin widths of the monochromator and analyser crystals are adjusted to fit the data at one wave-vector transfer.

A more complicated theory, involving numerical convolution of the Darwin profiles, enables the detailed form of the resolution function to be calculated in the high-resolution configuration. This theory not only successfully describes the central part of the resolution function, but also the qualitative features of the scattered intensity away from the Bragg peak. The streaks, which appear at low intensity levels, are caused by the asymmetric form of the monochromator and analyser response functions. A simple account of the origin and direction of the streaks is given in § II.2. Unfortunately a detailed description requires a full knowledge of the monochromator and analyser response functions. These depend critically on the surface roughness of the crystals which is not usually controlled in an experiment.

We are grateful for the technical support of H. Vass, and for the financial support of the Science and Engineering Research Council.

References

ANDREWS, S. R. & COWLEY, R. A. (1985). *J. Phys. C*, **18**, 6427–6439.
ANDREWS, S. R. & COWLEY, R. A. (1986). *J. Phys. C*, **19**, 615–635.
BATTERMAN, B. & COLE, H. (1964). *Rev. Mod. Phys.* **36**, 681–717.
BJERRUM-MØLLER, H. & NIELSEN, M. (1970). *Instrumentation for Neutron Inelastic Scattering Research*, pp. 49–76. Vienna: International Atomic Energy Agency.
CHESSER, N. J. & AXE, J. D. (1973). *Acta Cryst.* A**29**, 160–169.
COOPER, M. J. & NATHANS, R. (1967). *Acta Cryst.* **23**, 357–367.
COWLEY, R. A. (1987). *Acta Cryst.* A**43**, 825–836.
COWLEY, R. A. & RYAN, T. W. (1987). *J. Phys. D*, **20**, 61–68.
GARTSTEIN, E. (1989). In preparation.
PYNN, R., FUJII, Y. & SHIRANE, G. (1983). *Acta Cryst.* A**39**, 38–46.
ROBINSON, I. K. (1986). *Phys. Rev. B*, **33**, 3830–3836.
RYAN, T. W. (1986). PhD thesis. Univ. of Edinburgh, Scotland.
RYAN, T. W., NELMES, R. J., COWLEY, R. A. & GIBAUD, A. (1986). *Phys. Rev. Lett.* **56**, 2704–2707.
STEDMAN, R. (1968). *Rev. Sci. Instrum.* **39**, 878–883.
ZACHARIASEN, W. H. (1945). *Theory of X-ray Diffraction in Crystals.* New York: Wiley.

Acta Cryst. (1989). A**45**, 422–427

Distortion of the Zeroth-Order Laue-Zone Pattern Caused by Dislocations in a Silicon Crystal*

BY JIANGUO WEN, RENHUI WANG AND GANGHUA LU†

Department of Physics, Wuhan University, 430072 *Wuhan, People's Republic of China*

(*Received* 7 *November* 1988; *accepted* 18 *January* 1989)

Abstract

The effect of dislocations in a silicon single crystal on the zeroth-order Laue-zone (ZOLZ) pattern in large-angle convergent-beam electron diffraction (LACBED) has been studied experimentally. It is found that edge dislocations cause the ZOLZ pattern to be compressed or elongated and screw dislocations cause it to be dislocated. This phenomenon is the consequence of opposite shifts of the two halves of the Tanaka pattern, separated by the shadow image of the dislocation line along directions **b** and $-\mathbf{b}$ of the Burgers vector. The shift direction of each half

* Project supported by the National Natural Science Foundation of China.

† Also with Laboratory of Atomic Image of Solids, Institute of Metal Research, Academia Sinica, 110015 Shenyang, People's Republic of China.

0108-7673/89/060422-06$03.00

Reprinted from

Journal of
APPLIED PHYSICS

Volume 63 15 March 1988 Number 6

Characterization of nanometer-scale epitaxial structures by grazing-incidence x-ray diffraction and specular reflectivity

C. A. Lucas, P. D. Hatton, S. Bates, and T. W. Ryan
Department of Physics, University of Edinburgh, Mayfield Road, Edinburgh EH9 3JZ, Scotland
S. Miles and B. K. Tanner
Department of Physics, University of Durham, South Road, Durham DH1 3LE, England

pp. 1936-1941

a publication of the American Institute of Physics

Characterization of nanometer-scale epitaxial structures by grazing-incidence x-ray diffraction and specular reflectivity

C. A. Lucas, P. D. Hatton, S. Bates, and T. W. Ryan[a)]
Department of Physics, University of Edinburgh, Mayfield Road, Edinburgh EH9 3JZ, Scotland
S. Miles and B. K. Tanner
Department of Physics, University of Durham, South Road, Durham DH1 3LE, England

(Received 13 July 1987; accepted for publication 10 November 1987)

X-ray rocking curve analysis is a powerful and nondestructive technique for the characterization of heteroepitaxial structures. Conventionally, measurements are performed in symmetrical scattering geometry using a double-crystal x-ray diffractometer but the technique can be extended to the study of very thin layers (<200 Å) by the use of glancing-incidence scattering geometry and a triple-crystal diffractometer. These structures can also be studied by the technique of total external x-ray reflectivity. This is sensitive to the electron-density profile of the heterostructure as a function of depth. By combining the above techniques we have found it possible to obtain structural information on layers as thin as 20 Å. Such measurements permit accurate measurement of individual layer thicknesses and interface roughnesses on the angstrom level. The lattice parameter strain can be obtained by modeling of the intensity distribution of the crystal truncation rod.

I. INTRODUCTION

The technological importance of semiconductor heterostructures has led to increasing interest in the characterization of internal interfaces and buried layers. Although internal interfaces have many properties in common with surfaces, they are inaccessible to most standard surface analysis techniques which are nonpenetrating in nature. As a consequence, considerable attention has been focused on developing innovative experimental methods and data-analysis procedures with which to study these thin-layer systems. Although x-ray diffraction is normally considered a bulk structural characterization technique, three types of surface, or thin-film, sensitive x-ray measurements are available: (1) specular x-ray reflectivity, (2) crystal truncation rods, and (3) grazing-incidence x-ray crystallography.

At sufficiently small angles of incidence, x rays undergo total external reflection in matter and their penetration depth is greatly reduced. This idea was extended by Kiessig,[1] who showed that the modulation of the reflected intensity, at incident angles above the critical angle for total reflection, could provide information about the changes in electron density as a function of depth. The technique can therefore be used to study amorphous or crystalline films and accurately determine film thickness and interface roughness.[2]

A complimentary technique, applicable only to crystalline materials, is to measure the diffuse scattering arising near the Bragg reflected intensity from the underlying crystal lattice. In addition to the thermal diffuse scattering, which is almost isotropically distributed around the Bragg reflection, a well-defined rod of scattering occurs with wave-vector transfers $\mathbf{Q} = \mathbf{G} + \mathbf{q}$, where $\mathbf{G}$ is a reciprocal lattice vector and $\mathbf{q}$ is a wave vector perpendicular to the surface plane. This scattering is commonly known as a crystal truncation rod. The $|q|$ dependence of the truncation rod intensity is determined by the way in which the periodic lattice terminates.[3,4] If the crystal lattice is terminated on both sides, as in a crystalline heteroepitaxial layer, the substrate Bragg peaks are accompanied by a series of interference fringes which modulate the crystal truncation rod intensities.[5] We have previously shown that these fringes can be used to obtain values of the lattice parameter strain, film thickness, and interface roughness.[6]

In this paper we describe the contribution of the two outlined techniques in characterizing a GaAs/AlInAs/InP heteroepitaxially grown single quantum well structure.

II. EXPERIMENTS

The experiments were carried out at Edinburgh University using a triple-crystal x-ray spectrometer based on a Huber 430/440 goniometer, and utilizing a GEC Avionics GX21 rotating anode x-ray generator with a copper target. The incident and scattered wave vectors were defined by flat Ge(111) monochromator and analyzer crystals, giving a wave vector resolution in the scattering plane of the order 5×10^{-4} Å^{-1}. The wave-vector resolution of a triple-crystal diffractometer, and its advantages over the more conventional double-crystal instrument, have been discussed in detail elsewhere.[2,7,8]

The sample crystal, identification code MV494, was a single quantum well structure of AlInAs heteroepitaxially grown on [100] orientated InP. This layer was then capped with an ultrathin film of GaAs. The sample was grown by molecular-beam epitaxy (MBE), at British Telecom Research Laboratories, and its construction is shown schematically in Fig. 1. From growth rates the active layer was believed to be some 200 Å thick with the cap being only 20 Å thick.

In order to maximize the scattering contribution of the surface layers with respect to the substrate, it is advanta-

a) Permanent address: Phillips I&E, Lelyweg 1, 7602 EA, Almelo, The Netherlands.

 0021-8979/88/061936-06$02.40

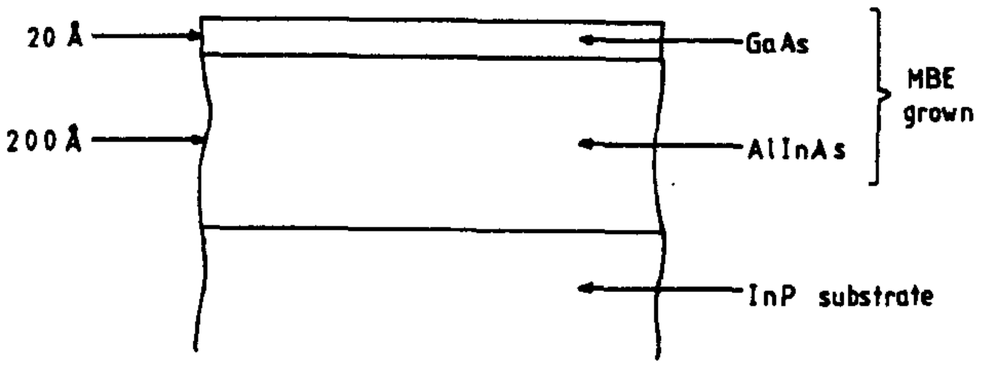

FIG. 1. The sample crystal consists of a 20-Å GaAs capping layer and a 200-Å AlInAs quantum well epitaxially grown on [100] oriented InP. The layer thicknesses were estimated from the growth conditions.

geous to adopt an extremely asymmetric Bragg scattering geometry. For a [100] surface orientated InP sample the (4,4,0) reflection, where the Bragg angle is 47.75° and the incidence angle is approximately 2.9°, is particularly suitable for glancing-incidence x-ray diffraction studies. The triple-crystal diffractometer provides high resolution in two dimensions in the scattering plane and it is therefore possible to map out the intensity distribution of scattered x rays in an area of reciprocal space. Figure 2 illustrates the intensity

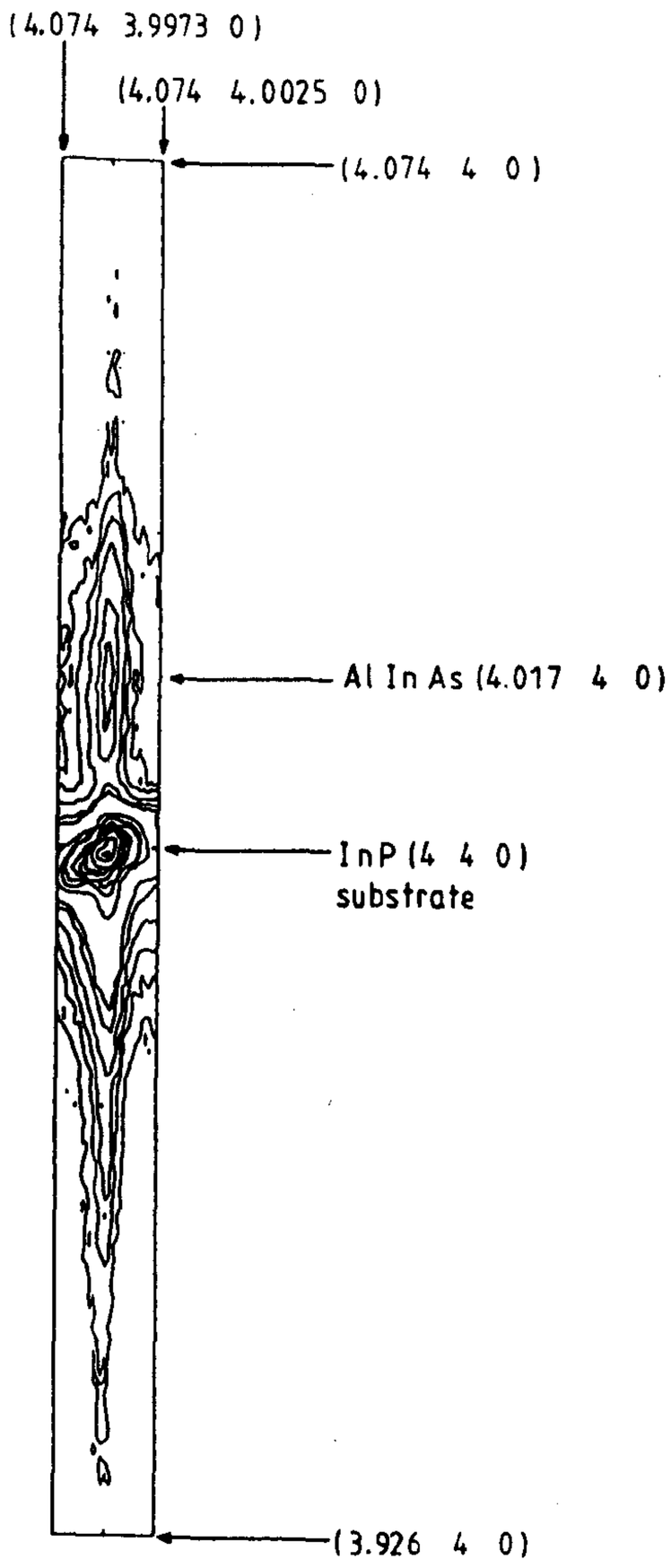

FIG. 2. An isointensity contour plot of the observed x-ray scattering in the region of the InP (440) Bragg peak. The data are presented on a quasi-logarithmic scale over four decades of intensity.

distribution for our sample, around the InP (440) reciprocal lattice point.

The equal-intensity contours are on a quasi-logarithmic scale over four decades of intensity and show the crystal truncation rod to be almost coincident with the [100] axis. The small peak at (4.0178,4,0) has an intensity approximately 10^{-3} that of the substrate (440) Bragg peak and originates in the quantum well layer of AlInAs. The width of the Bragg peaks in the [010] direction is a measure of sample mosaicity and homogeneity across the layer. High-resolution double-crystal rocking curve measurements give a width of 50 s which is approximately twice the instrumental resolution. The epitaxial layer is thus of excellent crystalline quality. The presence of the secondary Bragg peak is clearer in Fig. 3 which plots the integrated intensity along the face normal direction, over the scan range $\mathbf{q} = \pm 0.075a^*$. The logarithmic scale over five orders of magnitude emphasizes the weak scattering observed around the (440) Bragg peak. Such extremely weak features can only be observed by the enhanced sensitivity of the triple-crystal geometry. The Bragg peak positions and weak satellites highlighted in Fig. 3 give an apparent lattice parameter mismatch ($\Delta a/a$) between the tetragonally strained AlInAs layer and the InP substrate of -4.45×10^{-3} and are consistent with a layer thickness of $\sim$225 Å.

The sample was then examined using the specular x-ray reflectivity method, at glancing angles just above the critical angle for total external reflection. The refinements to the conventional x-ray reflectivity techniques and the precise experimental methods have been dealt with previously.[2] Results were obtained for values of the reflectivity R between 1 and 10^{-6} as a function of the scattering angle ϕ. It is convenient to describe the results in terms of $T = R\phi$.[4] The reflectivity data obtained from our sample is plotted on a logarithmic scale in Fig. 4. Fringes, arising from the 200-Å AlInAs layer, are clearly seen, and the pattern is modulated by a larger period, corresponding to reflection from a thin surface layer.

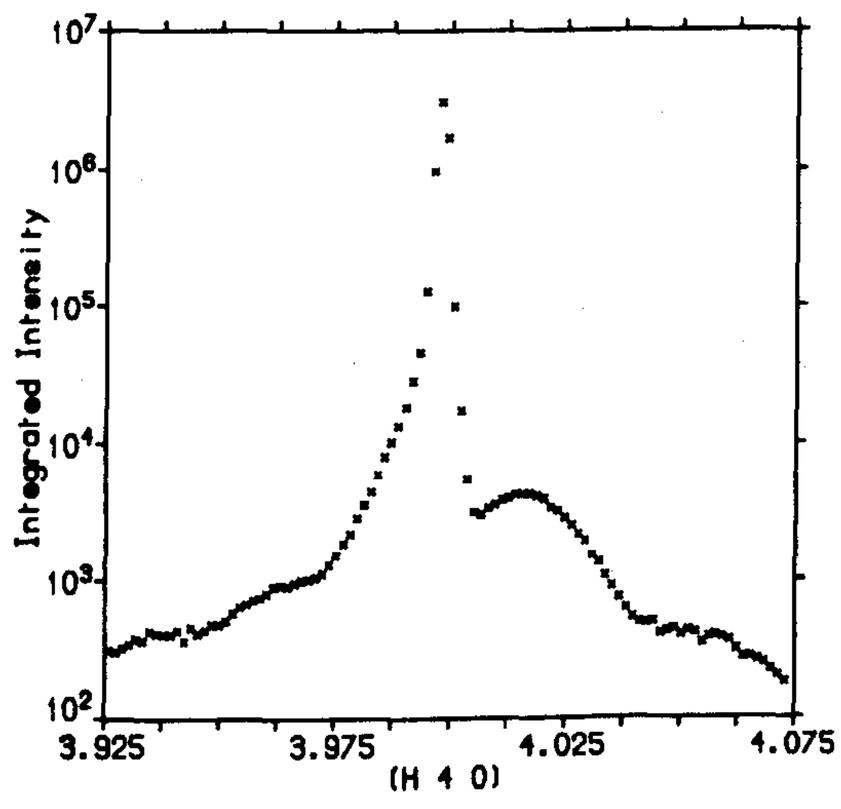

FIG. 3. The intensity distribution along [100], the face normal direction, through the InP (440) Bragg peak. The intensity is shown on a logarithmic scale.

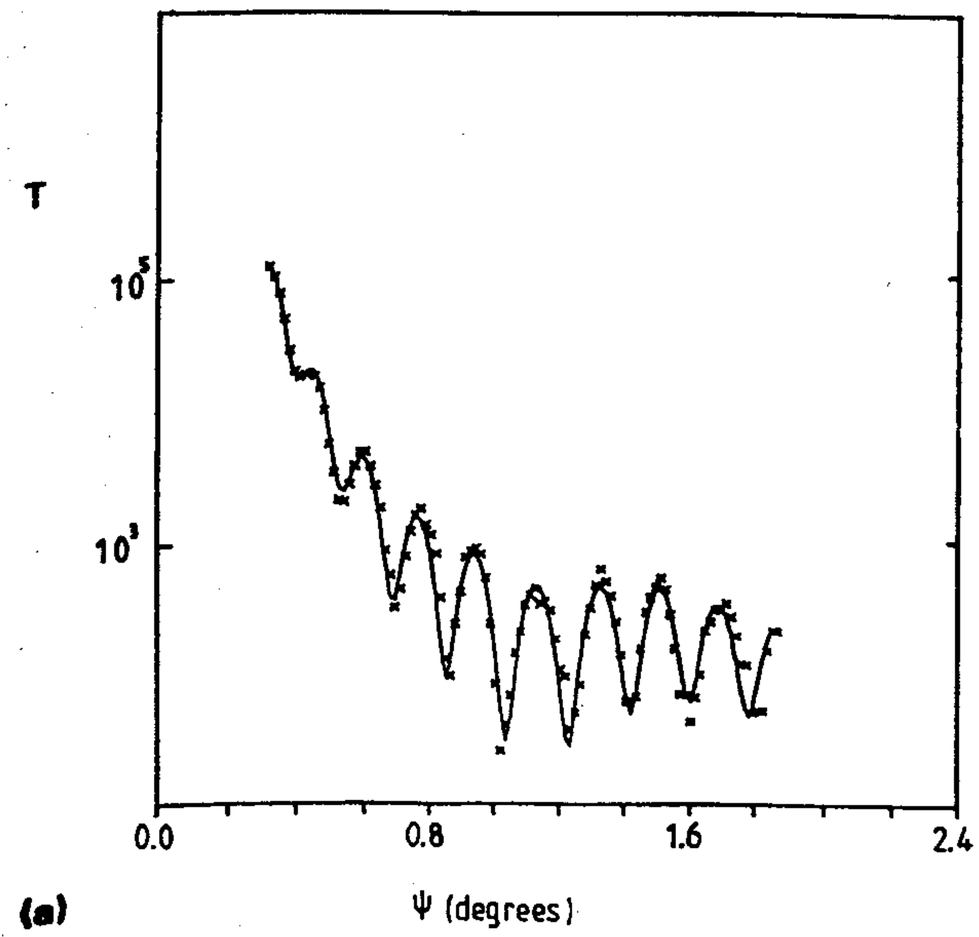

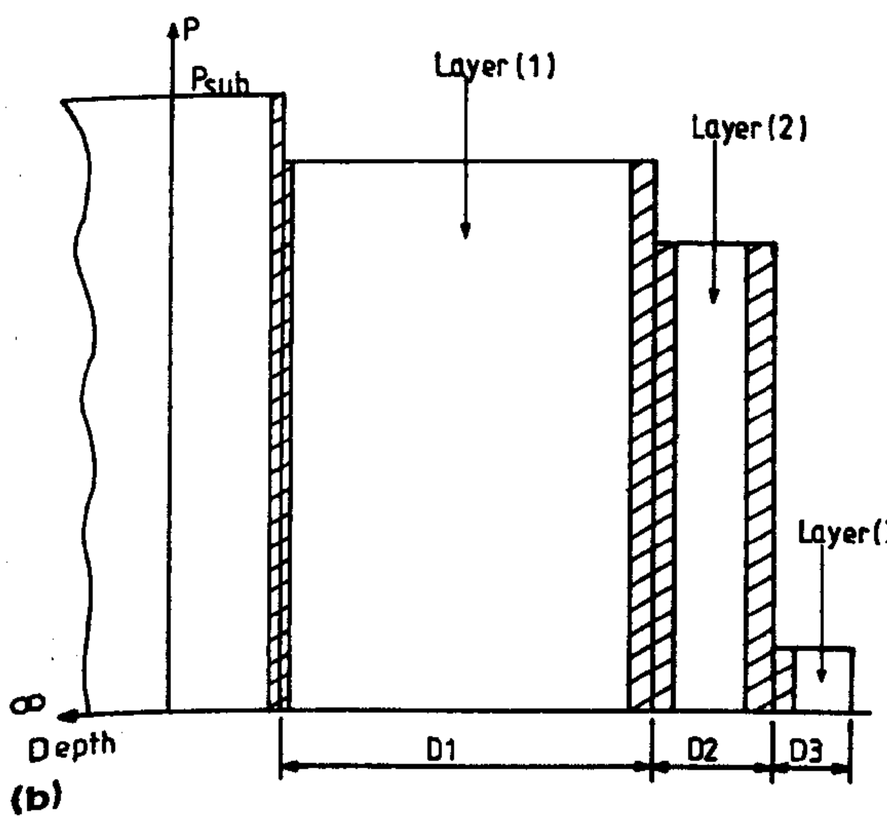

FIG. 4. (a) T, the reflectivity R multiplied by ϕ^4, plotted on a logarithmic scale against ϕ. The full curve gives the four-layer fit to the results, as defined by the parameters shown in Table II. (b) The electron density profile used for the calculated fit of Fig. 4(a).

III. THEORY AND ANALYSIS OF RESULTS

A. Crystal truncation rods

X-ray diffraction from a layered structure consisting of "thin" crystalline sheets can be expressed as a sum of the contributions from each interface of each crystalline layer.[5] Within the kinematic theory each of these terms assumes the general form

$$\pm A_0 G_j e^{i\mathbf{Q}\cdot\mathbf{r}_j} R_j Y_j (1 - e^{iQ_z a_j})^{-1}. \quad (1)$$

A_0 is an amplitude constant and G_j is the usual unit cell structure factor. The phenomenological damping term Y_j can be written as $e^{-\mu t_j}$ and is dependent on the path length t_j of the x rays before reaching the interface and the linear absorption coefficient μ_j of the propagation media. The roughness term R_j assumes a different Q dependence than the equivalent roughness term used in the reflectivity models, being periodic and centered on each Bragg peak. One of the most useful crystalline roughness expressions is

$$R_j = \exp[-\sigma_{pj}^2 \sin^2(Q_z a_j/2)], \quad (2)$$

where σ_{pj}^2 is the variance of the Poisson random variables used to model the random surface crystalline roughness.[9] For small Q_z the variance of this roughness expression σ_{pj}^2 can be directly compared with the equivalent reflectivity variance σ_n^2; with $\sigma_n^2 = a_j^2 \sigma_{pj}^2/2$. The phase term $e^{i\mathbf{Q}\cdot\mathbf{r}_j}$ is dependent on the position vector $\mathbf{r}_j$ of the layer, and the $(1 - e^{iQ_z a_j})^{-1}$ term generates the Bragg peaks arising from the periodic crystal lattice with lattice parameter a_j parallel to Q_z and normal to the layer.

For layers of thickness greater than the x-ray extinction length, the above kinematical expression ceases to be valid near the Bragg condition and dynamical effects need to be taken into consideration. In general this is of little consequence in the modeling of layered crystal stuctures where the interference effects away from the Bragg peaks are more sensitive to the details of the model.

The observed x-ray scattering in the region of the InP(440) Bragg peak (Fig. 3) was fitted within a least-square routine, assuming the heterostructure consists of a semi-infinite substrate and two thin crystalline layers. The resulting fit is shown in Fig. 5 with the fitting parameters listed in Table I. The values of the lattice parameter mismatch, and the thickness of the AlInAs [layer (1)] obtained from the fit, are considerably different from the parameters derived by inspection of the data. These differences arise from the interference effects taking place between the x rays diffracted from the different crystal layers, leading to false maxima and apparent peak shifting.

B. X-ray reflectivity

Parratt[10] showed how the x-ray reflectivity from a layered system could be derived by solving Maxwell's equations in the appropriate limit. This produces a recursion formula for the reflectivity from an interface.

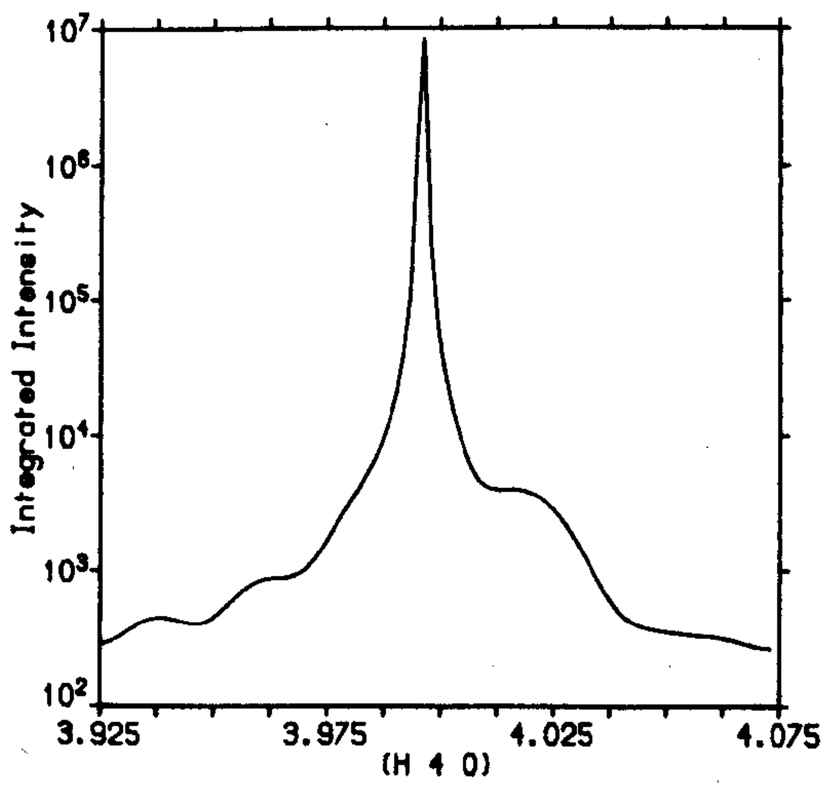

FIG. 5. A least-squares fit to the crystal truncation rod data in Fig. 3 according to a kinematical scattering model and the parameters in Table I.

TABLE I. Results of least-squares fit to the (440) truncation rod of Fig. 3. The rms roughness values σ_i have been expressed in angstroms to be compatible with the equivalent reflectivity roughness.

Layer (2)	$d_2 = 29 \pm 0.4$ Å	$\sigma_2 < 1$ Å	$\Delta a_2/\Delta a = 1.2\times10^{-3} \pm 0.3\times10^{-3}$
Disordered layer (2)	$d = 15 \pm 0.5$ Å		
Layer (1)	$d_1 = 204 \pm 0.4$ Å	$\sigma_1 = 1 \pm 0.7$ Å	$\Delta a_1/\Delta a = -8.1 \pm 0.2\times10^{-3}$
Disordered layer (1)	$d = 20 \pm 1$ Å		
InP substrate		$\sigma_0 = 2.5 \pm 1$ Å	

$$R_{n-1,n} = a_{n-1}^4 \left(\frac{R_{n,n+1} + F_{n-1,n}}{R_{n,n+1} F_{n-1,n} + 1} \right), \tag{3}$$

where

$$F_{n-1,n} = (f_{n-1} - f_n)/(f_{n-1} + f_n), \tag{4}$$

and for a layer of thickness d_n, with a critical angle $\psi_c(n)$

$$f_n = [\psi^2 - \psi_c^2(n)]^{1/2}, \tag{5}$$

and $a_n = \exp(-i\pi/\lambda f_n d_n)$.

The effect of absorption is the addition of a complex component to f_n

$$f_n = A_n - iB_n,$$

where

$$A_n = (1/\sqrt{2})(\{[\psi^2 - \psi_c^2(n)]^2 + 4\beta_n^2\}^{1/2} + [\psi^2 - \psi_c^2(n)])^{1/2},$$

$$B_n = (1/\sqrt{2})(\{[\psi^2 - \psi_c^2(n)]^2 + 4\beta_n^2\}^{1/2} - [\psi^2 - \psi_c^2(n)])^{1/2},$$

and

$$\beta_n = \lambda\mu_n/4\pi,$$

where μ_n is the linear absorption coefficient of the layer n. Roughness is most simply incorporated into the model by assuming a Gaussian form, whereby each interface reflectivity is multiplied by a factor

$$\exp -\tfrac{1}{2}[(4\pi\sigma_n/\lambda)\sin\psi]^2. \tag{6}$$

σ_n is the root-mean-square value of roughness for the layer n. The equation is solved by setting $R_{N,N+1} = 0$, for the substrate, and carrying out N recursive calculations, the ratio of reflected to incident intensity being obtained by taking the product of $R_{1,2}$ with its complex conjugate.

It has previously been shown that a simple two-layer system (film on substrate) displays a steadily decreasing intensity as ϕ increases, with superimposed oscillations arising from the interference between waves reflected from the first and second interfaces.[2] However, the general form of the data in Fig. 4(a) suggests a more complex behavior, characteristic of a number of layers. For a chosen model, the variable parameters of the theory are fitted to the data using least-squares refinement. The values of ψ_c are converted to mass density using the formula,

$$\psi_c = 1.64\times10^{-3}\lambda p^{1/2}, \tag{7}$$

and $\Delta p_i/p$ is the fractional difference in the density of the layer i from that of the substrate. The fit to the data in Fig. 4(a) was obtained using the parameters listed in Table II in a model represented by Fig. 4(b). Two thin surface layers, in addition to the 210 Å of AlInAs (layer 1) are required to produce the fit. Layer 2 corresponds to the GaAs "capping layer" of thickness 30 Å and there is an additional surface layer (layer 3) with a very low electron density. Previous experiments performed on Si/SiO_2 wafers (unpublished data) indicate that thin layers of surface contaminates, such as H_2O, can have a dramatic effect on the x-ray reflectivity from a surface. Reflectance infrared spectroscopic measurements of our sample showed complex absorption features at $\sim$2700 nm, corresponding to OH vibrations at or near the surface.

III. DISCUSSION

The fits to both the reflectivity and crystal truncation rods give the same crystalline layer thickness to within one unit cell, although the diffraction measurements are relatively insensitive to the thin capping layer [layer (2)]. The major discrepancy between the values obtained from the two different techniques lies in the nature of the internal interfaces. The reflectivity measurements suggest that the interfaces are rough, with a typical root mean square deviation of $\sim$7 Å. In contrast, the truncation rod measurements indicate that the crystal interfaces are relatively smooth with rms roughnesses of less than 1 Å. However, in order to achieve the observed fit it was necessary to introduce thin noncrystalline layers between the crystalline slabs (see Ta-

TABLE II. Results of least-squares fit to the x-ray reflectivity data of Fig. 4(a).

Layer (3)	$d_3 = 22.3 \pm 0.7$ Å	$\sigma_3 < 1$ Å	$\Delta p_3/p_0 = -0.90 \pm .0.02$
Layer (2)	$d_2 = 30.5 \pm 0.7$ Å	$\sigma_2 = 8.8 \pm 0.6$ Å	$\Delta p_2/p_0 = -0.24 \pm .0.02$
Layer (1)	$d_1 = 210.0 \pm 0.8$ Å	$\sigma_1 = 8.9 \pm 0.7$ Å	$\Delta p_1/p_0 = -0.11 + .0.04$
InP Substrate		$\sigma_0 = 4.2 \pm 0.8$ Å	

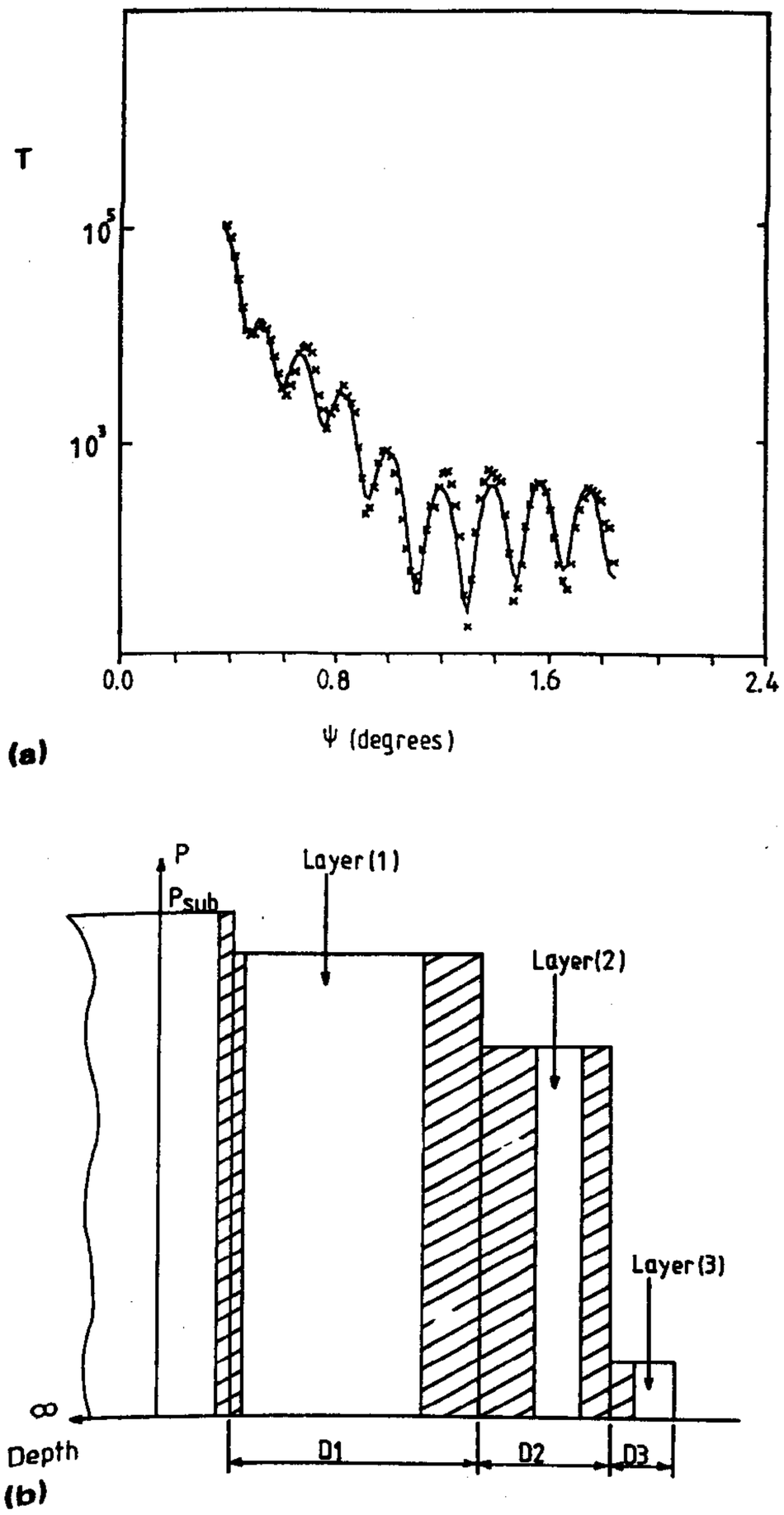

FIG. 6. (a) T, the reflectivity R multiplied by ϕ^4 plotted on a logarithmic scale, after baking at the sample in a vacuum oven. The dark line is the least-squares fit according to the parameters in Table III. (b) The electron density profile for the fit in Fig. 6(a) shows how the layer thicknesses have changed after oxidation into the quantum well.

ble I). These discrepancies are consistent with the existence of disordered or noncrystalline regions separating the crystalline layers. The disordered regions will not contribute to the scattering around the Bragg peaks, but will appear in the reflectivity data as an additional rough contribution to the underlying crystalline layers. Indeed if a loss of material occurs simultaneously with the disordering then the disordered region may appear as a roughened low-density layer. The effects of such regions on both the reflectivity and truncation rod measurements are treated in detail in the Appendix.

A comparison of the results obtained by the different techniques now shows them to be in excellent agreement. The thicknesses of the disordered noncrystalline layers (Table I) correspond to the Gaussian spreads of the interface roughnesses in the reflectivity model (Table II). The additional surface layer (layer 3) used in modeling the x-ray reflectivity profile is probably a disordered region containing absorbed water. The presence of water is indicated by the infrared measurements. During the investigation of contaminant layers on Si/SiO_2 wafers (unpublished data), it was discovered that baking of the wafer reduced the contamination to a level at which its effect, on the x-ray reflectivity measurements, was negligible. Due to the long timescale of the absorption process, x-ray data taken immediately after sample heating was found to be insensitive to any residual contamination. Prompted by the evidence of absorbed water, we heated our sample in a vacuum oven at 200 °C for 2 h before repeating the x-ray reflectivity and infrared measurements. The new reflectivity data are shown in Fig. 6(a). For simplicity, a four-layer model is again used to fit the data and this is represented by Fig. 6(b). Table III shows that the fitting parameters are significantly different from those used to describe the original data. The AlInAs layer has decreased in thickness to 197 Å, resulting in a proportional increase of layer 2. Considerable roughening of the interface between these layers indicates transfer across the boundary and it is concluded that the heating of the sample has induced oxidation into the AlInAs layer. The "roughness layer" (layer 3) is not altered by the heating process and the repeated infrared measurements again indicate the presence of adsorbed water. This manifestation of surface roughness, as a low-density surface layer, has also been observed in x-ray reflection studies of metal films.[11,12] A perfect fit to the data of Fig. 6(a) was impossible to obtain and this may be due to the inability of the model to account for graded electron density layers, which are likely to be present after oxidation.

IV. CONCLUSIONS

The experimental results presented in this paper have demonstrated that a combination of high-resolution x-ray diffraction and x-ray reflectivity measurements can reveal structural features on an angstrom scale in heteroepitaxial layer materials. The diffraction measurements are sensitive only to crystalline components of the sample and can be used to measure lattice parameter strain and layer thickness. The reflectivity measurements are also sensitive to amorphous or even liquid layers and so can reveal the presence of an oxide or contaminant layers with thicknesses down to 10 Å. The

TABLE III. Results of least-squares fit to the x-ray reflectivity data of Fig. 6(a).

Layer (3)	$d_3 = 23.1 \pm 0.7$ Å	$\sigma_3 < 1$ Å	$\Delta p_3/p_0 = -0.89 + 0.02$
Layer (2)	$d_2 = 45.4 \pm 0.8$ Å	$\sigma_2 = 9.3 \pm 0.7$ Å	$\Delta p_2/p_0 = -0.26 + 0.02$
Layer (1)	$d_1 = 197.0 \pm 0.9$ Å	$\sigma_1 = 20.3 \pm 0.8$ Å	$\Delta p_1/p_0 = -0.08 \pm 0.04$
InP substrate		$\sigma_0 = 4.0 \pm 0.8$ Å	

experimental measurements are quite straightforward, although the use of a triple-crystal x-ray spectrometer is essential in order to resolve the weak, diffuse scattering features from the background scattering.

A straightforward interpretation of the reflectivity measurements is possible by modeling the structure as a series of homogeneous dielectric slabs, a good approximation in the case of MBE grown heteroepitaxial layers. The diffraction data are modeled within a kinematic approximation which, although not correct for describing the main Bragg peak, enables the structural information, contained in the diffuse scattering, to be parameterized. Comparison of the results obtained by the two techniques shows good agreement between the common parameters and affirms the validity of the assumptions made in both cases.

Heating of the sample, a procedure intended to reduce surface contamination, caused a change in the x-ray reflectivity curve, consistent with oxidation into the AlInAs layer. Further studies of different systems under varying conditions are anticipated, together with a development in the theoretical treatment of the results. Wide applications for the combination of the two x-ray techniques in surface and structural studies are expected in the future.

ACKNOWLEDGMENTS

The authors would like to thank Professor R. A. Cowley for helpful discussions. The work was supported by a grant from the Science and Engineering Research Council.

APPENDIX: LOSS OF CRYSTALLINITY AT A CRYSTALLINE INTERFACE

For simplicity consider a semi-infinite crystalline block that can be divided into a perfect crystalline bulk and a gradually disordered surface region. Within the disordered region, on moving away from the perfect interface, the probability of finding each crystal unit cell in the correct crystal plane becomes progressively smaller. Such a probability function can be represented by the normalized Gaussian probability function

$$P(N) = (2\pi Na^2 w)^{-1/2} \exp(-Z^2/2Na^2 w). \quad \text{(A1)}$$

Here only the effects normal to the surface, the Z direction, are considered with a being the lattice parameter in that direction. N is the crystal layer index within the disordered region and w is the disordering constant. This probability function, in effect, describes a surface region that changes from perfect crystalline order to disorder within a few crystal layers as governed by the constant w. Ignoring absorption, the scattering from a general layer within the disordered region will be proportional to the Fourier transform of the probability function

$$A_N = A_0 G_j \int_{-\infty}^{\infty} P(N) e^{iQ_z Z}\, dZ,$$

$$= A_0 G_j e^{(-Q_z^2 Na^2 w/2)}. \quad \text{(A2)}$$

Taking the surface region to be n unit cells thick with the crystalline interface positioned at $\mathbf{r} \equiv 0$. The complete crystalline scattering amplitude can now be expressed as

$$A = A_0 G_j \left(\sum_{N=0}^{n-1} e^{iQ_z Na} e^{-(Q_z^2 Na^2 w/2)} + \sum_{N=0}^{-\infty} e^{iQ_z Na} \right). \quad \text{(A3)}$$

Away from Bragg peaks (i.e., $Q_z \neq 2n\pi/a$),

$$A = A_0 G_j \left(\frac{[1 - e^{iQ_z na}\ e^{(-Q_z^2 na^2 w/2)}]}{[1 - e^{iQ_z a}\ e^{(-Q_z^2 na^2 w/2)}]} + \frac{1}{(1 - e^{iQ_z a})} - 1 \right). \quad \text{(A4)}$$

Close to the high indexed Bragg peaks where Q_z is large, the two exponential damping terms tend to zero, giving a resultant scattering amplitude characteristic of a single interface.

$$A = A_0 G_j (1 - e^{iQ_z a}) - 1. \quad \text{(A5)}$$

By comparison with the general scattering amplitude expression for a single interface [Eq. (1)] we can say that the effective interface of the scattering system is smooth and positioned at $\mathbf{r} \equiv 0$, i.e., the disordered system is not observed.

As $Q_z \to 0$, for example reflectivity measurements, the form of the scattered amplitude changes. Assuming $e^{(-Q_z^2 na^2 w/2)} \sim 1$, then

$$A = -A_0 G_j e^{iQ_z na} e^{(-Q_z^2 na^2 w/2)} (1 - e^{iQ_z a})^{-1}. \quad \text{(A6)}$$

The effective interface of the system has now moved to $\mathbf{r} = na$, so at small Q_z the system appears to be thicker, increasing by the thickness of the disordered surface region. In addition, the interface appears to be rough with a roughness term $e^{(-Q_z^2 nq^2 w/2)}$. Replacing Q_z by $(4\pi/\lambda)\sin\theta$ the roughness assumes the same form as the general Gaussian roughness term used in the reflectivity model, with $\sigma_n = \sqrt{wna^2}$.

[1] H. Kiessig, Ann. Phys. **10**, 715 (1931).
[2] R. A. Cowley and T. W. Ryan, J. Phys. D **20**, 61 (1987).
[3] S. R. Andrews and R. A. Cowley, J. Phys. C **18**, 6427 (1985).
[4] I. K. Robinson, Phys. Rev. B **33**, 3830 (1986).
[5] S. Bates, P. D. Hatton, and T. W. Ryan (unpublished).
[6] T. W. Ryan, P. D. Hatton, S. Bates, M. Watt, C. Sotomayor-Torres, P. A. Claxton, and J. S. Roberts, Semicond. Sci. Technol. **2**, 241 (1987).
[7] R. A. Cowley, Acta Crystallog. A **37**, 825 (1987).
[8] T. W. Ryan, Ph.D. thesis (University of Edinburgh, 1986).
[9] D. Chrzan and P. Dutta, J. Appl. Phys. **59**, 1504 (1986).
[10] L. G. Parratt, Phys. Rev. **95**, 359 (1954).
[11] L. A. Smirnov and S. B. Anokhin, Opt. Spectrosc. **48**, 315 (1980).
[12] L. A. Smirnov, T.D. Sotnikov, V.S. Anokhin, and B. Z. Taibin, Opt. Spectrosc. **46**, 329 (1979).